



ACTIVE GALAXIES:

A Study of Local Seyferts and Ultra Luminous Infrared Galaxies

ECE KILERCI ESER

Dissertation
Submitted for the Degree

PHILOSOPHIÆ DOCTOR

Dark Cosmology Centre
The PhD School of Science
Faculty of Science
University of Copenhagen

Submission: 3/06/2014
Defence: 8/08/2014

Supervisor: *Prof. Marianne Vestergaard (NBI)*

Opponents: *Prof. Johan P. U. Fynbo (Chair, NBI)*
Prof. Sarah Gallagher (University of Western Ontario, Canada)
Prof. Alessandro Marconi (University of Florence, Italy)

ACKNOWLEDGMENT

I would like to thank my advisor, Marianne Vestergaard, for all her guidance, support, help and for being available to answer my questions all the time. I am grateful to my thesis committee Jens Hjorth and Michelle Cumming Løkkegaard for their continuous support and advice. I wish to thank Tomotsugu Goto, for introducing me the most exciting galaxies in the Universe and for inspiring me to find my own questions.

I thank all of my collaborators. I extend a special thanks to Brad Peterson and Kelly Denney for their help. I would like to acknowledge the OSU astronomy department for hosting me.

My DARK family, all the post-docs, faculty, admin and PhDs turned my PhD into a wonderful life experience with a lot of good memories. I would especially like to thank my dear friends Tayyaba Zafar, Martina Falco, Ia Kochiashvili for their support and hugs. I also thank Hanne Clausen, Hasse Calusen and Signe Byrdal Terenziani.

I thank my family for their support. My sister Vahide deserves a special thank. Last, I thank to my husband Oguz Omer Eser for his patience and love. He followed me through continents, he always believed in me and supported my scientific carrier with all means.

ABSTRACT

Galaxy formation and evolution is one of the main research themes of modern astronomy. Active galaxies such as Active Galactic Nuclei (AGN) and Ultraluminous Infrared Galaxies (ULIRGs) are important evolutionary stages of galaxies. The ULIRG stage is mostly associated with galaxy mergers and interactions. During the interactions of gas-rich galaxies, the gas inflows towards the centers of the galaxies and can trigger both star formation and AGN activity. The ULIRG stage includes rapid star formation activity and fast black hole growth that is enshrouded by dust. Once the AGN emission is sufficiently powerful, energy feedback from the AGN blows away the gas fuel and shuts off both the star formation and the black hole growth.

In this thesis I study local AGN and ULIRGs. I address 2 different studies of AGN: one is related to the potential use of AGN to measure cosmic distances and the other one is related to the mass estimates of supermassive black holes (SMBHs). Mass estimates of SMBHs are important to understand the formation and evolution of SMBHs and their host galaxies. Black hole masses in Type 1 AGN are measured with the reverberation mapping (RM) technique. Reverberation mapping analyses of ~ 50 nearby AGN show a tight correlation between the broad line region (BLR) radius (R) and the mean optical luminosity (L) that is known as the $R - L$ relationship. The $R - L$ relationship traditionally is used to formulate the mass scaling relationships, which are used estimate BH masses based on a single-epoch spectrum.

Recently, it has been shown that the $R - L$ relationship can also be used to measure cosmic distances beyond redshifts that can be probed by supernovae. The current local ($z < \sim 0.3$) RM AGN sample has a scatter of ~ 0.33 mag in the distance modulus. This scatter is directly related to the observed scatter of 0.13 dex in the $R - L$ relationship. In Chapter 2, I investigate the origin of the scatter in the $R - L$ relationship. I find that usage of the UV luminosity can potentially reduce the observed scatter in the $R - L$ relationship and thus the scatter in the AGN Hubble diagram which would help for our use of quasars as cosmic distance indicators.

The mass scaling relationships enables us to estimate BH masses of Type 1 AGN with an uncertainty of a factor of ~ 4 . An accurate line width characterization is important in order to minimize the uncertainty of the mass estimates based on the scaling relationships. In Chapter 3, I investigate the potential effect of the accretion luminosity on the line width characterization of the broad emission lines that are used in BH mass estimates. I use publicly available optical, UV and X-ray data to obtain quasi-simultaneous spectral energy distributions and directly measure the accretion luminosity. I find an inverse correlation between the Eddington luminosity ratio (accretion luminosity normalized by the BH mass) and the $H\beta$ line shape.

In Chapter 4, I present a catalog of local ULIRGs identified in the *AKARI* All-sky Survey. I identify new ULIRGs and increase the number of known ULIRGs in the local Universe. I use infrared and optical imaging and spectroscopic data from *AKARI* and SDSS. I investigate morphologies, optical spectral types, star formation rates (SFR), stellar masses (M_*), metallicities and, colors of the ULIRGs in my sample.

CONTENTS

Acknowledgment	iii
Abstract	iv
Contents	v
1 Introduction	1
1.1 A Brief Overview of Black Holes	1
1.2 Active Galactic Nuclei	3
1.2.1 Observational Properties	3
1.2.2 Structure and Unification	3
1.2.3 Spectral Energy Distributions	4
1.2.4 Accretion Luminosity	7
1.3 Mass Measurements of Supermassive Black Holes	8
1.3.1 Stellar - Gas Dynamics	10
1.3.2 Reverberation Mapping	10
1.3.3 Virial Black Hole Masses Based on Reverberation Mapping	11
1.3.4 Radius Luminosity Relationship	13
1.3.5 Mass Scaling Relationships	15
1.4 Ultraluminous Infrared Galaxies	16
1.5 Structure of the Thesis	21
2 ON THE SCATTER IN THE RADIUS – LUMINOSITY RELATIONSHIP FOR ACTIVE GALACTIC NUCLEI	23
2.1 Introduction	23
2.2 The Sample and Data	26
2.2.1 The Database for the Optical-UV Luminosity Relationship	26
2.2.2 Data for the $R - L(5100\text{\AA})$ Relationship for Seyfert 1 Galaxy NGC 5548	28
2.3 Analyses and Results	29
2.3.1 The Optical–UV Continuum Luminosity Relationship	29
2.3.2 The Radius–Luminosity Relationships of NGC 5548	32
2.3.3 The Effect of Intrinsic AGN Variability on the Global $R(H\beta) - L(5100\text{\AA})$ Relationship: Monte Carlo Simulations	34
2.4 Discussion	36
2.4.1 The Scatter in the Global $R - L$ Relationships	36
2.4.2 On the slope differences between the local and global relationships.	38
2.4.3 Alternate Proxy for the Ionizing Luminosity	38

2.4.4	Implications for Cosmology Studies	39
2.5	Conclusion	39
3	ON THE RELATION BETWEEN THE BROAD EMISSION LINE SHAPE AND ED-	
	DINGTON LUMINOSITY RATIO FOR LOCAL SEYFERT GALAXIES	53
3.1	INTRODUCTION	53
3.2	The Sample	58
3.3	Data	58
3.3.1	Optical–UV Data	58
3.3.2	X-ray Data	60
3.3.3	Applied Corrections and Luminosity Calculations	62
3.4	Generating the Optical–UV–X-ray Spectral Energy Distributions	63
3.4.1	Estimating the Continuum Level in the SED Gaps	63
3.4.2	Extrapolation to $1\mu\text{m}$	64
3.5	Measurements Based on the SEDs	64
3.5.1	The SEDs	64
3.5.2	Bolometric Luminosities	65
3.5.3	The Bolometric Correction Factor	67
3.5.4	The Eddington Luminosity Ratio	68
3.6	SED – Line Shape Correlation	69
3.6.1	Matching the SEDs with the Spectra	69
3.6.2	$H\beta$ Line Shape - Eddington Ratio Correlation: Collin et al. (2006) follow up study	69
3.6.3	C IV Line Shape - Eddington Ratio Correlation	71
3.6.4	Effect of Uncertainty in R_{BLR} on the Eddington Ratio – Line Shape Cor- relation	71
3.6.5	Line Shape - Eddington Ratio Correlation of SDSS DR3 Quasars	72
3.6.6	Line Shape - Continuum Luminosity Relation	72
3.7	Variations in the SEDS	73
3.7.1	Variations in Bolometric Luminosity and Eddington Ratio	73
3.7.2	Bolometric Correction Variations	73
3.8	Discussion	74
3.8.1	Is the Line Shape - Eddington Ratio Correlation Real?	74
3.8.2	The Interpretation of the Line Shape - Eddington Ratio Correlation	75
3.8.3	Implications for Black Hole Mass Estimates	75
3.8.4	Uncertainties in the Bolometric Luminosities	76
3.9	Summary and Conclusions	78
4	ULTRALUMINOUS INFRARED GALAXIES IN THE AKARI ALL SKY SURVEY	109
4.1	INTRODUCTION	109
4.2	IDENTIFICATION OF ULTRALUMINOUS AND HYPERLUMINOUS INFRARED GALAXIES IN THE <i>AKARI</i> ALL-SKY SURVEY	112
4.2.1	The Samples	112
4.2.2	Infrared Luminosity Measurements	113
4.2.3	Elimination of the Mismatches	114
4.2.4	The Final Sample	115
4.3	Analysis and Results	116
4.3.1	Basic Properties Of the <i>AKARI</i> ULIRGs and HLIRG Samples	116

4.3.2	The Visual Morphologies and Interaction Classes	118
4.3.3	The Spectral Classification of Our Sample	119
4.3.4	Stellar Masses - Star Formation Rates - Metallicities and Optical Colors of ULIRGs	120
4.4	Discussion	125
4.4.1	FIR Colors	125
4.4.2	Interaction Classes	126
4.4.3	AGN Fraction of OUR ULIRG Sample	127
4.4.4	The offset of ULIRGs from the Main Sequence of Star Forming Galaxies	127
4.4.5	Comparison of SFRs With Observations and Simulations of Mergers	129
4.4.6	ULIRGs in the Fundamental Metallicity–Mass–SFR Plane	130
4.4.7	ULIRGs in Color – Magnitude Diagram	131
4.5	Conclusions	131
5	Conclusion	167
5.1	Summary	167
5.2	Future work	168
	Appendices	171
A	Appendix	173
A.1	Error-bar Sensitivity Test	173
A.2	SEDs of my Sample	175
A.3	Measurements Based on Korista et al. (1997a) Model	189
A.4	Bolometric Luminosity Based on the OPTXAGNF Model	192
A.5	Line Shape vs. Optical and UV Continuum Luminosity Plots	196
	Bibliography	197

1

INTRODUCTION

Astronomy started with light. First it was all about understanding the light of the heavens, then the darkness of the Universe came into play. The collective scientific knowledge of the last century made it possible to formulate the light into the laws of physics by means of the equations of mathematics. As recognized by Zwicky (1933) the light contains the imprints of the dark matter. Furthermore, the light from the stars or matter near the centers of the galaxies indicate that they are under the gravitational influence of the enormous mass concentrations of billions of solar mass, which are called supermassive black holes (SMBHs).

Evolution of galaxies is one of the fundamental questions in astronomy. Supermassive black holes seem to be residing at the center of all galaxies (e.g., Ferrarese & Ford, 2005a). The formation of SMBHs and their evolution with their host galaxies are important open questions (e.g., Volonteri & Bellovary, 2012). Active galactic nuclei (AGN), containing central growing black holes, provide a major tool to understand the role of SMBHs in the formation of cosmic structure.

This thesis mainly focus on active galaxies namely, AGN and Ultra Luminous Infrared Galaxies (ULIRGs). These galaxies are important evolutionary stages in galaxy and black hole evolution (e.g., Hopkins et al., 2008a). In this thesis I investigate 2 different aspects of systems with SMBHs: a) The scatter in the $R - L$ relationship [also used for mass estimates] and its potential origin. If we can understand the scatter in the global relation, we can potentially mitigate it and recently suggested methods to use quasars as cosmic distance indicator can be improved to the point of being competitive with existing distance indicators. b) The potential interrelationship between the production of ionizing photons from material in process of accretion onto the black hole and the properties of the gas (especially the velocities) emitting the broad lines that we use to estimate the black hole mass. I also investigate the properties of a type of young galaxy, the ULIRGs that may be an earlier evolutionary stage of AGN host galaxies (Sanders et al., 1988a; Hopkins et al., 2008a). In this chapter, I give an overview of AGN and ULIRGs that is relevant for the further chapters.

1.1 A BRIEF OVERVIEW OF BLACK HOLES

Laplace and Michell proposed the concept of a *dark body* based on Newton's theory of gravitation in the eighteenth century (Michell, 1784; Gillispie, 1997). A very massive object whose escape velocity is greater than the speed of light would be a *dark body* for a distant observer. Following Einstein's publication of "General Theory of Relativity", Schwarzschild (1916) derived the solution for Einstein's equations for a spherical, non-rotating object. The Schwarzschild

metric (Schwarzschild, 1916) describes the gravitational field of a point mass M at a distance r . The *Schwarzschild radius* is defined as

$$R_s = 2GM/c^2, \quad (1.1)$$

where G is the gravitational constant, M is mass and c is the speed of light. The Schwarzschild metric have singularities at $r = 0$ and $r = R_s$ for the so-called *Schwarzschild radius*. These singularities indicate an undetectable object by a distant observer.

Oppenheimer & Snyder (1939) showed that the Schwarzschild metric is relevant for the gravitational collapse of a massive spherically symmetric star. Despite this work, the singularity in the Schwarzschild metric was ignored until the 1960's. Kerr (1963) derived a solution for Einstein's equations for a static, symmetric, and rotating object. Newman et al. (1965) solved Einstein's equations for a charged rotating object and Penrose (1965) revised the theory of gravitational collapse and showed that singularities can form from the gravitational collapse of dying stars. The *black hole* term was first used by John Wheeler in 1967 (Wheeler, 1968).

The definition of a *black hole* as used in modern astronomy is a truly black, compact object with a strongly curved space-time inside the event horizon that nothing, not even light, can escape. Black holes (BHs) can be described by three parameters: charge (Q), mass (M_{BH}) and spin (a^*) or angular momentum ($J = a^* M_{\text{BH}}$). While an uncharged, non-rotating BH is called as a Schwarzschild black hole (meaning that the geometry is described by Schwarzschild metric), a spinning, uncharged BH is called as a *Kerr black hole*. Some of the characteristic radii around a BH are: (1) The Schwarzschild radius (Eq. 1.1) is the radius for a spherically symmetric non-rotating BH; (2) The gravitational radius ($R_g = GM/c^2$, half of R_s) is used as a distance unit around a black hole; (3) The radius of the event horizon, R_h , is the boundary of space-time within which events cannot affect the outside observers; (4) The Innermost Stable Circular Orbit, R_{ISCO} , defines the minimum radius of a stable circular orbit around a black hole. For a non-rotating BH $R_{\text{ISCO}} = 6R_g$ and for a maximally rotating BH $R_{\text{ISCO}} \sim 1R_g$.

Although we can not directly see black holes, the influence of their strong gravitational fields on the matter around them provides the required indicator for their identification. In general astrophysical black holes are classified according to their masses: stellar-mass black holes ($3 M_\odot < M_{\text{BH}} < 10^2 M_\odot$), intermediate-mass black holes ($10^2 M_\odot < M_{\text{BH}} < 10^5 M_\odot$), supermassive black holes ($10^5 M_\odot < M_{\text{BH}} < 10^{10} M_\odot$).

Stellar-mass BHs are the last stages in the evolution of massive stars ($> 20 M_\odot$, Camenzind, 2007). Such BH candidates have been identified in Galactic high-mass X-ray binary systems. The first confirmed stellar-mass BH candidate is Cygnus X-1 which was discovered 50 years ago (Bowyer et al., 1965) with a companion star (Murdin & Webster, 1971). The companion star allow us to constrain the mass of the invisible compact object and to rule out the possibility for a neutron star because the mass range of neutron stars is between $1.4 M_\odot - 3.0 M_\odot$, and the inferred mass of the compact object is larger than $3 M_\odot$ (e.g., Gies & Bolton, 1986; Orosz et al., 2011). Stellar-mass BHs are unique Galactic laboratories to observe and to understand the accretion flow around BHs.

Intermediate-mass BHs are thought to be remnants of metal free massive population III stars (Madau & Rees, 2001). Another formation mechanism proposed for such BHs is the merging of stellar-mass BHs in dense stellar clusters (Miller & Hamilton, 2002). Although observational confirmation of Intermediate-mass BHs is an active research field, they have not been successfully confirmed yet.

The most convincing evidence for a SMBH is in the center of our own galaxy, Sagittarius A* where the motions of individual stars in the center of Milky Way can be resolved. The traced

orbits of these stars over time indicate that they are orbiting an invisible mass concentration of $\sim 4 \times 10^6 M_\odot$ (Ghez et al., 2008; Gillessen et al., 2009). Since other galaxies are too far away to resolve individual stars, other methods (Chapter 1.3) are used to find SMBHs across the Universe. The first extragalactic SMBH candidate was detected by the *Hubble Space Telescope* (Harms et al., 1994). The existence of both quiescent (like the one in our own galaxy) and actively mass accreting (like the scaled up versions of stellar-mass BHs in X-ray binaries) SMBHs is widely accepted.

1.2 ACTIVE GALACTIC NUCLEI

1.2.1 OBSERVATIONAL PROPERTIES

The term Active Galactic Nuclei refers to galaxies with distinct continuous central luminosity produced by central accreting SMBHs. These sources are typically more luminous ($10^{42} - 10^{46}$ erg s⁻¹) compared to average quiescent galaxies. A variety of sources such as Seyfert galaxies, quasars, and blazars belong to the AGN class. Seyfert galaxies are nearby (redshift, $z \leq 0.1$) AGN with moderate luminosity ($10^{43} - 10^{45}$ erg s⁻¹). They were originally discovered by Carl Seyfert (Seyfert, 1943) due to their strong broad emission lines. They are divided into two groups (Khachikian & Weedman, 1974) according to the broadness of the emission lines in their spectra: (a) Type 1 Seyferts exhibit broad (≥ 2000 km s⁻¹) permitted lines, narrow forbidden lines, powerful non-stellar optical and ultraviolet (UV) continua, and host galaxy stellar light; (b) Type 2 Seyferts show only narrow permitted and forbidden lines with host galaxy dominated continua. *Quasi-stellar radio sources* (QSRS) were first discovered as stellar-like cores in radio sources. *Quasar-stellar object* (QSO) is the radio-quiet equivalent to QSRS. Now, *quasars* is used to refer to both types. Their broad emission-lines revealed their high redshift origin (Schmidt, 1963). Quasars are high luminosity ($M_V < -23$) AGN predominately residing at high redshift. In general, AGN emit a non-stellar nuclear continuum, and strong emission lines which are produced by non-stellar radiation. AGN often exhibit emission-line and continuum variations. Additionally, AGN emit at a wide range of wavelengths and they are sub-classified according to their multi-wavelength properties. For example, blazars are a sub-class of AGN with their variable multi-wavelength emission (especially radio and gamma-rays, but also optical and UV). Low-ionization nuclear emission-line regions (LINERs) show strong emission lines that are excited by non-stellar radiation and therefore they are another sub-class of AGN. Radio galaxies with non stellar nuclear continuum also belong to the AGN family. AGN with extended (up to hundreds of kiloparsecs) radio jets are referred as radio-loud and those objects without the large jets and powerful radio emission from the center are 'radio-quiet'. (Kellermann et al., 1989). Classification depends on the ratio of radio to optical flux in the center, essentially. Kellermann et al. (1989) defined the radio-loudness based on the ratio (R) of the radio flux at 5 GHz to optical B-band flux, for radio-loud AGN $R \geq 10$. The vast majority ($\sim 80\%$ or more) of the AGN population are radio-quiet. For example, Seyfert galaxies generally have weak radio emission (non-thermal emission from the central engine) and therefore they are classified as radio-quiet sources.

1.2.2 STRUCTURE AND UNIFICATION

The classification of Seyfert galaxies has been generalized to the AGN population under the unification picture. According to the unification scheme (Antonucci, 1993; Urry & Padovani, 1995) Type 1 and Type 2 are same objects except, they are viewed from different angles. Figure

1.1 illustrates the AGN unification model based on viewing angle. According to this unified model all AGN have a SMBH and an accretion disk as the central engine. The accretion disk generates optical-UV continuum emission. Near the central engine (within about 1 pc), fast-moving, hot, and dense gas forms the broad-line region (BLR) (Peterson, 1997; Osterbrock & Ferland, 2006). The BLR gas is under the influence of SMBHs gravity and moves with a speed of several thousand km s^{-1} . The broad emission-lines are produced in this region via photo-ionization of the gas by the optical-UV continuum.

A dusty and parsec-scale torus surrounds the accretion disk and BLR. The torus absorbs the continuum emission and reemits the received emission in the infrared (IR). The inner edge of the dusty torus is about 1 pc and set by the dust sublimation temperature. Although the torus has a donut shape in Figure 1.1, recent theoretical studies suggest a circumnuclear and clumpy dust distribution (e.g., Hönig et al., 2006; Schartmann et al., 2008).

The narrow-line region (NLR) is an extended (1-1000 pc) region, which has low velocity ($< 1000 \text{ km s}^{-1}$), low density and cool gas beyond the torus. The narrow emission lines seen in the spectra are produced in this region by the photo-ionized gas by the nuclear continuum emission (Peterson, 1997; Osterbrock & Ferland, 2006).

This unification scheme suggests that orientation is the only difference between Type 1 and Type 2 AGN. Type 1 AGN are viewed directly face-on (low inclination with respect to the axis of rotational symmetry of the system) and the Type 2 AGN are viewed edge-on (high inclination) and therefore the central emission is blocked along the line of sight by the obscuring torus. As discovered by Antonucci & Miller (1985) hot electrons outside the torus scatter and polarize the nuclear continuum and the broad-line emission and therefore BLR emission of Type 2 AGN is visible only in polarized light. As shown in Figure 1.1 the unification of the radio-loud AGN are similar to radio-quiet AGN but includes the radio jet (Urry & Padovani, 1995). For example, blazars are viewed directly down the jet which is believed to produce the highly variable Doppler boosted emission at radio, optical, UV and X-ray energies.

1.2.3 SPECTRAL ENERGY DISTRIBUTIONS

The spectral energy distributions (SEDs) of AGN span the entire electromagnetic spectrum, from radio to Gamma-rays. The SEDs of AGN are composed of distinct emission features that hint the physical processes forming the observed energy output. AGNs are believed to be powered by accretion of matter into the central supermassive black hole (Rees, 1984). The SEDs display different forms of the accretion power across the electromagnetic spectrum.

Optical-UV Emission: Figure 1.2 shows an example mean SED adapted from Elvis et al. (1994). AGN exhibit almost equal energy per unit logarithmic frequency interval (the horizontal line in Figure 1.2 shows equal energy per unit logarithmic frequency). The highest peak of the SED in the optical and UV region is called as the ‘Big Blue Bump’ (BBB). As seen from Figure 1.2 the BBB covers the region between $1\mu\text{m}$ to 1000\AA and contains a significant fraction of the total energy output. BBB is generated by the thermal blackbody radiation from the accretion disk around the central SMBH, the disk is considered as annuli at different temperatures, each annulus radiates like a blackbody and the combination of these black body curves form a power law (Shields, 1978; Malkan, 1983). The peak of the accretion disk is expected to be around 100\AA (see §1.2.4) that is in the extreme-ultraviolet (EUV) region of the SED. However, due to absorption by neutral hydrogen in our Galaxy, we are unable to observe the spectral range between 912\AA – 100\AA . Therefore, the possible extension of the BBB to the EUV region is observationally

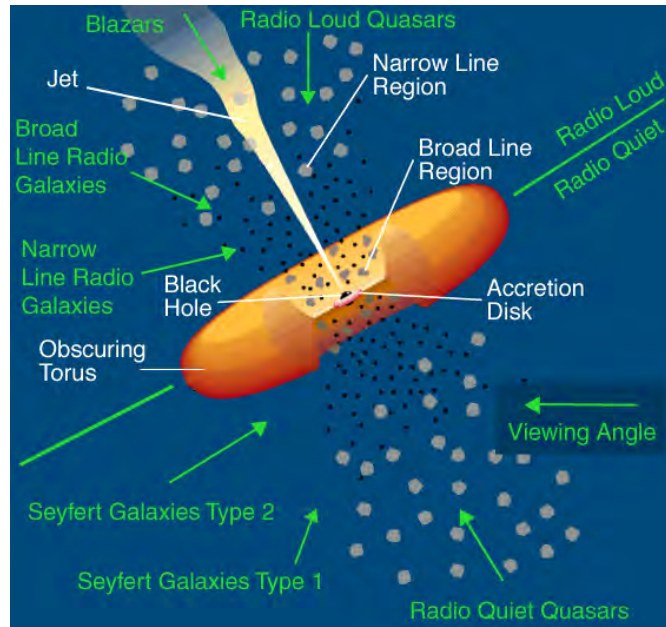


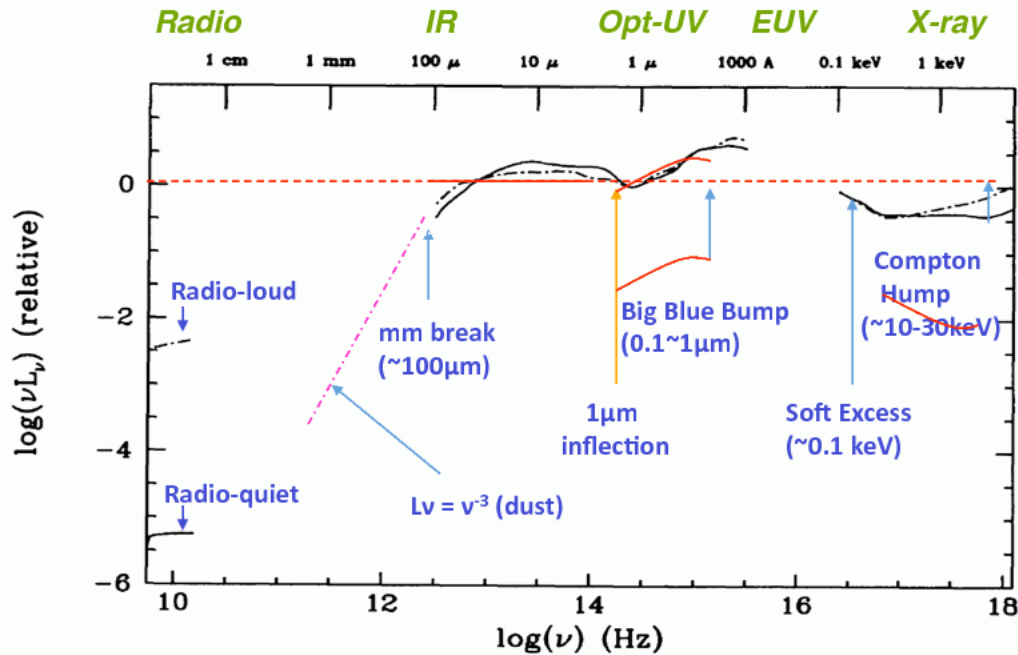
Figure 1.1 Schematic view of AGN unification model. Figure adapted from Urry & Padovani (1995) and copied from https://www.cta-observatory.ac.uk/?page_id=1196.

unclear. This turns out to have an important impact on our ability to accurately characterize the SED and to measure accurately the bolometric luminosity (Chapter 3).

X-ray Emission: The X-ray spectra of AGN cover a large range from 0.1 keV to ~ 300 keV and exhibit separate components. The *primary X-ray continuum* of AGN is well described as a power-law extending from 1 keV to 100 keV with a high energy cutoff above 100 keV (e.g., Mushotzky et al., 1993; Nandra & Pounds, 1994; Molina et al., 2013). The hard X-ray (>2 keV) power law that is also referred as the primary X-ray continuum is in the form of $F(X) \propto E^\Gamma$, where $F(X)$ is the X-ray flux, E is the energy and Γ is the power law index. X-ray observations show that the mean power law index is ~ 1.9 (Nandra & Pounds, 1994). The primary X-ray continuum is produced by the Compton up-scattered (inverse-Compton scattered) accretion disk radiation (optical/UV photons) to X-rays (Sunyaev & Titarchuk, 1980). This process happens in the corona of hot electrons above the accretion disk (e.g., Haardt & Maraschi, 1991; Sobolewska et al., 2004; Jin et al., 2012a).

The primary X-ray continuum reflects back and irradiates the accretion disk and produces the reflection component including the scattered continuum emission peaking at ~ 20 -30 keV (also referred as the Compton hump) and X-ray emission lines (e.g., George & Fabian, 1991; Nandra & Pounds, 1994; Reynolds & Nowak, 2003). The strongest emission line produced in the disk is the Fe K_α line at ~ 6.4 keV (e.g., Reynolds, 1997; Nandra et al., 1997). This line often exhibits a broad profile due to relativistic Doppler effects occurring at a few gravitational radii of the SMBH (e.g., Tanaka et al., 1995).

The X-ray spectra may also have additional components such as the soft excess emission and absorption features. The so-called *soft excess* appears at soft energies (below 2 keV) as an excess emission over the power-law continuum (e.g., Turner & Pounds, 1989). The soft excess emission is characterized by blackbody (single or multiple) emission with a temperature of ~ 0.1 -0.2 keV



Elvis et al., 1994, ApJS, 95, 1

Figure 1.2 Radio to X-ray spectral energy distribution of quasars (Elvis et al., 1994). Solid and dot-dashed lines represent radio-quiet and radio-loud quasars, respectively. The horizontal line shows equal power per decade, the power output of a quasar is almost equal from the far-infrared to X-rays. Figure is copied from <http://hea-www.harvard.edu/~elvis/quasarsed.gif>.

(e.g., Crummy et al., 2006). The physical origin of the soft excess X-ray emission is a matter of debate. This emission was first interpreted as the tail of the thermal emission from the accretion disk (e.g., Pounds et al., 1987; Walter & Fink, 1993), but the temperature of the soft excess is higher compared to the predictions of standard accretion disk model (e.g., Gierliński & Done, 2004; Crummy et al., 2006). One possible explanation includes the produced emission lines at soft energies by the reflection, such that, due to relativistic effects, these lines are blurred into a broad emission component (e.g., Ross & Fabian, 2005; Crummy et al., 2006). An other view explains the soft excess emission as the thermal inverse-Comptonization of seed accretion disk photons in a lower temperature corona (e.g., Magdziarz et al., 1998a; Done et al., 2012).

Infrared Emission: In Figure 1.2 the broad feature longward of $1\mu\text{m}$ is the *infrared bump* formed by the re-processed accretion disk radiation. The optical/UV photons from the accretion disk heat the surrounding dust grains (to 50–1000 K) in the dusty torus (e.g., Rieke, 1978; Antonucci, 1993). The warm dust grains re-emits the absorbed energy in the mid-IR, between 2 and $100\mu\text{m}$. Additionally, dust in the NLR may contribute to this mid-IR emission (e.g., Mason et al., 2006). The hot dust close to the sublimation temperature ($\sim 1500 - 2000$ K) produces the

‘near-infrared inflection’ point between $1\mu\text{m}$ and $1.5\mu\text{m}$ (Sanders et al., 1989; Elvis et al., 1994). The ‘submillimetre break’ appears as a strong drop in the far-IR emission, but the strength of the drop is larger for ‘radio-quiet’ sources compared to ‘radio-loud’ sources (Elvis et al., 1994). The re-processed radiation from the torus do not extend to the far-IR region; the far-IR dust emission is mostly dominated by the star formation in the host galaxy.

Radio and γ -ray Emissions: The SEDs of some AGN (depending on the type, e.g., Urry & Padovani, 1995) may include non-thermal radio and γ -ray emissions, which are generated in relativistic jets. Jets radiate from the radio to the gamma-ray range via the synchrotron and the inverse-Compton scattering processes.

1.2.4 ACCRETION LUMINOSITY

Accretion of matter onto the SMBH forms an optically thick and geometrically thin accretion disk in order to dissipate angular momentum (Shakura & Sunyaev, 1973). The accreted material is transported inward while its angular momentum is transported outward by for example viscosity. The gravitational potential energy at radius R in the disk is:

$$E = -\frac{GM_{\text{BH}}}{R}, \quad (1.2)$$

where M_{BH} is the mass of the black hole. As matter with mass dM spirals inward through the accretion disk, the change in the gravitational potential energy is:

$$\Delta E = \frac{GM_{\text{BH}}}{R^2} dM dR. \quad (1.3)$$

Half of this energy change converts into kinetic energy of the accreting material and the other half turns into thermal energy that radiates. This is the luminosity produced by the accretion, L_{acc} , and it is in the form of:

$$L_{\text{acc}} = \frac{GM_{\text{BH}}}{2R^2} \dot{M} dR \quad (1.4)$$

where \dot{M} is the mass accretion rate. To first order it is assumed that the disk radiates locally like a black body, therefore luminosity per unit radiating area ($2 \times 2\pi R \times dR$, assuming spherical symmetry) is equal to the energy loss by blackbody radiation:

$$L_{\text{acc}} = \frac{GM_{\text{BH}}\dot{M}}{8\pi R^3} = \sigma T^4, \quad (1.5)$$

where σ is the Stefan-Boltzman constant and T is temperature. The accretion disk has many annuli at different temperatures and the resultant accretion disk spectrum is power-law that is a superposition of many black body spectra. If the temperature of the inner disk is $\sim 10^5$ K, the peak of the emission is at $\sim 100\text{\AA}$. This is only a rough approximation and in reality the observed spectral energy distributions of AGN are not fully consistent with this standard accretion disk spectrum (e.g., Koratkar & Blaes, 1999). One of the main problems is the absence of a Lyman edge of hydrogen in the observed spectra (Hubeny et al., 2001). In general, the details of AGN accretion disks are still not well understood.

The conversion of mass to energy depends on the accretion efficiency, η . The energy is $E = \eta Mc^2$ and the rate at which the accretion energy is released is:

$$L_{\text{acc}} = \frac{dE}{dt} = \eta \dot{M} c^2, \quad (1.6)$$

where $\dot{M} = \frac{dM}{dt}$ is the mass accretion rate.

The accretion luminosity also generates radiation pressure in the form of:

$$F_{rad} = \frac{L_{acc}\sigma_T}{4\pi cr^2}, \quad (1.7)$$

where σ_T is the Thomson cross-section. If we consider an electron-proton pair as the accreting matter (we assume material to be fully ionized and mostly hydrogen), this pair is under the influence of the gravitational force:

$$F_{grav} = \frac{GM_{BH}(m_p + m_e)}{r^2} \simeq \frac{GM_{BH}m_p}{r^2}. \quad (1.8)$$

The balance of the F_{rad} and F_{grav} acting on this electron-proton pair defines the critical luminosity for spherically symmetric and steady accretion which is also known as the *Eddington luminosity*, L_{Edd} :

$$L_{Edd} = \frac{4\pi GM_{BH}m_p c}{\sigma_T} = 1.3 \times 10^{38} \frac{M_{BH}}{M_\odot}. \quad (1.9)$$

Since L_{Edd} is proportional to M_{BH} and L_{acc} is proportional to the amount of accreted matter (\dot{M}), the ratio of these luminosities, called the *Eddington luminosity ratio*, $\lambda_{Edd} = L_{acc}/L_{Edd}$. It gives the mass accretion rate normalized to the black hole mass. In order to measure L_{Edd} and thus the accretion rate, if the mass of the BH is known, one needs to measure L_{acc} from the spectral energy distribution.

The total energy output of AGN depends strongly on the mass accretion rate and thus the Eddington ratio. The Eddington luminosity ratio is proposed to affect the broad emission lines (e.g., Collin et al., 2006) and the SEDs (e.g., Vasudevan & Fabian, 2007). The link between the SEDs, Eddington ratio and the broad emission lines is one of the main issues studied in this thesis. In Chapter 3 I attempt to measure L_{Edd} from the observed spectral energy distributions. This is not an easy task because, as stated in §1.2.3, SEDs of AGN span a large wavelength range and there is a huge gap in the EUV that requires a gap repair. On the other hand one needs to separate the luminosity, which is produced by the accretion from the reprocessed emission generated by the accretion luminosity itself. For example, the reprocessed IR radiation longward of $1\mu m$ is not part of the accretion luminosity. Our lack of knowledge of the exact intrinsic SED shape brings a significant limitation to our ability to measure L_{acc} . The characteristic variations of the optical, UV and X-ray continua brings an additional challenge to the problem. In Chapter 3, I eliminate this latter challenge by using simultaneous optical, UV and X-ray measurements.

1.3 MASS MEASUREMENTS OF SUPERMASSIVE BLACK HOLES

The presence of SMBHs at the centers of most massive and some low-mass galaxies gained acceptance over the last two decades (e.g., Kormendy & Ho, 2013). As a result, SMBHs became a fundamental component in the galaxy anatomy; SMBHs can either be dormant/quiescent or active. The existence of actively mass accreting SMBHs have been considered since the discovery of quasars (Lynden-Bell, 1969; Rees, 1984). Over the last decade observations of local galaxies supported the existence of quiescent SMBHs that are the remnants of active SMBHs (e.g., Kormendy & Ho, 2013). More notably, these observations showed that in the local Universe the mass of the central quiescent SMBH correlates with the host galaxy properties such as the stellar velocity dispersion (σ_*), mass (M_{bulge}) and the luminosity (L_{bulge}) of the bulge. These correlations are referred to as the $M_{BH} - \sigma_*$ (e.g., Ferrarese & Merritt, 2000; Gebhardt et al., 2000; Gültekin et al., 2009), the $M_{BH} - M_{bulge}$ (e.g., Häring & Rix, 2004; Kormendy & Ho, 2013) and

the $M_{\text{BH}} - L_{\text{bulge}}$ (e.g., Magorrian et al., 1998; Marconi & Hunt, 2003; Gültekin et al., 2009) relationships, respectively. The immediate interpretation of the observed correlations is not an easy task because the bulge component of a galaxy is far beyond the gravitational influence of the central BH. However, the general consensus is that there should be a link between the formation and growth of galaxies and their SMBHs such that the bulge and the BH should affect each other as they evolve. The relevant processes are unknown, however given their importance, subject to intense study.

On the theory side, the origin of the observed correlations between M_{BH} and host galaxy is controversial. There are several proposed explanations for these empirical correlations. One scenario includes the feedback between the BH and the host galaxy (e.g., Silk & Rees, 1998; Fabian, 1999; King, 2003; Murray et al., 2005). When the radiation pressure from the highly accreting quasar sweeps away the gas, the equilibrium of the inward gravitational force and the outward radiation force result in a relation in the form of $M_{\text{BH}} \propto \sigma_*^4$ (e.g., Fabian, 2012). An other explanation is galaxy-galaxy mergers (e.g., Di Matteo et al., 2005; Hopkins et al., 2009b): When two galaxies merge, gas funnels toward the center and the BH grows by accreting this gas; then the AGN feedback blows away the gas, and shuts off the accretion process and the star formation at the same time. In this case, both the evolution of the galaxy and the central BH are influenced. There is even a simpler explanation which is based on number statistics and the central limit theorem of the mergers (Peng, 2007; Jahnke & Macciò, 2011). In this case, the BH and the galaxy are not related and the tightness of the resultant correlation depends on the number of merger events between the galaxies.

The empirical correlations between the BH mass and the host galaxy is currently limited to nearby galaxies for which the masses are directly measurable. To understand the evolution of galaxies, namely how and when active BHs turn into dormant BHs, and how the host galaxies are affected during this phase transition, we need to determine the BH demographics that shows the mass distribution of quasars at different redshifts. The black hole mass function is the space density of BHs as a function of mass and redshift (e.g., Greene & Ho, 2007; Vestergaard et al., 2008; Vestergaard & Osmer, 2009; Schulze & Wisotzki, 2010; Kelly & Merloni, 2012; Kelly & Shen, 2013a; Shen & Kelly, 2012). The BH mass function allow us to study BH population as function of redshift and put some constraints on BH seeding models (e.g., Natarajan & Volonteri, 2012). For example the mass distribution of Type 1 quasars as function of redshift shows that distant quasars are very massive (between $10^8 M_{\odot} - 10^{10} M_{\odot}$) and very luminous ($10^{45} - 10^{48} \text{ erg s}^{-1}$) and $10^{10} M_{\odot}$ seems to be the maximum mass limit of quasars (e.g., Vestergaard et al., 2008; Vestergaard & Osmer, 2009). Moreover, the most massive black holes are the most actively accreting at high redshift. With decreasing redshift the less massive black holes are the most active ones. This is down-sizing (see figure 5 of Vestergaard & Osmer, 2009). In order to understand the formation and evolution of SMBHs we need to determine masses for quiescent and active SMBHs over a large redshift range. There are different methods to measure the BH masses in quiescent and active SMBHs. For quiescent SMBHs masses can be measured by stellar and gas dynamics, however this method is limited by our capable resolution and distance to the galaxy. Mass measurements of active SMBHs require variability and temporal resolution. And we can only obtain BH demographics by measuring masses of the active SMBHs because, the masses of quiescent SMBHs can not be measured beyond the local Universe (§1.3.1), therefore mass measurements of active SMBHs are extremely important. To understand the basics and limitations of these different methods I will explain them briefly.

1.3.1 STELLAR - GAS DYNAMICS

The mass measurement of the SMBH at the center of our galaxy is based on the resolved orbits of the individual stars. Although individual stars in other galaxies can not be resolved, dynamical methods (e.g., Kormendy & Richstone, 1995; Ferrarese & Ford, 2005a; Kormendy & Ho, 2013) can be used to measure BH masses. The gravitational radius of influence (R_{inf}) of the SMBHs, of order ~ 1 -100 parsecs, require spatially resolved spectroscopy and can be resolved in nearby galaxies located within ~ 300 Mpc (Ferrarese & Ford, 2005a). The velocities of the populations of stars within R_{inf} can be measured by high resolution spectroscopy. Observed stellar light are fitted with stellar dynamics models that are determined by BH mass and as a result, the BH mass can be inferred based on the models. In addition, gas dynamics via nebular emission lines can also be used to obtain BH mass. Both of these methods, stellar and gas dynamics, allow the BH mass in any galaxy, both in quiescent galaxies and in AGN to be measured. However, since bright AGN outshine their host galaxies, it is difficult to measure stellar/gas properties for bright AGN and quasars. Also AGN are more distant which is yet another challenge for the required spatial resolution. Therefore, BH masses based on stellar/gas dynamics are difficult to obtain for distant, luminous AGN.

Another successful method to measure BH masses is to use the Megamaser (e.g., Lo, 2005) emission that can be seen in Type 2 AGN due to the obscured disk. The maser emission allow us to trace molecular gas around the SMBH and thus it gives very accurate BH mass measurement (e.g., Miyoshi et al., 1995). But because of the special alignment needed in our line of sight to see the maser emission these sources are very rare. Also, because of this special alignment along our line of sight this emission can only be seen at Type 2 AGN where we look through the disk. In Type 1 AGN, BLR gas within the gravitational potential of the central BH allow us to measure BH mass (§1.3.2 and 1.3.3).

1.3.2 REVERBERATION MAPPING

The standard, but incomplete, picture of the BLR of an AGN includes dense, warm ($\sim 10^4$ K) and photo-ionized (e.g., Ferland et al., 1992) gas. Probably the BLR gas is not in the form of many clouds because we do not see small scale structures in the emission-line profiles and this put a lower limit on the number of clouds as 10^8 which is a large number for discrete clouds and therefore BLR should be more like flow (e.g., Arav et al., 1998). Rather the BLR may be in the form of a wind from the accretion disk (e.g., Elvis, 2000). Although our current knowledge about the structure and kinematics of the BLR is highly immature, observations show that broad emission lines vary on short timescales (within days to weeks) in response to continuum variations. This indicates that the BLR gas is reprocessing the ionizing continuum produced by the accretion disk and it is located very close to the central engine (light days to 100 light days, micro arcsecond scales, ~ 0.1 pc) and therefore it is spatially unresolved and can not be studied by direct imaging. The broad emission lines of Type 1 AGN allow us to indirectly probe this region and measure the distance to the BLR, R_{BLR} . The BLR gas reprocesses the continuum photons and emit the AGN characteristic broad emission lines. Although this process is nearly instantaneous, the changes in the line flux is delayed from that of the continuum because the BLR is not co-spatial with the continuum region. The time delay, τ , corresponds to the light travel times to the BLR and $R_{BLR} = c\tau$ (c is the speed of light) is the distance travelled by the photons. Reverberation Mapping (RM) (Blandford & McKee, 1982; Peterson, 1993) is a method to measure the time delay, τ , between the continuum and broad emission line flux variations, thus it provides the responsivity weighted distance to the BLR. There are two analysis methods

to extract the time delay between the two light curves: CCF and JAVELIN. In Chapter 2 I will use the results of the two RM analysis methods, therefore below I briefly outline these methods.

The Cross-Correlation Function (CCF) Analysis Method: The light curves are not continuous but consist of discrete data points that may not be regularly sampled. To allow intra-day time delays to be detected, the amplitude of the flux densities between the observed data points need to be estimated. This can be done by the interpolation cross-correlation function method (ICCF), which simply generates a linear interpolation of the data points in the light curve (Gaskell & Peterson, 1987; White & Peterson, 1994; Peterson et al., 1998, 2004). Thereafter, the interpolated continuum and emission-line light curves are cross correlated. The cross correlation function (CCF) is the distribution of the cross correlation coefficients as a function of the time-delay. In the CCF analysis method, the τ value adopted is the centroid of the cross correlation function between the continuum and emission-line variations.

The Stochastic Process Estimation for AGN Reverberation Analysis Method (JAVELIN): Zu et al. (2011) present this new light curve analysis method with the aim of modeling an irregularly sampled light curve with a more advanced statistical technique. Previous studies show that an AGN light curve can be well described as a damped random walk process (Kelly et al., 2009; Kozłowski et al., 2010; MacLeod et al., 2010). The JAVELIN analysis models the continuum light curve by such a damped random walk, characterized by two parameters, the amplitude and the damping time scale. All the variability information in the continuum light curve is used as a prior to a joint model of the emission-line and the continuum light curves, assuming a top hat transfer function between the observed continuum and emission line flux variations. A likelihood function is obtained for the possible time delays, and the best-fit parameters are constrained by maximizing this likelihood function. In the likelihood distribution, the time delay corresponding to the peak of the distribution, is adopted as the time lag between the continuum and emission-line light curves.

1.3.3 VIRIAL BLACK HOLE MASSES BASED ON REVERBERATION MAPPING

If the motion of the BLR gas is assumed to be dominated by the gravity of the central BH, and therefore the emission lines are Doppler-broadened, then the distance and the velocity dispersion (ΔV_{BLR}) of the gas can be used to directly measure the mass of the BH, M_{BH} . The virial relationship gives the reverberation mapping based M_{BH} as (e.g., Peterson et al., 2004):

$$M_{BH} = f \frac{R_{BLR}(\Delta V_{BLR})^2}{G}, \quad (1.10)$$

where R_{BLR} is the average radius of the BLR measured from RM analysis, G is the gravitational constant, f is a dimensionless factor (probably it has a different value for each AGN, e.g., Pancoast et al., 2013) accounting for the unknown geometry and inclination of the BLR (Onken et al., 2004; Peterson et al., 2004). The velocity dispersion of the BLR gas is measured from the width of the emission-line. For RM spectroscopic monitoring datasets, the line width is measured from the root mean square (rms) of the mean spectrum. The rms residual spectrum is preferred because it eliminates constant features and contains only the variable component of the line that is responding to continuum variations.

If the BLR is virialized, then from equation 1.10 one expects the velocity dispersion to scale with the BLR distance such that $\Delta V_{BLR} \propto c\tau^2$. The RM studies that provide lag measurements

for multiple emission lines (Onken & Peterson, 2002; Kollatschny, 2003; Peterson et al., 2004; Bentz et al., 2010) confirm this expected relation between the line width and time delay, which support the notion that the BLR is virialized. Although observations indicate that gravity is the primary force in the BLR, as suggested by Marconi et al. (2008) radiation pressure may have a significant contribution that works against gravity. The radiation pressure force can be added to equation 1.10 as:

$$M_{BH} = f \frac{R_{BLR}(\Delta V_{BLR})^2}{G} + gL, \quad (1.11)$$

where L is the luminosity and g is a correction factor for radiation pressure that depends on the column density of BLR clouds and geometrical properties of the BLR (Marconi et al., 2008). This equation implies that if the radiation pressure correction factor (gL) is not taken into account, BH masses will be underestimated. Based on the Marconi et al. (2008) analysis the effect of radiation pressure is expected to be significant especially for objects accreting near the Eddington limit. Since both gravitational force and radiation pressure depend on the distance square it is difficult to separate the two forces without an independent measure of M_{BH} . Netzer (2009) argue that in most AGN the column density of the BLR clouds is greater than 10^{23} cm^{-2} (radiation pressure is expected to be significant when the column density is below 10^{23} cm^{-2} Marconi et al., 2008), and therefore the effect of the radiation pressure is much smaller than expected. However, as stated by Marconi et al. (2009) AGN have a wide column density distribution and thus the overall effect of the radiation pressure is difficult to evaluate. Netzer & Marziani (2010) take into account column density variations as a function of location in their modeling and find that even when the radiation pressure is important the mean cloud location and line width gives a reasonable M_{BH} . Since the significance of radiation pressure for virial BH masses is a matter of debate, the effect of radiation pressure is neglected (or g is assumed to be zero) for the RM based BH mass estimates adopted in this thesis.

The effect of radiation pressure, the unknown geometry and the inclination of the BLR are the main uncertainties in RM based BH masses. The f factor in equation 1.10 accounts for the unknown geometry and the inclination that we do not take into account (Onken et al., 2004; Peterson et al., 2004). The unknown f factor in equation 1.10 provides the largest uncertainty in M_{BH} measurements. Onken et al. (2004) measured an average f factor, $\langle f \rangle$, by assuming that the RM based M_{BH} measurements follow the $M_{BH} - \sigma_*$ relationship of local quiescent galaxies. The nearby AGN are expected to follow the relation of quiescent SMBHs because they have low accretion rate and they ought to be close to their final mass. Other studies (Woo et al., 2010; Graham et al., 2011; Park et al., 2012a; Grier et al., 2013a) also investigated the average f factor of AGN. Woo et al. (2013) claim to have better data for the $M_{BH} - \sigma_*$ relationship and they find a different value of $f = 5.1$. Recently, Grier et al. (2013a) included new σ_* measurements to the AGN $M_{BH} - \sigma_*$ sample and remeasured time lag measurements of this sample from the JAVELIN analysis of (Zu et al., 2011). Grier et al. (2013a) report an average f factor of $\langle f \rangle = 4.31 \pm 1.05$ based on the zero point of the most recent $M_{BH} - \sigma_*$ relation (Woo et al., 2013). There are new efforts that are being pursued that can directly estimate the f factor for individual sources based on dynamical modeling of RM data (e.g., Pancoast et al., 2013). However, this method requires a large RM data set that makes it difficult to apply for large samples, but it has potential. AGN display an intrinsic scatter of ~ 0.4 dex around their $M_{BH} - \sigma_*$ relationship (Woo et al., 2013). This scatter can be taken to represent the typical uncertainty in M_{BH} . As a result, the derived virial BH masses are uncertain to within a factor of a few.

Despite the caveats related to radiation pressure and the f factor, for a few Type 1 AGN where independent M_{BH} measurements are available, RM based BH masses agree with stel-

lar/gas dynamics results to within the measurement errors (Peterson, 2010, and references therein). It is encouraging that both of these methods agree because it means both methods are likely reasonably reliable. Reverberation mapping does not depend on spatial resolution and therefore it is not restricted to the local Universe and can be applied to Type 1 AGN at any redshift. Instead it requires temporal resolution and spectroscopic monitoring campaigns, i.e., for local objects typically covering a couple of months. But for high redshift objects RM is restricted by the required long term (e.g., over years Kaspi et al., 2007a) monitoring. Since the required monitoring campaigns are expensive to be put into practice, RM based direct M_{BH} measurements have been obtained for about ~ 50 nearby ($z \leq 0.3$) AGN that are often referred as the ‘Reverberation Mapping Sample’ or the ‘RM sample’ (Peterson et al., 2004; Bentz et al., 2009b, 2010; Denney et al., 2010; Grier et al., 2012b; Bentz et al., 2013, and references therein).

1.3.4 RADIUS LUMINOSITY RELATIONSHIP

Reverberation mapping of local AGN has led to estimates of BLR sizes and BH masses for the RM sample. These measurements reveal a tight relationship between the mean optical continuum luminosity at 5100\AA , $L(5100\text{\AA})$, and the size of the $H\beta$ emitting region, $R(H\beta)$. This relationship is referred to as the ‘radius–luminosity relationship’ (or ‘ $R - L$ relationship’) (e.g. Kaspi et al., 2000, 2005; Bentz et al., 2009a, 2013). Figure 1.3 shows the latest revised version of the $R - L$ relationship based on $L(5100\text{\AA})$ measurements corrected for the host galaxy contamination and new $R(H\beta)$ measurements of additional AGN (Bentz et al., 2013). The AGN sample of Bentz et al. (2013) includes 41 sources that cover 4 orders of magnitude in $L(5100\text{\AA})$. The $R - L$ relationship is in the form of a power law with a slope of $\alpha = 0.546 \pm 0.027$ (Bentz et al., 2013). This slope is consistent with the expected slope of 0.5 from photo-ionization physics (Osterbrock & Ferland, 2006). If gas density and the ionization parameter is assumed to be similar in all AGN, as observations suggest (Peterson, 1997; Dietrich et al., 2002), then the distance to the BLR is expected to scale with the ionizing luminosity, $L(\text{ionizing})$, as $R_{BLR} \propto L(\text{ionizing})^{0.5}$ (see Chapter 2 for more details on this discussion).

The $R - L$ relationship can be used to estimate the distance to the BLR from a single continuum luminosity measurement without applying RM analysis that requires long term monitoring. Therefore, it has been used mainly for virial BH mass estimates based on ‘single-epoch’ spectrum (e.g. Vestergaard & Peterson, 2006) (see §1.3.5). Recently, Watson et al. (2011) showed that the $R - L$ relationship can be used to measure AGN distances and therefore AGN and quasars can be used as standard candles such as Type Ia supernovae (SNe). This method relies on performing RM monitoring and directly measuring R_{BLR} from the RM analysis and the mean continuum flux, $F(\text{cont})$, from the mean spectrum. By using the $R - L$ relationship the intrinsic luminosity of the AGN can be measured for the given R_{BLR} . Then this luminosity, L , can be used to infer the AGN luminosity distance, D_L , via:

$$L = 4\pi D_L^2 F(\text{cont}). \quad (1.12)$$

As shown by Watson et al. (2011), D_L inferred from the $R - L$ relationship are consistent with the actual distances within errors, which supports the hypothesis that this method works.

Cosmic distances measured from standard candles are very important to understand the cosmological evolution of the Universe. The expansion of the Universe was discovered by measurements of Type Ia supernovae (SNe) (Riess et al., 1998; Perlmutter et al., 1999). The expansion of the Universe is also confirmed by other cosmological probes (Planck Collaboration et al., 2013, e.g., the cosmic microwave background). The driver of the accelerating expansion of the

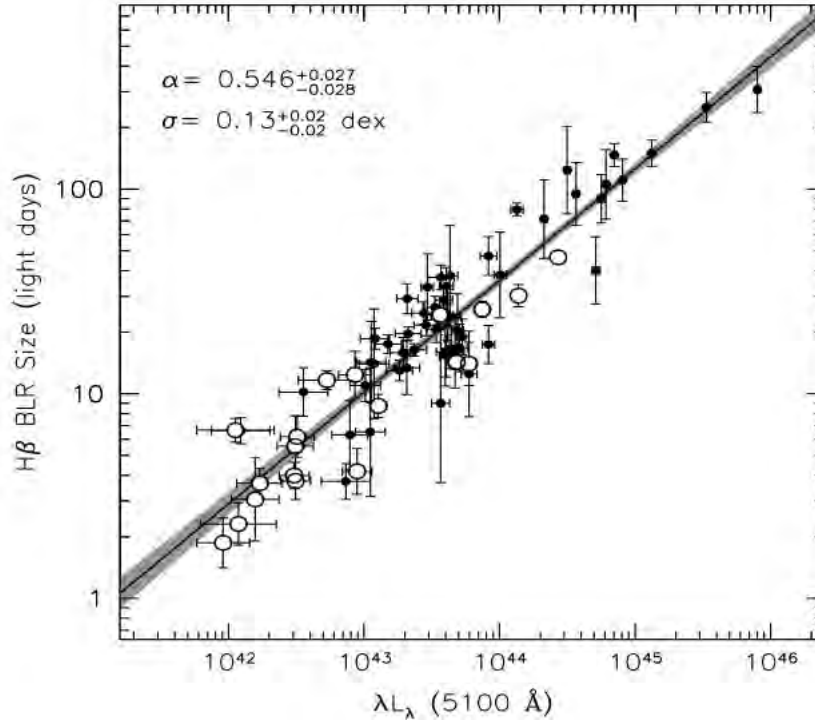


Figure 1.3 The revised $R-L$ relationship of 41 local AGN (Bentz et al., 2013). The scatter around the $R-L$ relationship in R is $\sigma = 0.13$ dex.

Universe is generally referred to as the dark energy. Understanding the origin of the dark energy is one of the most important scientific aspirations of this century.

Since the luminosity distance depends on the assumed cosmological model, the Hubble diagram (D_L vs. redshift) of Type Ia SNe can be used to constrain cosmological parameters such as the sum of the matter density (Ω_m), the cosmological constant (Ω_Λ) and the radiation density (Ω_r). Observations of Type Ia SNe are consistent with the cosmological model of a flat Universe ($\Omega_m + \Omega_\Lambda + \Omega_r \sim 1$). The equation of state of dark energy (w) may change with the expansion of the Universe across cosmic time. Unfortunately, Type Ia SNe are rare and difficult to detect and measure at $z > 1.5$ thus, they can not constrain the dark energy equation of state. Therefore, other independent distance indicators are needed in order to measure the expansion of the Universe.

Figure 1.4 shows the AGN Hubble diagram of local RM AGN as presented by Watson et al. (2011). Compared to Type Ia SNe the current AGN Hubble diagram has a larger scatter; a scatter of ~ 0.5 mag. With the latest revised version of the $R-L$ relationship (Bentz et al., 2013) this scatter becomes ~ 0.3 mag (Chapter 2). But AGN are promising cosmic probes because they are continuously emitting sources: they can be observed multiple times and they are numerous at higher redshifts, $z > 1.5$. Therefore, AGN provide an independent, complementary distance indicator to study the expansion of the Universe. Especially, high redshift AGN have a great potential to probe the time derivative of the dark energy equation of state (King et al., 2013a).

The current hope is to reduce the scatter in the AGN Hubble diagram and to use AGN as cosmological probes effectively. This depends on the scatter in the $R-L$ relationship that is currently estimated as 0.13 dex in R . In Chapter 2, I further investigate the scatter in the $R-L$

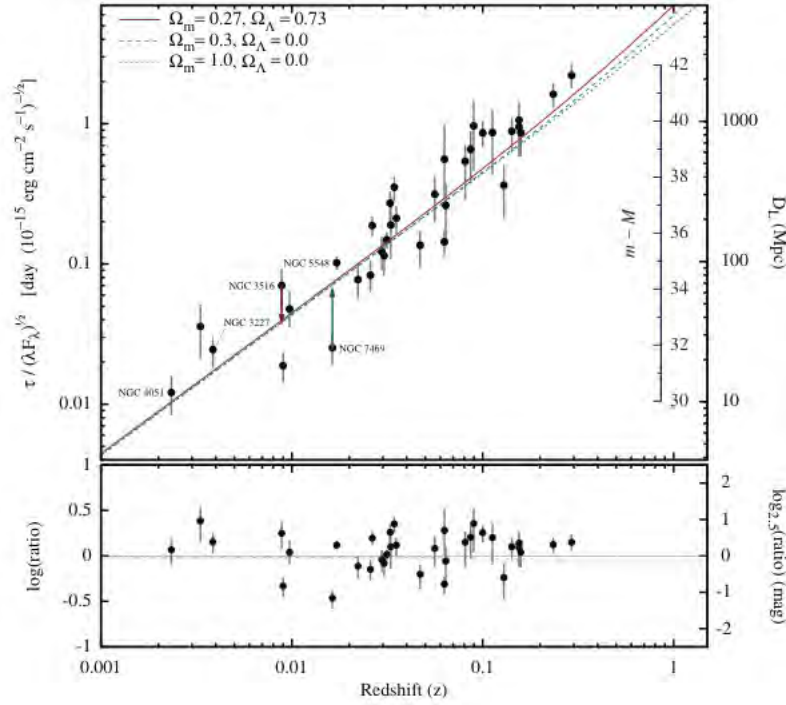


Figure 1.4 The AGN Hubble diagram for 38 AGN (Figure 2 of Watson et al., 2011). The solid, dashed and dotted lines represent different cosmologies as labeled. The lower panel shows the ratio of the data compared to the current best cosmology (Komatsu et al., 2011).

relationship. According to Bentz et al. (2013) a large fraction of this scatter is attributed to the inaccurate AGN distances, however as I present in Chapter 2, there are other sources of significant scatter related to the variability of individual objects.

1.3.5 MASS SCALING RELATIONSHIPS

With the $R-L$ relationship we can estimate R_{BLR} from a monochromatic continuum luminosity that is measured from a single spectrum (equation 1.10). When R_{BLR} is combined with a broad emission-line width measured from the same spectrum, M_{BH} can be calculated from equation 1.10. These formulations are referred to as ‘mass scaling relationships’ and they provide virial masses based on individual single-epoch (so-called S-E) spectra (e.g., McLure & Jarvis, 2002a; McLure & Dunlop, 2004; Wu et al., 2004; Greene & Ho, 2005; Vestergaard & Peterson, 2006; McGill et al., 2008; Vestergaard & Osmer, 2009; Park et al., 2013). For example, the optical mass scaling relationship for $H\beta$ is presented by Vestergaard & Peterson (2006) in the form of:

$$M_{BH} = 8.3 \times 10^6 \left(\frac{FWHM(H\beta)}{10^3 km s^{-1}} \right)^2 \left(\frac{L(5100)}{10^{44} ergs s^{-1}} \right)^{0.5} M_{\odot}, \quad (1.13)$$

where the full width half maximum (FWHM) represents the velocity of the BLR gas. Similar relationships also exist for other emission lines and continuum luminosities such as, C IV (Vestergaard, 2002; Warner et al., 2003; Vestergaard & Peterson, 2006; Park et al., 2013) and Mg II (McLure & Jarvis, 2002a; Vestergaard & Osmer, 2009; Wang et al., 2009). Mass scaling relationships can be easily applied to single-epoch spectra obtained in large surveys like *Sloan Digital*

Sky Survey (SDSS) and provide BH mass determinations for large number of Type 1 AGN in a large redshift range (e.g., Corbett et al., 2003; Greene & Ho, 2007; Vestergaard et al., 2008; Schulze & Wisotzki, 2010; Shen et al., 2011, and references therein). These masses allow us to investigate the space density of SMBH from redshift zero to six and to infer properties of SMBH populations (e.g., Jiang et al., 2007; Vestergaard & Osmer, 2009).

Mass scaling relationships are typically calibrated to the mass measurements of the RM sample (Peterson et al., 2004), obtained from the $H\beta$ line. Therefore, the first limitation of these scaling relations is the uncertainty of RM based BH masses of about ~ 0.4 dex (Vestergaard & Peterson, 2006). The statistical uncertainty of the mass scaling relations relative to the RM masses is ~ 0.3 dex – 0.5 dex (or a factor of ~ 2.5 –3). When the two uncertainties are combined, the absolute 1σ statistical uncertainty of the mass scaling relationships becomes as large as a factor of ~ 3.5 –4 (Vestergaard & Peterson, 2006; Vestergaard & Osmer, 2009).

While mass calling relations can be applied by means of two measurements - the emission-line width and the nuclear continuum luminosity- these measurements have several systemic uncertainties (Denney et al., 2009a). The uncertainties related to continuum luminosity include the host galaxy contamination, blending with other spectral features, data quality and AGN variability. The emission line width measurements are affected by the presence of narrow-line components, data quality (signal to noise, S/N), absorption features, and blending of emission-lines. Equation 1.13 includes the second power of the line width and therefore, the uncertainty of the emission line-width measurement leads to a significant uncertainty in M_{BH} .

The broad emission-line widths are typically parametrized by FWHM or the line dispersion (the second moment of the line profile, σ_{line}). Both parameters have advantages and disadvantages (e.g., Peterson et al., 2004): FWHM is more sensitive to spectral noise, narrow line components and multiple-peaked lines; σ_{line} is sensitive to line blending with other lines and noise in the line wings (Peterson et al., 2004; Denney et al., 2009a, e.g.,). It is difficult to model broad-emission lines because they do not have any particular shape. For example, for a Gaussian profile the FWHM to σ_{line} ratio is $FWHM/\sigma_{line}=2.355$, and $FWHM/\sigma_{line} > 2.355$ indicates a rectangular (or ‘boxy’) profile whereas $FWHM/\sigma_{line} < 2.355$ is a ‘peaky’ profile (e.g., Peterson et al., 2004). Collin et al. (2006) divided the RM sample into two groups based on the $FWHM/\sigma_{line}$ ratio of the mean $H\beta$ lines and showed that the average f factor, $\langle f \rangle$, obtained from the $M_{BH} - \sigma_*$ relationship depends on this ratio. This suggests that the $FWHM/\sigma_{line}$ ratio may be important to obtain more accurate BH masses. Additionally, Collin et al. (2006) showed that the mean $H\beta$ $FWHM/\sigma_{line}$ ratio of the RM sample correlates with Eddington ratio, this correlation is shown in Figure 1.5. However, their Eddington ratio estimates were somewhat crude because they scaled the optical continuum luminosity with a constant bolometric correction factor to obtain the bolometric luminosity. In Chapter 3, I further investigate the relationship between the $FWHM/\sigma_{line}$ ratio and the Eddington ratio for single epoch $H\beta$ and C IV profiles. In order to obtain more accurate Eddington ratio values, I use simultaneous SEDs to measure the bolometric luminosity and the Eddington ratio.

1.4 ULTRALUMINOUS INFRARED GALAXIES

Galaxies that emit a large fraction ($\sim 90\%$) of their total energy output in the infrared (IR) are called “infrared galaxies”. The bolometric IR luminosity between 8 – $1000\mu\text{m}$, L_{IR} , of these galaxies is between $L_{IR} = 10^{10} - 10^{14} L_{\odot}$. IR galaxies are classified according to their IR luminosities as: Luminous Infrared Galaxies (LIRGs) with $10^{11} L_{\odot} < L_{IR} < 10^{12} L_{\odot}$; Ultra Luminous Infrared Galaxies (ULIRGs) with $10^{12} L_{\odot} < L_{IR} < 10^{13} L_{\odot}$; and Hyper Luminous Infrared

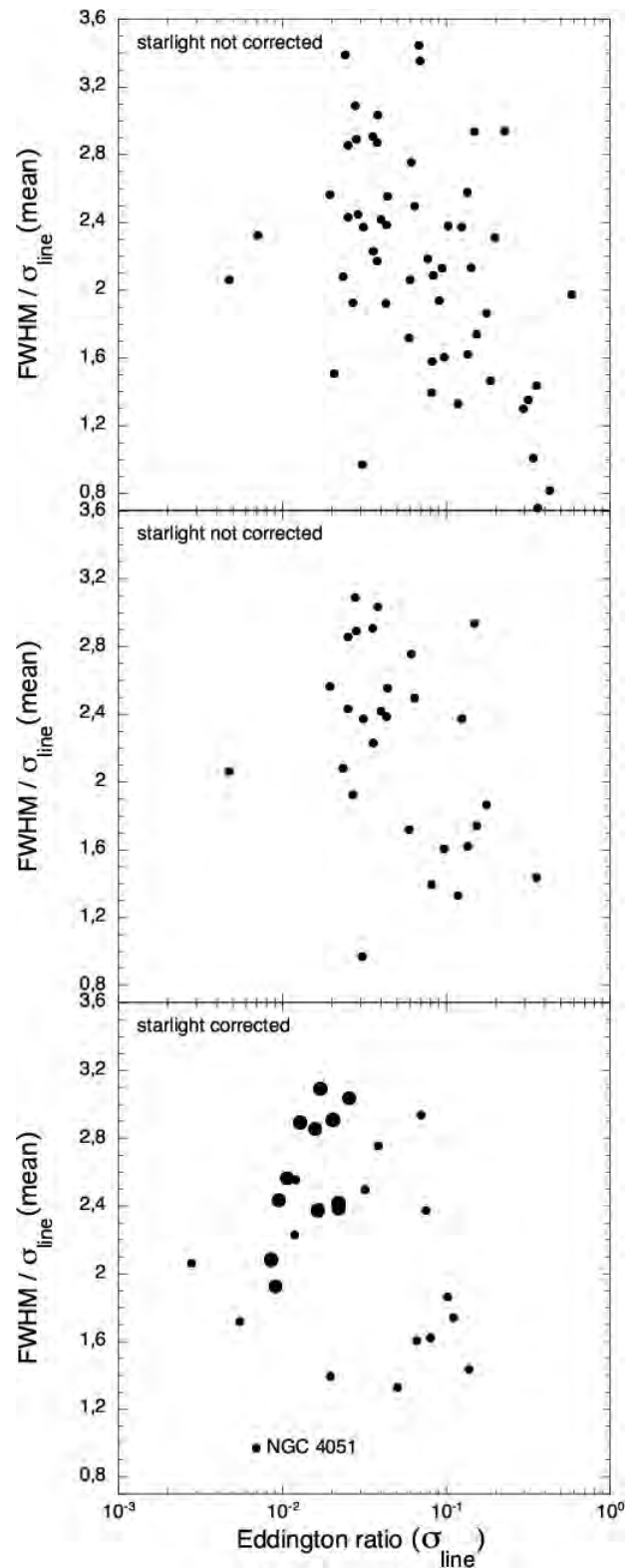


Figure 1.5 The $\text{FWHM}/\sigma_{\text{line}}$ ratio of mean $\text{H}\beta$ profiles, versus the Eddington luminosity ratio. This figure is adapted from Collin et al. (2006). The middle panel shows the data points from the top panel which can be corrected for the host-galaxy starlight contribution. The bottom panel shows the points from the middle panel that are corrected for starlight contamination. The larger circles in the lower panel represent multiple measurements of NGC 5548.

Galaxies (HLIRGs) with $10^{13} L_{\odot} < L_{IR}$.

IR galaxies are known since the early seventies. Rieke & Low (1972) did the first systematic ground based IR study and found several IR bright AGN, and some ULIRGs and LIRGs (U/LIRGs). The *Infrared Astronomical Satellite* (IRAS, Neugebauer et al., 1984), launched in 1983, performed the first all sky IR survey and identified most of the IR galaxy population in the local universe ($z < 0.3$) (e.g., Sanders & Mirabel, 1996a). Among these IR galaxies, ULIRGs stand out with their high IR luminosities. The Revised Bright Galaxy sample (RBGS; Sanders et al., 2003) and IRAS Faint Source Catalog (FSC; Moshir & et al., 1990) include the nearest local ULIRGs discovered by IRAS. The IRAS 1 Jy sample selected from the IRAS FSC is a very well studied sample of 118 local ULIRGs (Kim & Sanders, 1998a). This sample has increased our understanding of these extreme galaxies. Local ULIRGs are most often interacting galaxies and major mergers (Veilleux et al., 2002). They are powered predominantly by star formation and/or AGN activity (Veilleux et al., 1999a,b, 2002; Ishida, 2004).

The spectral energy distribution of ULIRGs is dominated by the dust emission in the infrared. The main energy source of ULIRGs is the strong UV to near-infrared emission generated mainly by stellar radiation from starbursts but presumably have some contribution from an AGN. This emission is absorbed by dust and re-emitted in the mid-infrared to millimeter range. Figure 1.6 shows example mean SEDs for a sample of IR galaxies (Sanders & Mirabel, 1996a). As seen from the figure, the SED shape changes with the total L_{IR} ; the top two SEDs represents ULIRGs. ULIRGs were classified based on their IRAS colors, namely according to $f(25\mu\text{m})/f(60\mu\text{m})$, the ratio of the $25\mu\text{m}$ flux to $60\mu\text{m}$ flux. A large fraction ($\sim 75\%$) of the local ULIRGs are "cold" with $f(25\mu\text{m})/f(60\mu\text{m}) < 0.2$; these are dominated by star formation. Warm ULIRGs have $f(25\mu\text{m})/f(60\mu\text{m}) > 0.2$; observations show that they usually harbor an AGN and their total IR luminosity is produced by both AGN activity and star formation (Downes & Solomon, 1998; Sanders et al., 1988b; Veilleux et al., 1999b).

ULIRGs and LIRGs are rare sources in the local ($z < 0.2$) Universe (e.g., Soifer et al., 1987). Compared to optically selected galaxies that very rarely have $L_{BOL} > 10^{11.5} L_{\odot}$, the only galaxies with high bolometric luminosities similar to U/LIRGs are quasars. But the number density of U/LIRGs is larger than that of quasars (e.g., Sanders & Mirabel, 1996a; Kim & Sanders, 1998a). Therefore, U/LIRGs dominate the high end of the local infrared galaxy luminosity function. With sensitive satellites like *Infrared Space Observatory* (ISO), the *Spitzer Space Telescope* and *Herschel* the population of U/LIRGs is observed to increase out to redshift 2–3 (e.g., Elbaz et al., 2005; Amblard et al., 2010). At high redshifts ($z \geq 2$), ULIRGs are more common sources despite their relative rarity in the local Universe (e.g., Chapman et al., 2005). LIRGs and ULIRGs provide a significant contribution to the cosmic IR background radiation at $z = 1$ and $z = 2$, respectively (e.g., Le Floch et al., 2005; Caputi et al., 2007). Since infrared emission traces the obscured star formation in the Universe, U/LIRGs represent the most rapidly star forming and highly obscured galaxies. Observations show that at $z \sim 1.5 - 3$ a significant fraction of the massive galaxies ($> 10^{11} M_{\odot}$) are ULIRGs and LIRGs (Daddi et al., 2005; Caputi et al., 2006). This shows that understanding ULIRGs and LIRGs is important for obtaining a complete picture of how galaxies evolve across cosmic time. In this respect, the main question is the nature of these galaxies: do they have the same origin as the low redshift U/LIRGs? Is it the same process that is responsible for the entire $10^{11} - 10^{13} L_{\odot}$ luminosity range up to $z \sim 2-3$? Local U/LIRGs are important because they represent the nearby examples of the high redshift star forming IR galaxies and they allow us to study the star formation activity in greater detail.

As proposed by Sanders et al. (1988a), ULIRGs may be an important phase in the formation of quasars. This is supported by numerical simulations showing that mergers can drive

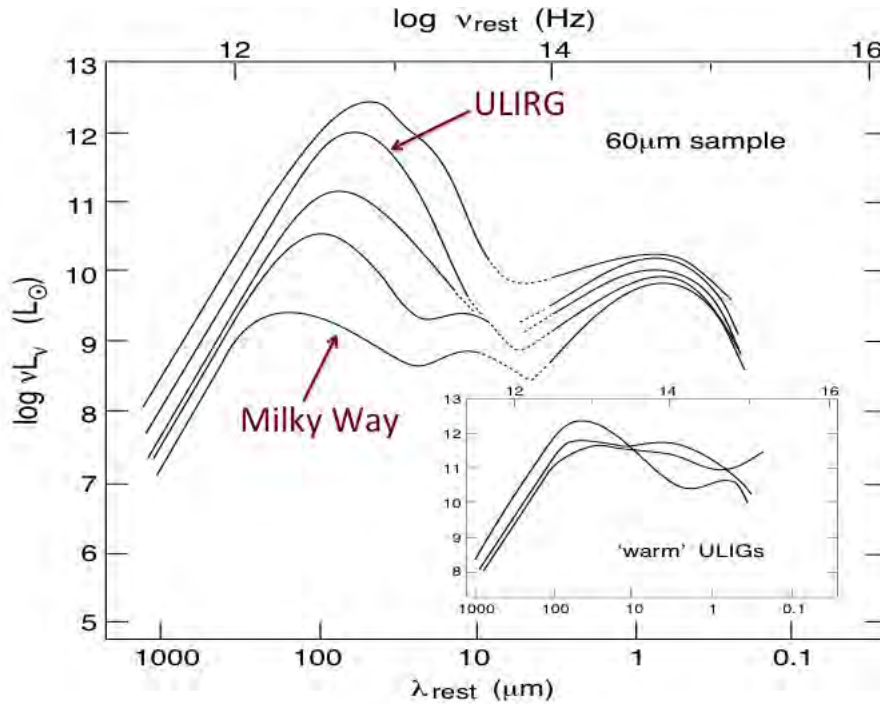


Figure 1.6 Mean SEDs of *IRAS* selected IR galaxies. The bottom SED is an example for Milky Way like galaxies where the top two represents ULIRGs. Inserted panel shows examples of warm ULIRGs. Figure is copied from Sanders & Mirabel (1996a).

material from a gas-rich galaxy disk towards the nucleus and fuel starbursts and an AGN (e.g., Barnes & Hernquist, 1991). Hopkins et al. (2008a) showed that mergers play an important role in the formation of elliptical galaxies. A schematic description of the formation of quasars and elliptical galaxies through gas-rich major mergers is shown in Figure 1.7. The evolution of the quasar luminosity is shown in the bottom panel and the top panel shows the star formation rate (SFR). ULIRGs represent an important phase during the strong interactions of gas-rich galaxies (panel d). As the merger stage evolves, a lot of gas and dust has been transported into the center of the galaxies. The accumulated gas and dust generate very intense star formation with bright IR emission, and make the central BH grow. Due to the central dust the early BH growth and AGN activity will be dust obscured. Then the feedback from the AGN and star formation blows out the gas and dust in the center and the AGN will be bright at optical through X-ray energies. Once the gas and dust supply runs out, the star formation and AGN activity will stop and an elliptical galaxy will form. This scenario shows ULIRGs as an important phase in the evolution of galaxies.

The merger-induced evolution of ULIRGs is supported by several observational evidences. A large fraction (56%) of the 118 local ULIRGs studied by Veilleux et al. (2002) and Ishida (2004) are post/old mergers that are coalesced to a single nucleus. These studies also show that the fraction of post/old mergers increases with L_{IR} . Similarly, the fraction of U/LIRGs hosting an AGN increases with L_{IR} (e.g., Veilleux et al., 1999a; Yuan et al., 2010). However, the identification of the central AGN in these systems is not an easy task because of their dusty nature. A common way to make this separation is to use BPT (named after "Baldwin, Phillips and

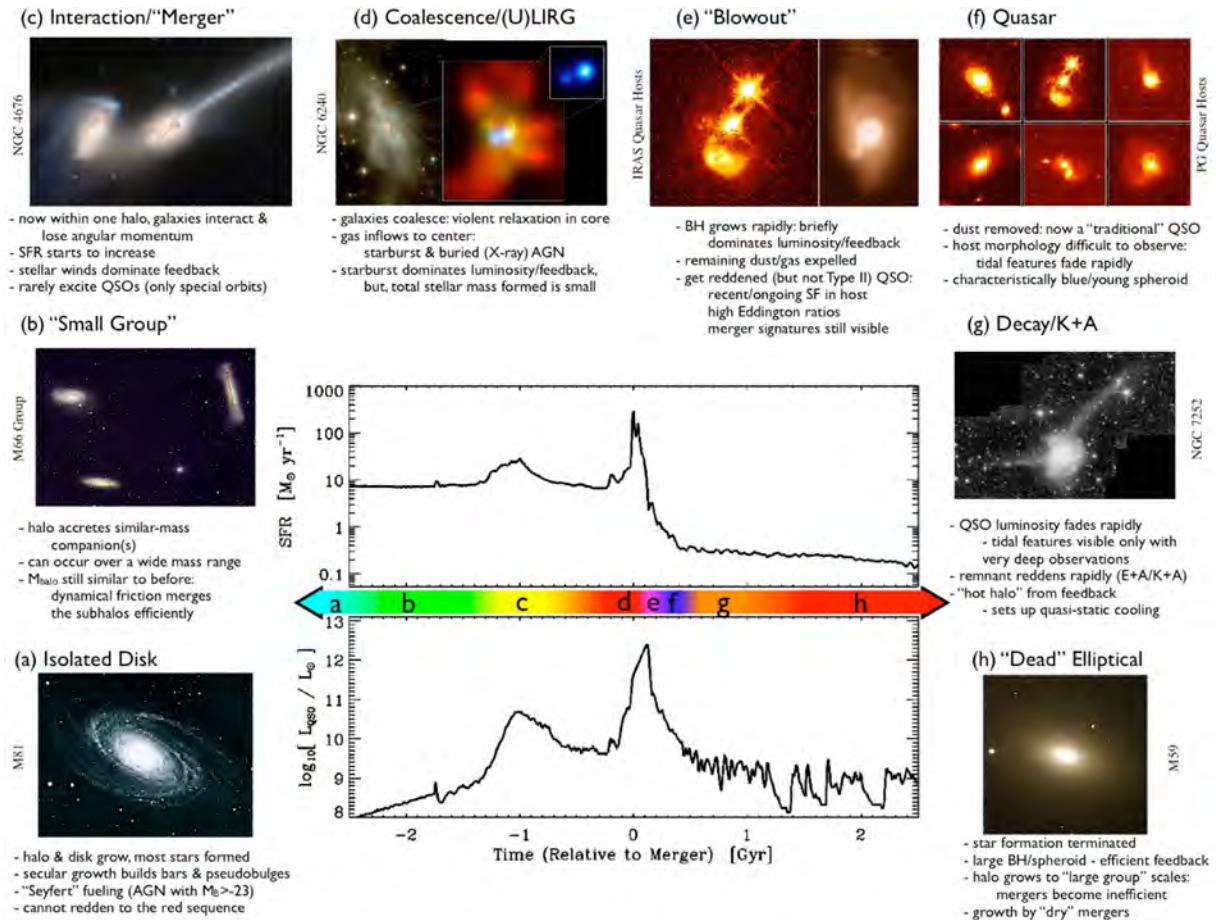


Figure 1.7 Schematic illustration of quasar formation as a result of major mergers. ULIRGs represent the evolution stage when the mergers coalesce and SFR peaks. Figure is copied from Hopkins et al. (2008a).

Telervich") diagrams (e.g., Baldwin et al., 1981; Kewley et al., 2006) that can distinguish the ionization mechanism based on emission lines. When lines are available BPT diagrams allow us to separate star forming galaxies and AGN based on optical spectroscopy. Optical emission lines (such as $H\alpha$ and $H\beta$) used for BPT diagrams can be affected by dust and therefore it is difficult to use BPT diagrams if the central emission is obscured by dust. Mid-infrared and hard X-ray radiation that can penetrate dust provide additional tools to uncover an obscured AGN in U/LIRGs. Star formation dominated ULIRGs and quasars exhibit different spectral features between $5\mu\text{m}$ – $30\mu\text{m}$ (Veilleux et al., 2009); quasars have a shallower continuum and less silicate absorption but strong high ionization lines. Based on the mid-IR spectral properties Veilleux et al. (2009) report that the mean AGN contribution of ULIRGs is $\sim 38.8 \pm 21.1\%$ and ULIRGs are therefore composite galaxies that are mostly powered by star formation.

AKARI all-sky survey: The Japanese IR satellite *AKARI* (Murakami et al., 2007) was launched in 2006. *AKARI* performed a new far-IR and mid-IR all-sky survey 20 years after *IRAS*. Compared to *IRAS*, *AKARI* has a better spatial resolution ($\sim 1'$) and wider wavelength coverage (six bands between $9\mu\text{m}$ and $160\mu\text{m}$). *AKARI* has two mid-IR bands centered at $9\mu\text{m}$ and $18\mu\text{m}$,

and four far-IR bands centered at $65\mu\text{m}$, $90\mu\text{m}$, $140\mu\text{m}$ and $160\mu\text{m}$. Especially the $90\mu\text{m}$ flux is crucial to measure the total L_{IR} because it is near the peak of the far-IR SED. In Chapter 4, I present a new catalog of local ULIRGs and HLIRGs identified in the *AKARI* all-sky survey. Local ULIRGs are important to understand a significant fraction of high redshift star forming galaxies. My work increases the number of local ULIRGs.

1.5 STRUCTURE OF THE THESIS

In this thesis I investigate and address 2 important evolutionary phases of galaxies: ULIRGs and AGNs. Both AGN and ULIRG are thought to be individual phases of galaxy evolution - especially of the most massive galaxies. ULIRGs are an earlier phase where the black holes grow during a fast but obscured accretion phase accompanied by intense star formation activity. When the black hole is massive enough the accretion process produces an energetic feedback that drives the gas away shutting off star formation and black hole growth on a short time scale. AGNs are thought to be this particular phase before the black hole runs out of fuel.

For the AGNs I address two aspects related to their use as cosmological probes; namely first in Chapter 2 I investigate the origin of the scatter in the $R - L$ relationship which has recent relevance for the accuracy with which this relation can be used for cosmic distance measurements. Chapter 2 has been submitted for publication. Then, in Chapter 3 I investigate the impact of the BH accretion luminosity on the shape of the line profiles that are used for BH mass measurements and therefore impacts BH mass measurements. I also address the potential impact from the source variability. Chapter 3 will be submitted for publication in the immediate future.

For the ULIRG phase my work in Chapter 4 contributes by providing a new catalog of nearby ULIRGs from the *AKARI* all-sky survey that help to increase the number of known ULIRGs in the local Universe. I investigate morphological and spectroscopic properties of local ULIRGs based on the public SDSS data. I compare star formation rates, metallicities and colors of the local ULIRGs with the local star forming galaxies. Chapter 4 has been submitted for publication.

Chapter 5 presents the main conclusions and future prospects.

2

ON THE SCATTER IN THE RADIUS – LUMINOSITY RELATIONSHIP FOR ACTIVE GALACTIC NUCLEI

ABSTRACT – *We investigate and quantify the observed scatter in the empirical relationship between the broad line region size R and the luminosity of the active galactic nucleus (AGN) and find it has a correctable dependence on color. The possible importance of this relationship for cosmological studies, including accurate measurements of cosmic distances and black hole masses, is the motivation for this study as we seek to further reduce the scatter. We examine six nearby reverberation-mapped AGN for which simultaneous UV and optical monitoring data exist. We also examine the optical luminosity variations of Seyfert 1 galaxy NGC 5548 for which more than 20 years of optical monitoring data are available and employ Monte Carlo simulations to study the effects of the intrinsic variability of individual AGN on the scatter in the global relationship for a sample of ~ 40 AGN. Our study shows that for individual sources, the size of the $H\beta$ emitting region has a steeper dependence on the optical nuclear luminosity that can introduce a scatter of ~ 0.08 dex into the global relationship. This is because of the non-linear relationship between the variations in the ionizing continuum and those in the optical continuum. Yet the dependence on the UV luminosity is consistent with expectations from photoionization physics. Also, our analysis highlights the importance of understanding and minimizing the scatter in the relationship traced by the intrinsic variability of individual AGN, since it propagates directly into the global relationship. We find that using the UV luminosity as a substitute for the ionizing luminosity can reduce a sizable fraction of the current observed scatter of ~ 0.13 dex in the $R - L$ relationship with a positive impact on the accuracy of cosmic distance measurements. The uncertainty in the luminosity distance modulus can potentially be reduced from 0.33 mag to 0.26 mag or lower by updating the current, relatively tight $R - L(\text{optical})$ relationship to a well-calibrated $R - L(\text{UV})$ relationship, void of object-to-object differences, such as internal reddening.*

2.1 INTRODUCTION

Owing to their powerful and persistent emission that can be observed across most of the observable Universe (e.g., Mortlock et al., 2011), there has been a strong interest in using quasars as cosmological probes since their discovery. Because active galactic nuclei (AGN) and quasars are powered by accretion of matter onto supermassive black holes centered in their host galaxies and the majority reside at cosmic distances (e.g., Peterson, 1997), there are multiple ways in which these enigmatic sources can be used as cosmic probes:

1. A quasar can be used as a background light source to study the intervening intergalactic

medium as it absorbs the quasar emission (e.g., Wolfe et al., 2005; Krogager et al., 2013; Fynbo et al., 2013);

2. Quasars can act as ‘light houses’ by which to locate and study some of the most massive galaxies in the Universe out to the earliest epochs. This can be done because quasars are powered by the most massive black holes known (e.g., Vestergaard, 2004; Vestergaard et al., 2008; Jiang et al., 2010; De Rosa et al., 2013) and the most massive black holes tend to reside in the most massive galaxies (e.g., Tremaine et al., 2002; Ferrarese & Ford, 2005b);
3. Only for AGN and quasars can the mass of the central black hole be measured for galaxies beyond our local neighborhood (e.g., Ferrarese & Ford, 2005b), permitting studies of black hole growth (e.g., Vestergaard & Osmer, 2009; Kelly et al., 2010; Trakhtenbrot & Netzer, 2012; Kelly & Shen, 2013b) and feedback – as manifested in observations of galaxy clusters (e.g., McNamara & Nulsen, 2007) and galaxies (e.g., Merloni & Heinz, 2007; Werner et al., 2014) and in numerical simulations (e.g., Hopkins et al., 2006; Croton et al., 2006);
4. An AGN or quasar can act as a standard candle or standard ruler to measure cosmological distances or constrain cosmological parameters (e.g., Collier et al., 1999; Elvis & Karovska, 2002; Cackett et al., 2007; Watson et al., 2011; Haas et al., 2011; King et al., 2013b; Hönig, 2014).

The use of AGN as standard candles/rulers has previously been attempted by means of the broad line equivalent width (i.e., the Baldwin Effect; Baldwin, 1977) and/or accretion disk emission (e.g., Collier et al., 1999; Elvis & Karovska, 2002; Cackett et al., 2007), but neither method has yet proven particularly useful. The situation has changed in the last few years as the empirical relationship between the ‘size’ (or radius, R) of the broad emission line region (BLR) and the nuclear continuum luminosity L (i.e., the $R - L$ relationship; e.g., Bentz et al., 2013) has proven to be especially tight, permitting a more robust measure of the AGN luminosity. While the relationship has traditionally been used to predict the BLR distance from the black hole for estimates of black hole masses of distant quasars (e.g., Vestergaard, 2002; McLure & Jarvis, 2002b; Vestergaard & Peterson, 2006; McGill et al., 2008; Wang et al., 2009; Rafiee & Hall, 2011; Shen et al., 2011; Park et al., 2013), recent studies suggest its use as a cosmological probe also at high redshifts (Watson et al., 2011; Haas et al., 2011; Melia, 2013). In particular, Watson et al. (2011) suggest the reverse use of the relationship to predict the luminosity from a direct measure of the BLR size and propose ways in which the scatter in the relationship at the time (~ 0.2 dex, corresponding to a distance modulus $\Delta\mu=0.5$ mag) can be reduced.

The AGN Radius – Luminosity Relationship The emission from the central engine in AGN and quasars is not constant in time, but varies, likely in response to variations in the rate at which matter falls onto the supermassive black hole from the accretion disk surrounding it. Gas in their immediate vicinity, the so-called broad line region, is photoionized by the continuum photons emitted by the central accretion disk and emits the characteristic broad emission lines that are among the defining spectral features of Type 1 AGN. The emission line fluxes vary in response to the changes in the driving continuum luminosity with a certain time delay, τ . This delay is the light travel time of the ionizing photons to the BLR, and we can infer the size of this region, i.e., the distance to the gas, as: $R_{BLR} = c\tau$, where c is the light speed. The reverberation-mapping (RM) technique (Blandford & McKee, 1982; Peterson, 1993) measures τ by comparing the continuum and line emission light curves. There are now nearly 50 measurements of the size of the $H\beta$ broad line-emitting regions, $R(H\beta)$, in nearby AGN (Peterson et al., 2004; Bentz

et al., 2010, 2013, and references therein) plus several measurements of lags for other emission lines. We observe a tight relationship between the size R_{BLR} and the optical nuclear continuum luminosity, $L(\text{optical})$ (e.g. Bentz et al., 2009a, 2013, and references therein). In the following, we use R_{BLR} to refer to the BLR size in general, and $R(\text{H}\beta)$ and $R(\text{C IV})$ to refer to the sizes of the $\text{H}\beta$ and C IV emitting regions, respectively.

The empirically established $R_{BLR} - L$ relationship is expected from the underlying photoionization physics. The main parameters of photoionization equilibrium models are: (i) elemental abundances, (ii) the shape of the ionizing continuum, (iii) the particle density of the photo-ionized gas, and (iv) the ionization parameter U (Osterbrock & Ferland, 2006) defined for hydrogen as:

$$U = \frac{1}{4\pi R^2 c n_H} \int_{\nu_0}^{\infty} \frac{L_\nu}{h\nu} d\nu = \frac{Q(H)}{4\pi R^2 c n_H} \propto \frac{L(\text{ionizing})}{4\pi R^2 c n_H} \quad (2.1)$$

where n_H is the total hydrogen number density; R is the distance to the ionized gas (here, it is the BLR radius for the hydrogen broad emission lines); ν_0 is the threshold ionization frequency for hydrogen; $Q(H)$ is the production rate of hydrogen ionizing photons and $L(\text{ionizing})$ is the ionizing luminosity. To first order, AGN spectra look the same across a wide range in luminosity (Dietrich et al., 2002). This suggests that the values of n_H and U (or the product $U n_H$) are generally the same for all BLRs (e.g., Peterson, 1997). Under this assumption, the distance to the line emitting gas is expected to scale as $R_{BLR} \propto L(\text{ionizing})^{0.5}$.

There have been several attempts in the past 20 years to test the existence of the $R_{BLR} - L$ relationship and to measure its slope. Davidson (1972) was the first to emphasize the importance of the ionization parameter in early photoionization calculations. The $R_{BLR} - L$ relationship appeared explicitly in the early reviews that covered emission-line variability (Mathews & Capriotti, 1985; Peterson, 1988). The first attempts at establishing the relationship were made in the early 1990's (e.g. Koratkar & Gaskell, 1991; Peterson, 1993) based on the early compilations of the first reverberation data. Laor (1998) and Wandel, Peterson, & Malkan (1999) used the reverberation data available at the time for the first calibration of the black hole mass scale based on radii calculated from the photoionization formula. The observed $R_{BLR} - L(5100)$ relationship finally became convincing with the addition of higher luminosity quasars (Kaspi et al., 2000) that not only doubled the size of the reverberation database but also expanded the luminosity range by another two orders of magnitude (Wandel et al., 1999).

Although the larger reverberation mapping sample size solidified the existence of an $R_{BLR} - L(5100\text{\AA})$ relationship, the observed slope (Kaspi et al., 2000, 2005) was steeper than that expected from photoionization physics – a consequence, it turns out, of reverberation mapping campaign observing strategies. The large aperture used for accurate spectrophotometry lets in more host galaxy light and the observed continuum luminosity contains an unwanted contribution from star light that can be significant for nearby AGN and is relatively larger for Seyferts than for quasars. This is so for two reasons: (1) Seyferts tend to be nearby objects for which the host galaxies are larger and brighter on the sky, and (2) the large intrinsic brightness of the nuclear source in quasars results in a large contrast of this emission relative to that of its host galaxy. Using *HST* and ground-based imaging Bentz et al. (2006a, 2009a, 2013) determine the host star light contribution to $L(5100)$ for the reverberation-mapped AGN sample (Peterson et al., 2004; Bentz et al., 2009b; Denney et al., 2010; Grier et al., 2012b). Based on the most recent corrected AGN luminosities that also account for the recently updated extinction maps for our Galaxy (Schlafly & Finkbeiner, 2011), Bentz et al. (2013) present the most well determined $R(\text{H}\beta) - L(5100)$ relationship for the $\text{H}\beta$ line emission to date and measure a slope of 0.53,

consistent with the theoretical prediction of the slope of 0.5 to within the errors ($\pm\sigma = 0.03$ dex).

The slope of the ‘global’ $R_{BLR} - L(5100\text{\AA})$ relationship (i.e., that traced by a sample of AGN with different black hole mass and intrinsic accretion state) is consistent with expectations based on photoionization physics, because the optical and ionizing luminosities are related (see also § 2.4.2). However, $L(5100)$ is only a proxy for the ionizing luminosity that drives the changes in R_{BLR} . We cannot directly observe or measure $L(\text{ionizing})$ ($\lambda < 912\text{\AA}$) due to absorption by Galactic hydrogen. Bentz et al. (2007) found that on the scale of an individual object, that of NGC 5548, the ‘local’ $R_{H\beta} - L(5100)$ relationship (i.e., that traced by its intrinsic variability and formed from multiple RM campaigns of this object) has a slope of ~ 0.7 that is statistically different from the photoionization physics expectations. Yet, Bentz et al. examine the empirical relationship between simultaneous pairs of optical and UV flux measurements and, combined with the available $H\beta$ lags at the time, estimate a slope of 0.55 for the local $R(H\beta) - L(UV)$ relationship for NGC 5548. These results indicate the likelihood not only that $L(UV)$ is a better proxy for $L(\text{ionizing})$ than $L(5100)$, but also that the movement of individual objects along their own local $R_{BLR} - L(5100)$ relationships, as they vary, is a source of scatter in the global $R_{BLR} - L(5100)$ relationship.

Motivated by the growing interest to investigate possible ways to improve the methods by which quasars and AGN can be used as cosmic probes, we examine in this work the scatter in the AGN $R - L$ relationship, since it is the heart of the quasar distance indicator method and of quasar black hole mass estimates. In particular, we are interested in the amount of scatter that may be attributed to the global $R_{BLR} - L(5100\text{\AA})$ relationship by the use of $L(5100\text{\AA})$ as a stand-in for $L(\text{ionizing})$, and whether such scatter can be mitigated by adopting a better proxy. In the following, § 2.2 describes the sample and database used for our analyses presented in § 3. In § 2.3.1 we examine the $L(\text{optical}) - L(UV)$ relationship for a small sample of nearby AGN for which near-simultaneous UV and optical luminosity observations exist. In § 2.3.2 and § 2.3.3, we investigate the effect that the steep local $R_{H\beta} - L(5100\text{\AA})$ relationship of Seyfert 1 galaxy NGC 5548 (slope ~ 0.7 ; Bentz et al., 2007; Zu et al., 2011) has on the scatter in the global $R_{BLR} - L(5100\text{\AA})$ relationship and consider the extension of such an effect for the larger RM sample in the global relationship. We discuss our results in § 4 and summarize our conclusions in § 5. A cosmology with $H_0 = 72 \text{ km s}^{-1} \text{ Mpc}^{-1}$, $\Omega_\Lambda = 0.7$ and $\Omega_m = 0.3$ is adopted throughout.

2.2 THE SAMPLE AND DATA

2.2.1 THE DATABASE FOR THE OPTICAL-UV LUMINOSITY RELATIONSHIP

We select six sources (NGC 5548, NGC 7469, NGC 3783, NGC 4151, 3C 390.3, and Fairall 9) from the sample of reverberation-mapped nearby AGN (Peterson et al., 2004) based on the availability of multiple epochs of quasi-simultaneous optical and UV data. Some basic properties of these objects (hereafter referred to as ‘the RM sub-sample’) are listed in Table 3.1. Our study is based on the publicly available optical and UV spectroscopic data from the International AGN Watch¹ database. The UV luminosities are derived from *IUE* and *HST* spectral data. Accurate host galaxy fluxes (Bentz et al., 2013) are available for all objects in this study. Each optical flux density measurement is matched with a single-epoch UV flux density that is the temporally closest UV luminosity measurement to within two days. When there is more than one observation in one day, we adopt the mean flux density and consider this daily average as ‘one epoch’.

¹<http://www.astronomy.ohio-state.edu/~agnwatch/>

We compute the rest frame monochromatic luminosity as $L_{\lambda(\text{rest})} = (1 + z)F_{\lambda(\text{obs})}4\pi D_L^2$, where $F_{\lambda(\text{obs})}$ is the observed monochromatic flux density, z is the redshift, $\lambda(\text{obs}) = \lambda(\text{rest})(1 + z)$, and D_L is the luminosity distance of the source; the values of z and D_L adopted here are listed in Table 3.1. For NGC 4151 and NGC 3783 we adopt the distances determined by Tully et al. (2009) because these galaxies are so nearby that the Hubble flow distance is inaccurate.

The optical monochromatic flux density is the average flux density in a $\sim 20 - 30$ wide range centered at a rest frame wavelength of 5100\AA . For 3C 390.3, the optical flux density is measured between 5170 and 5180 since the wavelength region around 5100\AA is contaminated by Fe II emission (Dietrich et al., 1998). Similarly, the UV continuum fluxes are the mean flux densities measured over a range of $\sim 30\text{\AA}$ in the UV spectra. Table 3.2 presents the object names (column 1), the Julian dates of the optical and UV observations (columns 2 and 4, respectively), and the wavelength range (column 7) centered at the specific rest frame wavelength (column 6) over which the monochromatic UV luminosities were measured. References to the original studies that first presented these data are listed in columns 3 and 5. In the following, we address the calibrations and the corrections applied to the data prior to our analyses.

Calibration and Measurements of the RM Sub-sample Data

In reverberation-mapping studies, it is common to use the [O III] $\lambda\lambda 4959, 5007$ line emission as an internal flux calibrator to place the spectra on an absolute flux scale. Internal flux calibration is necessary to account for varying atmospheric transparency, seeing conditions and potential slit losses due to seeing changes during the observations. The internal flux calibration is based on the assumption that the [O III] line emission is constant over the variability time scale (\sim days to weeks) of the broad line emission. This is a reasonable assumption because the [O III] line flux is typically constant on timescales of many years (Peterson, 1993) because it is produced by the narrow line gas located at spatial scales of ~ 100 pc, much farther from the BLR, and because the narrow-line region gas density is so low, that the recombination time scale is also very long. All the data analyzed here are calibrated by scaling the observed [O III] $\lambda 5007$ line flux to an absolute [O III] flux measurement based on spectrophotometric observations (see Table 3.2 for references). Correction of the calibrated flux densities for reddening and host galaxy contribution is addressed in §2.2.1 and §2.2.1, respectively.

We note that in the case of NGC 5548 for which we have over 20 years of monitoring data, Peterson et al. (2013a) do see long term variations in the [O III] line flux and have, based thereon, re-calibrated the continuum and $H\beta$ flux measurements. We adopt these new flux values for our study and use the recently updated host galaxy flux measurements of Bentz et al. (2013) to compute the corresponding nuclear 5100\AA continuum flux densities and luminosities for each available monitoring campaign (Table 2.3).

For a couple of the datasets, further processing and/or measurements are required. For NGC 4151, the only optical spectra obtained during a UV monitoring campaign are those presented by Kaspi et al. (1996) from the *IUE* monitoring campaign in 1993. Among these data, we restrict our consideration to the OSU spectra (dataset C), obtained with the CCDS instrument on the Perkins 1.8-m telescope. This spectroscopic aperture ($5'' \times 7.5''$) is large enough to minimize aperture and seeing effects but small enough that the host galaxy star light correction to the observed flux is smaller than the AGN flux. To perform the absolute flux calibration for this object we compute the scaling factor to be applied from the observed [O III] $\lambda 4959$ line emission in order to avoid issues with potential saturation of the [O III] $\lambda 5007$ line (Bentz et al., 2006b). We adopt the absolute [O III] $\lambda 4959$ line flux measured by Bentz et al. (2006b) from spec-

trophotometric data. The continuum flux densities, F_{cont} , listed in Table 2.4 are measured as the average flux density in the observed reference frame between 5100Å and 5125Å.

Also for NGC 7469, we use only the OSU subset of the optical dataset presented by Collier et al. (1998) for data homogeneity reasons. These data were obtained with the Bollen and Chivens spectrograph on the 1.8-m Perkins telescope and a $5'' \times 7.5''$ spectroscopic aperture. For each spectrum we measure the observed continuum flux density, tabulated in Table 2.4, as the mean flux between 5176Å and 5200Å in the observed frame since Collier et al. (1998) measured the continuum at 4845Å that is likely to have He II $\lambda 4686$ and Fe II contamination.

Reddening Correction

We correct the optical and UV continuum flux densities for extinction due to the Galaxy using the extinction curve of Cardelli et al. (1989) and the $E(B - V)$ values relevant for each source based on the Schlafly & Finkbeiner (2011) recalibration of the dust maps of Schlegel et al. (1998) as listed in the NASA/IPAC Extragalactic Database (Table 3.1). With no robust way to estimate the nature and amount of the dust extinction of the intergalactic medium between the AGN and us or the interstellar medium of the AGN host galaxy, we do not apply any correction for these two potential sources of extinction. However, internal reddening is typically expected to be rather low in these objects, as we do not observe a UV-optical spectrum deviating strongly from a power-law (e.g., Crenshaw et al., 2001; Richards et al., 2003). Therefore, we do not expect the lack of internal dust correction to adversely affect our analyses and results.

Host Galaxy Star Light Correction

We subtract the starlight flux measured by Bentz et al. (2013) for each AGN from the observed optical flux density to obtain the *nuclear* luminosity $L(5100)$, adopting the host galaxy flux measured for the same specific aperture size and position as was used for the spectroscopic observations; these are listed in Table 3.1. We note that NGC 7469 has a nuclear star-forming ring with a diameter of $\sim 5''$ that is visible in both optical and UV imaging (Díaz-Santos et al., 2007). The optical fluxes from this spatially resolved star-forming ring is included in the host flux measurements adopted here, but the UV luminosities are not corrected for the contribution from young stars in the starburst ring.

2.2.2 DATA FOR THE $R - L(5100\text{Å})$ RELATIONSHIP FOR SEYFERT 1 GALAXY NGC 5548

For our analysis of the local $R(H\beta) - L(5100)$ relationship for NGC 5548 we use the results of 15 individual monitoring campaigns that each provide independent measurements of $R(H\beta)$ for a given $L(5100)$. NGC 5548 was monitored for 13 years by the International AGN Watch program (Peterson et al., 2002) starting in 1988, and again in 2005 (‘Year 17’; Bentz et al., 2007), (‘Year 19’; Denney et al., 2010), and 2008 (‘Year 20’; Bentz et al., 2009b). Collectively, these campaigns provide 16 individual measurements of $R(H\beta)$ for various luminosity states spanning more than 20 years. However, we exclude ‘Year 19’ because the results were somewhat ambiguous: the cross-correlation function (CCF) is broad and flat-topped with a “maximum” ranging from ~ 3 to ~ 23 days (Figure 3 of Denney et al., 2010). The velocity resolved time delay (Figure 4 of Denney et al., 2010) corroborates that the $H\beta$ emitting line region responds at this range of time scales. Although this may be real, such a broad range of possible lags for a single epoch does not provide sufficient information to be useful here. For the other 15 campaigns, we compute

the nuclear AGN luminosities (listed in Table 2.3) based on the most recent recalibration of the [O III] $\lambda 5007$ narrow-line flux of NGC 5548 (Peterson et al., 2013a), the most recently updated host-galaxy flux measurements (Bentz et al., 2013), and the source distance listed in Table 3.1.

NGC 5548 is the only object for which we can generate a local $R(\text{H}\beta) - L(5100)$ relationship because other objects in the RM sample have only been monitored during a single reverberation mapping campaign, or at most a couple of campaigns, insufficient for this study. Because of this, as well as the fact that intrinsic variability drives this local $R(\text{H}\beta) - L(5100)$ relationship, we first verify that NGC 5548 is representative of other objects in the RM sample, with respect to variability properties. In the histogram in Figure 2.1 we compare the fractional variation, $F_{var}(\text{continuum})$, a measure of the intrinsic variation amplitudes of the nuclear continuum (Rodríguez-Pascual et al., 1997), for all the sources in the RM sample based on the previous published RM studies. The F_{var} values for NGC 5548 (listed in Table 2.3, column 2) we computed based on equation (3) of Rodríguez-Pascual et al. (1997) using the updated host fluxes and Galactic reddening of Bentz et al. (2013) and the re-calibrated measured flux densities in column 3 of Table 2.3. Since the $F_{var}(\text{continuum})$ values for NGC 5548 (gray shaded histogram) fall in the middle of the sample distribution, it is reasonable to assume for the purpose of this investigation that NGC 5548 is representative of the RM sample. Yet, this comparison also shows that NGC 5548 does not probe the most extreme variability of the RM sample, which is about 50% larger than that of NGC 5548. Sergeev et al. (2007a) present light-curves from 30 years of monitoring NGC 5548 from 1972 – 2001 and find similar variability characteristics during this period and when comparing the earlier (1972 – 1988) and later (1989 – 2001) campaigns. This demonstrates that the 20 year period over which our observations span is representative of all known variability characteristics of this source.

We use the results of two different analysis methods to determine the $R(\text{H}\beta)$ values because they yield different uncertainties that can affect the scatter that we aim to quantify. The cross-correlation function (CCF) method uses cross-correlation of the intra-day interpolated continuum and emission-line light curves to determine the time delay (see Peterson et al., 2004, for details), while ‘JAVELIN²’ (Zu et al., 2011) uses more advanced statistical Markov Chain Monte Carlo techniques to derive the delay, taking advantage of the observation that AGN variability can be well described as a damped random walk process (Kelly et al., 2009; Kozłowski et al., 2010; MacLeod et al., 2010). The 15 $R(\text{H}\beta)$ measurements based on the CCF analysis are adopted from Peterson et al. (2004), Bentz et al. (2007), and Bentz et al. (2009b). The JAVELIN analysis of Zu et al. (2011) provides 13 of the 15 measurements of $R(\text{H}\beta)$, since that study did not include the Bentz et al. (2007) and Bentz et al. (2009b) data. To allow a direct comparison with the CCF database we add our own, similar, JAVELIN analysis (following Grier et al., 2012a) of these two campaigns for which we obtain $\tau_{\text{rest}} = 5.54^{+2.32}_{-1.85}$ days for year 17 (Bentz et al., 2007) and $\tau_{\text{rest}} = 4.52^{+0.36}_{-0.33}$ days for year 20 (Bentz et al., 2009b).

2.3 ANALYSES AND RESULTS

2.3.1 THE OPTICAL–UV CONTINUUM LUMINOSITY RELATIONSHIP

We investigate the relationship between multiple epochs of simultaneous measurements of optical and UV continuum luminosities for individual sources and for the sample as a whole. The goals are to establish whether the optical and UV luminosities are mutually interchangeable

²JAVELIN (‘Just Another Vehicle for Estimating Lags In Nuclei’) is formerly known as ‘SPEAR’; <https://bitbucket.org/nye17/javelin>.

and, if not, to estimate how much scatter can be introduced into the radius – luminosity relationship by adopting $L(5100\text{\AA})$ rather than $L(\text{UV})$ as a proxy for $L(\text{ionizing})$. For this analysis, we compile quasi-simultaneous measurements (within two days) of $L(\text{optical})$ and $L(\text{UV})$, as described in §2.2.1. We show the relationship between the quasi-simultaneous optical and UV luminosities for the RM sub-sample in Figure 2.2, where each object is identified by its own symbol. For NGC 5548 we have two datasets obtained during two different monitoring campaigns. ‘NGC 5548 year 1’ (‘NGC 5548 year 5’) refers to the monitoring campaign that ran in 1988 (1993). We refer to the combined dataset of years 1 and 5 as ‘NGC 5548 All’. A clear, positive trend between $L(\text{optical})$ and $L(\text{UV})$ is seen in Figure 2.2, as expected. Yet, we find that each individual object exhibits its own, i.e., ‘local’, $L(\text{optical}) - L(\text{UV})$ correlation that differs in slope from that of other objects and also from the ‘global’ relationship that exists across the entire sample.

To characterize the $L(\text{optical}) - L(\text{UV})$ relationship, we adopt the following parameterization:

$$\log \left[\frac{\lambda L_{\lambda}(\text{optical})}{10^{43} \text{ erg s}^{-1}} \right] = A + \alpha \log \left[\frac{\lambda L_{\lambda}(\text{UV})}{10^{44} \text{ erg s}^{-1}} \right] + \epsilon_i. \quad (2.2)$$

where A is the zero point, α is the slope, and ϵ_i is the estimated scatter³. We establish the best fit relationship for each object and the sample as a whole by use of the Bayesian regression method⁴ of Kelly (2007) because it is more robust than the commonly used FITEXY χ^2 minimization method (Press et al., 1992) for small samples. The Bayesian method accounts for measurement uncertainties in both variables and the scatter, ϵ_i , and computes the posterior probability distributions of the parameters in Equation (2.2). This method uses Gaussian distributions to describe the measurement errors and the scatter, and a ‘Gaussian mixture model’ to represent the distribution of the independent variable. Since our dataset is relatively small, we use only a single Gaussian in the ‘mixture modeling’ to speed up the computations.

The results of our regression analysis are listed in Table 2.5, which contains the source name (column 1), the best fit parameters: intercept and slope (columns 2 and 3, respectively), the rms scatter, σ_{RMS} , of the data relative to the individual best fit relationships (column 4), and the estimated scatter, ϵ_i (column 5). Light curve statistics for the six AGN in our sample are listed in Table 2.6 with the time span for which we have simultaneous optical and UV data in column 2, the number of data pairs (epochs) in column 3, and the F_{var} values (§2.2.2) for the optical and UV continuum light curves in columns 4 and 5, respectively.

In Figure 2.2, we also show the best fit relationship for the entire sample (i.e., the global fit; solid line) by taking into account all the individual data points. The global $L(\text{optical}) - L(\text{UV})$ relationship has a slope $\alpha = 0.84 \pm 0.02$, while the slope is different for each individual AGN, with values in the range between 0.12 to 0.84 (Table 2.5). With these slopes being different from unity, there is not a one-to-one correspondence between the two luminosities for most of the AGN; only for Fairall 9 and 3C 390.3 are the measured slopes consistent with unity to within 2σ . The $F_{var}(\text{UV})$ values are clearly all larger than $F_{var}(\text{optical})$, showing stronger variability amplitudes at UV energies, as also indicated by the shallow $L(\text{optical}) - L(\text{UV})$ slopes.

NGC 7469 and NGC 4151 exhibit somewhat shallower slopes and lower variability amplitudes than the other AGN in the sub-sample. This is likely related to the very few available

³Note that while mathematically this is often referred to as the ‘intrinsic scatter’ (i.e., the additional scatter required, above that accounted for by the measurement errors, so that the regression analysis produces a χ^2 value of 1.0), by the nature of the observations we do not know if this scatter really is intrinsic or contains contributions from uncertainties in measurements and flux corrections. Therefore, we will refer to this scatter as the ‘estimated scatter’.

⁴implemented in IDL as ‘LINMIX_ERR.pro’

data points, obtained over a brief time span. Although these data are not likely to be representative of the intrinsic variability properties of these two AGN over similar time scales as that covered by the observations of the rest of this sub-sample, omitting these datasets do not change the results. This is verified by the unchanged regression result and inferred scatter (Table 2.5) when NGC 7469, with the larger F_{var} values of the two sources and uncorrected star light contribution to its UV luminosities (§ 2.2.1), is omitted.

Figure 2.2 shows that the local $L(\text{optical})-L(\text{UV})$ relationships do not fall on top of the best fit to the global relationship (solid line in Figure 2.2) but instead show slight zero-point offsets. These offsets can be due to, e.g., (1) imperfect host galaxy flux subtraction, (2) intrinsic differences in the spectral energy distributions between objects, (3) imperfect absolute spectrophotometric calibration, which was performed differently for the optical and UV data, or (4) uncorrected internal dust reddening in the AGN host galaxy that will be different for each object. Note that while the former two effects can impact both the zero-point and slope of the local $L(\text{optical}) - L(\text{UV})$ relationship, the latter two should not affect the slope of the local relationship. Combined with the local slopes being shallower than the global slope, this introduces a scatter in the global relationship. Our Bayesian analysis estimates the scatter of all the data pairs relative to a unity global relationship to be $\epsilon_0 = 0.09$ dex. Given the relatively short time scales for which we have quasi-simultaneous optical and UV luminosities, this scatter must represent a lower limit of the scatter we can expect by our use of $L(\text{optical})$ rather than $L(\text{ionizing})$ for the luminosity in the global $R(\text{H}\beta) - L(\text{ionizing})$ relationship.

One effect that can explain object-to-object differences is the accretion state of the central engine. Depending thereon, the specific $L(\text{optical})-L(\text{UV})$ relationship may change significantly in time: in the case of NGC 5548, the slope changes from 0.65 (year 1) to 0.39 (year 5). However, the ‘year 5’ dataset only covers 37 days, while ‘year 1’ covers 236 days, so the shallower slope and lower F_{var} value may also be related to the time span over which we have simultaneous optical and UV data, in this case. Nevertheless, because the paired UV and optical data only cover relatively short time spans, the slopes of the local $L(\text{optical})-L(\text{UV})$ relationship for each AGN are related to their short term continuum variations only. Since AGN continuum variations are unpredictable, we cannot assume that the slopes measured here are valid at other times, separated by several years⁵.

Another potential effect that can alter the slopes of the local $L(\text{optical})-L(\text{UV})$ relationships is the accuracy of the measured host galaxy flux values, F_{host} (Table 3.1, column 5). Given the shallow slopes, the only way to get a linear relationship is to assume that the host galaxy flux level of each object is underestimated. To test this, we iteratively subtract an increasing amount of host galaxy flux in addition to that listed in Table 3.1 until we measure a slope of 1.0 for each source. We list this additional amount of host galaxy flux needed as $F_{\text{gal,extra}}$ in Table 2.7. We find $F_{\text{gal,extra}}/F_{\text{host}}$ ratios in the range between $\sim 20\%$ and $\sim 300\%$ and for most of the sources $F_{\text{gal,extra}}$ is at least $\sim 40\%$ of F_{host} (Table 2.7). These $F_{\text{gal,extra}}$ values correspond to $4\sigma_{\text{host}} - 30\sigma_{\text{host}}$, a statistically significant change. Furthermore, the value of $F_{\text{gal,extra}}$ estimated for NGC 5548 is particularly unrealistic because if we were to subtract this extra flux from the continuum measurements presented by Peterson et al. (2013a), the continuum fluxes would be negative for some epochs. We consider it very unlikely that the host galaxy flux would be so grossly underestimated and conclude that the observed optical and UV variability amplitude

⁵Measurements separated by the damping time scale of the damped random walk can be considered to be truly independent. While the damping time scale is not well established and may be different for individual AGN, it appears to be of the order of 200 days in the restframe for SDSS quasars (Kelly et al., 2009; Kozłowski et al., 2010; MacLeod et al., 2010).

differences cannot be attributed to an inaccurate correction for host galaxy flux contamination at optical wavelengths.

2.3.2 THE RADIUS–LUMINOSITY RELATIONSHIPS OF NGC 5548

Our second study addresses the contribution to the observed scatter in the global $R(\text{H}\beta) - L(5100\text{\AA})$ relationship (i.e., based on the full sample of RM AGN) from the scatter introduced by a *single* object as it varies in luminosity over time. Longer term variations over time scales of several years will better probe this scatter as each measurement on the global relationship was obtained at a random time during the lifetime of each AGN. Ideally, we would want to examine how $R(\text{H}\beta)$ changes with the UV luminosity for all the objects in the RM sample, as $L(\text{UV})$ is expected to be a better estimate than $L(5100)$ of the ionizing luminosity that dictates the size of the $\text{H}\beta$ emitting region. Unfortunately, only for one object, NGC 5548, can the available data address its long term variability properties. Because the data are not available for a detailed analysis of the $R(\text{H}\beta) - L(\text{UV})$ relationship itself for NGC 5548, we examine instead the $R(\text{H}\beta) - L(5100\text{\AA})$ relation and the implications for its scatter from the observed $L(5100\text{\AA}) - L(\text{UV})$ relationship, presented above. We then examine the inferred $R(\text{H}\beta) - L(1350\text{\AA})$ relationship in order to test our assumption that $L(\text{UV})$ is a better proxy for $L(\text{ionizing})$.

The $R - L(5100)$ Relationship for NGC 5548

Figure 2.3 shows the $R(\text{H}\beta) - L(5100\text{\AA})$ relationships for the CCF (top) and JAVELIN (bottom) datasets. The red dashed lines are the best fit regressions to each dataset. We describe the $R - L(5100)$ relationship as:

$$\log \left[\frac{R_{BLR}}{1 \text{ light-day}} \right] = K + \beta \log \left[\frac{\lambda L_{\lambda}(5100)}{10^{44} \text{ erg s}^{-1}} \right] + \epsilon_0, \quad (2.3)$$

where K is the zero point, β is the slope, and ϵ_0 is the estimated scatter. Because the regression method cannot account for the asymmetric uncertainties in our R_{BLR} measurements we performed an extensive ‘error-bar sensitivity test’ (described in Appendix A.1) to test the effects of adopting a particular symmetric uncertainty on R_{BLR} . The test revealed that the regression results are not significantly affected by which of the possible error-bars we adopt. To be conservative we adopt the larger of the upper and lower 1σ uncertainties for each object and quote the best fit parameters to equation (2.3) based thereon. The best fit slope and intercept obtained from the Bayesian analysis are the median values of the posterior probability distributions while the quoted uncertainties are the standard deviations with respect to the median. For each of the CCF and JAVELIN datasets, Table 2.8 lists the resultant zero-point and slope of the $R - L(5100)$ relationships (columns 2 and 3, respectively); the root mean square scatter, σ_{RMS} , of the R_{BLR} data (column 4) relative to the best fit relationship; the estimated scatter ϵ_0 (column 5); and the precision of the scatter estimate (column 6).

The regression slopes obtained from both datasets agree to within the errors. This is expected since Zu et al. (2011) found mostly consistent lag measurements (R_{BLR}) for the CCF and JAVELIN analysis methods. However, the CCF dataset has larger R_{BLR} uncertainties. Bentz et al. (2007) examine the $R(\text{H}\beta) - L(5100\text{\AA})$ relationship for NGC 5548 using only the CCF data of the first 14 campaigns (Year 1 – 17) and find a slope $\beta = 0.73 \pm 0.14$. Zu et al. (2011) examine the same relationship with the JAVELIN dataset and obtain a slope $\beta = 0.73 \pm 0.10$. We note that our current dataset is somewhat improved compared to these studies owing to updates to

the host galaxy contribution measured for individual spectral apertures and Milky Way reddening corrections (Bentz et al., 2013) and the improved calibration of the nuclear fluxes (Peterson et al., 2013a). As a result, we obtain slightly steeper slopes ($\beta = 0.79 \pm 0.20$ for the CCF data; $\beta = 0.88 \pm 0.17$ for the JAVELIN data) than these previous studies, but our results are still consistent to within the uncertainties.

The best fit slope for each of the CCF and JAVELIN dataset is steeper than the global slope, $\beta = 0.53$, established by Bentz et al. (2013). For the CCF dataset, the uncertainty on the slope shows that there is less than a 20% probability that the local slope is intrinsically similar to the global one and, therefore, we consider this steeper local slope to be real. Since we argue that NGC 5548 is representative of reverberation mapped AGN (§2.2.2), a steeper local slope is likely typical of AGN. This suggests that the intrinsic variability of individual sources introduces additional scatter into the global relationship. We are, therefore, interested in assessing the scatter on the global relationship introduced by this particular well-studied object. We estimate the scatter of the NGC 5548 $R(\text{H}\beta)$ measurements relative to the global relationship (black solid lines in Figure 2.3) by fitting each of the CCF and JAVELIN datasets with a fixed slope of $\beta = 0.53 \pm 0.03$. We derive a scatter of 0.09 dex and 0.12 dex for the CCF and JAVELIN datasets, respectively; each is insensitive to the size of the adopted errorbar (see Appendix A.1). For completeness we report two types of scatter in Table 2.8 and Figure 2.3: one relative to the local $R(\text{H}\beta) - L(5100\text{\AA})$ relationship for NGC 5548 (red dashed curve) and the scatter contribution of this source to the global relationship (with slope $\beta = 0.53$; black solid curve), which is the scatter of prime interest to this study. We infer a larger amount of scatter based on the JAVELIN dataset compared to the CCF dataset. This is easily understood because the measured local slope is steeper in this case and the degree of estimated scatter depends⁶ on the amplitudes of the uncertainties of the R_{BLR} and $L(5100)$ measurements and the JAVELIN dataset has smaller R_{BLR} uncertainties.

Since we demonstrate above that the variability of NGC 5548 is representative of reverberation-mapped AGN, we can extrapolate these results to predict that the variability of individual objects will add a scatter of order 0.1 dex into the global $R(\text{H}\beta) - L(5100\text{\AA})$ relationship. We verify this in §2.3.3 by means of Monte Carlo simulations.

The $R - L(\text{UV})$ Relationship of NGC 5548

Because $L(\text{ionizing})$ is the luminosity that sets the BLR size, and $L(\text{UV})$ is closer in energy to $L(\text{ionizing})$ than $L(\text{optical})$, we test here if an inferred local $R(\text{H}\beta) - L(1350\text{\AA})$ relationship for NGC 5548 will have a slope of ~ 0.5 , more consistent with the physical expectations. This is a zeroth-order test because the $L(1350\text{\AA})$ values are not direct measurements but inferred from the available optical luminosities for most $R(\text{H}\beta)$ measurements. To convert the $L(5100\text{\AA})$ values to $L(1350\text{\AA})$, we use the $L(5100\text{\AA}) - L(\text{UV})$ relationship established for the ‘NGC 5548 All’ dataset and given in Table 2.5. The data from the two separate monitoring years do produce somewhat different $L(5100\text{\AA}) - L(\text{UV})$ slopes. However, using all available data to cover a longer temporal baseline over which to calculate a single relationship is likely to be more representative⁷ of the overall relationship between $L(5100\text{\AA})$ and $L(\text{UV})$ over the time scales covered by our full set of $L(5100\text{\AA})$ measurements.

To convert $L(5100)$ to $L(1350)$ we adopt the following parameterization, obtained by re-

⁶The sum of the quadratures of the measurement uncertainties and the estimated scatter ϵ_0 (see equation (2.3)), respectively, must sum to the quadrature of the observed scatter, the σ_{rms} .

⁷If we adopt the ‘Year 1’ slope for the conversion, the slope changes but the observed scatter inferred from a similar analysis to that outlined below does not change significantly.

gressing the NGC 5548 data with $L(5100\text{\AA})$ as the independent measurement⁸:

$$\log \left[\frac{\lambda L_{\lambda}(1350)}{\text{erg s}^{-1}} \right] = 43.06 \pm 0.10 + (1.73 \pm 0.34) \log \left[\frac{\lambda L_{\lambda}(5100)}{10^{43} \text{erg s}^{-1}} \right]. \quad (2.4)$$

The normalizations of the luminosities are introduced to better constrain the uncertainties in the regression procedure (e.g., Tremaine et al., 2002). The errors on $L(1350\text{\AA})$ are propagated from the uncertainties in the $L(5100\text{\AA})$, slope, and intercept values according to standard error propagation rules (Taylor, 1997) and are therefore larger than we expect from direct UV measurements. The results of this luminosity conversion are demonstrated in Figure 2.4, which shows the $R(\text{H}\beta) - L(1350\text{\AA})$ relationships based on the CCF (top) and JAVELIN (bottom) datasets.

Regression analysis on these new relationships yields best-fit slopes for the CCF and JAVELIN datasets of $\beta = 0.47 \pm 0.15$ and $\beta = 0.52 \pm 0.12$, respectively, close to the theoretically expected slope. This suggests that $L(\text{UV})$ is a better proxy of $L(\text{ionizing})$ and for that reason we may also expect a reduction in the scatter of the $R(\text{H}\beta) - L$ relationship by adopting the $L(\text{UV})$ luminosity. Unfortunately, we cannot strictly address this latter issue because the larger propagated uncertainties on $L(1350\text{\AA})$ in our current investigation may be suppressing the estimated scatter artificially.

The similar work of Bentz et al. (2007) also obtains best-fit slopes ~ 0.5 . However, the current work supersedes that earlier effort because it is based on (a) a larger database of NGC 5548 monitoring data with improved flux calibration; (b) improved luminosity measurements and uncertainties owing to improved host galaxy light determinations, Galactic extinction corrections, and updated uncertainty determinations; (c) an analysis to specifically address how the connection between the optical and UV luminosities factors into the scatter in the observed global $R(\text{H}\beta) - L(5100\text{\AA})$ relationship based on $R(\text{H}\beta)$ values derived from both the classical CCF method and the new JAVELIN method; (d) Monte Carlo simulations (§2.3.3) to predict the effects of the local $R(\text{H}\beta) - L(5100\text{\AA})$ and $R(\text{H}\beta) - L(1350\text{\AA})$ relations on the corresponding global relationships (addressed next).

2.3.3 THE EFFECT OF INTRINSIC AGN VARIABILITY ON THE GLOBAL $R(\text{H}\beta) - L(5100\text{\AA})$ RELATIONSHIP: MONTE CARLO SIMULATIONS

Our analysis of the local $R(\text{H}\beta) - L(5100\text{\AA})$ relationship for NGC 5548 in §2.3.2 shows that its steep slope can introduce a scatter of order 0.1 dex in the global $R(\text{H}\beta) - L(5100\text{\AA})$ relation. If this steep local relationship is characteristic for all the reverberation mapped AGN, the question remains: how much of the current scatter in the global $R(\text{H}\beta) - L(5100\text{\AA})$ relation is due to this effect? To examine this, we performed Monte Carlo simulations using mock databases of R and L pairs that sample the local NGC 5548 $R(\text{H}\beta) - L(5100\text{\AA})$ relationship and apply it to the sample of reverberation mapped AGN presented by Bentz et al. (2013).

To generate the mock database, we assume that each AGN in the sample varies in a similar manner to NGC 5548. We let each object vary in luminosity along its own local $R(\text{H}\beta) - L(5100\text{\AA})$ relationship with an assumed slope $\beta = 0.79$ and scatter $\epsilon_0 = 0.081$ dex in $R(\text{H}\beta)$ (i.e., applying the results of the CCF dataset shown in the top panel of Figure 2.3). We describe the luminosity distribution by a Gaussian function centered at the mean luminosity, $\langle L \rangle$, observed for each AGN (Bentz et al., 2013) with a standard deviation of $\sigma_L = 0.30$ dex, as measured for NGC 5548 for the 15 epochs analyzed here (§2.2.2). For the purpose of this test, a Gaussian function is a

⁸This is consistent with inverting equation (2.2) but setting $\epsilon_i = 0$.

reasonable approximation of AGN variability behavior, which can be described by a damped random walk (e.g., Kelly et al., 2009; Kozłowski et al., 2010), i.e., a stochastic process with an exponential covariance matrix. We perform 2000 Monte Carlo realizations, where each realization samples a given object at a random point along its simulated local relationship, and we make a mock global $R(H\beta) - L(5100\text{\AA})$ relationship by sampling 69 (R, L) pairs for the 39 AGN to match the sample size presented by Bentz et al. (2013); i.e., we use multiple (R, L) pairs for objects⁹ where Bentz et al. (2013) includes multiple RM results. Next, for a given realization of the mock global $R(H\beta) - L(5100)$ relationship, we compute for each of the 69 randomly selected (R, L) pairs, the residuals between the simulated values of R and the radius predicted from the Bentz et al. (2013) $R(H\beta) - L(5100)$ relationship. For the resulting distribution of the 69 R -residuals, we adopt the standard deviation as the observed scatter for this particular realization.

With 2000 realizations we obtain a distribution of the estimated scatter with a mean (i.e., the most likely scatter) and standard deviation of $\mu_{MOCK} \pm \sigma_{MOCK} = 0.106 \pm 0.009$ dex. This means that the combination of a steep local relationship and an assumed scatter in R around the local relationship of $\epsilon_0 \sim 0.08$ dex will result in a typical scatter in the global relationship of ~ 0.11 dex, if all AGN vary like NGC 5548. The steep slope of the local relation alone (i.e., when $\epsilon_0=0$) contributes a mean scatter of $\mu_{MOCK} = 0.077$ dex ± 0.007 dex in the global relationship, entirely consistent with the scatter contributions adding in quadrature.

In reality, each AGN will vary with a different local slope, β , and scatter, ϵ_0 , and a different σ_L around its mean luminosity, $\langle L \rangle$, and will thereby contribute with a higher or lower scatter to the global $R(H\beta) - L(5100\text{\AA})$ relationship than we estimate for NGC 5548. There are insufficient data to address the likely distributions of β and ϵ_0 for the $R(H\beta) - L(5100\text{\AA})$ relationships of individual AGN, but there are indications that σ_L is luminosity dependent and therefore lower for quasars (e.g. Vanden Berk et al., 2004; Bauer et al., 2009; Schmidt et al., 2010). Although Figure 2.1 shows that NGC 5548 does not have the most extreme optical variability properties of the RM AGN, it has exhibited the largest $L(5100\text{\AA})$ differences, ΔL , on long time scales (Bentz et al., 2013); a larger σ_L will result in larger ΔL . Therefore, by adopting the same $\sigma_L = 0.3$ dex value for all AGN in the simulations, we obtain an upper limit on the expected global scatter. Our tests show that as the luminosity distributions narrow to $\sigma_L = 0.1$ dex, the mean scatter μ_{MOCK} approaches 0.085 dex, a scatter slightly higher than the assumed scatter in the local relationship, ϵ_0 . Our analyses also show that as β approaches the slope of the global relationship (i.e., the AGN vary *along* the global relationship, as opposed to across it), the expected global scatter μ_{MOCK} converges on the assumed value of ϵ_0 . This underscores the importance of further understanding the existing scatter in the local relationship and its effect on the global relationship.

Our estimates of the expected global scatter of ~ 0.11 dex, assuming all AGN vary like NGC5548, is a significant fraction of the observed scatter of 0.13 dex determined by Bentz et al. (2013) for the empirical global $R(H\beta) - L(5100)$ relationship. We note that while our simulated local relationships do contain a scatter (or noise) contribution (i.e., $\epsilon_0 > 0$) that can include some measurement uncertainties due to, for example, small inaccuracies in the R measurements, the scatter we simulated will not take into account other known sources of scatter in the global $R(H\beta) - L(5100)$ relationship due to distance measurements or poorly constrained lags that are included in the scatter measured by Bentz et al. (2013). The fact that we can account for a large fraction of the observed global scatter is good news. Understanding the origin of the scatter

⁹However, our tests show that the results are insensitive to how the 69 data pairs are selected among the AGN, as expected given the assumed similar variability properties of all the objects.

means that there is a potential for mitigating it.

2.4 DISCUSSION

2.4.1 THE SCATTER IN THE GLOBAL $R - L$ RELATIONSHIPS

Since the relationship was first established (e.g., Kaspi et al., 2000, 2005), the largest improvement imposed was the correction for host star light contamination of the optical luminosities (e.g., Bentz et al., 2006a, 2009a) that changed the global slope from ~ 0.7 to 0.54. Upon correcting for host galaxy contamination for the 35 AGN in the RM sample at the time, Bentz et al. (2009a) estimate the observed scatter, ϵ , using the FITEXY method (Press et al., 1992) to be $\sim 40\%$ or 0.15 dex (in R_{BLR}). As the measurements in recent years have improved, the observed $R(H\beta) - L(5100\text{\AA})$ relationship has become increasingly tighter. Peterson (2010) found a scatter of just 0.11 dex when including only the most robust measurements, namely those based on light curves so well-behaved that the time delay can be estimated by eye. The most recent work (Bentz et al., 2013) suggests that for 41 nearby AGN, that cover a wide optical luminosity range from 10^{42} erg s $^{-1}$ to 10^{46} erg s $^{-1}$, the observed scatter amounts to 0.19 dex when all data are included. When restricting the analysis to the better dataset where two AGN, Mrk 142 and PG 2130+099, with poorly constrained lags¹⁰ are omitted, the more robust Bayesian regression method of Kelly (2007) reveals a scatter of 0.13 dex. The Bentz et al. (2013) study includes new measurements of low-luminosity AGN and improved corrections for host galaxy light and Galactic reddening.

Understanding the origin of the observed scatter can help us understand how to minimize the scatter for future studies and application of the relationships. While high-quality data and accurate lag measurements are important for application to precision measurements of black hole mass and cosmic distances, other issues affect the scatter. Bentz et al. (2013) find that a large contribution to the observed scatter is in fact the accuracy to which we know the physical distance to some of the nearby AGN. These objects are so nearby that they do not follow the Hubble flow but have significant peculiar velocities, making their redshifts poorly suited for distance measurements; alternative distance measurements are often lacking or have large errors. Watson et al. (2011) also discuss known contributions to the currently observed scatter due to uncorrected but significant internal reddening in a few objects and remaining inaccurate lag measurements, the latter of which recent or ongoing studies are continuing to address (see e.g., Du et al., 2014, Peterson et al. 2014, in prep.). The main goal of our investigation has been to quantify the amount of scatter that can be introduced by the use of $L(5100\text{\AA})$ in the observed global radius – luminosity relationship and which can potentially be mitigated by adopting a better proxy of the ionizing luminosity $L(\text{ionizing})$ that drives this relationship (see eqn. (2.1)), such as the UV luminosity $L(1350\text{\AA})$.

In our study of how $L(5100\text{\AA})$ changes with $L(1350\text{\AA})$ for a sample of six RM AGN (§ 2.3.1; Figure 2.2), we find that the two luminosities are not linearly related (the global slope is ~ 0.84 ; Table 2.5) and therefore not directly interchangeable. Also, the shallow slopes and the F_{var} values (Table 2.6) indicate stronger UV variability, consistent with previous observations (e.g., Clavel et al., 1991; Korista et al., 1995; Vanden Berk et al., 2004; Wilhite et al., 2005; Zuo et al., 2012). Based on our Bayesian analysis, we find that the non-linearity between the optical and UV luminosities for individual AGN may introduce a scatter into the observed global $R(H\beta) -$

¹⁰Recent work suggest that the lag measurements for PG 2130+099 and Mrk 142 are in error. See Grier et al. (2013b), Bentz et al. (2013), and Du et al. (2014) for details and discussion.

$L(5100\text{\AA})$ relationship of 0.09 dex (Table 2.5), which is the best constraint that can be placed on this effect with the currently available data.

To study the impact of long-term variability on the scatter in the global $R(H\beta) - L(5100\text{\AA})$ relation, we turn to the well-studied Seyfert 1 galaxy, NGC 5548, the only source for which we have data spanning decades. Although this is just a single source, its variability nature is representative of the current RM sample (§2.2.2) and it is fair to assume that this AGN will provide a representative measure of the observed scatter in the global $R(H\beta) - L(5100\text{\AA})$ relationship.

While we analyze both the CCF and JAVELIN datasets of $R(H\beta)$ values in Section 2.3.2 we mainly focus on the results based on the standard CCF method as this allows a direct comparison with previous work. On account of the steep slope ($\beta = 0.79 \pm 0.20$; Table 2.8) and the scatter ($\epsilon_0 = 0.08$ dex) observed for the local $R(H\beta) - L(5100\text{\AA})$ relationship for NGC 5548, our Monte Carlo simulations (§2.3.3) show that if this local relationship is representative of each of the 39 AGN in the current global $R(H\beta) - L(5100\text{\AA})$ relationship, we can expect a scatter of 0.11 dex ± 0.01 dex in the global relationship, a significant fraction of the current scatter of 0.13 dex measured by Bentz et al. (2013). This estimate may likely be an upper limit to the scatter we can expect in the global relationship, because most AGN and, especially, the higher luminosity quasars are expected to vary with smaller luminosity amplitudes than assumed in our simulations, as discussed in §2.3.3. We find that for a decreasing typical variability amplitude for the AGN on the global relationship, the global scatter approaches a floor just above the level of the assumed local scatter, ϵ_0 . This emphasizes the importance of the scatter in the relationships traced by individual AGN, as they vary intrinsically, for the global scatter. Future work should focus on better understanding this scatter, as this is outside the scope of this work. The fact that the steep local slope alone can account for ~ 0.08 dex of the expected 0.11 dex global scatter implies that a significant fraction of the estimated scatter of 0.13 dex measured for the empirical global relation (Bentz et al., 2013) can potentially be mitigated by adopting a more accurate proxy for $L(\text{ionizing})$. In that case, we expect the local slope to be close to 0.5, as we see for the inferred local $R(H\beta) - L(1350\text{\AA})$ relationship for NGC 5548 (§2.3.2), such that the individual AGN vary *along* the global relationship. This particular situation highlights, again, the importance of the scatter in the relationship of individual AGN, which propagates directly through to the global relationship.

Effects of JAVELIN-based measurements. We note that our parallel analyses of the $R(H\beta) - L(5100\text{\AA})$ and $R(H\beta) - L(1350\text{\AA})$ relationships based on $R(H\beta)$ measurements with the JAVELIN analysis method corroborate the regression results based on the standard CCF method, showing a steeper slope of the optical relation and a slope consistent with 0.5 for the relation based on UV luminosities. However, they also suggest that the actual scatter in these relationships may be larger than estimated previously by means of the CCF method (e.g., Bentz et al., 2013). The estimated scatter depends on the measurement uncertainties (i.e., the size of the error bars). With its fuller use of information, the JAVELIN method yields $R(H\beta)$ measurements with smaller measurement errors. As a result, we infer a larger scatter for the JAVELIN-based radius – luminosity relationships. Specifically, we estimate a scatter of 0.12 dex ± 0.04 dex for the $R(H\beta) - L(5100\text{\AA})$ relationship of NGC 5548, $\sim 30\%$ larger than the value inferred based on the classical CCF method. Repeating the Monte Carlo simulations of §2.3.3 for the local $R(H\beta) - L(5100\text{\AA})$ relationship for the JAVELIN method, we obtain a predicted mean scatter $\mu_{\text{mock}} = 0.13 \text{ dex} \pm 0.01 \text{ dex}$ for the RM sample, assuming all the AGN vary like NGC 5548. However, we cannot quantify the relative contribution of this scatter to the scatter in the global relationship because, at present, JAVELIN-based lags (Zu et al., 2011) do not exist for the full

dataset presented by Bentz et al. (2013).

2.4.2 ON THE SLOPE DIFFERENCES BETWEEN THE LOCAL AND GLOBAL RELATIONSHIPS.

Given the photoionization physics predictions that $R \propto L(\text{ionizing})^{0.5}$, it is notable that when we use $L(5100\text{\AA})$, as opposed to $L(\text{ionizing})$, in the observed radius – luminosity relationship the global slope is very close to a value of 0.5 (Bentz et al., 2009a, 2013). Yet, on the contrary, the local $R(H\beta) - L(5100\text{\AA})$ relationship appear to be somewhat steeper than this global relation. What may appear as a conundrum is in fact easily explained by a general AGN property and the intrinsic source variability properties studied here. The regression results in Table 2.5 show that the mean optical and UV luminosities of individual AGN, marked in Figure 2.2 by black symbols, trace a linear $L(\text{optical}) - L(\text{UV})$ relationship across the AGN sample to within the uncertainties: the mean luminosities scale with a power of 0.96 ± 0.21 . This can be understood from the perspective that a more massive black hole will result in a higher mean luminosity that on average scales equally across the optical-UV region. This means that the average optical luminosity is typically a good proxy of the average UV luminosity. If the UV luminosity is a good proxy of $L(\text{ionizing})$, so is the mean optical luminosity and we can expect a global slope of the $R(H\beta) - L(5100\text{\AA})$ relationship close to 0.5. The steep slope of the local $R(H\beta) - L(5100\text{\AA})$ relationship for individual objects, as seen for NGC 5548 in Figure 2.3, is simply a result of the optical source flux varying typically with smaller amplitudes than the UV flux. This is verified by the higher F_{var} values for the UV continuum (Table 2.6) and the shallow slopes of the $L(\text{optical}) - L(\text{UV})$ relationship for individual AGN (Figure 2.2). That this is a luminosity color effect is confirmed by the local $R(H\beta) - L(1350\text{\AA})$ relationship for NGC 5548 having a slope ~ 0.5 .

2.4.3 ALTERNATE PROXY FOR THE IONIZING LUMINOSITY

The $H\beta$ line luminosity, $L(H\beta)$, is considered to be a good measure of the ionizing luminosity because $H\beta$ is a recombination line (Osterbrock & Ferland, 2006) and it, therefore, carries the potential of providing a good readily accessible proxy in the optical observing window (Wu et al., 2004; Greene et al., 2010). For that reason, one might expect that $L(H\beta)$ could provide a better measure of slope and scatter of the intrinsic $R(H\beta) - L(\text{ionizing})$ relationship than the propagated $L(1350\text{\AA})$. Unfortunately, the $R(H\beta) - L(H\beta)$ relationship does not offer any more information than that of the UV luminosities estimated in this work. Because $H\beta$ exhibits a Baldwin Effect when time delays are correctly accounted for (Gilbert & Peterson, 2003), there is not a one-to-one correspondence between the number of ionizing photons and the number of $H\beta$ photons. We verified this by measuring the narrow-line subtracted $H\beta$ luminosity from the mean spectra of NGC 5548 obtained from each of the epochs spanning the 20-year monitoring database available (§ 2.2.2). The resulting $R(H\beta) - L(H\beta)$ relationships (not shown) exhibit an even steeper slope than that of $R(H\beta) - L(5100\text{\AA})$ and only by applying a similar correction for the luminosity color (Gilbert & Peterson, 2003) as that applied here, do we confirm that the $R(H\beta) - L(\text{UV})$ relationship has a slope of 0.5. We therefore conclude that the best proxy for the ionizing luminosity is a directly measured luminosity at energies close to the peak of the ionizing spectral energy distribution, such as $L(\text{UV})$.

2.4.4 IMPLICATIONS FOR COSMOLOGY STUDIES

The amount of observed scatter in the global $R(\text{H}\beta) - L(5100\text{\AA})$ relationship is important for cosmological implications (Watson et al., 2011). It introduces an uncertainty in the inferred luminosity for a given measured $R(\text{H}\beta)$ and, as a result, in the luminosity distance. However, to use the relationship as a distance indicator, it is reasonable to use the better data and exclude clearly bad measurements. Bentz et al. (2013) show that the current $R(\text{H}\beta) - L(5100\text{\AA})$ relationship has an observed scatter of 0.13 dex when Mrk 142 and PG 2130+099 with a poorly constrained lags are omitted, which corresponds to an uncertainty in the distance modulus of $\Delta\mu = 0.33$ mag. This is already an improvement over the value of 0.5 mag reported by Watson et al. (2011). Our analysis shows that by adopting a more accurate proxy of $L(\text{ionizing})$ than $L(5100\text{\AA})$, such as $L(\text{UV})$, we may eliminate a scatter of ~ 0.08 dex (as estimated in this work based on the CCF method), thereby bringing the total observed scatter of 0.13 dex to 0.10 dex and reduce the uncertainty to $\Delta\mu = 0.26$ mag. The scatter in the global $R - L(\text{UV})$ relationship depends, however, on the scatter in the local relationships. This scatter may well be lower for a better proxy of $L(\text{ionizing})$. With additional attention to other sources of uncertainties and scatter in the $R(\text{H}\beta) - L(\text{ionizing})$ relationship, such as reddening, improved $R(\text{H}\beta)$ lag measurements, and distance measurements for some of the most nearby RM AGN (see Watson et al., 2011; Haas et al., 2011; Bentz et al., 2013, for discussion), the observed scatter can potentially be reduced further. For the $R(\text{C IV}) - L(1350\text{\AA})$ relationship applied to high-redshift AGN, our discussion earlier emphasizes again the importance of understanding the origin of the scatter in the local relationship of each individual AGN as the typical local scatter defines the scatter in the global relationship. Future studies of the large reverberation mapping datasets, obtained from multi-object spectroscopic monitoring campaigns of hundreds of AGN (some of which are currently underway), hold promise to establish how this scatter in the global relationships can be mitigated or minimized through a better understanding of the potential systematics involved. As a result, there is a large potential for the global $R(\text{C IV}) - L(1350\text{\AA})$ relationship to be a competitive luminosity distance indicator, both at low and high redshift.

2.5 CONCLUSION

Since the ionizing luminosity is what drives the radius – luminosity relationship, we have investigated whether the use of the optical luminosity $L(5100\text{\AA})$, as opposed to the ionizing luminosity, can account for some of the scatter in the observed global $R(\text{H}\beta) - L(5100\text{\AA})$ relationship (e.g., Bentz et al., 2013). Based on our analysis of the relationship between multiple near-simultaneous pairs of optical and UV continuum luminosity measurements (to within two days) available for six reverberation-mapped AGN (NGC 5548, NGC 7469, NGC 3783, NGC 4151, 3C 390.3, Fairall 9), the long-term optical and UV continuum flux variations of Seyfert 1 galaxy, NGC 5548, and a suite of Monte Carlo simulations, our main findings are as follows:

1. We present the most recent updates of the local $R(\text{H}\beta) - L(5100\text{\AA})$ relationship for NGC 5548 that takes into account the recalibration of the flux measurements of Peterson et al. (2013a) and the updates of Bentz et al. (2013). We present the relation for the $\text{H}\beta$ lags, $R(\text{H}\beta)$, determined by both the CCF and the JAVELIN methods (Table 2.8), finding slightly steeper slopes $\beta = 0.79$ and $\beta = 0.88$, respectively, than previously reported. The scatter measured in this local relation amounts to 0.07 dex – 0.08 dex. We also present JAVELIN-based lags of the Year 17 (Bentz et al., 2007) and Year 20 (Bentz et al., 2009b) monitoring campaigns, not included in the Zu et al. (2011) study.

2. We confirm $L(1350\text{\AA})$ to be a better proxy for $L(\text{ionizing})$ than is $L(5100\text{\AA})$. Our analysis of the local NGC 5548 $R(\text{H}\beta) - L(1350\text{\AA})$ relationship shows a slope consistent with the theoretically expected slope $\beta=0.5$ in contrast to the local $R(\text{H}\beta) - L(5100\text{\AA})$ relation.
3. The $\text{H}\beta$ luminosity is not a more suitable substitute for the ionizing luminosity than $L(5100\text{\AA})$ as it needs a similar color correction.
4. The typical lower variability amplitudes of the AGN optical continuum compared to the UV continuum suggest that the local $R(\text{H}\beta) - L(5100\text{\AA})$ relationship for individual AGN will typically be steep, as seen for NGC 5548. If all AGN vary like NGC 5548 with a similar slope of the local relationship, this steep slope alone will contribute a typical scatter of 0.08 ± 0.01 dex (§ 2.3.3) to the currently observed scatter of 0.13 dex (Bentz et al., 2013) in the global $R(\text{H}\beta) - L(5100\text{\AA})$ relationship. This suggests that a sizable fraction of the observed scatter can be mitigated by the use of a UV luminosity in lieu of $L(5100\text{\AA})$.
5. Assuming NGC 5548 is representative of the AGN population, the combined effect of the steep local slopes and the scatter in the local $R(\text{H}\beta) - L(5100\text{\AA})$ relationship can account for most (~ 0.11 dex) of the current scatter in the observed global $R(\text{H}\beta) - L(5100\text{\AA})$ relationship.
6. A significant contribution to the scatter in the global $R(\text{H}\beta) - L(5100\text{\AA})$, $R(\text{H}\beta) - L(1350\text{\AA})$, and $R(\text{C IV}) - L(1350\text{\AA})$ relationships comes from the scatter in the corresponding relationships traced by the individual AGN as they exhibit intrinsic luminosity variations. If the local (i.e., ‘intrinsic’) $R(\text{H}\beta) - L(5100\text{\AA})$ relationship for NGC 5548 is typical for AGN, then it can contribute a scatter ~ 0.08 dex to the global scatter, which is about half of the current observed scatter. To minimize the global scatter we need to better understand this local scatter. Future studies will need to focus on this effort as it is beyond the scope of the current work.
7. By adopting a UV luminosity as a better proxy for the ionizing luminosity than $L(5100\text{\AA})$, the scatter in the global $R(\text{H}\beta) - L(\text{UV})$ relationship is expected to be lower by ~ 0.08 dex than the current global $R(\text{H}\beta) - L(5100\text{\AA})$ relationship. This will invoke a reduction of the uncertainty in the distance modulus from 0.33 mag to 0.26 mag for cosmic distances derived from the $R(\text{H}\beta) - L(\text{UV})$ relationship. A further decrease of this uncertainty is expected when the scatter in the relationships traced by the intrinsic variability of individual AGN is better understood and when object-to-object differences, such as internal reddening, are corrected for.
8. Even though we see a steeper $R(\text{H}\beta) - L(5100\text{\AA})$ relationship for individual AGN than the global relationship for the entire reverberation mapped sample – because AGN typically vary with lower optical luminosity amplitudes than the ionizing luminosity that drives the relationship – the average optical luminosity of a given AGN is an equally good proxy of the average ionizing luminosity as the UV luminosity (§ 2.4.2).

By extrapolating these result we can expect that a well-populated version of the existing, but tentative, $R(\text{C IV}) - L(1350\text{\AA})$ relationship (Kaspi et al., 2007b) will similarly have less observed scatter. Along with the emphasis made by Bentz et al. (2013) on the pressing need to obtain accurate distances of the nearest AGN that define the lower end of this relationship, there is therefore a strong impetus to obtain additional monitoring data in the restframe UV energy range.

Table 2.1. Reverberation Mapping Sub-sample

Object	Redshift ^a	$E(B - V)$ ^a	Distance ^b (Mpc)	Host Flux ^c (10^{-15} erg s ⁻¹ cm ⁻² Å ⁻¹)	Aperture ("×")	P.A (°)
(1)	(2)	(3)	(4)	(5)	(6)	(7)
Fairall 9	0.04702	0.023	202.8±7.2	3.21 ± 0.16	4.0 × 9.0	0.0
3C 390.3	0.05610	0.063	243.5±7.2	0.99 ± 0.05	5.0 × 7.5	90.0
NGC 7469	0.01632	0.061	68.8±7.0	10.18 ± 0.94	5.0 × 7.5	90.0
NGC 5548	0.01718	0.018	72.5±7.0	3.97 ± 0.40	5.0 × 7.5	90.0
NGC 3783	0.00973	0.105	25.1±5.0	6.55 ± 0.65	5.0 × 10.0	0.0
NGC 4151	0.00332	0.024	16.6±3.3	16.17 ± 1.51	5.0 × 7.5	90.0

^aRedshifts and $E(B - V)$ values are adopted from NASA/IPAC Extragalactic Database. $E(B - V)$ values are based on the Schlafly & Finkbeiner (2011) dust maps.

^bLuminosity distances calculated from the redshifts with exception of NGC 3783 and NGC 4151, for which we adopt the the distances determined by Tully et al. (2009). They more reliable than the redshift-based distance because these two AGN have large peculiar velocities relative to the Hubble flow. The distances and the associated uncertainties for NGC 3783 and NGC 4151 are adopted from Bentz et al. (2013), while we assign an uncertainty of 500 km s⁻¹ in recession velocity for the remaining distance uncertainties.

^cHost galaxy flux densities, contaminating the spectral data, are adopted from Bentz et al. (2009a, 2013) and corrected for Galactic reddening as described in §2.2.1. For NGC 4151, the host galaxy flux is a new measurement for the specified spectroscopic aperture.

We thank Michael Goad, Kirk Korista, and Roberto Assef for helpful discussions. Brandon Kelly is thanked for helping with minor modifications of the *'linmix_err'* code to allow estimates of the scatter for a given, fixed slope. This work has benefited from the discussions at the workshop on *Improving Black Hole Masses in Active Galaxies* at the DARK Cosmology Center, 2012 July Copenhagen, Denmark. MV acknowledges support from a FREJA Fellowship granted by the Dean of the Faculty of Natural Sciences at the University of Copenhagen and a Marie Curie International Incoming Fellowship. KD acknowledges support from a Marie Curie International Incoming Fellowship and a National Science Foundation Postdoctoral Fellowship. MV thanks the Kavli Institute for Theoretical Physics at University of California, Santa Barbara for their hospitality while finalizing this work. The research leading to these results has received funding from the People Programme (Marie Curie Actions) of the European Union's Seventh Framework Programme FP7/2007-2013/ under REA grant agreement No. 300553 (MV and KD). The Dark Cosmology Centre is funded by the Danish National Research Foundation. This research was supported in part by the National Science Foundation through grant AST-1008882 to The Ohio State University (BMP), grant AST-1302093 (KD), CAREER Grant AST-1253702 to Georgia State University (MCB), and under Grant No. NSF PHY11-25915 (MV). This research has made use of the NASA/IPAC Extragalactic Database (NED), which is operated by the Jet Propulsion Laboratory, California Institute of Technology, under contract with the National Aeronautics and Space Administration.

Table 2.2. Datasets and References

Object (1)	Optical Data Julian Dates (2)	Optical Data ^a References (3)	UV Data Julian Dates (4)	UV Data ^a References (5)	λ_{rest} for $\lambda L_{\lambda}(UV)$ (6)	UV Continuum Window Range (7)
Fairall 9	2449476 – 2449664	1	2449477 – 2449665	8	1327Å	30Å
3C 390.3	2449734 – 2450068	2	2449735 – 2450068	9	1297Å	50Å
NGC 7469	2450249 – 2450274	3 ^b	2450248 – 2450273	10	1294Å	20Å
NGC 5548	2447509 – 2447746	4	2447510 – 2447745	10	1350Å	40Å
NGC 5548	2449095 – 2449133	4	2449097 – 2449135	11	1350Å	10Å
NGC 3783	2448610 – 2448832	5	2448612 – 2448833	12	1445Å	30Å
NGC 4151	2449318 – 2449335	6 ^c	2449318 – 2449335	13	1275Å	30Å

^aReferences: (1) Santos-Lleo et al. (1997); (2) Dietrich et al. (1998); (3) Collier et al. (1998); (4) Peterson et al. (2013a); (5) Stirpe et al. (1994); (6) Kaspi et al. (1996); (7) Rodriguez-Pascual et al. (1997); (8) O’Brien et al. (1998); (9) Wanders et al. (1997); (10) Clavel et al. (1991); (11) Korista et al. (1995); (12) Reichert et al. (1994); (13) Crenshaw et al. (1996).

^b For the NGC7469 spectra described by Collier et al. (1998) we chose only those obtained through the $5'' \times 7.5''$ aperture for which we have host galaxy flux density measurements (Bentz et al., 2009a, 2013). The observed flux densities at rest frame 5100Å that we re-measured for this work are listed in Table 2.4.

^c The NGC4151 data from Kaspi et al. (1996) are the subset obtained with the Perkins 1.8-m telescope at Lowell Observatory with a $5'' \times 7.5''$ spectroscopic aperture, re-calibrated for this study using the [O III] flux from Bentz et al. (2006b).

Table 2.3. Updated NGC 5548 Mean Flux Densities and Luminosities

Data Set	$F_{var}(continuum)^a$	$F(5100\text{\AA})\pm\sigma^b$ ($10^{-15} \text{erg s}^{-1} \text{cm}^{-2}$)	$\log[\lambda L_\lambda(5100)/\text{erg s}^{-1}]^c$ $\pm\sigma$
(1)	(2)	(3)	(4)
Year 1	0.188	6.176 ± 0.648	43.33 ± 0.09
Year 2	0.272	3.378 ± 0.546	43.07 ± 0.10
Year 3	0.154	5.336 ± 0.551	43.26 ± 0.09
Year 4	0.386	2.901 ± 0.504	43.00 ± 0.10
Year 5	0.148	5.375 ± 0.546	43.27 ± 0.09
Year 6	0.173	5.620 ± 0.588	43.29 ± 0.09
Year 7	0.117	7.918 ± 0.508	43.44 ± 0.08
Year 8	0.244	6.021 ± 0.554	43.32 ± 0.08
Year 9	0.209	3.765 ± 0.509	43.11 ± 0.09
Year 10	0.146	8.344 ± 0.630	43.46 ± 0.08
Year 11	0.229	6.899 ± 0.597	43.38 ± 0.08
Year 12	0.424	2.407 ± 0.502	42.92 ± 0.11
Year 13	0.293	2.323 ± 0.510	42.90 ± 0.11
Year 17	0.187	0.975 ± 0.527	42.53 ± 0.20
Year 19	0.157	1.346 ± 0.484	42.67 ± 0.15
Year 20	0.227	1.210 ± 0.409	42.62 ± 0.14

^aBased on the recalibrated nuclear flux densities at 5100Å, F(5100Å) (Peterson et al., 2013a)

^bUncertainty includes the mean spectral flux measurement uncertainty and the host flux uncertainty. The latter contains an additional 5% uncertainty due to seeing effects (for details, see Bentz et al., 2013).

^cMonochromatic nuclear (i.e., host-corrected observed) luminosity at 5100Å, calculated from Galactic reddening corrected F(5100Å) values. Luminosity errors include the distance uncertainties listed in Table 3.1.

Table 2.4. Continuum Flux Densities for NGC 4151 and NGC 7469

Object	JD ^a	F_{cont} ^b
NGC 4151	49324.0	6.46 ± 0.04
	49325.9	6.58 ± 0.02
	49326.9	6.64 ± 0.02
	49327.9	6.69 ± 0.02
	49328.9	6.61 ± 0.02
	49329.9	6.61 ± 0.02
	49330.9	6.59 ± 0.02
	49331.9	6.61 ± 0.02
	NGC7469	50248.5
50253.5		1.31 ± 0.08
50262.7		1.35 ± 0.08
50273.5		1.30 ± 0.08

^aJulian Dates subtracted by 240000.

^b Continuum flux densities at rest frame 5100Å, in units of 10^{-14} erg s⁻¹ cm⁻² Å⁻¹ measured in this work. Host galaxy light is not subtracted.

Table 2.5. Regression Results for the Optical-UV Luminosity Relationships

Object	Zeropoint, A^a	Slope, α^a	σ_{RMS}^b (dex)	ϵ_0^c (dex)
(1)	(2)	(3)	(4)	(5)
Fairall 9	0.56 ± 0.06	0.78 ± 0.13	0.049	0.027 ± 0.014
3C 390.3	0.70 ± 0.02	0.84 ± 0.14	0.074	0.037 ± 0.018
NGC 7469	0.36 ± 0.25	0.40 ± 0.23	0.038	0.035 ± 0.034
NGC 5548 All	0.55 ± 0.05	0.63 ± 0.12	0.043	0.017 ± 0.008
NGC 5548 year1	0.56 ± 0.05	0.65 ± 0.14	0.050	0.019 ± 0.012
NGC 5548 year5	0.45 ± 0.10	0.39 ± 0.22	0.020	0.025 ± 0.015
NGC 3783	0.15 ± 0.05	0.54 ± 0.05	0.036	0.037 ± 0.004
NGC 4151	0.04 ± 0.05	0.12 ± 0.09	0.005	0.006 ± 0.004
All Sources	0.61 ± 0.01	$0.84^d \pm 0.02$	0.114	0.055 ± 0.010
All Sources	0.63 ± 0.01	[1.00 \pm 0.00]	0.109	0.089 ± 0.009
All Sources except NGC 7469	0.61 ± 0.01	$0.84^d \pm 0.02$	0.115	0.054 ± 0.009
All Sources except NGC 7469	0.63 ± 0.01	[1.00 \pm 0.00]	0.109	0.090 ± 0.010
Mean Luminosities ^f	0.59 ± 0.11	0.96 ± 0.21	0.804	0.121 ± 0.129

^aBest fit parameters for $\log[\lambda L_\lambda(\text{optical})] = A + \alpha \times \log[\lambda L_\lambda(\text{UV})] + \epsilon_0$. The parameters are the median values of the posterior probability distributions, while the uncertainties are the standard deviation of the posterior distributions.

^bThe RMS scatter relative to the listed relationship.

^cThe measured scatter: the square-root of the median of the posterior probability distribution of the variance of the scatter.

^dThis slope of the measurements for the entire source sample is referred to in the text as ‘the global slope’.

^eThe slope is held fixed to unity during the regression to allow a measure of the scatter.

^fThe mean luminosities, shown as black symbols in Figure 2.2.

Table 2.6. Light Curve Statistics of the Optical-UV Database

Object	Simultaneity Time Frame ^a (days)	N^b	$F_{var}(\text{optical})$	$F_{var}(\text{UV})$
(1)	(2)	(3)	(4)	(5)
NGC 4151	17	8	0.012	0.077
NGC 5548 year5	37	24	0.056	0.158
NGC 7469	25	4	0.080	0.229
NGC 3783	221	44	0.142	0.218
NGC 5548 All	1624	75	0.176	0.291
NGC 5548 year1	236	51	0.197	0.302
Fairall 9	188	24	0.233	0.287
3C 390.3	333	20	0.268	0.319

^aThe time span covered by the simultaneous optical and UV data analyzed here.

^bNumber of optical-UV data pairs.

Note. — The entries in this Table pertain only to the subset of RM AGN analyzed in Figure 2.2 for the listed subset of monitoring data. The F_{var} histogram in Figure 2.1 is based on the full dataset of monitoring data for the full sample of RM AGN.

Table 2.7. Host Galaxy Flux Density Comparison

Object	$F_{gal,extra}^a$ ($\text{erg s}^{-1} \text{cm}^{-2} \text{\AA}^{-1}$)	$F_{gal,extra}/\sigma_{host}^b$	$F_{gal,extra}/F_{host}^b$ (%)
(1)	(2)	(3)	(4)
Fairall 9	6.60×10^{-16}	4.4	22
3C 390.3	1.73×10^{-16}	4.2	21
NGC 7469	3.00×10^{-15}	3.8	35
NGC 5548 All	2.48×10^{-15}	6.6	65
NGC 3783	2.64×10^{-15}	5.6	55
NGC 4151	4.24×10^{-14}	30.3	282

^a The amount of additional host galaxy flux density needed to obtain a slope of one in the $\lambda L_\lambda(\text{optical})-\lambda L_\lambda(\text{UV})$ relationship for each AGN.

^b The values of the host galaxy flux, F_{host} , and the measurement uncertainty, σ_{host} , are listed in Table 3.1 and are adopted from Bentz et al. (2009a) and Bentz et al. (2013).

Table 2.8. Regression Results for NGC 5548

Type of Relationship (1)	Intercept K^a (dex) (2)	Slope β^a (3)	σ_{RMS}^b (dex) (4)	ϵ_0^a (dex) (5)	$\Delta\epsilon_0^c$ (dex) (6)
$R - L(5100)$ Relationship					
CCF R_{BLR}					
Local relationship	1.83 ± 0.15	0.79 ± 0.20	0.118	0.076	± 0.047
Global relationship	1.62 ± 0.04	[0.53 \pm 0.03]	0.127	0.087	± 0.046
JAVELIN R_{BLR}					
Local relationship	1.89 ± 0.13	0.88 ± 0.17	0.096	0.071	± 0.039
Global relationship	1.59 ± 0.04	[0.53 \pm 0.03]	0.107	0.118	± 0.041
$R - L(1350)$ Relationship					
CCF R_{BLR}					
Local relationship	1.48 ± 0.10	0.47 ± 0.15	0.118	0.081	± 0.052
Global relationship	1.52 ± 0.04	[0.53 \pm 0.03]	0.130	0.072	± 0.050
JAVELIN R_{BLR}					
Local relationship	1.45 ± 0.05	0.52 ± 0.12	0.097	0.073	± 0.052
Global relationship	1.51 ± 0.03	[0.53 \pm 0.03]	0.100	0.065	± 0.041

Note. — The values in square brackets (slope β ; Bentz et al., 2013) are held fixed during the regression in order to estimate the scatter relative to this particular slope. The zero-point is the best fit value given the data and the adopted slope. The UV luminosities are computed as described in § 2.3.2.

^aBest fit parameters for the relationship in Equation (2.3) based on adopting the larger of the two error-bars; this is option (d) of the ‘error bar sensitivity test’, described in Appendix A.1. These parameters and their uncertainties are the median and standard deviation of the posterior probability distributions.

^bThe rms scatter of the data points relative to the best fit relationships.

^cThe standard deviation of the posterior probability distribution of the scatter, i.e., the precision of the scatter estimates.

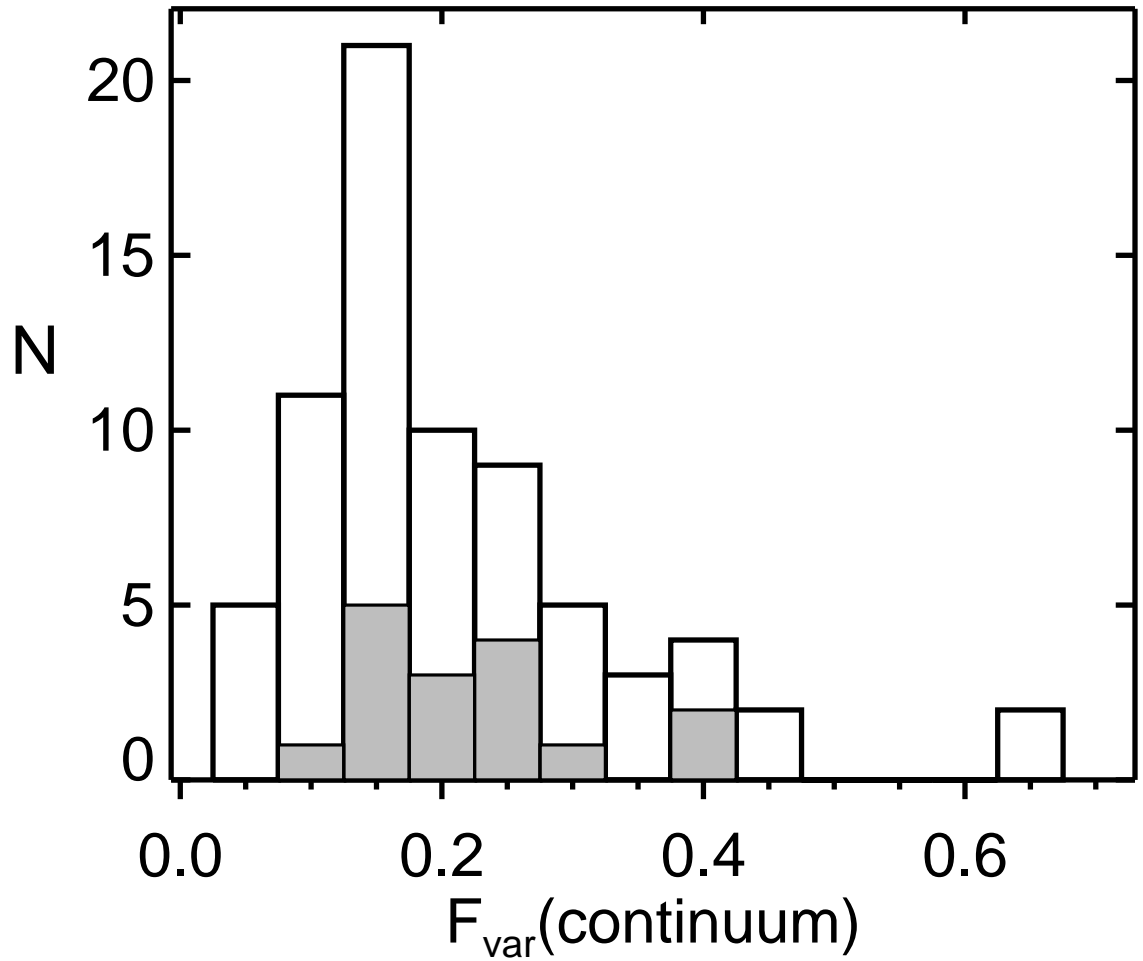


Figure 2.1 Histogram of the $F_{var}(\text{continuum})$ distribution for the full RM sample of Bentz et al. (2013). The $F_{var}(\text{continuum})$ distribution for NGC 5548 is shown with a gray shade. The F_{var} values are adopted from Peterson et al. (2004); Denney et al. (2006); Bentz et al. (2009b); Denney et al. (2010); Grier et al. (2012a); Peterson et al. (2013a) and corrected for the host galaxy contribution to the spectrally measured monochromatic source luminosities.

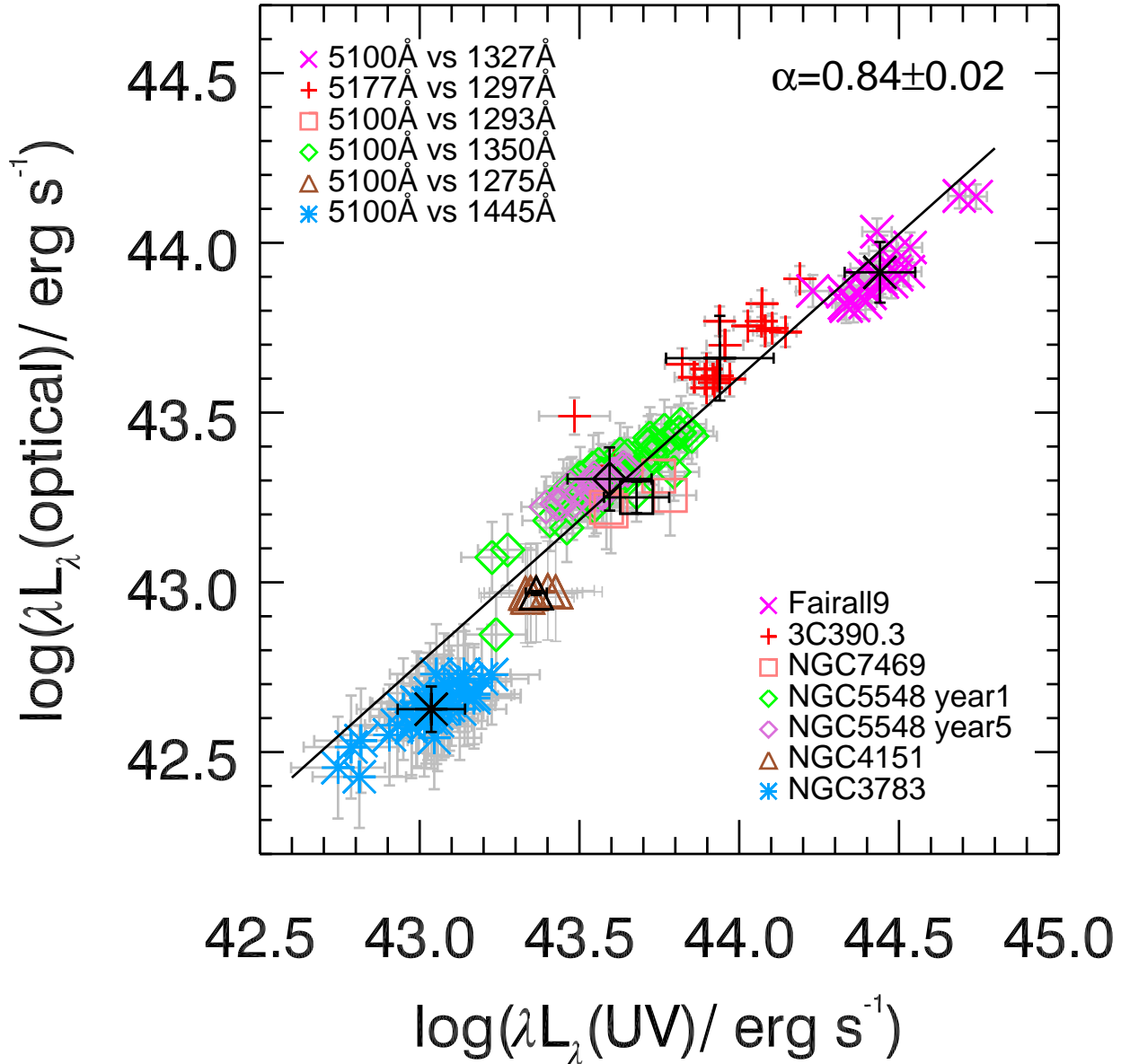


Figure 2.2 Optical continuum luminosity versus ultraviolet continuum luminosity for the six nearby AGN in our sample; the optical and UV measurements are paired to within two days. The optical luminosities are corrected for the host galaxy star light entering the spectroscopic aperture. The luminosities are measured at the specific wavelengths for each source as listed in the upper left corner of the diagram. Black points denote the mean luminosities of the AGN and their error-bars represent the 1σ standard deviation of the luminosities for each object. The solid line shows the (global) best-fit to all sources.

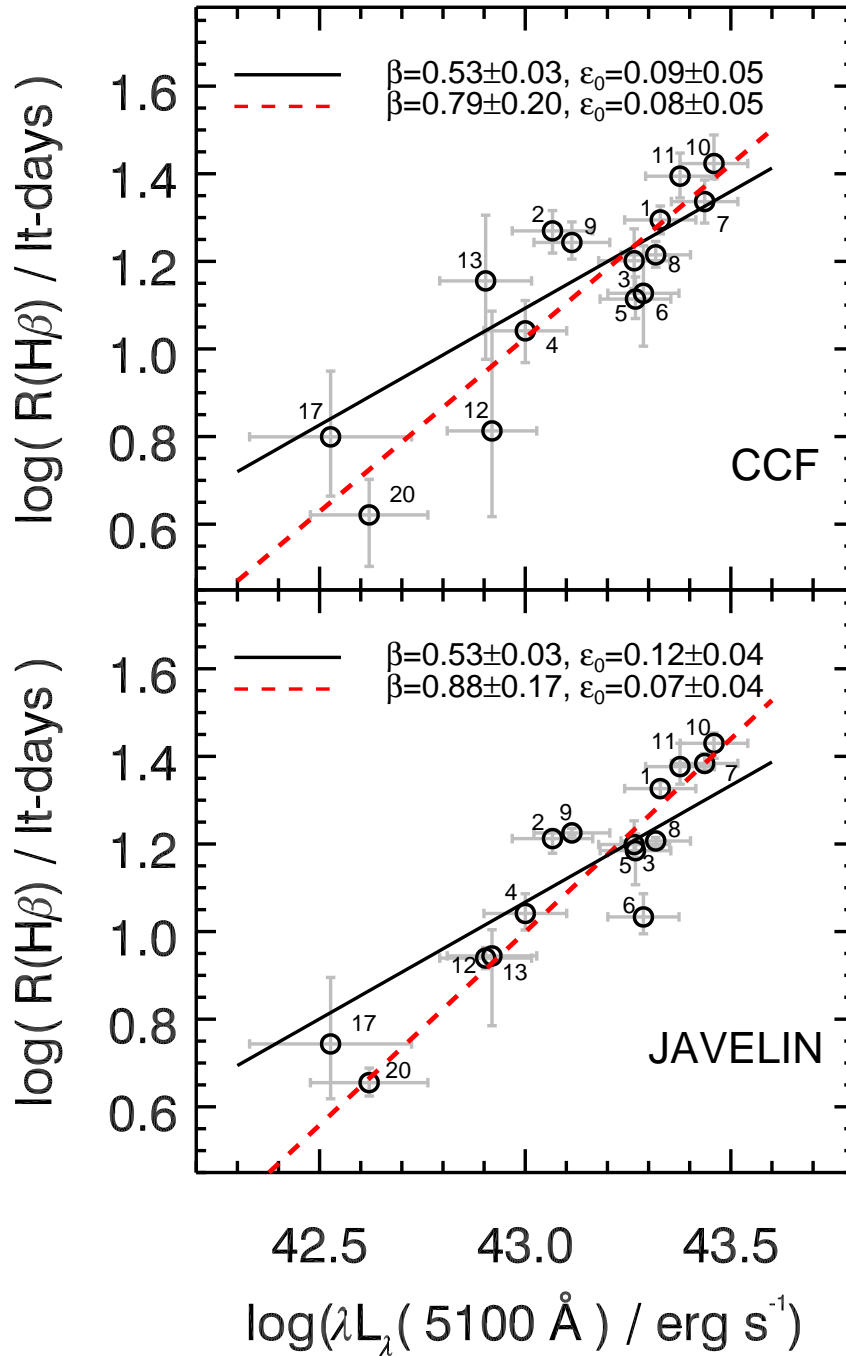


Figure 2.3 The $R - L(5100)$ relationships for NGC 5548 based on the CCF dataset (top) and the JAVELIN dataset (bottom) updated to account for the new flux calibration of Peterson et al. (2013a). The numbers refer to the year of the reverberation mapping campaign as described in § 2.2.2. The red dashed lines in each panel show the best fit relationship to each dataset (the ‘local’ relation). The black solid lines show the global relationship with slope $\beta = 0.53$ (Bentz et al., 2013).

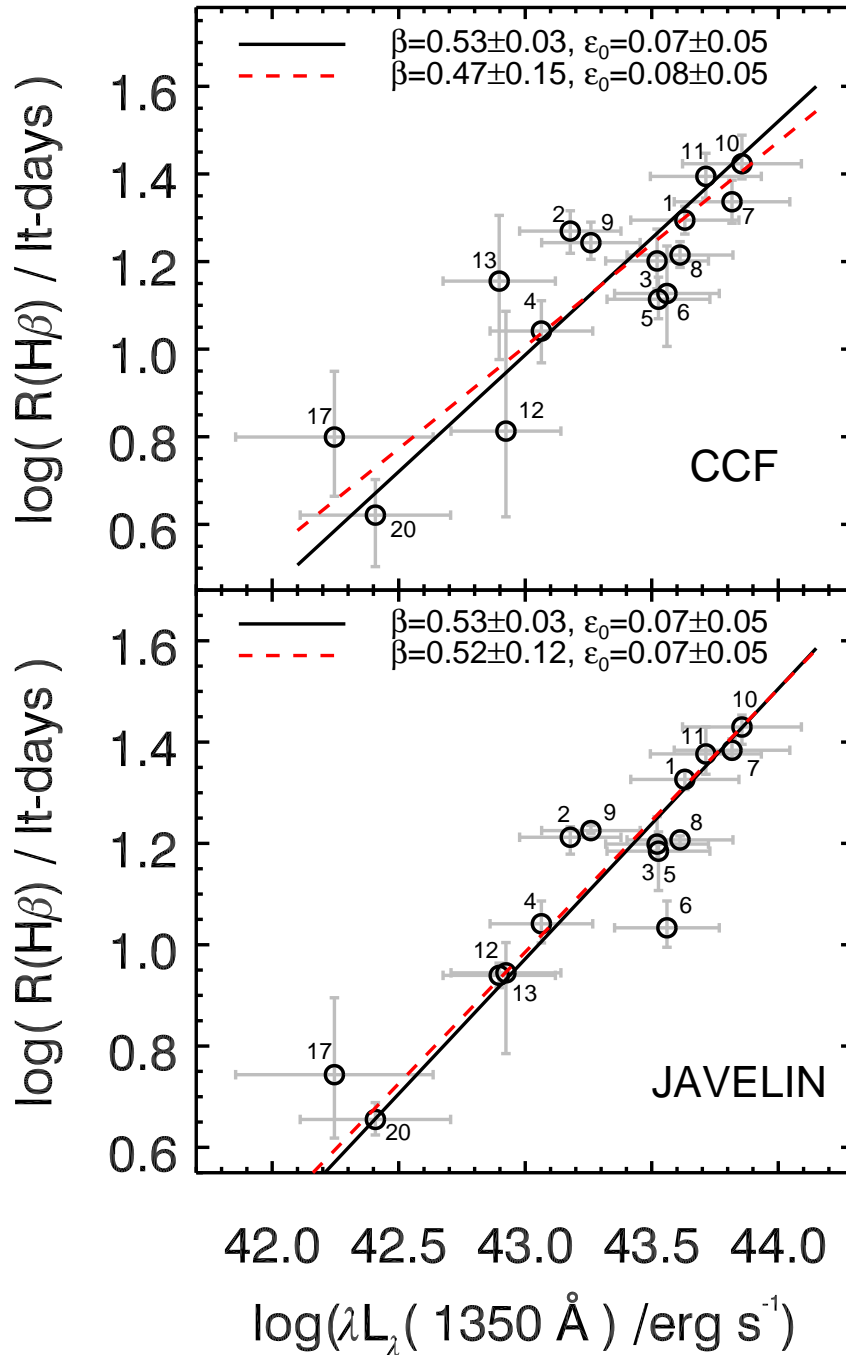


Figure 2.4 The $R - L(1350)$ relationships for NGC 5548 using the CCF dataset (top), and the JAVELIN dataset (bottom). The $L(1350)$ luminosities are computed based on the measured $L(5100)$ values and the $L(\text{optical}) - L(\text{UV})$ analysis as outlined in Section 2.3.2. See Figure 2.3 for symbols and color code.

ON THE RELATION BETWEEN THE BROAD EMISSION LINE SHAPE AND EDDINGTON LUMINOSITY RATIO FOR LOCAL SEYFERT GALAXIES

ABSTRACT – *The black hole mass scaling relationships of Type 1 active galactic nuclei (AGN) provide black hole mass estimates based on single-epoch spectra with a typical uncertainty of a factor of ~ 4 . A significant fraction of this uncertainty is related to the characterization of the emission-line widths. Previously, an inverse correlation between the Eddington luminosity ratio and the ratio of $H\beta$ full-width at half maximum, $FWHM$, to the line dispersion was observed for 35 reverberation-mapped (RM) AGN. I revisit this inverse correlation for a smaller sample, for which I have direct Eddington ratio measurements based on SEDs of quasi-simultaneous optical, UV and X-ray data. Although I use archival data, the single-epoch SEDs of the seven RM AGN in my sample are generated for the first time and I investigate the SED variability of these sources. In this work I investigate the dependence of the shape of the broad $H\beta$ and $C\text{IV}$ profiles on the Eddington ratio. The line shape – Eddington ratio correlation of $C\text{IV}$ profiles are investigated for the first time in this work. For a sample of seven RM AGN, I confirm an inverse correlation between the Eddington ratio and $H\beta$ profile, but I do not see a similar trend for the $C\text{IV}$ profile for my sample of 7 nearby AGN. Moreover, I examine the effect on this relationship of obtaining Eddington ratios from bolometric correction scalings, and I obtain very similar line shape – Eddington ratio distributions. Based on this I conclude that for this small AGN sample quasi-simultaneous SEDs are not a requisite for this investigation. I further investigate the line shape – Eddington luminosity ratio relation for a sample of ~ 3600 quasars selected from the Sloan Digital Sky Survey (SDSS). This quasar sample shows a similar inverse correlation between the line shape – Eddington luminosity ratio for $H\beta$ and $C\text{IV}$ profiles. By performing a partial correlation test, I eliminate the possibility of this inverse correlation being an artifact of FWHM.*

3.1 INTRODUCTION

The search for super-massive black holes (BHs) at the centers of nearby massive galaxies has successfully exposed the presence of $10^6 - 10^9 M_\odot$ central mass concentrations (Kormendy & Richstone, 1995; Ferrarese & Ford, 2005a). Black hole masses of local ($z \leq 0.1$) galaxies inferred from stellar and gas dynamics, show correlations with the bulge stellar velocity dispersion ($M_{\text{BH}} - \sigma_*$ relation), mass and luminosity of the bulges in their host galaxies (e.g Kormendy & Richstone, 1995; Magorrian et al., 1998; Ferrarese & Merritt, 2000; Gebhardt et al.,

2000; Tremaine et al., 2002; Marconi & Hunt, 2003; Graham, 2007; Gültekin et al., 2009; Graham et al., 2011, and references therein). These empirical correlations suggest a link between the growth of the galaxy bulge and the BH at the center. A possible link is the feedback from the BH during the quasar phase that may quench star formation and regulate both BH and galaxy growth (e.g., Silk & Rees, 1998; King, 2003; Di Matteo et al., 2005). However the origin and the nature of the scaling relationships between the black hole mass and the host galaxy properties are not fully understood yet. Understanding the physical drivers and the reliability of these empirical relationships requires studying large samples of galaxies with accurate BH mass, M_{BH} , measurements over cosmic time.

When using stellar and gas dynamics to measure M_{BH} , the stellar/gas velocity dispersion and the radius of the sphere of the influence of BH must be obtained. Therefore due to the technical capabilities (i.e., sensitivity and spatial resolution) of the current ground and space based telescopes this method is applicable only to nearby galaxies (explained in Chapter 1.3.1). Currently, the most powerful tool to directly measure BH mass without source distance limitations is reverberation mapping (RM; Blandford & McKee, 1982; Peterson, 1993) that can be applied to Type 1 (broad-line) active galactic nuclei (AGN) due to their variability characteristics. The continuum radiation generated by the accretion disk is absorbed and re-emitted by the gas in the broad line region (BLR). This process produces the broad emission lines at some specific wavelengths that are broadened due to the Doppler effect, the high gas motions are induced by the black hole gravity. BLR varies in strength at specific line transitions (for ions and atoms in the gas) in response to variations in the continuum, because the continuum is reprocessed by the BLR. Reverberation mapping analysis uses the light curves of the continuum and broad emission-lines to measure the time delay, τ , between the two light curves (see Chapter 1.3.2 for details). The responsivity weighted distance of the gas in the BLR from the continuum emitting region is given by $R = c\tau$. If broadening of the emission-lines is assumed to be due to Keplerian rotation of the BLR, then the rotation speed of the BLR gas, V_{rot} , can be measured from the emission-line velocity width (ΔV). Since the kinematics, geometry and the inclination of the BLR is unknown, the measured emission-line width should be multiplied by a fudge factor, f , in order to obtain V_{rot} such that: $V_{\text{rot}} = f^{0.5} \times \Delta V$. Once we have measured R and V_{rot} and further assume that the BLR gas dominated by the BH gravity, the mass of the central BH can be estimated by the following equation (e.g., Peterson et al., 2004):

$$M_{\text{BH}} = f \frac{R(\Delta V)^2}{G}, \quad (3.1)$$

G is the gravitational constant and f is the dimensionless constant accounting for the unknown geometry and structure of BLR. In this equation, R is directly measured from the RM analysis and in order to measure the velocity of the gas that is responding to the continuum variations, ΔV is measured from the the root mean square (rms) spectrum. Due to the unknown kinematics of BLR, the f factor brings the largest uncertainty to Equation 3.1. However, for a small sample with high quality RM data, f can be constrained for individual objects by dynamical modeling (e.g., Brewer et al., 2011; Pancoast et al., 2012, 2013). Also, an average f factor (~ 4) is calculated for the RM sample as a whole by calibrating the RM-based BH masses to the $M_{\text{BH}} - \sigma_*$ relation of the quiescent galaxies (Onken et al., 2004; Woo et al., 2010, 2013; Graham et al., 2011; Park et al., 2012a; Grier et al., 2013a). In principle, R can be measured via RM at any redshift. However it requires well sampled, long term monitoring. The required duration of the monitoring campaign depends on the luminosity of the source because R increases with luminosity (e.g Bentz et al., 2013). Since the continuum variations of high-redshift luminous quasars are slow with small amplitude, applying RM to such sources is not practical and resource expen-

sive. Furthermore, for high-redshift sources cosmological time dilation is also important which increases the required duration of the monitoring campaign.

Reverberation mapping studies of local AGN ($z \leq 0.3$) have over the past ~ 25 years revealed the following important results: (1) The radius of the broad-line region and BH masses of ~ 50 AGN have been measured (hereafter this sample is referred to as the RM sample, e.g., Peterson et al., 2004; Bentz et al., 2009b; Denney et al., 2010; Grier et al., 2012b); (2) A relatively tight relationship between the mean optical continuum luminosity at rest frame 5100\AA , $L(5100\text{\AA})$, and $R(H\beta)$ (the so-called $R - L$ relation, where $R \propto L^{0.5}$) is established (Kaspi et al., 2000, 2005; Bentz et al., 2006b, 2009a, 2013). Moreover, the $R - L$ relationship can be used to estimate R simply from a measured monochromatic continuum luminosity and hence allows mass estimates from a ‘single-epoch’ (SE) spectrum also for high-redshift Type 1 AGN. The mass scaling relationships that are obtained by calibrating SE masses to the RM based mass measurements of local AGN (e.g., McLure & Dunlop, 2004; Wu et al., 2004; Greene & Ho, 2005; Vestergaard & Peterson, 2006; McGill et al., 2008; Vestergaard & Osmer, 2009), provide a practical tool for M_{BH} estimates of distant luminous objects. Different mass scaling relationships are available for different broad emission-line and continuum luminosity combinations: $H\beta - L(5100\text{\AA})$ (e.g., McLure & Dunlop, 2004; Vestergaard & Peterson, 2006), $\text{Mg II } \lambda 2798 - L(3000\text{\AA})$ (e.g., McLure & Jarvis, 2002a; Vestergaard & Osmer, 2009; Wang et al., 2009) and $\text{C IV } \lambda 1549 - L(1350\text{\AA})$ (e.g., Vestergaard, 2002; Warner et al., 2003; Vestergaard & Peterson, 2006; Park et al., 2013). These mass scaling relationships allow M_{BH} estimates of quasars at high redshifts and they can easily be applied to large AGN samples (e.g., Vestergaard et al., 2008; Shen et al., 2011).

The mass scaling relations are accurate to within a factor of ~ 4 on an absolute scale and a factor of ~ 3 with respect to the RM masses (e.g., Vestergaard & Peterson, 2006). If we ignore the accuracy of the RM masses that depends on the f factor and just consider the difference between the SE and RM masses, a large part of this difference arises from our estimates of the velocity width of the emission-line (see e.g., Denney et al., 2009b; Vestergaard et al., 2011; Denney, 2012, for a discussion of systematic uncertainties of SE mass estimates). The SE BH mass estimates are mainly restricted by the velocity information that depends on how the line width is measured from the line profile. The line width can be characterized by the full-width-half-maximum FWHM and/or the line dispersion (i.e, the second moment of the line, σ_{line} ; e.g., Peterson et al., 2004). There is a difference between the rms spectrum that represents the variable emission-line component obtained during a monitoring campaign which we ideally want and the emission-line width measured from the SE, or equivalently the mean, spectrum that may also contain non-variable velocity components. We do not often have multiple epoch spectra of high-redshift AGN - or have large samples of AGN with such data. It is too resource-requiring. Therefore, the scaling relations were made to approximate what we ideally want. The quest is thus to minimize the differences between the rms profile and the single-epoch profile in our measurements. Comparison of the mean and the rms $H\beta$ profile shows that the mean profiles have a non-variable high velocity component that dominates the line wings, and therefore it is broader than the rms profile (e.g., Collin et al., 2006). Denney (2012) showed that the mean C IV profiles are not the same as the rms profiles because the mean profiles have a low-velocity core component that is not reverberating and or cause a change in the shape of the line as the line width change. On the other hand the $H\beta$ profile does not change its shape as it gets wider (Denney, 2012). It has been shown by Denney (2012) that the line shape differences between the $H\beta$ and C IV profiles explain the differences between $H\beta$ and C IV based masses.

The shape of the broad emission line parameterized as the ratio of FWHM to σ_{line} (Collin et al., 2006; Denney et al., 2013) is an important parameter that helps to characterize the velocity

field in the BLR. For the virial BH mass estimates it is assumed that the measured emission-line velocities are virial velocities (e.g., Keplerian velocities), but in reality the velocity field in the BLR might be complex, and have additional components such as inflows, outflows and turbulence. We observe different line shapes, some are peakier than Gaussians (more like Lorentzians) while some are stubbier than Gaussians. The Gaussian profile can be used for reference, as there is a clear scaling between FWHM and σ_{line} for a Gaussian function. The FWHM to σ_{line} ratio is a useful parameter to determine if the profile is more boxy than a Gaussian function ($FWHM/\sigma_{line} > 2.35$) or if it is relatively peakier ($FWHM/\sigma_{line} < 2.35$). Denney (2012) found that C IV has a non-variable component that creates a more ‘peaky’ profile. Since the FWHM measurements are sensitive to the emission-line peak such an ‘peaky’ profile result in a narrower line width and thus an underestimated BH mass. As shown by Denney (2012) the line shape creates some bias for C IV based BH masses, but the bias is not so strong to make C IV based BH masses completely unreliable. This bias results in a larger uncertainty in the black hole mass estimates since the masses based on C IV will deviate from that expected based on the H β line width. This bias gets stronger when the line width measurements are affected by absorption features or bad data quality (Denney et al., 2013). But using high quality data can not entirely account for this bias alone. Since σ_{line} is not sensitive to the peak of the emission-line by using the σ_{line} as oppose to the FWHM, this line shape bias can be reduced to some degree (Denney et al., 2013). Line width measurements are very important for BH mass estimates because we use the square of the line velocity in equation 3.1; note that the uncertainty of the R in this equation is relatively small (0.13 dex, Bentz et al., 2013). Since line width measurements from FWHM and σ_{line} have different weights of sensitivity to the line shape, the FWHM to σ_{line} ratio can affect the single-epoch BH mass estimates significantly. Therefore, it is important to understand why we observe different line shapes and if it depends on other physical parameters of the AGN.

Collin et al. (2006) investigated the FWHM to σ_{line} ratio of the mean H β profiles of the RM sample. They separated the RM AGN sample into two groups based on the $FWHM/\sigma_{line}$ ratio: (1) narrower profiles that have extended wings; (2) lines have broader relatively boxy profiles. For 35 AGN they found an inverse correlation between the Eddington luminosity ratio and the mean H β shape. Their Eddington luminosity ratio estimates are based on the BH masses obtained from the RM analysis and the bolometric luminosities that are scaled from the mean L(5100Å) by applying a mean bolometric correction of 10. Collin et al. (2006) show that, for a single AGN (NGC 5548) that has been monitored for 14 years, the $FWHM/\sigma_{line}$ ratio of the mean and the rms H β profiles change in time. This means that for an individual object the line shape does not depend on the inclination or the BH mass. But of course across the AGN population the line widths and shapes may change with BH mass and inclination. As shown by Collin et al. (2006) the Eddington ratio may potentially affect the H β line shape. This is not surprising because the emission-line width and shape should depend on the velocity field and geometry of the line emitting gas in the BLR. At the same time, the line emission process depends on the mass accretion rate that controls the ionizing continuum luminosity. This is because, as the mass accretion rate changes (increases or decreases), the ionization front will change as well (it may expand or shrink). As the ionization front changes the location of the responding gas will change within the BLR. Since the velocity of the gas depends on the distance from the central BH, and the velocity of the line emitting gas changes as the ionization front moves (an inverse correlation between the line widths and the continuum luminosity has been observed for individual sources, Peterson et al., 2004; Park et al., 2012b), higher Eddington luminosity ratios may result in low velocity dominated, peaky profiles.

The aim of this study is to explore what fundamental parameters related to the black hole accretion process, if any, that the line shape (FWHM to σ_{line}) may depend on. The focus of my investigation is the possible dependence of the broad emission-line profiles of the RM AGN sample on the Eddington luminosity ratio. In order to be able to eliminate intrinsic differences in the BLR geometries, kinematics and inclinations between objects, I will look at line shape variations measured from multiple single-epoch spectra of individual sources. This is mainly because, if the Eddington ratio affects the line shape, we should see this effect for individual sources as they vary and also between objects of different Eddington ratio in our sample. In this work I will investigate the relation between the C IV line shape and the Eddington luminosity ratio for the first time. In order to obtain Eddington luminosity ratios one needs BH mass and bolometric luminosity measurements. I will use the RM based BH mass from (Peterson et al., 2004). The bolometric luminosity, L_{BOL} , of an AGN, is the total integrated luminosity produced by the central engine. It is not an easy quantity to measure because it needs to be measured from the spectral energy distribution that covers a wide energy range from optical to X-rays. To observe the full broadband SED, observations from multiple ground and space based telescopes operating at different wavelengths (radio to X-rays) are needed. In practice, such observations are very difficult to coordinate. The variable nature of AGN brings an additional challenge to L_{BOL} measurements. Depending on the luminosity state of the AGN, the optical/UV emission that originate from the accretion disk, vary on time scale of days to weeks. Therefore, variability characteristics of AGNs necessitate simultaneous multi-wavelength observations in order to build intrinsic SEDs and measure inherent L_{BOL} values. One practical way to calculate L_{BOL} , without dealing with these observational challenges, is to scale the monochromatic continuum luminosity by a bolometric correction (BC) factor (e.g., Elvis et al., 1994; Kaspi et al., 2000; Richards et al., 2006a; Runnoe et al., 2012). However, mean bolometric corrections that are obtained from average spectral energy distributions of large AGN samples have large standard deviations (e.g., 20%–50% Elvis et al., 1994; Richards et al., 2006a). For individual objects the BC also depends on the source Eddington ratio (e.g., Vasudevan & Fabian, 2007, 2009). Therefore, the Eddington ratio estimates of Collin et al. (2006) may be crude approximations, and based on the standard deviations of the mean bolometric corrections they might have of order 20%–50% uncertainties. On the other hand, the effect of the bolometric correction scalings to their study can only be quantified by obtaining the SEDs. In this study, in order to obtain more accurate Eddington ratio values I avoid using mean bolometric corrections that are widely used in the literature (e.g., Elvis et al., 1994; Richards et al., 2006a). Instead, I use spectral energy distributions generated by quasi-simultaneous optical, UV and X-ray spectra to directly measure the bolometric luminosity. With the available multi-epoch quasi-simultaneous SEDs that give a snap-shot for an AGN that varies, I also investigate SED variations and its impact on the L_{BOL} , Eddington luminosity ratio, bolometric corrections and line shapes.

This chapter is organized as follows: sections 3.2 and 3.3 introduce the sample and the data, respectively. In section 3.4 I present the SEDs of my sample and describe measurements of SED related parameters such as the bolometric luminosity, bolometric corrections and Eddington ratio in §3.5. The Eddington ratio – line shape relation is presented in §3.6. In §3.7 I investigate spectral energy distribution variations. I discuss my results in section 4.4 and my conclusions are summarized in §4.5. I use a cosmology with $H_0 = 72 \text{ km s}^{-1} \text{ Mpc}^{-1}$, $\Omega_\Lambda = 0.7$ and $\Omega_m = 0.3$.

3.2 THE SAMPLE

In order to investigate the potential effects of the accretion state on the broad emission line profiles, I base my study on the ~ 50 reverberation-mapped AGN (Peterson et al., 2004; Bentz et al., 2009b; Denney et al., 2010; Grier et al., 2013b; Bentz et al., 2013, and references therein). These are well studied local AGN with robust measurements of black hole mass and distance to the BLR obtained from the homogeneously analyzed and calibrated dataset presented by Peterson et al. (2004). The multi-wavelength spectroscopic monitoring data available for this sample provide a particularly suited database to probe intrinsic variations in the bolometric luminosity and Eddington luminosity ratio as gleaned from quasi-simultaneous SEDs.

The International AGN Watch¹ database provides optical and UV light curves and spectra from several monitoring campaigns running between 1988 and 2001. From this database I select AGN for which there are quasi-simultaneous optical-UV and X-ray data available to generate SEDs I match the optical observation Julian Dates (JD) with the closest UV observation JD to within two days. I searched the *IUE HST* and *FUSE* archives for UV observations that are not officially part of the AGN Watch database but obtained for other reasons during the optical monitoring campaigns. Once the simultaneous optical-UV data epochs are selected, I then search the literature for archival X-ray observations obtained during these epochs. While I aim to obtain the contemporaneous data sets within a few days, for a couple of epochs (see the footnotes to Table 3.6) I take the closest data to within three weeks in order to increase the number of available SED epochs as I would otherwise have a rather limited database.

My final sub-sample consists of seven RM AGN (NGC 5548, NGC 7469, NGC 3783, Mrk 509, NGC 4151, 3C 390.3, Fairall 9). I list several source properties of these AGN in Table 3.1 namely: object name (column 1); redshift (column 2); Galactic color excess $E(B-V)$ value based on the dust maps from Schlafly & Finkbeiner (2011) (column 3); distance (column 4); adopted host galaxy flux measurement from Bentz et al. (2009b, 2013) (column 5); the aperture size and position angle used for the host galaxy flux measurements (columns 6 and 7, respectively); the adopted central black holes mass (M_{BH}) estimate from Peterson et al. (2004) (column 8).

3.3 DATA

3.3.1 OPTICAL–UV DATA

I extract the ground-based optical and the space-based (*IUE* and *HST*) UV spectra from the International AGN Watch database. The two UV spectra of Mrk 509 obtained by *IUE* during the optical monitoring campaign in 1990, that are not provided in the AGN Watch database are available in the MAST² *IUE* archive³. I extract the processed *IUE* spectra observed during JD=2448187.7 and JD=2448187.8 and create an average spectrum for further analysis. Details of the observations, data processing and calibration are provided by the reference work listed in Table 3.2. Since the optical spectra provided in the AGN Watch database are not calibrated, I performed an absolute flux calibration based on the $[O\ III]\lambda 5007$ line flux that is given by the references listed in Table 3.2. For NGC 5548, I use the updated fluxes presented by Peterson et al. (2013b). The details of this calibration is outlined in Chapter 2. In the following subsections, I explain the continuum measurements that are used in the SED analysis and the line width measurements that are used for the line shape correlation analysis.

¹<http://www.astronomy.ohio-state.edu/~agnwatch/>

²Multimission Archive at STScI

³<http://archive.stsci.edu/iue/>

Continuum Emission Measurements

The Optical Continuum I model the optical spectra with a power-law continuum in the observed wavelength ranges listed in column 2 of Table 3.3. I parametrize the continuum as $F(\lambda) = N \times \lambda^\alpha$, where α is the slope and N is the normalization at 5100\AA . The best fit values of these parameters were determined by the Levenberg-Marquardt least-squares fit IDL routine (MPFIT) (Markwardt, 2009). In order to constrain the uncertainty of the best-fit continuum I compute the root mean square (rms) of the continuum flux density, σ_C , within the continuum windows relative to the best fit continuum. I use the best-fit continuum and σ_C to construct my extreme continua levels: a) best-fit continuum + σ_C , b) best-fit continuum - σ_C , c) the bluest continuum possible, and d) the reddest slope possible within the measurement error, σ_C . I adopt the largest difference between the best-fit continuum and these 4 extreme continuum levels as my conservative uncertainty on the continuum level setting. Similarly, I take the difference between the best-fit slope and the slopes of the bluest and the reddest continuum levels and adopt the largest difference as the slope uncertainty. I measure the monochromatic continuum flux density at rest frame 5100\AA as the average over the optical continuum windows listed in Table 3.3. The measured 1σ rms flux density in this continuum window is adopted as the error of the monochromatic continuum flux density. The best-fit continuum will be used in the SED and it will be subtracted from the spectrum to measure the emission-line widths. The uncertainty of the best-fit continuum will be used in the SEDs to infer the bolometric luminosity uncertainty and in line width measurements to infer their uncertainties. The continuum measurements will also be used to obtain bolometric corrections.

The Ultraviolet Continuum I also model the UV spectra as a power-law similar to the optical spectra based on the UV continuum windows listed in column 3 of Table 3.3. The normalization of the UV power-law continuum is defined at 1000\AA . The adopted monochromatic continuum flux density at rest frame 1350\AA is the average over the relevant UV continuum windows and its uncertainty is obtained in a similar way as for the optical continuum.

Emission Line Measurements

H β Line Widths Measurements I subtract the best fit linear continuum from the rest frame optical spectrum. The red side of the H β profile blends with the [O III] $\lambda 4959$ emission line. To reveal the H β line flux potentially extending under the [O III] $\lambda 4959$ line, I need to remove the [O III] $\lambda 4959$ profile accurately. To do so, I model each of the narrow [O III] $\lambda 4959$ and [O III] $\lambda 5007$ lines with a double Gaussian function and subtract these models from the spectrum. An example is shown in Figure 3.1. I tie the position and velocity widths of the Gaussians between the two [O III] lines and the line flux ratio is held fixed at the value of 1 : 3.03 expected from atomic physics (Osterbrock & Ferland, 2006). Thereafter, for a given AGN I scale the modeled [O III] $\lambda 5007$ profile by the relevant ratio presented by Peterson et al. (2004) or Marziani et al. (2003) and use this profile template to remove the narrow line component of H β . No Fe II template fit and removal was performed since the Fe II contribution is very weak for my targets. To measure the FWHM I need to define the maximum flux density between the line limits and to measure the line dispersion I need to integrate the line within the line limits. Therefore, I need to define the wing limits of the line on the blue and red sides. Between 4700\AA and 4840\AA I applied an automated box car algorithm to define the line limits on the blue and red sides of the H β line. I move the box car of 9 pixels from the line center pixel toward the wings of H β and define the wing limits as the middle pixel of the box car for which the average flux

of the 9 pixels is less than the mean noise level. To avoid any line wing limit dependence on my results I measured the line widths, FWHM and line dispersion, for both the fixed and variable (i.e., the box car) and tabulate these in Table 3.4. In this Table column (1) gives the object name, the SED epoch is listed in column (2), the BLR radius appears in column (3), the JD of the spectrum that is matched with the SED epoch is given in column (4). Columns (5), (6) and (7) gives the FWHM, σ_{line} and line shape measured from the fixed line limits. Columns (8) lists the variable line limits and columns (9) and (10) gives the σ_{line} and line shape measured from these variable limits. I measure FWHM and line dispersion and correct these measurements for spectral resolution following Peterson et al. (2004). Since the measured line widths depend on the underlying continuum level, I compute the uncertainties in the line widths by accounting for the uncertainty in the best continuum fit, as follows: I measure line width for each continuum setting and compute the difference relative to the width measured based on the best fit continuum setting. I adopt as the measurement uncertainty the largest of these difference.

CIV Line Width Measurements I subtract the best fit power-law UV continuum from the spectrum. It is not obvious which CIV profile wing limits are the most ideal to adopt for the IUE spectra owing to the blending of NIV in the blue wing and and the ‘red shelf’ (e.g., Fine et al., 2010) with He II $\lambda 1640$ blending in the red wing. One reasonable limit for the CIV is at $\pm 10,000 \text{ km s}^{-1}$ from the line center (e.g., Vestergaard & Peterson, 2006) because it falls almost half ways between CIV and He II. For my spectra, a limit of $10,000 \text{ km s}^{-1}$ may truncate the line wings and it is, therefore, not a robust CIV wing limit. I applied an automated algorithm similar to the box car algorithm described for $H\beta$ in order to identify the optimal wing limits. Here, I compare the fluxes in each pixel between the line center and the He II and NIV profiles. I adopt the minimum flux pixels as the ‘variable line limit’ on either sides of the CIV line. The line width measurements listed in Table 3.5 are corrected for the IUE spectral resolution of 6\AA following Peterson et al. (2004). I measure the line widths and their uncertainties similar to what is described for $H\beta$.

Line Shape Measurements For comparison with other work (Collin et al., 2006), I parametrize the optical and UV broad emission line shapes by the $FWHM/\sigma_{line}$ ratio. Since FWHM is sensitive to line peak and σ_{line} is sensitive to line wings, the $FWHM/\sigma_{line}$ ratio is a good way to characterize the line shape.

3.3.2 X-RAY DATA

I collect X-ray data obtained by the *GINGA*, *ASCA*, *RXTE*, *EXOSAT*, and *ROSAT* satellites from the Tartarus database and from the literature. The references for the work from which I adopt the X-ray data are provided in column (3) of Table 3.2; these references present the details of the X-ray data processing and analysis. In this work, I do not perform X-ray data analysis, but I adopt the results of the analysis already performed by other authors.

X-ray Power-law Continuum Measurements

The ‘primary’ continuum (i.e., that is not reprocessed) in AGN X-ray spectra is typically well described by a power-law function (Haardt & Maraschi, 1991). More complex models are available to account for other spectral features in the spectra such as the hard reflection component (Ross & Fabian, 1993) and the fluorescent $\text{FeK}\alpha$ line (e.g. Fabian et al., 2000). Although the

AGN X-ray emission can extend up to 100 keV and beyond (e.g., Molina et al., 2013), I restrict my analysis to the available X-ray data between 2–10 keV.

The reference works listed in Table 3.2 provide the results of the X-ray spectral analysis. This includes a power law fit to the observed fluxes, between 2–10 keV, typically. To construct the SEDs I adopt the quoted photon index Γ and the broadband flux between 2–10 keV, $F(2 - 10 \text{ keV})$. Since I am interested in the continuum emitted by the AGN, I adopt the unabsorbed X-ray power-law component from the model of the X-ray data. I express the broadband flux between 2–10 keV as given in the XSPEC (Arnaud, 1996) manual¹

$$F(2 - 10 \text{ keV}) = \int_{2\text{keV}}^{10\text{keV}} f_E dE = \int_{2\text{keV}}^{10\text{keV}} N E^{-\alpha} dE \text{ (erg cm}^{-2} \text{ s}^{-1} \text{ keV}^{-1}) \quad (3.2)$$

where $f_E = N E^{-\alpha}$ is the monochromatic flux at energy E , N is the normalization, α is the power law index: $\alpha = \Gamma - 1$, where Γ is the photon index. Equation 3.2 can be written as

$$F(2 - 10 \text{ keV}) = N \left. \frac{E^{-\alpha+1}}{(-\alpha+1)} \right|_2^{10} = N \frac{10^{-\alpha+1} - 2^{-\alpha+1}}{(-\alpha+1)} = \frac{f_E}{E^{-\alpha}} \frac{10^{-\alpha+1} - 2^{-\alpha+1}}{(-\alpha+1)} \quad (3.3)$$

From Equation 3.3 the monochromatic flux at energy E , $F_\nu(E)$, in units of $\text{erg cm}^{-2} \text{ s}^{-1} \text{ Hz}^{-1}$ is obtained as

$$f_E = \frac{F(2 - 10 \text{ keV}) h (1 - \alpha) E^{-\alpha}}{10^{(1-\alpha)} - 2^{(1-\alpha)}} \quad (3.4)$$

where h is Planck's constant in units of keV sec. I follow this formalism to calculate the monochromatic fluxes at different energies in units of keV. I adopt the uncertainties on Γ and $F(2 - 10 \text{ keV})$ from the references listed in Table 3.2. I propagate the uncertainties on Γ and the broad band flux to estimate the uncertainty of $F_\nu(E)$ using standard error propagation rules.

For all AGN in my sample, except NGC 3783, I adopt the $F(2 - 10 \text{ keV})$ broad band flux from the original references (listed in Table 3.2) and I use equation 3.4 to calculate the monochromatic flux for energies between 2 keV and 10 keV. For NGC 3783 I adopt the broadband flux between 1–2 keV, $F(1 - 2 \text{ keV})$, observed with *ROSAT* from Alloin et al. (1995) because there is no X-ray observations at the energies between 2 keV and 10 keV. I calculate the monochromatic fluxes at 1 keV and 2 keV using equations 3.2 and 3.4. I estimate the 2-10 keV flux for this AGN by extrapolating the 1-2 keV fluxes, assuming a Γ of 1.9 presented by Alloin et al. (1995). I note that, the adopted X-ray measurements for NGC 3783 are not robust because the X-ray exposure was very short (~ 402 seconds) due to operational problems of *ROSAT* (see Alloin et al., 1995, for the details of X-ray observations). Therefore, the count rates obtained from this short observation were not sufficiently high to obtain an acceptable power-law fit. However, the X-ray observations repeated after 21 days with longer exposure, and an acceptable power-law fit is constrained for the data. The X-ray flux of the first observation is estimated based on the count rate comparison of the two observations.

Estimated X-ray Fluxes

NGC 5548: Estimated X-ray Fluxes For NGC 5548, there are several epochs for which there are simultaneous optical-UV data but no X-ray observations. In order to optimize the number of epochs with SEDs available I opt to estimate the observed $F(2 - 10 \text{ keV})$ flux during those epochs that are straddled by actual X-ray measurements. I have X-ray data within year 1 (JDs =

¹<https://heasarc.gsfc.nasa.gov/xanadu/xspec/manual/XSmodelPowerlaw.html>

2447534 – 2447722) and within year 2 (JDs = 2448035 – 2448078) of the AGN WATCH monitoring campaigns. The available data are shown in Figure 3.2 as the black filled points. I estimate the X-ray flux level between the two epochs with X-ray measurements by linearly interpolating between the average flux levels measured for each of these two epochs. I show in Figure 3.2 (top) the interpolation by a black solid line between the mean X-ray fluxes (red open circles) of year 1 and year 2. The uncertainties in the interpolated X-ray fluxes (dashed gray lines) are based on the interpolated $\pm 1\sigma$ uncertainties of the mean X-ray fluxes showed by the red circles. For the epochs during year 1 without direct X-ray measurements I adopt a Γ value estimated as the mean of the year 1 photon index values, $\Gamma = 1.57 \pm 0.12$. For the epochs between year 1 and 2 I estimate the photon index as the mean of all observed Γ values, $\Gamma = 1.65 \pm 0.11$. Then, I use equation (3.4) to calculate $F(2-10 \text{ keV})$. Table 3.6 lists the SEDs that are based on these estimated X-ray fluxes (epoch numbered from 12 to 45).

Fairall 9: Estimated X-ray Fluxes I have an X-ray observation at JD=24429312 and seven X-ray observations between JDs =2449688–2449712 (for references see Table 3.2). There are many simultaneous optical and UV data between JDs=2449470–2449688 without X-ray measurements. Again, I choose to estimate the $F(2 - 10 \text{ keV})$ flux for the epochs with missing X-ray data by linearly interpolating between the X-ray flux on JD=24429312 and the mean $F(2 - 10 \text{ keV})$ observed between JDs =2449688–2449712. Figure 3.2 (bottom) shows the available X-ray data and the interpolation. Again, I adopt the mean of the observed photon index values, $\Gamma = 1.9 \pm 0.11$, for the epochs between JDs=2449470–2449688. The SEDs that are based on the estimated X-ray fluxes are listed in Table 3.6 from epochs 1 to 26.

3.3.3 APPLIED CORRECTIONS AND LUMINOSITY CALCULATIONS

Galactic Extinction Correction The intrinsic emission produced by the AGN is contaminated by dust and gas extinction in the AGN host galaxy, the intergalactic medium (IGM) and our Galaxy. Since the extinctions caused by the AGN host galaxy and IGM respectively are not very well constrained, I only apply Galactic reddening correction. To correct the optical/ UV spectra and the observed flux densities, $F_{\lambda_{obs}}$ (λ_{obs} is the observed wavelength) for Galactic reddening I use the reddening curve of Cardelli et al. (1989) with the color excess values adopted from NASA/IPAC Extragalactic Database based on the dust maps of Schlafly & Finkbeiner (2011). The Galactic color excess $E(B-V)$ for each object is listed in column (3) of Table 3.1. Galactic absorption correction is included when modeling the X-ray power law.

Correction for Host Galaxy Starlight Contamination The AGN host galaxy emission contributes to the nuclear continuum emission in the observed optical and UV spectra. Therefore it is necessary to remove the host galaxy contamination to assure that the observed spectra represents only the intrinsic AGN emission. Bentz et al. (2009a, 2013) measured the observed host galaxy flux densities at rest frame 5100\AA for the RM sample using *HST* optical images. Bentz et al. (2009a, 2013) used the exact apertures that were used for the spectroscopic observations that I am analyzing. In order to subtract the right amount of stellar contribution, I adopt the host galaxy type and flux densities for the specific apertures of my sample as presented by Bentz et al. (2009a, 2013); these values are listed in Table 3.1. I correct the stellar fluxes for Galactic extinction as described above. Kinney et al. (1996) provide template spectra for the different morphological types between $1200\text{\AA} - 1\mu\text{m}$. I scale each of the elliptical, Sa, S0 galaxy templates presented by Kinney et al. (1996) to match the mean $5090\text{\AA} - 5115\text{\AA}$ flux density to that

reported by Bentz et al. (2013) and listed in Table 3.1. For each AGN I use the appropriate template for the galaxy type quoted by Bentz et al. (2013). I subtract the scaled host galaxy template from the observed optical-UV spectra of each of my sources.

Optical-UV Luminosity I compute the optical and UV nuclear power-law continuum and monochromatic luminosities as $L_{\nu_{rest}} = 4\pi D_L^2 F_{\nu_o}/(1+z)$ (e.g. Peterson, 1997), where z is the redshift, ν_{rest} is the rest frame frequency, D_L is the luminosity distance, and F_{ν_o} is the observed flux density at observed frequency ν_o . I list z and D_L in Table 3.1. The nuclear power-law continuum luminosity will be used for the SEDs and the monochromatic luminosities will be used to compute bolometric corrections.

X-ray Luminosity I apply the following power-law K-correction (Peterson, 1997) to calculate the X-ray luminosities at energy E :

$$L_{\nu}(E) = 4\pi D_L^2 \times F_{obs} \times (1+z)^{\Gamma-2} = \frac{F_{\nu}(E)4\pi D_L^2}{(1+z)^{(2-\Gamma)}}. \quad (3.5)$$

3.4 GENERATING THE OPTICAL–UV–X-RAY SPECTRAL ENERGY DISTRIBUTIONS

I combine the multi-wavelength data described in §3.3 to build single-epoch SEDs for each of the seven sources in my sample. The advantage of a single epoch SED, a snapshot of the AGN emission, is that intrinsic source variability does not introduce an uncertainty in the integrated luminosity. By generating such single-epoch SEDs at a range of epochs, we can study how the SED varies as the AGN varies with time. I restrict my SEDs to cover a frequency range from $1\mu\text{m}$ up to 10 keV because I am interested in the accretion luminosity (Chapter 1.2.4) to which the radio and IR emission does not contribute.

I show the SEDs in $\log(\nu L_{\nu})$ versus $\log(\nu)$ representation in Figure 3.3: source names and SED epochs (in parenthesis) are listed in each panel (Table 3.6 lists the specific JDs of the SED epochs). The optical and UV spectra are shown in gray and the underlying AGN continuum fit is shown as the black solid thin lines. The X-ray data are represented by a ‘butterfly shape’ that indicates the 2 keV to 10 keV X-ray continuum (§ 3.3.2) represented by the best fit power-law slope and its 1σ confidence limit. I mark a couple of wavelength regions of interest by vertical dashed lines for reference.

3.4.1 ESTIMATING THE CONTINUUM LEVEL IN THE SED GAPS

For all the SEDs, gaps exist between the optical–UV and X-ray regions due to Galactic gas absorption in the Extreme ultraviolet (EUV) region. I have two options for estimating the intensity levels in these gaps: (a) I can adopt specific accretion disk models, e.g., a thin accretion disk (Shakura & Sunyaev, 1973) or a thin disk plus an X-ray corona (Jin et al., 2012b); or (b) I can adopt the most simple approach of linearly interpolating the continuum emission between the observed data sets (e.g., Elvis et al., 1994). I chose option (b) in order to avoid any model dependence to enter my analysis. However, I briefly examine option (a) in Appendix A.4. I interpolate the continuum from the optical to the X-ray in log-log space.

3.4.2 EXTRAPOLATION TO $1\mu\text{M}$

For completeness and comparison with other studies, I present the SEDs and measure bolometric luminosities starting from $1\mu\text{m}$. Since my reddest data point is at $\sim 5400\text{\AA}$ I linearly extrapolate the best-fit optical continuum fit to $1\mu\text{m}$. The applied linear extrapolation/interpolations are shown as the red solid lines in Figure 3.3. The dotted blue lines represent the 1σ uncertainty in the interpolation based on the observed $\pm 1\sigma$ continuum uncertainties (described in §3.3.2 and §3.3.3). The extrapolation of the optical continuum to $1\mu\text{m}$ is reasonable because adopting e.g., the $\nu^{1/3}$ dependence expected for a pure, thin accretion disk provides an insignificant difference to L_{BOL} (the analysis showing this result is presented in §3.5.2), which is the parameter of main interest here.

3.5 MEASUREMENTS BASED ON THE SEDS

In order to investigate the relationship between the line shape (FWHM to σ_{line}) and main parameters related to the black hole accretion process I need to measure the bolometric luminosity and the Eddington ratio. In this section I describe the measurements based on the SEDs.

3.5.1 THE SEDS

The most luminous part of the SED is the optical-UV bump. For individual sources the intrinsic source variations in the continuum emission give rise to SED variations over time. Particularly X-ray and UV variations affect the amplitude of the interpolated EUV range which has the largest frequency span over the full SED. If the intrinsic variation amplitudes of the EUV flux are much higher than that of the UV and X-ray fluxes, then such a interpolation would only give a lower limit on the SED variations. Without data across the EUV frequency range the intrinsic EUV variability amplitude is unknown and this brings a large uncertainty the SED variation amplitude. As a first order approximation, I assume that the observed changes over the interpolated EUV region represents the intrinsic continuum variations at these energies.

With multi-epoch SEDs, it is possible to compare the changing SED shape over time for individual sources. In Figure 3.4 I show the observed single-epoch SED for the five AGN where I have multi-epoch SEDs. To distinguish the SEDs, each epoch is color coded. The dashed lines show the extrapolated and interpolated regions and the ‘butter fly’ shape represents the X-ray continuum and its 1σ uncertainty. For NGC 4151 and NGC 7469 for which I only have SEDs spanning very short periods of seven and 25 days, respectively, I do not see a dramatic change in the overall SED shape. This is also true for 3C 390.3 for which I only have two epochs in a time span of 113 days. For Fairall 9, I have 27 epochs spanning 248 days. Here, I see the most dramatic changes in the optical-UV region and the change in the X-ray region is relatively small as expected, since I *estimate* the average X-ray level by interpolation (§3.3.2). For NGC 5548, I have a total of 47 SED epochs. Among those, eleven SEDs are based on simultaneous optical-UV and X-ray data to within two days. I show these SEDs in panel (e) of Figure 3.4. These SEDs span a time period of two years and here I see dramatic changes across the entire SED. The variations in continuum emission give rise to SED variations over time. In panel (f) I show ten representative SEDs of NGC 5548 with simultaneous optical-UV data (within two days) and estimated X-ray continuum (§ 3.3.2). Across the period of ~ 200 days that these SEDs cover, I see dramatic changes in the optical-UV fluxes. The interpolated X-ray flux clearly contain no variability information. We quantify these SED changes in §3.7.

Figure 3.4 indicates that the amplitude of the SED variations depend on the time span over

which these variations are measured: long term variations appear to result in more dramatic changes in the SEDs. I address this issue in §3.7. The UV spectral region typically exhibit higher amplitude variations compared to the optical region. Kilerci Eser et al. (2014, Chapter 2 of this thesis) quantify this by means of simultaneous optical and UV measurements and the AGN variability statistics. This is consistent with the general variability characteristics of AGNs that the higher frequency emission exhibits larger variation amplitudes (e.g. Clavel et al., 1991; Korista et al., 1995; Vanden Berk et al., 2004) compared to lower energy emission.

3.5.2 BOLOMETRIC LUMINOSITIES

The bolometric luminosity of an AGN is the total luminosity of the source integrated across all wavelengths produced by the source. However, the luminosity produced by the central SMBH and accretion disk system is the total luminosity from $\sim 1\mu\text{m}$ to $\sim 10\text{ keV}$ - 100 keV (e.g., Vasudevan & Fabian, 2009; Jin et al., 2012b). The total luminosity from 13.6 eV to $\sim 100\text{ keV}$ is the ionizing luminosity (e.g., Korista et al., 1997a) that produces the broad emission lines in the BLR by photoionization of the BLR gas. Since the data in $10\text{--}100\text{ keV}$ range are unavailable I adopt an upper energy limit of 10 keV for the SEDs. Because I am interested in the bolometric luminosity produced by the accretion, $L_{\text{BOL}}(\text{acc})$, I exclude the radio through IR regime because they do not contribute to this accretion luminosity (defined in Chapter 1.2.3). For my sample I have the SEDs (§ 3.4) with appropriate wavelength coverage from which I can calculate $L_{\text{BOL}}(\text{acc})$ by integrating the SEDs from $1\mu\text{m}$ to 10 keV .

Bolometric Luminosity Measurements: The Interpolation Method

In each SED the lowest energy data point is at the end of the observed optical spectrum ($\lambda \sim 5400\text{Å}$). In order to estimate the luminosity between $1\mu\text{m}$ and the optical continuum, I linearly extrapolate the optical continuum from $\sim 5400\text{Å}$ to $1\mu\text{m}$. I test two methods by which to extrapolate the SED to $1\mu\text{m}$: (A) I linearly extrapolate the best-fit optical continuum power-law from $\sim 5400\text{Å}$ to $1\mu\text{m}$; (B) between $1\mu\text{m}$ and the longest optical wavelength I use an accretion disk model in the form of $F_\nu \propto \nu^{1/3}$ (Shakura & Sunyaev, 1973). I show the linear extrapolation and the accretion disk model for the NIR region for one representative SED in Figure 3.5. To quantify the difference in the bolometric luminosities caused by choosing one of the two approaches, I calculate the bolometric luminosities by integrating the SED from $1\mu\text{m}$ to 10 keV for both cases for all sources. For each object the difference in bolometric luminosities between methods (A) and (B) is very small. For the sample as a whole I obtain an average difference of $1.6 \pm 0.7\%$, or $0.007 \pm 0.003\text{ dex}$ (uncertainties quoted are the standard deviations of the mean differences). As this is an insignificant change I do not use method (B) for my analysis later.

I tabulate the integrated bolometric luminosities $L_{\text{BOL}}(\text{interpolation})$ based on method (A) in column (4) of Table 3.6. In this table, object names, SED epoch numbers and SED Julian Date intervals are listed in columns (1), (2) and (3), respectively. The errors on the $L_{\text{BOL}}(\text{interpolation})$ values are obtained by propagating the measurement uncertainties on the continuum. Namely, I integrate the SEDs over the $\pm 1\sigma$ luminosity ranges (the blue dotted lines in Figure 3.3) of each data point and obtain the upper and lower ($L_{\text{BOL}}(\text{interpolation}) \pm 1\sigma$) bolometric luminosities. These uncertainties do not include the uncertainty due to my lack of knowledge of the intrinsic SED shape in the EUV region. I also measured $L_{\text{BOL}}(\text{interpolation})$ by adding the emission lines on top of the continuum measurements and find that the emission line flux contribution to $L_{\text{BOL}}(\text{interpolation})$ is an additional 5%.

The distribution of $L_{\text{BOL}}(\text{interpolation})$ for my sample is shown in Figure 3.6; the gray his-

tograms represent NGC 5548. The bolometric luminosities cover the range between 43.56 dex and 45.25 dex which is in the mid-to-upper luminosity range observed for Seyferts (Elvis et al., 1994; Vasudevan & Fabian, 2009).

Bolometric Luminosity Based on The SED Model of Korista et al. (1997a)

As noted earlier, the largest gap in the SEDs is in the EUV region, from $\sim 1100\text{\AA}$ to 2 keV. To bridge this gap it is common practice to linearly interpolate between the UV and X-ray data points (e.g. Elvis et al., 1994; Laor et al., 1997) because it is simple and does not impose any model assumptions. Runnoe et al. (2012) show that linear interpolation in the EUV region underestimates the bolometric luminosity relative to the SED model of Korista et al. (1997a). I therefore also compute the bolometric luminosity by this model in order to quantify the differences. The continuum SED adopted from Korista et al. (1997a) is an empirical SED of the ionizing continuum generated from the observed average SEDs of radio-quiet AGN. The photoionization calculations by the authors show that such an ionizing continuum is successful at producing the observed broad emission line properties. Their SED is a combination of a thermal UV bump of the form $f_\nu \propto \nu^{-0.5} \exp(-h\nu/kT_{cut})$ and a power-law component for the X-ray emission. At energies of 13.6 eV and above a power-law with a slope of -1.0 ($f_\nu \propto \nu^{-1}$) is used. I follow Korista et al. (1997a) and adopt their typical values for the SED parameters including the cutoff temperature T_{cut} at $10^6 K$ and the peak energy of the UV bump E_{peak} at 44 eV. Figure 3.7 compares the Korista et al. (1997a) model (brown dashed line) to the linear interpolation in the EUV region for a sample SED. I normalize the Korista et al. (1997a) model to the UV continuum luminosity at 1350\AA and extrapolate the observed X-ray power-law component towards the UV region until it intersects the model (brown dotted line). I integrate the SED between $1\mu\text{m}$ – 10 keV and obtain the bolometric luminosity, $L_{BOL}(K97)$. For completeness, I list in §A.3 the $L_{BOL}(K97)$ values for all SEDs of my sample. In Figure 3.8 I compare the bolometric luminosities obtained from the two methods (interpolation and the Korista et al. (1997a) model). I confirm the results of Runnoe et al. (2012) that the Korista et al. (1997a) SED model yields slightly higher luminosities. $L_{BOL}(K97)$ is on average 23.3% (equivalent to 0.09 dex) higher than $L_{BOL}(\text{interpolation})$ and the 1σ standard deviation is 10.0% (equivalent to 0.03 dex). This comparison indicates that the uncertainty in the $L_{BOL}(\text{interpolation})$ values due to an assumed different EUV spectral shape is at least $\sim 23\%$ on average. And, obviously, if the Korista et al. (1997a) SED model represents the intrinsic AGN SED, then I systematically underestimate the bolometric luminosities by $\sim 23\%$ by use of the simple interpolated SED adopted here.

It is worth noting that the mean percent difference between the two luminosities is large and comparable to the observed $L_{BOL}(\text{interpolation})$ variability amplitudes (§3.7.1) of individual sources. Even with the thermal bump of the Korista et al. (1997a) SED model included I may not entirely capture the intrinsic SED and, furthermore, the BLR clouds may actually see a different continuum than we do (e.g. Korista et al., 1997b). Because it is unclear which of the two methods gives the best estimate for the $L_{BOL}(acc)$ of the two methods, I opt for the simpler method that provides the minimum bolometric luminosity by measuring directly the data and which has the advantage of being model independent. I also applied an accretion disk model (the *optxagnf* model Done et al., 2012) to one SED to infer $L_{BOL}(acc)$. The details of this analysis is given in §A.4. The accretion disk model is not robust enough for $L_{BOL}(acc)$ measurements but it provides at best a somewhat conservative lower limit that is 23% lower compared to $L_{BOL}(\text{interpolation})$. As it happened, $L_{BOL}(\text{interpolation})$ is between the two extremes. Hereafter I use $L_{BOL}(acc)$ and $L_{BOL}(\text{interpolation})$ interchangeably.

Bolometric Luminosity Comparison with Previous Studies

The SEDs and bolometric luminosity measurements of my sample are presented by previous studies in the literature. For completeness and mere curiosity I briefly compare in Table 3.8 my SEDs and bolometric luminosity measurements with those published earlier. To compare my results with Vasudevan & Fabian (2009) I extrapolate 2-10 keV X-ray power-law up to 100 keV and re-measure the bolometric luminosities between $1\mu\text{m}$ - 100 keV. Those luminosities are listed in Table 3.9, note that the epoch-averaged luminosities are listed for the sources with multi-epoch SEDs for easy comparison.

For some objects (Fairall 9, NGC 7469, NGC 3783) I see significant changes ($5 - 10\sigma$) between literature SEDs and ours. For some studies (Elvis et al., 1994; Runnoe et al., 2012) it is due to non-simultaneous data, for others (Vasudevan & Fabian, 2009; Elvis et al., 1994; Grupe et al., 2010) it is likely due to a change in the source accretion state because there are several years difference between our and their SED epochs. I understand and expect these changes because nearby (low luminosity AGN) are highly variable (e.g., Peterson et al., 2004; Vanden Berk et al., 2004).

3.5.3 THE BOLOMETRIC CORRECTION FACTOR

It is not straightforward to obtain and coordinate observing time on a large range of telescopes covering the entire electromagnetic spectrum over which AGN emit. Therefore, it is not always possible to obtain simultaneous multi-wavelength data from which to construct the SED that allow us to directly measure the bolometric luminosity. A practical way to overcome this problem is to apply mean bolometric corrections to monochromatic luminosities and estimate the bolometric luminosity. However, this may not be a good approach for all applications, especially if the source is strongly varying. Also, the mean bolometric correction values obtained for large samples have large sample spreads (e.g., Elvis et al., 1994; Richards et al., 2006a). In order to check the difference between those BCs and the ones obtained from quasi-simultaneous of individual sources, in the following, I determine single epoch bolometric corrections at 5100 \AA , 1350 \AA and the 2-10 keV X-ray band. I am interested in these wavelengths and energies because these are widely used to estimate AGN bolometric luminosities.

Bolometric Correction Measurements

I calculate the bolometric corrections by assuming:

$$BC(\lambda) = L_{BOL}/\lambda L_{\lambda}. \quad (3.6)$$

Here L_{BOL} is $L_{BOL}(\text{interpolation})$ $BC(\lambda)$ is the bolometric correction at wavelength λ and L_{λ} is the monochromatic luminosity. The $L_{BOL}(\text{interpolation})$ monochromatic optical luminosity at 5100\AA , $\lambda L_{\lambda}(5100)$, monochromatic UV luminosity at 1350\AA , $\lambda L_{\lambda}(1350)$, and the total X-ray band luminosity, $L_{2-10\text{keV}}$ measured from my data are listed in Table 3.6. The bolometric corrections for 5100\AA , $BC(5100)$, for 1350\AA , $BC(1350)$ and for 2-10 keV X-ray band, $BC(2-10 \text{ keV})$ of my sample sources are listed in columns (7, 9 and 11) of Table 3.6, respectively. The errors on the BC values are propagated based on Equation 3.6 and standard error propagation rules (Taylor, 1997, Chapter 4.4).

In Figure 3.6 I present the distributions of the optical (top), UV (middle) and X-ray (bottom) bolometric corrections for my sample. It is noteworthy that there is there is a considerable range of bolometric correction factors even for my small sample, namely: $BC(5100\text{\AA}) = 8.0 - 23.1$,

$BC(1350\text{\AA}) = 3.2 - 12.0$ and $BC(2 - 10\text{keV}) = 3.5 - 44.0$ and even for individual objects (NGC 5548 is clearly seen).

Bolometric Correction Comparison with Previous Studies

I compare the mean BC values for my sample (listed in Table 3.7 as ‘All Sample’) with the widely used mean BCs of Elvis et al. (1994) and Richards et al. (2006a). The mean BCs of my sample are computed by averaging the 86 individual BC measurements. Elvis et al. (1994) have a X-ray bright, local quasar sample of 47 sources with sample properties similar to ours. My mean $BC(5100\text{\AA})$ (12.24 ± 2.71) is consistent with the mean BC in the V-band ($BC(V) = 14.2 \pm 5.1$) given by Elvis et al. (1994) to within 1σ . However, do note that the standard deviations are large. Richards et al. (2006a) have a sample of 259 bright, high redshift quasars, so their sample consists of more luminous objects than my AGN. Nevertheless, their mean BC in V-band ($BC(V) = 10.3 \pm 2.1$) is consistent with my $BC(5100\text{\AA})$ to within the 1σ standard deviations around the mean.

My average $BC(2-10\text{keV}) = 8.89 \pm 4.54$ is close to the mean $BC(2-10\text{keV})$ (between 10 and 20) presented by Vasudevan & Fabian (2009) for the low Eddington ratio sources. My measurements corroborate the previous works (Vasudevan & Fabian, 2009; Grupe et al., 2010) that show that Seyfert galaxies and quasars have similar mean SEDs and that each AGN type exhibit a range in M_{BH} , L_{BOL} and accretion state.

3.5.4 THE EDDINGTON LUMINOSITY RATIO

The intrinsic continuum luminosity is expected to be produced by the accretion of material onto the SMBH. The mass accretion rate (\dot{m}) is directly proportional to the emitted luminosity; the proportionality factor is the efficiency of energy conversion η : $L = \eta \dot{M} c^2$. The Eddington ratio, λ_{Edd} , is the accretion rate normalized by the mass of the central black hole and is defined as (e.g. Peterson, 1997):

$$\lambda_{Edd} = \frac{L_{BOL}(acc)}{L_{Edd}} = \frac{L_{BOL}(acc)}{1.38 \times 10^{38} (M_{BH}/M_{\odot})} \quad (3.7)$$

where L_{Edd} is the Eddington luminosity for the central black hole mass M_{BH} . In the accretion process the accreting matter is under the influence of gravitational and radiation forces. Note that, since it is the accretion luminosity that balances the radiation pressure in this equation we need to use $L_{BOL}(acc)$. L_{Edd} is the maximum luminosity satisfying the balance between the two forces and is therefore often used as a measure of the maximum luminosity that is possible for the central engine if the material is accreting spherically symmetrically.

To calculate the Eddington luminosities for my sample I adopt the M_{BH} measurements based on reverberation-mapping analyses, as presented by Peterson et al. (2004). I use the bolometric luminosity values obtained at each epoch (see Table 3.6). I tabulate the calculated λ_{Edd} values in column (5) of Table 3.6. I propagate the uncertainties in $L_{BOL}(acc)$ and M_{BH} through Equation (3.7) to estimate the uncertainties in the λ_{Edd} values. The Eddington ratio distribution of my sample is shown in Figure 3.6 with a range of 0.001 – 0.200. For the majority of my sample, the Eddington ratios are rather small ($\lambda_{Edd} \leq 0.1$). Only for NGC 7469, is the Eddington ratio moderate with a range $0.130 \leq \lambda_{Edd} \leq 0.200$ range.

I note that, my λ_{Edd} values agree with those of Vasudevan & Fabian (2009) for those objects where $L_{BOL}(acc)$ did not change significantly.

3.6 SED – LINE SHAPE CORRELATION

I address the Eddington luminosity ratio and the line shape correlation based on H β and C IV in separate sections.

3.6.1 MATCHING THE SEDS WITH THE SPECTRA

In my investigation of the single-epoch line shape dependence on Eddington ratio, I account for the light travel time of the continuum luminosity to the BLR in an attempt to connect the photons that generated the observed line profile. The available BLR radii are weighted mean measurements and represent the mean distance of the gas that is responding to continuum variations. Since R_{BLR} is a mean value gleaned from the RM analysis it has an uncertainty, ΔR . I account for light travel time and its uncertainty by using $FWHM/\sigma_{line}$ measurements on spectra obtained at a JD delayed from the $L_{BOL}(acc)$ epoch by the mean $R(H\beta)$ or $R(CIV)$ values, because it takes the photons the time $\Delta t = R/c \pm \Delta R/c$ to reach the BLR wherein the photons are reprocessed. Ideally I would select the JDs of the spectra according to the exact value $\tau = R/c$. However it is not always possible to find a spectrum for that specific epoch. Therefore, to select the JDs of the spectra I consider ΔR uncertainty and take the closest spectrum JD within the $\Delta t = R/c \pm \Delta R/c$ range. For my sample the R_{BLR} range for H β is between 11 to 80 days and for C IV between 0.5 to 36 days; these are object to object values (not for individual objects). The BLR radius of the relevant emission-line places the first limit to the required time resolution required to measure $L_{BOL}(acc)$. I have two options to obtain $L_{BOL}(acc)$ (and thus Eddington ratio): (1) I may apply a mean BC(5100Å) to continuum luminosities; (2) I may measure $L_{BOL}(acc)$ directly from the SEDs. To obtain more accurate bolometric luminosities and Eddington ratios, I directly measure $L_{BOL}(acc)$ from the SEDs. The time delay that I want to account for between the JDs of the measurements of the SED and the emission-line profile brings a limit to the SED time span, $\Delta T(SED)$: $\Delta T(SED) < R_{BLR}/c$. If the $\Delta T(SED) > R_{BLR}/c$ the ionizing continuum measured from such an SED can not be assumed to be producing the measured line profiles. Once I have this restriction, the unpredictable intrinsic source variability may bring an extra uncertainty to $L_{BOL}(acc)$ and the best way to minimize the effect of intrinsic source variability in the single-epoch $L_{BOL}(acc)$ measurements is to use quasi-simultaneous optical, UV and X-ray data (e.g., Vasudevan & Fabian, 2009; Vasudevan et al., 2009). Therefore, in §3.5 I measure the bolometric luminosities of individual sources at multiple epochs from the SED of simultaneous (or quasi-simultaneous) multi-wavelength data. I should note that, the preference of such SEDs brings the largest limitation to my sample size. Since obtaining such SEDs require several telescopes observing at different wavelengths, it is difficult to find such simultaneous multi-wavelength data obtained during RM monitoring campaigns.

3.6.2 H β LINE SHAPE - EDDINGTON RATIO CORRELATION: COLLIN ET AL. (2006) FOLLOW UP STUDY

Collin et al. (2006) reveal that the Eddington luminosity ratio may potentially affect the measured gas velocities used for the black hole mass estimates. They report an inverse-correlation between the mean H β line-width ratio ($FWHM/\sigma_{line}$) and the Eddington ratio for 35 reverberation-mapped AGN. The proposed correlation (if real) is important for our ability to improve black hole mass estimates because the line shape will influence the specific line width we measure - and hence the inferred black hole mass (§4.1). However the Eddington luminosity ratio estimates of Collin et al. (2006) depend on the bolometric luminosities obtained by applying a

mean $BC(5100\text{\AA})$ of 10. Since they do not use robust measurements of the nuclear bolometric luminosity their Eddington ratio estimates are not robust. I seek to re-examine this relationship for the situation where the bolometric luminosities are directly measured, as opposed to crudely approximated, which the BC scaling might be. Also, I impose a few additional changes to the original study of Collin et al. (2006). My investigation includes the following improvements compared to the previously applied analysis of Collin et al. (2006): (1) In order to measure the Eddington ratio I use the bolometric luminosity measured directly from quasi-simultaneous SED; (2) my bolometric luminosities are corrected for host galaxy star light contamination based on the recently updated measurements of Bentz et al. (2013); and (3) I take into account the effects of light-travel time between the ionizing continuum radiation and the emission-line radiation.

I am interested in the $L_{BOL}(acc)$ responsible for the line emission at a given epoch, therefore I measure the line shape in spectra obtained at a later epoch than the SED epoch corresponding to the expected $H\beta$ and/or C IV lag measured from RM analysis (these are adopted from Peterson et al., 2004, and listed in Tables 3.4 and 3.5). I thereby increase the probability that $L_{BOL}(acc)$ is a good proxy of the relevant continuum luminosity.

Following Collin et al. (2006), I use the $FWHM/\sigma_{line}$ parameter (Tables 3.4 and 3.5 column 7) to characterize the shape of the broad line profiles. In Figure 3.9 line widths and $FWHM/\sigma_{line}$ are shown respectively as a function of Eddington ratio for $H\beta$ (left) and C IV (right). I determine the significance of the correlations by Pearson correlation coefficient⁴ (r , Pearson, 1895) and its p-value that is the probability of the correlation happening by chance; both are shown in each panel. I find a strong inverse correlation between the $H\beta$ FWHM and the Eddington ratio. The correlation between $H\beta$ σ_{line} and the Eddington ratio is weak, however the resultant $H\beta$ line shape - Eddington ratio correlation is strong, and is driven by the FWHM.

Collin et al. (2006) found a clear inverse correlation between the line shape and Eddington ratio although with a large scatter (see Figure 1.5 in Chapter 1). When they corrected the optical luminosities for host galaxy starlight contamination, for the available 28 measurements the correlation vanished due to a lack of high Eddington ratio quasars in their sample. For the nearby sources for which host galaxy star light contribution is anticipated to be significant, where the authors can make that correction they do it. The bottom panel of Figure 1.5 in Chapter 1 shows the correlation only for the sources where star-light-corrected, high Eddington ratio quasars are not included in this panel. However, the authors discuss that since quasars are expected to have low stellar light contributions by adding the high Eddington ratio quasars the inverse correlation (shown in the bottom panel of Figure 1.5 in Chapter 1) would be strengthened. Thus they state that the inverse correlation should also hold for their full sample of Seyferts and quasars, not just the Seyferts alone. The inverse correlation is clear when their sample includes sources with $\lambda_{Edd} \geq 0.1$. Based on multiple measurements of NGC 5548 they suggest intrinsic variability as a source of the observed scatter. I have only 7 of the 35 AGN in the Collin et al. (2006) sample and the majority thereof have $\lambda_{Edd} \leq 0.05$. The vast majority of my AGN have $\lambda_{Edd} \leq 0.05$ and only two sources (Mrk 509 and NGC 7469) have $\lambda_{Edd} > 0.1$. As seen in Figure 3.9 I mostly have low Eddington ratio sources. Compared to the sample of Collin et al. (2006) my sample show a similar distribution with fewer data points, but the overall distributions

⁴Pearson correlation coefficient describes the degree of linear relationship between two parameters and it can have a value between -1 and 1. The negative sign of r means an inverse relation between the two parameters. I consider the strength of the correlation with respect to r as: $r = 0$ no correlation, $r < 0.3$ poor correlation, $0.3 \leq r \leq 0.5$ fair correlation, $0.6 \leq r < 0.8$ moderately strong correlation, $r \geq 0.8$ very strong correlation.

look similar. The inverse correlation seen in Figure 3.9 depends strongly on the presence of two higher λ_{Edd} sources. Therefore, with my small sample and data base I am not able to make firm conclusions regarding the existence of a correlation between $FWHM/\sigma_{line}$ and λ_{Edd} for $H\beta$. Despite my limited database, the observed inverse correlation is significant at 99% (or 5σ) level and therefore, I interpret Figure 3.9 as a strong hint of a possible $H\beta$ line shape - Eddington ratio inverse correlation.

In this work, I aimed to obtain the most accurate measurements of the bolometric luminosity responsible for the line shapes by obtaining single-epoch SED from semi-simultaneously obtained data. However, as it turned out, such data are only available for a small sample of the RM AGN and this severely limits this study. A practical way to increase my sample size is to use a mean BC as it is done by Collin et al. (2006). I test the effect of using a mean BC(5100\AA)=10 (as Collin et al., 2006, adopted) or BC(1350\AA)=4.2 (Runnoe et al., 2012) to the line shape- Eddington ratio correlation. In Figure 3.10 I show the line shape- Eddington ratio correlations based on Eddington ratios obtained from $L_{BOL}(BC5100 = 10)$ (top panels) and $L_{BOL}(BC1350 = 4.2)$ (bottom panels). The optical continuum luminosities used to compute Eddington ratios are corrected for host galaxy star light (§3.3.3). Comparison of Figure 3.10 with Figure 3.9 shows that the λ_{Edd} values move around but not so dramatically. As a result, the overall distribution shows the same trend as seen earlier and by Collin et al. (2006). This shows that the same line shape-Eddington ratio relations could be obtained by applying a constant BC(5100\AA) or BC(1350\AA) instead of directly measuring L_{BOL} from quasi-simultaneous SEDs. That said, there were no way of finding this out than by doing the current test - and therefore the study and analysis done here, still has value.

3.6.3 C IV LINE SHAPE - EDDINGTON RATIO CORRELATION

I have C IV measurements for the same objects that I studied the $H\beta$ line shape dependence on the Eddington ratio. Therefore, I can test if a similar Eddington luminosity ratio – line shape correlation holds for C IV or a high ionization UV line behave differently. This is interesting to look at because it has not been investigated before. In Figure 3.9, for C IV I do not find a similar linear correlation between line widths/shape and Eddington ratio, but this is not surprising given the small C IV $FWHM/\sigma_{line}$ range compared to that observed for $H\beta$. It is interesting to note that C IV profiles are mostly peakier than a Gaussian function.

3.6.4 EFFECT OF UNCERTAINTY IN R_{BLR} ON THE EDDINGTON RATIO – LINE SHAPE CORRELATION

I tested the impact of the uncertainties in R_{BLR} on the Eddington ratio – line shape correlation. I am only able to perform this test for the UV spectra of NGC 5548 and Fairall 9 because for optical data for these objects, and for both the optical and UV datasets of the other objects $\Delta R_{BLR}/c$ is very small and no spectra are available within this time interval. For this test I pick another spectrum within that time span from which to measure the line shape so to include in Eddington ratio – line shape/width distributions. For a couple of cases that there were multiple options for some SEDs I made a random selection; the available data is not large enough to make a sort of Monte Carlo test. For NGC 5548 and Fairall 9, when I match each of the single-epoch SEDs with a different C IV spectrum within the time period $\Delta t = R_{BLR}/c \pm \Delta R_{BLR}/c$, I find the resultant Eddington ratio – line shape/width distribution is very similar to Figure 3.9. For the data available the fact that there is an uncertainty in R_{BLR} and that in my analysis I match the SED and spectrum to the mean R_{BLR} does not affect the result of my analysis.

3.6.5 LINE SHAPE - EDDINGTON RATIO CORRELATION OF SDSS DR3 QUASARS

For my small, nearby AGN sample I could have obtained the same inverse correlation between the line shape and λ_{Edd} by applying a BC scaling (see §3.6.2 and Figure 3.10). However, applying a constant BC and using single-epoch BH mass estimates, may significantly (~ 0.5 dex) affect the λ_{Edd} estimates of a larger AGN sample of more luminous and higher-redshift quasars. Therefore, based on my small sample AGN sample I can not assume that applying a mean BC would have a small affect on the line shape– λ_{Edd} relation for a large sample of quasars. Such an assumption would be unrealistic. However, I can still check what might be seen if BC scaling and single-epoch mass estimates are used for a large quasar sample. In order to investigate the line shape– Eddington ratio relation for a large sample, I use a sample of ~ 8000 quasars from SDSS DR3 database (Richards et al., 2006b; Vestergaard et al., 2008). The measurements of this dataset are made with the semi-automated spectral decomposition method (see Vestergaard et al. (2008) for the details). Moreover, all the spectra are visually inspected to ensure the modeling and the spectral measurements are reliable. Here I have the advantage of having measurements of a large sample, despite the fact that some of the data are of lower S/N. The bolometric luminosities of the SDSS quasars are computed by the same BC factors ($BC(5100\text{\AA})=10$ and $BC(1350\text{\AA})=4.2$) used for the nearby AGN sample in §3.6.2, so the bolometric luminosities are comparable. In the top panel of Figure 3.11 302 high S/N (black diamonds, median $S/N \geq 20$) and 1033 lower S/N (red circles, median $10 \leq S/N < 20$) measurements are shown. Bottom panel shows 229 high S/N (black diamonds, $S/N \geq 20$) and 2033 lower S/N (red circles, $10 \leq S/N < 20$) measurements. Figure 3.11 shows a moderately strong inverse correlation both for $H\beta$ (top panel) and $C\text{ IV}$ (bottom panel). The correlation coefficients, p and r are calculated for the high S/N data. However, since the low S/N data follow the same inverse correlation this trend does not depend on the S/N level of the spectra. The reliability and the interpretation of the observed inverse correlations are further discussed in sections 3.8.1 and 3.8.2.

3.6.6 LINE SHAPE - CONTINUUM LUMINOSITY RELATION

Since the optical and UV continuum luminosities are also an other measure of the accretion emission I check if the line shapes have a luminosity dependence. Figure A.3 shows $H\beta$ and $C\text{ IV}$ line widths and shapes vs. $\lambda L_{\lambda}(5100)$ and $\lambda L_{\lambda}(1350)$. Again, also for these objects individually do I mostly see the data points scatter completely. In Figure 3.9 λ_{Edd} is a measure of luminosity normalized by the BH mass, so I can compare the intrinsic accretion luminosity across the sample. But when I have only the monochromatic continuum luminosities, BH masses are not taken into account. Therefore, in Figure A.3 it is more important to look at individual objects, because for those the BH mass is constant.

In Figure A.3 the uncertainties of the line widths and shape are large and different measurements of individual sources are consistent to be almost same within their measurement uncertainties. For NGC 5548 and Fairall 9 the luminosity changes are not dramatic enough to show a real difference in the profiles. Both for $H\beta$ and $C\text{ IV}$ I do not see a strong trend for individual objects, I mostly see a scatter. I do not probe a sufficiently dramatic luminosity changes to be able to probe significant change in the profiles. But the aspect of whether or not I can quantify profile differences that I know exist⁵ (e.g., Sergeev et al., 2007b) is an other issue. Namely, my ability to measure the shape accurately enough might be an other important issue here.

On the other hand, one can question how representative are the optical and UV continuum luminosities for ionizing continuum. As discussed in Chapter 2, $\lambda L_{\lambda}(5100)$ may not be the most

⁵I refer to the movie at <http://www.astronomy.ohio-state.edu/~peterson/AGN/30year.avi>

representative of the ionizing luminosity, and therefore it may not give us a complete picture of what is actually causing the profile changes even if it clearly correlates with the ionizing luminosity. Also, as I showed in Chapter 2 the optical luminosity does not vary as much as the UV luminosity. And, neither $L(\text{optical})$ or $L(\text{UV})$ is the ionizing luminosity.

3.7 VARIATIONS IN THE SEDS

3.7.1 VARIATIONS IN BOLOMETRIC LUMINOSITY AND EDDINGTON RATIO

The previous studies (listed in Table 3.2) provide evidence for intrinsic optical–UV–X-ray variability of the AGN in my sample. The propagation of multi-wavelength continuum variations into the broad-band SED properties has to my knowledge not been investigated for my dataset before. Here, I investigate the effect of continuum variations on the SED parameters by quantifying the rms and time resolved variations of bolometric luminosity, bolometric correction and Eddington ratio, respectively.

The mean and rms $L_{\text{BOL}}(\text{interpolation})$ values are tabulated in Table 3.7. The rms $L_{\text{BOL}}(\text{interpolation})$ (column 6) given as the percent deviation relative to the mean $L_{\text{BOL}}(\text{interpolation})$ is between $\sim 4\%$ and $\sim 38\%$. The rms variability depends strongly on the probed time span: SED variations over a week have a negligible effect on $L_{\text{BOL}}(\text{interpolation})$, but SED changes over a year may cause significant luminosity variations. In order to investigate time dependence of the SED variations further, I examine the time-resolved $L_{\text{BOL}}(\text{interpolation})$ variations of my sample in Figure 3.12. The top panel shows ΔL_{BOL} as a function of time; each source is color-coded. ΔL_{BOL} is the percent difference relative to the lower luminosity between any two L_{BOL} values. Here, ΔT is the difference in the mean JDs of the SEDs. For each source I use all of the available SED epochs when computing the statistics. Note that the long term variations (of a year or more) are available only for NGC 5548. For NGC 5548 the ΔL_{BOL} range expands and becomes larger than 100% as ΔT exceeds ~ 300 days. In the bottom panel, I show the mean ΔL_{BOL} within a set of time intervals; here error bars show the rms deviations. This panel shows the average ΔL_{BOL} and the rms around it to increase with ΔT . Based on NGC 5548 I conclude that the changes in the optical-UV and X-ray continuum over the time span of a year may alter L_{BOL} significantly (up to $\sim 200\%$). This will have importance when one is generating the SED from non-simultaneously observed data §3.8.4.

The Eddington ratio of individual AGN changes with the same amplitude as the bolometric luminosity (Table 3.7). For the vast majority of my sample I probe 20-36% rms variations. The highest Eddington ratio rms variations are moderate, around 32% (NGC 5548) and 36% (3C 390.3). As seen in Figure 3.9 individual sources do not spread out over a large λ_{Edd} range and this shows that the probed Eddington ratio variations are not dramatic. These moderate λ_{Edd} variations might affect my ability to see the true Eddington ratio – line shape relation of individual sources as it will generate scatter in the relation, as also noted by Collin et al. (2006).

3.7.2 BOLOMETRIC CORRECTION VARIATIONS

The continuum variations that alter the bolometric luminosities, affect the BCs similarly. In order to understand the robustness of bolometric corrections with respect to SED variations, I investigate bolometric correction variability and its spread over time. The rms variability in the mean BCs (listed in Table 3.7, columns 11, 13, 15) range between $\sim 4\%$ and $\sim 20\%$. This shows that BCs do not have a constant value for individual objects and they change according to continuum variations. In the case of NGC 5548, for which I have the most reliable measurements

based on 11 SED epochs with simultaneous optical/UV and X-ray data, the rms variability in the mean BCs is moderate (between 11%-18%).

Figure 3.13 shows the time resolved BC(5100Å) and BC(1350Å) percent differences of my sample. Since most of the X-rays fluxes of Fairall 9 and NGC 5548 are estimated (§3.3.2), they do not carry actual X-ray variability information and therefore I do not show the equivalent results for BC(2-10 keV). The comparison of the mean percent differences of BC(5100Å) and BC(1350Å) over 600 days indicates that the mean $\Delta BC(5100)$ and its rms is slightly ($\sim 5\%$) smaller. However, the rms of the mean percent differences are 10-15% and in comparison 5% is not significant. As shown in the bottom panels of Figure 3.13, the mean percent differences are almost constant ($\sim 10\%$) over the time scales probed here. So, the variations in the mean BC values do not increase with ΔT as seen for ΔL_{BOL} . However, the rms values of mean $\Delta BC(5100)$ gets larger with ΔT , and this is consistent with the behavior of mean ΔL_{BOL} . Even if the mean BC does not change more than 10% for the sample, it can be much larger for individual sources.

3.8 DISCUSSION

3.8.1 IS THE LINE SHAPE - EDDINGTON RATIO CORRELATION REAL?

In this work I investigated the Eddington ratio – line shape correlation for a sub-set of the RM sample. I aimed for having more accurate Eddington ratio measurements for my investigation. Therefore, I used quasi-simultaneous optical/UV spectra to build up SEDs and measure the bolometric luminosity. The simultaneous multi-wavelength data requirements brought the largest limitation to my investigation because such data turn out to be sparse and hard to obtain (for reasons discussed in Chapter 1). Then, in order to perform a time resolved analysis for the line shapes, I accounted for the light travel time between the continuum and the line-emission. For the small sub-set of the RM sample I found a moderately strong inverse correlation for H β line shapes. But I do not see this trend clearly for individual sources such as NGC 5548, Fairall 9 or NGC 7469 contrary to what Collin et al. (2006) found for NGC 5548. But note that, since I only have variations within two observing campaigns where Collin et al. (2006) have the mean spectra of 14 different campaigns, this might be the reason for not observing the same trend that they see. I only see the inverse correlation for my small sub-set of the RM sample for which I measured the Eddington ratios from quasi-simultaneous SED. Due to the small sample size that I analyzed, it is unclear if the trend that is seen is real. But, it is consistent with the result of Collin et al. (2006). Moreover, my analysis shows that the result of Collin et al. (2006) likely hold when the Eddington ratios are extracted from the SEDs directly. However, for C IV I have investigated the Eddington ratio- line shape relation for the first time and found that for my small sample of nearby RM AGN the C IV profiles do not appear to behave as the H β profiles do. The reality of the Eddington ratio – line shape relationship is not affected by the uncertainty in R_{BLR} or the way I selected the spectra to match the SEDS (§3.6.4).

For a larger quasar sample, I find that both H β and C IV exhibit an inverse correlation between the line shape and λEdd . This might mean that the Eddington ratio, and the mass accretion rate is affecting C IV or H β profiles in similar way. The measurements of the quasar sample have large uncertainties, both for Eddington luminosity ratios and line shapes, but considering the correlation statistics the inverse correlation is significant. However, the Eddington luminosities are computed by using the line widths measured from the single-epoch spectra, the same line width measurements are present in both variables. Since we do not have an independent M_{BH} measurements that is not based on FWHM of the single-epoch emission line, I

tested the influence of FWHM by performing a partial correlation test (Akritas & Siebert, 1996). Namely, the presence of a correlation between λ_{Edd} and line shape is tested accounting for the common dependence on the FWHM. Table 3.10 lists the results of the partial correlation test. There is less than a 5% probability that this correlation is caused by the influence of FWHM. This test indicates that there is a true inverse correlation between λ_{Edd} and line shape and it is not an artifact of FWHM.

3.8.2 THE INTERPRETATION OF THE LINE SHAPE - EDDINGTON RATIO CORRELATION

The interpretation of the Eddington ratio – line shape inverse correlation is not straightforward, but it can be understood physically. If the mass accretion rate increases, the ionizing continuum increases and the ionization front moves outward - as also stated by the $R - L$ relationship (see also discussion in Chapter 2). If we consider the locally optimally emitting cloud (LOC) model (Baldwin et al., 1995), in which clouds have a broad range of density and distance from the central ionization radiation, the emission from a certain line will come from the gas that is most efficient at emitting that particular transition. If we assume that the BLR gas is evenly distributed, as the ionization front moves outward from the central continuum source, the distance to the line emitting region will move outward as well. As the distance from the central BH increases, the broad line gas is expected to have a lower velocity (Peterson & Wandel, 1999) and the line profile would be dominated by lower velocities and may have a stronger core and this might produce a more peaky profile. On the other hand, a positive correlation between the line shape and λ_{Edd} is hard to understand in this context, because it would mean that as the luminosity increases the line profile is dominated by higher velocities. But, of course this picture assumes that the black hole mass is constant. For example, from object to object if the black hole mass changes, a higher M_{BH} means higher velocities for a given radius.

When we look at somewhat larger samples of AGN the inverse correlation is clearly seen. Under the assumption that to first order the central engine structure is the same for all AGN, this can be understood because the general AGN population will then probe the BLR subjected to a wider range of Eddington ratios that clearly result in a significant change in line shapes. However, differences in inclination and slight variations in the BLR velocity structure between objects will introduce scatter in the trend.

3.8.3 IMPLICATIONS FOR BLACK HOLE MASS ESTIMATES

Ideally, we want to measure the velocity width of the intrinsically emitted emission-line that respond to continuum variations and that represents only the virial motions. As shown by Denney (2012) the non-variable emission-line components in CIV profiles strongly affect the black hole mass measurements. If more peaky profiles always have such a non-variable component, then the inverse correlation between the line shape and the Eddington luminosity ratio would mean that the BH masses of high Eddington ratio objects are underestimated. Unfortunately, even if we assume that the observed correlation between the line shape and Eddington ratio and its interpretation is real we can not directly use at this time to correct our line width measurements that we need for the black hole mass estimates. This is mainly because BLR is a complex region and in order to be able to account for such non-variable, non-virial velocity components we need kinematic models (e.g., Collin et al., 2006; Brewer et al., 2011; Kollatschny & Zetzl, 2011; Pancoast et al., 2013). However, kinematic modeling of the BLR is beyond the scope of this work and more work is needed to settle the kinematics of the BLR and its under-

lying physics.

3.8.4 UNCERTAINTIES IN THE BOLOMETRIC LUMINOSITIES

Uncertainties in the Mean Bolometric Corrections and Eddington Luminosity Ratios

Collin et al. (2006) found an anti-correlation between the mean $H\beta$ line shape and the Eddington ratio for 35 reverberation-mapped AGN. The line-width ratio range of their sample is $0.9 < FWHM/\sigma_{line} < 3.5$ and the λ_{Edd} range of their sample is between 0.003 and 0.7. Since their goal is to compare the mean $H\beta$ profiles with the mean Eddington ratio of each object, they estimate the mean Eddington ratios as $\lambda_{Edd} \sim 10 \times \lambda L(5100\text{\AA})/L_{Edd}$. For their purpose, applying a mean BC is the most practical solution because they have the mean $\lambda L(5100\text{\AA})$ measurements and they aim for a mean Eddington ratio for each source. If we ignore the statistical accuracy of the RM BH masses themselves, the largest uncertainty contribution to the Eddington ratio estimate is from the applied mean BC(5100\AA) which has a value of 10. If I consider the mean BC(5100\AA) given in the literature, the values obtained from the mean SEDs of large AGN samples are between ~ 8.0 and 13.0 (Elvis et al., 1994; Richards et al., 2006a; Runnoe et al., 2012). The standard deviation of these mean bolometric corrections are between 0.4 and 5.0, so the bolometric luminosity values estimated from these are uncertain by up to $\sim 50\%$. The uncertainty in the applied BC(5100\AA)= 10 is ~ 5.0 (Elvis et al., 1994), and as a result the bolometric luminosity estimates of Collin et al. (2006) are uncertain by up to $\sim 50\%$. If we consider relative Eddington ratio variations of individual objects, since the Eddington ratio changes will be driven by bolometric luminosity in this case we may ignore the mass uncertainties. In this case, the uncertainty in the Eddington ratio will be the uncertainty of the bolometric luminosity and if it depends on BC it will be up to $\sim 50\%$. However, if we compare Eddington ratio estimates between objects then the mass uncertainties dominate. If we consider the uncertainty of RM M_{BH} that is factor of 3 (Peterson et al., 2004), then the resultant uncertainty in the Eddington ratio becomes $\sim 300\%$. So, the Eddington ratio estimates are highly uncertain. This also emphasizes the need for more accurate M_{BH} estimates.

Interpolation vs. Modeling of the SEDs

Although I have optical, UV and X-ray spectral coverage for my SEDs I am still missing the most luminous part of the SED, the EUV, and I have three large gaps from $1\mu\text{m}$ to optical, optical to UV and UV to X-rays. I followed the most simple and common approach to fill these gaps, by just linearly interpolating between the available data. For the UV to X-ray gap I also applied a thermal bump model as an alternative option in order to test if this may provide an improved and more realistic and robust measurements of $L_{BOL}(acc)$. The comparison between these two approaches to fill in the UV to X-ray gap (§3.5.2) show that this may cause a difference in $L_{BOL}(acc)$ of up to 23%. This uncertainty is larger than the $L_{BOL}(acc)$ uncertainty originating from the optical, UV and X-ray continuum measurement uncertainties. In §A.4 I attempt to fit the SEDs with the *optxagnf* model (Done et al., 2012) and find that I am not able to perform a robust fit without the soft X-ray data showing evidence of a strong soft X-ray excess as commonly observed for NLS1s, only. Since the intrinsic SED shape of AGN is not theoretically well understood beyond the basic thin accretion disk picture, I rely on the observed data and simply interpolate the gaps and consider this as a reasonable approach to measure $L_{BOL}(acc)$. Even with the optical, UV and X-ray spectral coverage that I have, my lack of knowledge of the intrinsic SED at the EUV range brings a $\sim 23\%$ accuracy uncertainty to my $L_{BOL}(acc)$ estimates

alone. This is comparable to the level of the BC(5100Å) uncertainty that I wanted to eliminate ($\sim 20\% - 50\%$ Richards et al., 2006a; Elvis et al., 1994) by using single-epoch SEDs of my targets. Although I put a lot of effort into finding quasi-simultaneous multi-wavelength data in order to measure $L_{BOL}(acc)$ I am still having an uncertainty level of $\sim 23\%$ due to the uncertainty related to the EUV gap. This unknown EUV emission will always limit bolometric luminosity measurements, with this limitation in mind we can get better measurements of the data that we can measure. However, all studies of the SEDs and measurements of bolometric luminosity will be affected by the same uncertainty and unknown. Despite the unknown SED shape across the gaps, I still measure the continuum level in a homogenous, systematic way. So, at the very least for individual sources the $L_{BOL}(acc)$ variations are physically related to accretion rate changes. And, I have relatively better $L_{BOL}(acc)$ and thus Eddington ratio measurements compared to Collin et al. (2006).

Interpolation of the SEDs vs. Applying Mean Bolometric Corrections

In Figure 3.14 I show the $L_{BOL}(acc)$ measured from the SEDs versus the bolometric luminosity calculated by applying a constant mean BC(5100Å), $L_{BOL}(acc)(BC5100 = 10)$ (left panel) and mean BC(1350Å), $L_{BOL}(acc)(BC1350 = 4.2)$ (right panel). The typical uncertainty of the $L_{BOL}(acc)$ values measured directly from the SEDs is $\sim 22\%$ (this is estimated from the uncertainties of the continuum measurements themselves). The difference between the $L_{BOL}(acc)$ measured directly from the SEDs and $L_{BOL}(acc)(BC5100 = 10)$ or $L_{BOL}(acc)(BC1350 = 4.2)$ is different for each source. If I were to use a mean BC(5100Å) I would underestimate the bolometric luminosity by 31% and 55% for Fairall 9 and 3C390.3, respectively. The accuracy of $L_{BOL}(acc)$ calculated from a mean BC depends on the source, on average usage of a optical or UV BC may result in a underestimated/overestimated $L_{BOL}(acc)$ by a factor of $\sim 13-14\%$, but again the level of the difference can be between 2%–62%. This shows that for some objects, using a mean BC will either significantly under or over-estimate $L_{BOL}(acc)$. And it is unclear which objects do not follow the mean trend. NGC 5548 had large variations, yet have SEDs consistent with the mean BCs, while Fairall 9 does not. The typical uncertainty of the directly measured $L_{BOL}(acc)$ is $\sim 22\%$ (mainly due to the uncertainties of the continuum measurements themselves). This means, if using a BC brings an uncertainty up to 22%, this comparable to the uncertainty of the $L_{BOL}(acc)$ measured from the SED and the two bolometric luminosities agrees within 1σ error budget. But if the difference is above 22% and high as 62%, then this is a significant difference and can be accounted within 3σ error budget.

Effects of Source Variability

Time resolved $L_{BOL}(acc)$ variations give us an estimate on the expected effect of the intrinsic source variability and this is helpful to place a constrain on how much I can extend the time span over which the data are taken which are adopted for the SEDs. The mean bolometric luminosity variation within 20 days is about 10% and even for 80 days (the largest R_{BLR}/c in my sample) it does not exceed 18%. This indicates that if I were to combine the multi-wavelength data obtained within 20 days or 80 days, this would result in a $\sim 10\%$ or $\sim 18\%$ uncertainty in the $L_{BOL}(acc)$ measurements, respectively. So I could expand my quasi-simultaneous $\Delta T(SED)$ limit up to 80 days and obtain semi-simultaneous data and take into account a possible 18% uncertainty. The typical uncertainty in the $L_{BOL}(acc)$ measurements themselves are about 22% (this is mainly due to the uncertainties of the continuum measurements), and thus using semi-simultaneous data as I did for a couple of cases does not affect the $L_{BOL}(acc)$ measurements

significantly. That is, if a $\sim 20\%$ uncertainty is acceptable a ~ 80 day range of the database making up the SED would be possible on average.

3.9 SUMMARY AND CONCLUSIONS

I have presented quasi-simultaneous optical-to-X-ray SEDs of seven AGN from the RM sample of Peterson et al. (2004). I used these SEDs to directly measure the accretion luminosity and infer the Eddington ratio by using the RM based black hole masses. I have investigated the Eddington ratio – line shape relation for single-epoch $H\beta$ and C IV profiles. The main conclusions of this work are:

1. I use quasi-simultaneous optical, UV and X-ray data and linearly interpolate the SEDs to measure $L_{BOL}(acc)$. The applied linear interpolation provides a model independent first order approach to measuring $L_{BOL}(acc)$. Based on the range of possible and reasonable methods by which I can estimate the SED shape in the EUV range I estimate the uncertainty in the integrated $L_{BOL}(acc)$ to be of order $\sim 23\%$, caused by the unknown intrinsic SED shape in the EUV range. I attempted to model the SEDs with the *optxagnf* model of Done et al. (2012). However, without the presence of a soft X-ray excess I am unable to obtain a robust fit.
2. I confirm the existence of an anti-correlation between the Eddington ratio and the $H\beta$ $FWHM/\sigma_{line}$ ratio for the seven AGN in my sample. I have investigated the Eddington ratio – line shape trend for C IV profiles for the first time and found that for these seven AGN they do show a similar inverse correlation as $H\beta$. I interpret the observed anti-correlation as the effect of the ionizing front on the velocities of the line-emitting region. As the Eddington ratio increases, the ionizing front reaches larger regions that are dominated by lower velocities. Therefore, we expect to observe peaky profiles for high Eddington ratio objects.
3. I observe a similar inverse correlation between the $H\beta$ and C IV line shape and the Eddington ratio for a larger sample of quasars. Since the FWHM present in both parameters I performed a partial correlation analysis and found that this inverse correlation is not a artifact of FWHM entering the parameterization of both variables.
4. I have demonstrated that Eddington ratios based on a scaling from $\lambda L(1350\text{\AA})$ and $\lambda L(5100\text{\AA})$ give similar results as the Eddington ratios based on quasi-simultaneous optical, UV and X-ray data for my handful of nearby Seyfert 1 galaxies. Therefore, I conclude that quasi-simultaneous SEDs are not a requisite to examine the Eddington ratio – line shape relation for this small sample.
5. My analysis of the multi-epoch SED variations of individual objects show that typical L_{BOL} variations over 20 days is about 10% and the mean ΔL_{BOL} increases with the longer time differences. For my sample, the mean ΔL_{BOL} is about 29% over ~ 600 days. This indicates the effect of the intrinsic source variability on the bolometric luminosity and shows that using semi-simultaneous data may decrease the uncertainty from the typical 22% to only $\sim 10\%$. The highest uncertainty in the L_{BOL} measurements is my inability to extract the intrinsic SED especially in the EUV regime, the non-simultaneity of the data is a minor limitation in this particular context.

Table 3.1. Local Seyfert Sample

Object	Redshift ^a	$E(B - V)^a$	Distance ^b (Mpc)	Host Flux ^c (10^{-15} erg s ⁻¹ cm ⁻² Å ⁻¹)	Aperture ('' × '')	P.A. (°)	BH Mass ^d ($10^6 M_{\odot}$)
(1)	(2)	(3)	(4)	(5)	(6)	(7)	(8)
Fairall 9	0.04702	0.023	202.8±7.2	2.99 ± 0.15	4.0 × 9.0	0.0	255 ± 56.0
NGC 3783	0.00973	0.105	25.1±5.0	4.72 ± 0.47	5.0 × 10.0	0.0	29.8 ± 5.4
NGC 4151	0.00332	0.024	16.6±3.3	15.00 ± 1.40	5.0 × 7.5	90.0	13.3 ± 4.6
NGC 5548	0.01717	0.018	72.5±7.0	3.75 ± 0.38	5.0 × 7.5	90.0	67.1 ± 2.6
3C 390.3	0.05610	0.063	243.5±7.2	0.83 ± 0.04	5.0 × 7.5	90.0	287 ± 64.0
Mrk 509	0.03440	0.051	147.1±7.3	2.43 ± 0.12	5.0 × 7.6	90.0	143 ± 12.0
NGC 7469	0.01632	0.061	68.8±7.0	8.43 ± 0.78	5.0 × 7.5	90.0	12.2 ± 1.4

^aAdopted from NASA/IPAC Extragalactic Database (NED). $E(B-V)$ values are based on Schlafly & Finkbeiner (2011) dust maps.

^bDistances are computed from the redshifts (Wright, 2006); uncertainties of the distances are calculated assuming a 500 km s^{-1} uncertainty in the recession velocities (similar to Bentz et al., 2013). The distances of NGC 4151 and NGC 3783 are adopted from Bentz et al. (2013).

^cHost galaxy flux densities for the relevant aperture sizes (column 6) and positions (column 7) are adopted from Bentz et al. (2009a, 2013); Kilerci Eser et al. (2014).

^dBlack hole masses based on reverberation mapping analysis are adopted from Peterson et al. (2004).

Table 3.2. References for the Optical, UV and X-ray Data

Object	Optical Data ^a References	UV Data ^a References	X-ray Data ^a References
(1)	(2)	(3)	(4)
Fairall 9	1	11	Tartarus ^b
NGC 3783	2	12	18
NGC 4151 ^c	3, 4	13	19
NGC 5548	5, 6, 7	14, 15	15, 20, 21
3C 390.3	8	16	Tartarus ^b
Mrk 509	9	IUE archive ^d	22
NGC 7469 ^c	10, 4	17	23

^aReferences: (1) Santos-Lleo et al. (1997); (2) Stirpe et al. (1994); (3) Kaspi et al. (1996); (4) Kilerci Eser et al. (2014); (5) Peterson et al. (1991); (6) Peterson et al. (1992); (7) Peterson et al. (2013b); (8) Dietrich et al. (1998); (9) Carone et al. (1996); (10) Collier et al. (1998); (11) Rodriguez-Pascual et al. (1997); (12) Reichert et al. (1994); (13) Crenshaw et al. (1996); (14) Clavel et al. (1991); (15) Clavel et al. (1992); (16) O'Brien et al. (1998); (17) Wanders et al. (1997); (18) Alloin et al. (1995); (19) Warwick et al. (1996); (20) Nandra et al. (1991); (21) Magdziarz et al. (1998b); (22) Pounds et al. (1994); (23) Nandra et al. (2000).

^b<http://tartarus.gsfc.nasa.gov/>

^c See Kilerci Eser et al. (2014) for data selection and measurements.

^dNames of the used UV spectra are ads/Sa.IUE#swp39925 and #swp39926.

Table 3.3. Wavelength Windows for Optical, UV Continuum Fit

Object	Optical Continuum Windows(Å)	UV Continuum Windows(Å)
(1)	(2)	(3)
Fairall 9	4950-4970 & 5328-5352	1380-1390 & 1500-1520 & 1780-1810 & 1860-1900
NGC 3783	4800-4820 & 5130-5170	1350-1370 & 1450-1470 & 1710-1725 & 1800-1820
NGC 4151	4590-4610 & 5100-5125	1260-1290 & 1420-1460 & 1805-1835
NGC 5548	4790-4800 & 5182-5192	1350-1385 & 1445-1475 & 1710-1730 & 1845-1870
3C 390.3	4750-4790 & 5460-5470	1345-1385 & 1500-1520 & 1800-1830 & 1890-1910
Mrk 509	4905-4915 & 5270-5280	1380-1390 & 1500-1520 & 1780-1810 & 1860-1900
NGC 7469	4840-4890 & 5176-5200	1306-1327 & 1473-1495 & 1730-1750 & 1805-1835

Note. — Observed wavelengths are listed for the entire table. The second optical continuum window contains $5100\text{Å}(1+z)$ region.

Table 3.4 (cont'd)

Object (1)	SED Epoch (2)	R_{BLR}^a (days) (3)	JD ^b (-2400000) (4)	FWHM ^c (km s^{-1}) (5)	σ_{line}^c (km s^{-1}) (6)	FWHM/ σ_{line}^c (7)	Variable Line ¹ Limits (\AA) (8)	σ_{line}^d (km s^{-1}) (9)	FWHM/ σ_{line}^d (10)
Mrk 509	2	79.60 ^{+6.10} -6.10	49881.0	5821.8 \pm 2669.5	3316.6 \pm 428.4	1.76 \pm 0.84	4770.3–4974.9	3365.5 \pm 89.0	1.73 \pm 0.79
NGC 7469	1	11.70 ^{+0.50} -0.70	48230.0 ^e	2788.6 \pm 33.9	1548.0 \pm 76.7	1.80 \pm 0.09	4789.2–4945.9	1543.8 \pm 65.9	1.81 \pm 0.08
	1	...	50260.2	1711.6 \pm 163.0	1792.3 \pm 264.0	0.95 \pm 0.10	4794.0–4955.0	1803.9 \pm 288.0	0.94 \pm 0.17
	2
	3	...	50274.5	1177.4 \pm 143.0	1845.3 \pm 342.0	0.60 \pm 0.10	4787.0–4969.0	1922.6 \pm 634.0	0.50 \pm 0.20
	4	...	50285.5	1267.8 \pm 212.0	1866.3 \pm 705.0	0.67 \pm 0.20	4794.0–4955.0	1863.6 \pm 818.0	0.68 \pm 0.31

Note. — Spectra are matched with the SEDs by accounting the light travel time between the accretion disk and BLR such that Spectrum JD=SED epoch + R_{BLR} (H β). Since FWHM is not sensitive to line limits it is the same for the fixed and the variable line limits, therefore I do not list FWHM for the variable line limits.

^a Result from RM analysis. R_{BLR} is only listed in the first entry for each object since it is the same.

^b Spectrum JD. No entry (...) means that no appropriate spectrum was available at this epoch.

^c Measured based on the fixed line limits. In the rest frame they are: NGC5548: 4763–4951 \AA , NGC7469: 4791–4949 \AA , NGC4151: 4769–4949 \AA , 3C390.3: 4740–4967 \AA , NGC3783: 4764–4945 \AA .

^d Measured based on the variable line limits.

^e For Mrk 509 there is no available spectrum taken 80 days after the SED epoch. Instead I use the nearest available optical spectrum that is obtained 42 days after the SED epoch.

Table 3.5. CIV Line Line Width and Line Shape Measurements

Object	SED Epoch (2)	R_{BLR}^a (days) (3)	JD ^b (-2400000) (4)	FWHM ^c (km s^{-1}) (5)	σ_{line}^c (km s^{-1}) (6)	FWHM/ σ_{line}^c (7)	Variable Line ^d Limits (Å) (8)	σ_{line}^d (km s^{-1}) (9)	FWHM/ σ_{line}^d (10)
Fairall 9	1	$29.60^{+12.90}_{-14.40}$	49497.8	1852.3 ± 51.0	3410.9 ± 276.6	0.54 ± 0.05	1492.8–1617.6	3759.7 ± 463.0	0.49 ± 0.06
	2		49511.0	2907.3 ± 91.8	3667.0 ± 242.4	0.79 ± 0.06	1512.0–1604.8	3263.7 ± 236.0	0.89 ± 0.07
	3		49515.0	2531.4 ± 306.8	3593.6 ± 256.3	0.70 ± 0.10	1504.0–1617.6	3976.5 ± 325.8	0.64 ± 0.09
	4		49518.8	2042.4 ± 531.2	3149.3 ± 709.1	0.65 ± 0.22	1497.6–1596.8	3045.0 ± 664.1	0.67 ± 0.23
	5		49524.0	2661.1 ± 97.4	3651.2 ± 204.5	0.73 ± 0.05	1512.0–1604.8	3317.7 ± 185.4	0.80 ± 0.05
	6		49530.5	2213.9 ± 57.6	3340.3 ± 292.4	0.66 ± 0.06	1504.0–1604.8	3303.1 ± 283.5	0.67 ± 0.06
	7		49537.5	2399.8 ± 108.5	2863.0 ± 690.5	0.84 ± 0.21	1492.8–1606.4	2625.8 ± 1019.8	0.91 ± 0.36
	8		49542.5	2363.8 ± 310.7	3303.6 ± 681.9	0.72 ± 0.18	1496.0–1627.3	3723.6 ± 1285.9	0.63 ± 0.23
	9		49546.5	2924.0 ± 126.4	3408.1 ± 203.3	0.86 ± 0.06	1502.4–1596.8	3220.2 ± 163.8	0.91 ± 0.06
	10								
	11		49561.8	2792.3 ± 144.6	3498.8 ± 403.1	0.80 ± 0.10	1505.6–1596.8	3231.1 ± 303.0	0.86 ± 0.09
	12		49565.8	2949.1 ± 146.6	3380.4 ± 385.3	0.87 ± 0.11	1492.8–1596.8	3333.2 ± 411.5	0.88 ± 0.12
	13								
	14								
	15		49577.5	4948.1 ± 331.0	3789.6 ± 235.6	1.31 ± 0.12	1502.4–1595.2	3534.2 ± 180.0	1.40 ± 0.12
	16		49589.5	2368.0 ± 68.8	3549.3 ± 180.7	0.67 ± 0.04	1489.6–1619.3	4215.4 ± 298.0	0.56 ± 0.04
	17		49597.2	2111.2 ± 96.1	2751.6 ± 637.6	0.77 ± 0.18	1497.6–1596.8	2666.7 ± 592.0	0.79 ± 0.18
	18		49609.5	2818.5 ± 125.0	3372.2 ± 375.0	0.84 ± 0.10	1512.0–1596.8	3033.4 ± 232.1	0.93 ± 0.08
	19		49617.5	2216.2 ± 175.5	3406.2 ± 509.1	0.65 ± 0.11	1489.6–1595.2	3439.6 ± 547.7	0.64 ± 0.11
	20		49623.5	2389.7 ± 776.9	3586.0 ± 294.1	0.67 ± 0.22	1491.2–1604.8	3623.4 ± 413.4	0.66 ± 0.23
	21								
22									
23									
24		49653.5	2318.1 ± 129.9	3192.6 ± 516.9	0.73 ± 0.12	1500.8–1588.8	2919.8 ± 347.5	0.79 ± 0.10	
25									
26									
27									
NGC 3783	1	$3.80^{+1.00}_{-0.60}$	48805.2	2456.6 ± 34.0	3172.6 ± 176.0	0.77 ± 0.04	1501.0–1596.8	2969.0 ± 152.0	0.80 ± 0.04
NGC 4151	1	$0.42^{+0.10}_{-0.10}$	49327.5	4745.7 ± 54.8	4274.6 ± 56.4	1.11 ± 0.02	1492.6–1603.9	4469.9 ± 69.6	1.06 ± 0.02
	2								
	3		49329.0	4700.1 ± 63.0	4305.9 ± 61.6	1.09 ± 0.02	1489.3–1607.3	4661.4 ± 89.9	1.01 ± 0.02
	4		49331.5	4874.5 ± 89.5	4307.9 ± 64.7	1.13 ± 0.03	1489.3–1613.9	4788.9 ± 115.4	1.02 ± 0.03
NGC 5548	1	$10.00^{+2.00}_{-2.00}$	47543.0	3851.4 ± 76.1	3686.5 ± 161.6	1.04 ± 0.05	1489.4–1603.5	3834.1 ± 214.6	1.00 ± 0.06
NGC 5548	2	$10.00^{+2.00}_{-2.00}$	47565.0	3683.9 ± 63.0	3547.8 ± 168.0	1.02 ± 0.05	1472.7–1596.5	3486.3 ± 171.0	1.04 ± 0.05
	3		47696.0	4135.5 ± 59.0	3708.0 ± 136.0	1.11 ± 0.04	1472.7–1614.3	3970.5 ± 242.0	1.04 ± 0.06
	4		47729.0	5103.7 ± 43.0	3539.9 ± 135.0	1.44 ± 0.06	1490.4–1620.2	4049.5 ± 251.8	1.26 ± 0.08
	5	$6.00^{+2.00}_{-2.00}$	48041.0	2934.1 ± 795.0	3505.7 ± 222.4	0.84 ± 0.23	1503.6–1612.4	3521.2 ± 309.7	0.83 ± 0.24
	6		48048.5	4297.1 ± 424.4	3684.7 ± 173.1	1.17 ± 0.13	1492.1–1609.1	3921.4 ± 249.8	1.10 ± 0.13
	7		48055.5	2560.9 ± 51.5	3458.6 ± 266.9	0.74 ± 0.06	1492.1–1592.6	3473.7 ± 233.3	0.74 ± 0.05
	8		48062.5	3459.8 ± 59.5	3630.0 ± 178.0	0.95 ± 0.05	1492.1–1602.5	3687.9 ± 221.4	0.94 ± 0.06

Table 3.5 (cont'd)

Object	SED Epoch (2)	R_{BLR}^a (days) (3)	JD ^b (-2400000) (4)	FWHM ^c (km s ⁻¹) (5)	σ_{line}^c (km s ⁻¹) (6)	FWHM/ σ_{line}^c (7)	Variable Line ¹ Limits (Å) (8)	σ_{line}^d (km s ⁻¹) (9)	FWHM/ σ_{line}^d (10)
	9		48068.8	2517.5±368.7	3451.5±165.0	0.73±0.11	1502.0-1609.1	3328.1±229.2	0.76±0.12
	10		48076.8	1623.2±193.5	3322.4±247.6	0.49±0.07	1500.3-1620.6	3395.6±482.8	0.48±0.09
	11	
	12	10.00 ^{+2.00} _{-2.00}	47517.0	5374.5±45.3	3829.0±114.4	1.40±0.04	1490.4-1616.2	4488.7±176.9	1.20±0.05
	13		47522.0	4135.5±53.7	3876.9±133.6	1.07±0.04	1490.4-1616.2	4517.7±210.1	0.92±0.04
	14		47526.0	3897.6±59.8	3862.1±142.1	1.01±0.04	1490.4-1620.2	4474.6±260.1	0.87±0.05
	15		47530.0	4409.1±46.4	3502.7±186.3	1.26±0.07	1490.4-1596.6	3514.7±201.5	1.25±0.07
	16		47534.0	5003.5±57.2	3577.0±190.5	1.40±0.08	1498.3-1606.4	3734.6±214.3	1.34±0.08
	17		47538.0	4621.2±124.7	3667.3±196.9	1.26±0.08	1490.4-1596.6	3597.9±224.0	1.28±0.09
	18		47549.0	4890.4±57.1	3765.1±136.3	1.30±0.05	1489.4-1617.2	4502.3±213.4	1.09±0.05
	19	
	20		47561.0	3723.3±69.1	3724.5±102.6	1.00±0.03	1490.4-1616.2	4254.1±167.9	0.88±0.04
	21	
	22		47586.0	3239.5±46.1	3809.9±133.0	0.85±0.03	1490.4-1620.2	4223.7±273.5	0.77±0.05
	23		47594.0	2969.6±53.0	3614.7±155.6	0.82±0.04	1500.2-1600.5	3555.0±145.4	0.84±0.04
	24		47602.0	3914.8±143.1	3632.1±170.5	1.08±0.06	1490.4-1622.1	4072.8±355.3	0.96±0.09
	25	
	26		47613.0	4964.2±194.0	3709.5±208.4	1.34±0.09	1490.4-1616.2	4245.9±337.1	1.17±0.10
	27		47625.0	5288.6±59.8	3909.2±101.6	1.35±0.04	1498.3-1616.2	4212.4±156.9	1.26±0.05
	28	
	29	
	30	
	31		47669.0	5190.9±126.6	3556.5±164.4	1.46±0.08	1490.4-1600.5	3646.4±194.3	1.42±0.08
	32		47673.0	4893.9±38.3	3716.1±134.4	1.32±0.05	1488.4-1608.4	4062.1±193.6	1.20±0.06
	33		47677.0	5521.1±97.2	3814.0±111.9	1.45±0.05	1490.4-1620.2	4305.1±220.4	1.28±0.07
	34		47680.0	3500.0±47.3	3708.5±110.1	0.94±0.03	1492.4-1622.1	4115.4±227.0	0.85±0.05
	35	10.00 ^{+2.00} _{-2.00}	47685.0	3547.9±46.6	3796.5±129.7	0.93±0.03	1490.4-1610.3	4049.6±203.3	0.88±0.05
	36		47688.0	5049.4±75.6	3575.0±170.0	1.41±0.07	1490.4-1622.1	3916.8±371.5	1.29±0.12
	37	
	38		47700.0	4689.9±74.1	3519.4±150.1	1.33±0.06	1500.2-1600.5	3477.1±138.9	1.35±0.06
	39		47709.0	3675.4±44.9	3408.1±190.3	1.08±0.06	1500.2-1596.6	3228.2±162.7	1.14±0.06
	40		47717.0	5159.5±86.9	3563.8±184.3	1.45±0.08	1492.4-1604.4	3682.7±232.6	1.40±0.09
	41		47721.2	2938.6±36.8	3905.3±111.2	0.75±0.02	1490.4-1614.3	4431.7±174.4	0.66±0.03
	42		47725.0	4932.7±119.2	3530.0±130.0	1.40±0.06	1488.4-1620.2	4079.4±246.9	1.21±0.08
	43		47729.0	5103.7±43.0	3539.9±135.0	1.44±0.06	1490.4-1620.2	4049.5±251.8	1.26±0.08
	44		47737.0	3887.2±41.7	3064.1±217.5	1.27±0.09	1496.3-1614.3	2976.5±380.9	1.31±0.17
	45	
	46		47745.0	2671.5±69.2	3346.2±266.5	0.80±0.07	1494.3-1620.2	3558.1±516.7	0.75±0.11
	47	
3C 390.3	1	35.70 ^{+11.40} _{-14.60}

Table 3.5 (cont'd)

Object	SED Epoch (2)	R_{BLR}^a (days) (3)	JD ^b (-2400000) (4)	FWHM ^c (km s^{-1}) (5)	σ_{line}^c (km s^{-1}) (6)	FWHM/ σ_{line}^c (7)	Variable Line ¹ Limits (\AA) (8)	σ_{line}^d (km s^{-1}) (9)	FWHM/ σ_{line}^d (10)
Mrk 509 NGC 7469	2		49897.8	4049.6 \pm 71.0	4041.7 \pm 278.0	1.00 \pm 0.07	1492.6–1584.7	3294.0 \pm 316.0	1.23 \pm 0.12
	1		48188.2 ^e	4590.3 \pm 215.7	3002.1 \pm 352.0	1.53 \pm 0.19	1494.8–1595.3	2838.8 \pm 357.5	1.62 \pm 0.22
	1	10.60 ^{+0.20} _{-0.20}	50259.0	3096.5 \pm 63.4	3096.6 \pm 207.6	0.90 \pm 0.07	1499.5–1606.7	3168.8 \pm 228.8	0.97 \pm 0.07
	2		50264.2	2988.8 \pm 65.5	2843.8 \pm 326.1	1.05 \pm 0.12	1491.6–1605.7	2779.6 \pm 466.3	1.07 \pm 0.18
	3		50273.8	3384.6 \pm 37.8	3332.0 \pm 131.4	1.02 \pm 0.04	1497.6–1620.6	3998.7 \pm 177.5	0.85 \pm 0.04
	4		50284.0	3185.8 \pm 92.0	2999.0 \pm 298.0	1.06 \pm 0.11	1488.7–1607.8	3176.7 \pm 437.0	1.00 \pm 0.14

Note. — Spectra are matched with the SEDs by accounting the light travel time between the accretion disk and the BLR: Spectrum JD=SED epoch + R_{BLR} (CIV). For (a), (b), (d) and (1) see footnotes of Table 3.4.

^c Measured from fixed 10000 km s^{-1} line limits.

^e For Mrk 509 there are no UV monitoring data and therefore I do not know the R_{BLR} (CIV). To match a UV spectrum with the SED, I use the same UV spectrum that I used for the SED.

Table 3.6. SED Epochs, Bolometric Luminosities, Eddington Ratios, Continuum Luminosities, and Bolometric Corrections.

Object	Epoch Number	SED JD (-2400000)	$\log[L_{BOL}(\text{interpolation})]^a$	Eddington ratio ^b (λ_{Edd})	$\log(\lambda_{\Lambda, 5100 \text{ \AA}})$	$BC(5100)^c$	$\log(\lambda_{\Lambda, 1350 \text{ \AA}})$	$BC(1350)^c$	$\log(L_{2-10\text{keV}})$	$BC(2-10\text{keV})^c$
(1)	(2)	(3)	(4)	(5)	(6)	(7)	(8)	(9)	(10)	(11)
Fairall 9	1	49473.0-49475.5 ^d	44.94 ^{+0.06}	0.027 ^{+0.001}	43.83 ^{+0.06}	13.14 ^{+1.86}	44.22 ^{+0.07}	5.25 ^{+0.93}	44.02 ^{+0.05}	8.33 ^{+0.95}
	2	49477.0-49479.5 ^d	44.96 ^{+0.06}	0.028 ^{+0.006}	43.83 ^{+0.06}	13.48 ^{+2.08}	44.24 ^{+0.07}	5.15 ^{+0.93}	44.02 ^{+0.05}	8.54 ^{+1.99}
	3	49482.6-49484.5 ^d	44.97 ^{+0.06}	0.029 ^{+0.001}	43.79 ^{+0.05}	15.10 ^{+3.25}	44.28 ^{+0.05}	4.89 ^{+0.64}	44.02 ^{+0.08}	8.84 ^{+2.74}
	4	49486.6-49487.5 ^d	44.98 ^{+0.05}	0.029 ^{+0.000}	43.78 ^{+0.04}	15.71 ^{+3.78}	44.30 ^{+0.06}	4.81 ^{+0.67}	44.03 ^{+0.05}	8.95 ^{+2.04}
	5	49490.0-49491.5 ^d	44.96 ^{+0.05}	0.028 ^{+0.006}	43.82 ^{+0.04}	13.76 ^{+3.37}	44.26 ^{+0.06}	5.03 ^{+0.71}	44.03 ^{+0.05}	8.64 ^{+2.09}
	6	49497.0-49499.5 ^d	45.01 ^{+0.06}	0.031 ^{+0.000}	43.82 ^{+0.12}	15.46 ^{+6.25}	44.34 ^{+0.06}	4.64 ^{+0.66}	44.03 ^{+0.05}	9.54 ^{+1.10}
	7	49510.0-49511.5 ^d	45.07 ^{+0.05}	0.036 ^{+0.001}	43.85 ^{+0.04}	16.44 ^{+1.52}	44.44 ^{+0.06}	4.23 ^{+0.55}	44.03 ^{+0.05}	10.95 ^{+1.33}
	8	49514.0-49515.5 ^d	45.02 ^{+0.05}	0.032 ^{+0.006}	43.82 ^{+0.03}	15.87 ^{+3.57}	44.36 ^{+0.06}	4.55 ^{+1.18}	44.03 ^{+0.05}	9.76 ^{+1.84}
	9	49518.0-49519.5 ^d	45.05 ^{+0.08}	0.034 ^{+0.001}	43.85 ^{+0.03}	15.67 ^{+1.41}	44.41 ^{+0.10}	4.38 ^{+1.13}	44.03 ^{+0.05}	10.42 ^{+1.30}
	10	49523.0-49524.5 ^d	45.09 ^{+0.04}	0.038 ^{+0.008}	43.87 ^{+0.04}	16.66 ^{+3.89}	44.48 ^{+0.04}	4.12 ^{+0.96}	44.03 ^{+0.05}	11.66 ^{+2.89}
	11	49530.0-49531.5 ^d	45.04 ^{+0.05}	0.034 ^{+0.000}	43.86 ^{+0.03}	14.98 ^{+3.34}	44.39 ^{+0.06}	4.47 ^{+0.64}	44.03 ^{+0.05}	10.15 ^{+1.22}
	12	49533.0-49535.5 ^d	45.04 ^{+0.04}	0.034 ^{+0.001}	43.84 ^{+0.03}	15.84 ^{+1.06}	44.39 ^{+0.06}	4.43 ^{+0.52}	44.03 ^{+0.05}	10.24 ^{+1.25}
	13	49537.0-49539.5 ^d	44.99 ^{+0.05}	0.030 ^{+0.000}	43.81 ^{+0.04}	15.27 ^{+3.57}	44.31 ^{+0.06}	4.80 ^{+1.25}	44.03 ^{+0.05}	9.05 ^{+1.05}
	14	49542.0-49543.5 ^d	45.00 ^{+0.10}	0.031 ^{+0.002}	43.84 ^{+0.03}	14.49 ^{+1.23}	44.32 ^{+0.14}	4.77 ^{+1.87}	44.03 ^{+0.05}	9.36 ^{+2.14}
	15	49546.0-49547.5 ^d	45.00 ^{+0.09}	0.031 ^{+0.006}	43.79 ^{+0.03}	16.04 ^{+3.34}	44.32 ^{+0.14}	4.71 ^{+2.39}	44.03 ^{+0.05}	9.24 ^{+2.85}
	16	49559.0-49561.5 ^d	44.96 ^{+0.06}	0.028 ^{+0.001}	43.78 ^{+0.03}	15.12 ^{+3.62}	44.26 ^{+0.08}	4.99 ^{+1.05}	44.03 ^{+0.05}	9.24 ^{+2.06}
	17	49565.0-49567.5 ^d	45.01 ^{+0.06}	0.032 ^{+0.000}	43.83 ^{+0.05}	15.08 ^{+1.67}	44.34 ^{+0.07}	4.65 ^{+0.84}	44.03 ^{+0.05}	8.53 ^{+2.13}
	18	49577.0-49579.5 ^d	45.01 ^{+0.06}	0.032 ^{+0.000}	43.80 ^{+0.02}	13.12 ^{+2.98}	44.33 ^{+0.07}	4.78 ^{+0.87}	44.04 ^{+0.05}	9.48 ^{+1.13}
	19	49589.0-49591.5 ^d	45.05 ^{+0.05}	0.035 ^{+0.001}	43.89 ^{+0.02}	14.80 ^{+3.50}	44.41 ^{+0.05}	4.41 ^{+0.60}	44.04 ^{+0.05}	9.40 ^{+2.31}
	20	49593.0-49595.5 ^d	45.08 ^{+0.05}	0.037 ^{+0.008}	43.95 ^{+0.03}	13.47 ^{+3.32}	44.44 ^{+0.05}	4.36 ^{+1.17}	44.04 ^{+0.05}	11.05 ^{+2.60}
	21	49597.0-49599.5 ^d	45.09 ^{+0.04}	0.038 ^{+0.002}	43.88 ^{+0.04}	16.16 ^{+1.65}	44.47 ^{+0.04}	4.17 ^{+0.40}	44.04 ^{+0.05}	11.26 ^{+1.45}
22	49607.5-49609.3 ^d	45.07 ^{+0.06}	0.037 ^{+0.000}	44.00 ^{+0.02}	11.90 ^{+0.49}	44.43 ^{+0.07}	4.45 ^{+0.78}	44.04 ^{+0.07}	10.84 ^{+2.60}	
23	49617.0-49619.5 ^d	45.04 ^{+0.05}	0.034 ^{+0.001}	43.94 ^{+0.03}	12.55 ^{+2.72}	44.37 ^{+0.05}	4.66 ^{+1.10}	44.04 ^{+0.05}	10.60 ^{+2.34}	
24	49623.0-49624.5 ^d	45.07 ^{+0.05}	0.036 ^{+0.001}	43.94 ^{+0.03}	13.30 ^{+0.84}	44.42 ^{+0.05}	4.45 ^{+0.58}	44.04 ^{+0.05}	10.00 ^{+1.35}	
25	49653.0-49653.5 ^d	45.24 ^{+0.04}	0.054 ^{+0.008}	44.10 ^{+0.03}	13.70 ^{+3.26}	44.68 ^{+0.04}	3.63 ^{+0.91}	44.04 ^{+0.05}	15.64 ^{+3.94}	
26	49664.0-49665.5 ^d	45.25 ^{+0.04}	0.055 ^{+0.004}	44.10 ^{+0.02}	14.03 ^{+3.03}	44.69 ^{+0.03}	3.60 ^{+0.38}	44.04 ^{+0.05}	15.95 ^{+3.86}	
27	49712.5-49724.2 ^e	45.18 ^{+0.04}	0.047 ^{+0.005}	44.07 ^{+0.02}	12.86 ^{+1.37}	44.62 ^{+0.05}	3.61 ^{+0.93}	43.97 ^{+0.03}	16.22 ^{+3.86}	
NGC 3783	1	48801.0-48802.5 ^f	43.56 ^{+0.05}	0.001 ^{+0.000}	42.62 ^{+0.06}	8.71 ^{+1.44}	43.06 ^{+0.03}	3.17 ^{+0.34}	41.91 ^{+0.07}	43.92 ^{+8.79}
	2	48802.0-48803.5 ^f	43.95 ^{+0.02}	0.053 ^{+0.019}	42.96 ^{+0.01}	9.74 ^{+0.89}	43.34 ^{+0.03}	4.02 ^{+0.42}	42.91 ^{+0.01}	10.84 ^{+0.98}
NGC 4151	1	49326.0-49327.0	43.94 ^{+0.02}	0.052 ^{+0.019}	42.97 ^{+0.01}	9.37 ^{+1.07}	43.39 ^{+0.02}	3.60 ^{+0.69}	42.86 ^{+0.01}	12.04 ^{+1.25}
	2	49327.4-49328.0	43.96 ^{+0.02}	0.054 ^{+0.019}	42.96 ^{+0.01}	9.93 ^{+0.92}	43.35 ^{+0.02}	4.04 ^{+0.41}	42.94 ^{+0.01}	10.55 ^{+0.97}
	3	49328.5-49329.5	43.92 ^{+0.02}	0.050 ^{+0.021}	42.96 ^{+0.01}	9.10 ^{+1.67}	43.32 ^{+0.02}	3.97 ^{+0.70}	42.87 ^{+0.01}	11.39 ^{+1.77}
NGC 5548	1	47534.0-47536.0	44.31 ^{+0.04}	0.028 ^{+0.001}	43.36 ^{+0.02}	8.91 ^{+0.58}	43.68 ^{+0.05}	4.19 ^{+0.58}	43.39 ^{+0.01}	9.61 ^{+0.42}
	2	47555.0-47557.2	44.38 ^{+0.03}	0.033 ^{+0.002}	43.23 ^{+0.03}	14.09 ^{+1.33}	43.67 ^{+0.05}	5.12 ^{+0.70}	43.56 ^{+0.00}	6.67 ^{+0.39}
	3	47684.0-47685.5	44.28 ^{+0.04}	0.026 ^{+0.001}	43.28 ^{+0.05}	9.97 ^{+1.25}	43.52 ^{+0.06}	5.82 ^{+1.34}	43.48 ^{+0.00}	6.31 ^{+0.20}
	4	47719.0-47721.3	44.39 ^{+0.04}	0.034 ^{+0.001}	43.33 ^{+0.03}	11.44 ^{+2.06}	43.65 ^{+0.06}	5.47 ^{+0.77}	43.53 ^{+0.02}	7.11 ^{+0.31}
	5	48035.7-48036.7	44.21 ^{+0.06}	0.023 ^{+0.005}	43.08 ^{+0.08}	13.43 ^{+1.95}	43.45 ^{+0.06}	5.78 ^{+1.72}	43.41 ^{+0.03}	6.31 ^{+1.35}
	6	48040.0-48041.0	44.26 ^{+0.05}	0.025 ^{+0.001}	43.13 ^{+0.11}	13.41 ^{+3.95}	43.54 ^{+0.06}	5.29 ^{+1.24}	43.41 ^{+0.03}	7.17 ^{+0.46}
	7	48047.0-48048.5	44.20 ^{+0.05}	0.022 ^{+0.000}	43.11 ^{+0.05}	12.48 ^{+1.69}	43.49 ^{+0.07}	5.23 ^{+0.92}	43.32 ^{+0.03}	7.66 ^{+0.51}
	8	48054.3-48056.0	44.30 ^{+0.05}	0.027 ^{+0.001}	43.11 ^{+0.05}	15.31 ^{+3.40}	43.51 ^{+0.09}	6.08 ^{+1.35}	43.52 ^{+0.02}	5.93 ^{+0.28}

Table 3.6 (cont'd)

Object	Epoch Number (2)	SED ID (-2400000) (3)	$\log[L_{BOL}(\text{interpolation})]$ ^a (4)	Eddington ratio ^b (λ_{Edd}) (5)	$\log(\lambda L_{\lambda}(5100 \text{ \AA}))$ (6)	$BC(5100)$ ^c (7)	$\log(\lambda L_{\lambda}(1350 \text{ \AA}))$ (8)	$BC(1350)$ ^c (9)	$\log(L_{2-10\text{keV}})$ (10)	$BC(2-10\text{keV})$ ^c (11)
	2	49842.5-49861.0 ^e	44.93+0.09 -0.08	0.029+0.004 -0.006	43.57+0.07 -0.07	23.06+5.41 -6.00	43.93+0.17 -0.17	10.03+5.02 -5.35	44.35+0.03 -0.03	3.87+0.65 -0.78
Mrk 509	1	48187.0-48188.3	45.20+0.05	0.096+0.018	44.18+0.01	10.66+2.04	44.59+0.07	4.13+0.04	44.12+0.03	12.16+0.74
NCG 7469	1	50248.0-50249.0	44.38+0.03	0.194+0.007	43.30+0.06	12.05+1.90	43.71+0.03	4.63+0.38	43.34+0.00	10.83+0.17
	2	50253.0-50254.0	44.20+0.03	0.130+0.004	43.20+0.08	10.00+2.00	43.55+0.04	4.53+0.44	43.18+0.00	10.64+0.08
	3	50262.0-50263.0	44.39+0.04	0.199+0.008	43.24+0.07	14.08+2.57	43.75+0.03	4.31+0.25	43.30+0.00	12.27+1.84
	4	50273.0-50274.0	44.24+0.04	0.141+0.005	43.20+0.08	11.10+2.22	43.57+0.03	4.64+0.36	43.20+0.00	11.07+1.69

^a Bolometric Luminosity measured from linearly interpolated SED between $1 \mu\text{m} - 10 \text{ KeV}$.

^b Eddington ratio calculated as $\lambda_{Edd} = L_{BOL}(\text{interpolation})/L_{Edd}$ where $L_{Edd} = M_{BH} \times 1.3 \times 10^{38}$.

^c Bolometric correction for the stated monochromatic luminosity is calculated as $L_{BOL}(\text{interpolation}) = BC(\lambda) \times \lambda L_{\lambda}$.

^d Only the optical and UV data is simultaneous at this epoch. X-ray flux is estimated based on the available observations, see §3.3.2 for details.

^e Only the X-ray and UV data is simultaneous at this epoch. The optical data is from JD 2449724.

^f The X-ray flux is extrapolated from 0.1 KeV - 2 keV band to 2 keV - 10 keV by assuming the same x-ray spectral slope.

^g The optical and UV data are simultaneous at JD 2449861 whereas the X-ray data is from JD 2449842.

Table 3.7. Basic Statistics of L_{BOL} (interpolation), Eddington Ratios and Bolometric Corrections.

Object	Mean $\lambda L(1350)$ ($10^{43} \text{ erg s}^{-1}$)	$\lambda L(1350)$ rms variation ^a (%)	Mean $\lambda L(5100)$ ($10^{43} \text{ erg s}^{-1}$)	$\lambda L(5100)$ rms variation ^a (%)	Mean $\log(L_{\text{BOL}})$ ^b	L_{BOL} (interpolation) rms variation ^a (%)	Mean λ_{Edd}	λ_{Edd} rms variation ^a (%)	Mean BC(5100Å)	BC(5100Å) rms variation ^a (%)	Mean BC(1350Å)	BC(1350Å) rms variation ^a (%)	Mean BC(2-10 keV)	BC(2-10 keV) rms variation ^a (%)
Fairall19	25.56±8.35	32.7	7.77±1.89	24.4	45.04±0.08	20.1	0.035±0.007	20.5	14.59±1.31	9.0	4.52±0.43	9.5	10.48±2.16	20.6
NGC 4151	2.24±0.15	6.9	0.92±0.01	1.16	43.94±0.02	3.7	0.052±0.002	3.3	9.53±0.37	3.9	3.91±0.21	5.3	11.20±0.66	5.9
NGC 5548 ^c	3.17±1.18	37.0	1.46±0.48	32.9	44.20±0.16	32.4	0.023±0.008	32.5	11.70±2.14	18.3	5.49±0.61	11.1	7.00±1.16	16.5
NGC 5548 ^d	3.83±1.24	32.2	1.88±0.45	24.0	44.29±0.11	22.1	0.028±0.006	22.1	10.84±1.37	12.7	5.49±0.84	15.2	6.99±1.12	16.1
3C 390.3	6.29±3.14	49.9	3.03±0.97	32.0	44.81±0.17	38.1	0.023±0.008	36.9	22.18±1.24	5.6	11.03±1.41	12.8	3.67±0.28	7.5
NGC 7469	4.50±1.03	22.9	1.73±0.19	11.2	44.30±0.10	21.3	0.166±0.036	21.4	11.81±1.73	14.7	4.53±0.15	3.4	11.20±0.73	6.5
All Sample ^e	7.60±8.90	117.1	2.80±2.53	91.0	44.53±0.40	91.7	0.038±0.031	82.8	12.24±2.71	22.2	5.15±1.27	24.7	8.89±4.54	51.1

Note. — Mean measurements are listed with standard deviations with respect to the mean.

^aThe rms variation, σ , from the previous column is expressed as the percent deviation relative to the mean.

^b $\log[L_{\text{BOL}}(\text{interpolation})/\text{erg s}^{-1}]$.

^cBased only on the SEDs with simultaneous Optical, UV and X-ray data.

^dIncludes all available SEDs presented in this work.

^eIncludes the measurements of the 86 individual SEDs.

Table 3.8. Comparison of SED Measurements with Literature Studies in the Literature.

Object	Elvis et al. (1994)	SED Integration Range	Vasudevan & Fabian (2009) ^a	SED Integration Range	Grupe et al. (2010)	SED Integration Range	Runnoe et al. (2012)	SED Integration Range
$-\log(L_{\text{BOL}}/\text{ergs}^{-1})$								
Fairall9	$45.50^{+0.14}_{-0.15}$	$1\mu\text{m}-10\text{keV}$	44.8	$1\mu\text{m}-100\text{keV}$
NGC 4151	44.1	$1\mu\text{m}-100\text{keV}$
NGC 5548	44.3	$1\mu\text{m}-100\text{keV}$	43.26	$1\mu\text{m} - 2\text{keV}$
3C 390.3	45.2	$1\mu\text{m}-100\text{keV}$
NGC 7469	44.8	$1\mu\text{m}-100\text{keV}$
NGC 3783	44.2	$1\mu\text{m}-100\text{keV}$
Mrk 509	45.2	$1\mu\text{m}-100\text{keV}$	45.36	$1\mu\text{m} - 8\text{keV}$
$\text{BC}(2 - 10\text{keV})$								
Fairall9	$10.5^{+0.1}_{-0.1}$	$1\mu\text{m}-100\text{keV}$
NGC 4151	$18.34^{+3.29}_{-3.29}$	$1\mu\text{m}-100\text{keV}$
NGC 5548	$10.1^{+0.1}_{-0.1}$	$1\mu\text{m}-100\text{keV}$
3C 390.3	$6.32^{+0.04}_{-0.04}$	$1\mu\text{m}-100\text{keV}$
NGC 7469	$42.0^{+1.0}_{-1.0}$	$1\mu\text{m}-100\text{keV}$
NGC 3783	$15.8^{+2.1}_{-2.1}$	$1\mu\text{m}-100\text{keV}$
Mrk 509	$16.2^{+6.1}_{-0.1}$	$1\mu\text{m}-100\text{keV}$
λ_{Edd}								
Fairall9	0.0186	$1\mu\text{m}-100\text{keV}$
NGC 4151	0.0693	$1\mu\text{m}-100\text{keV}$
NGC 5548	0.0236	$1\mu\text{m}-100\text{keV}$	0.00	$1\mu\text{m} - 2\text{keV}$
3C 390.3	0.0466	$1\mu\text{m}-100\text{keV}$
NGC 7469	0.3690	$1\mu\text{m}-100\text{keV}$
NGC 3783	0.0398	$1\mu\text{m}-100\text{keV}$
Mrk 509	0.0951	$1\mu\text{m}-100\text{keV}$

Note. — If there are no errors, they were not presented in the original studies.

^aFor the cases where Vasudevan & Fabian (2009) list multiple measurements I list the mean value.

Table 3.9. Basic Statistics of SEDs integrated over $1\mu\text{m}$ -100 keV range.

Object	Mean $\log[L_{\text{BOL}}(\text{interpolation})/\text{ergs}^{-1}]^{\text{a}}$	Mean $\lambda_{\text{Edd}}^{\text{a}}$	Mean $\text{BC}(5100\text{\AA})^{\text{a}}$	Mean $\text{BC}(1350\text{\AA})^{\text{a}}$	Mean $\text{BC}(2\text{-}10\text{ keV})^{\text{a}}$
Fairall 9	45.10 ± 0.07	0.040 ± 0.007	16.74 ± 1.67	5.19 ± 0.62	11.96 ± 2.12
NGC 4151	44.07 ± 0.03	0.070 ± 0.004	12.71 ± 0.73	5.20 ± 0.10	14.95 ± 1.50
NGC 5548 ^b	44.34 ± 0.16	0.032 ± 0.011	15.82 ± 3.12	7.43 ± 1.06	9.42 ± 1.43
NGC 5548 ^c	44.43 ± 0.11	0.038 ± 0.008	15.07 ± 2.01	7.68 ± 1.53	9.66 ± 1.23
3C 390.3	45.05 ± 0.13	0.039 ± 0.012	38.06 ± 0.72	19.45 ± 3.92	6.43 ± 0.11
NGC 7469	44.34 ± 0.09	0.181 ± 0.035	12.89 ± 1.57	4.96 ± 0.26	12.25 ± 0.58

Note. — Mean measurements and the standard deviations relative to the main parameter are listed.

^bOnly the SEDs with simultaneous Optical, UV and X-ray data is used.

^cAll of the SEDs are used.

Table 3.10. Partial correlation coefficients

Line	N	τ	σ	P_{null}	rejection level
H β	302	-0.40	0.04		0.05
C IV	229	-0.15	0.06		0.05

Note. — Column (1): Emission-line for the line shape measurement. Column (2): Number of data points. Column (3): the partial Kendall's correlation coefficient. Column (4): the square root of the calculated variance. Column (5): The rejection level of the P_{null} (here P_{null} is the probability for accepting the null hypothesis that there is no correlation between λ_{Edd} and line shape.)

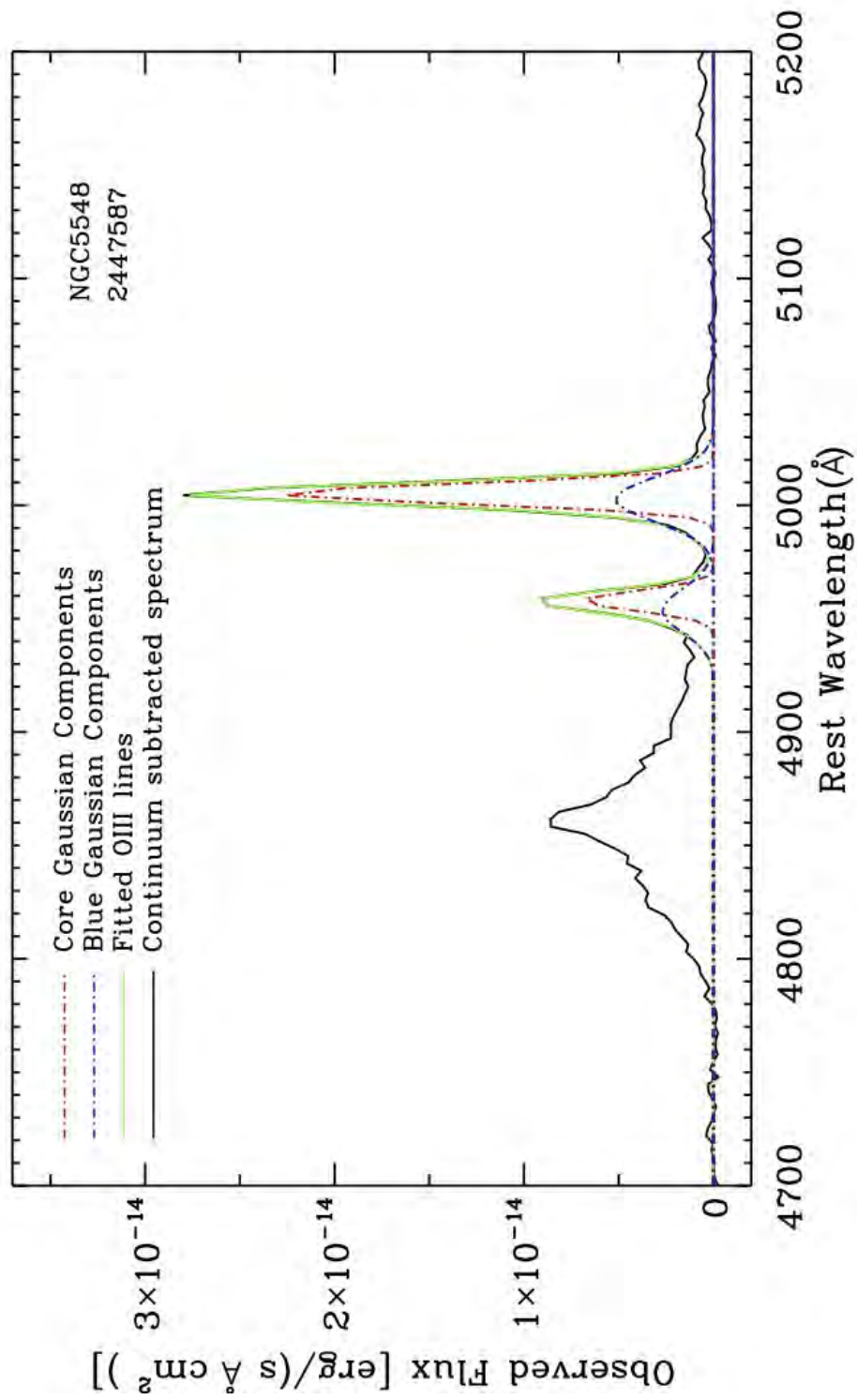


Figure 3.1 Sample spectrum of NGC 5548 showing the fitted model of the [O III] $\lambda 4959$ and [O III] $\lambda 5007$ lines based on a double Gaussian function. The solid green line shows the resultant model.

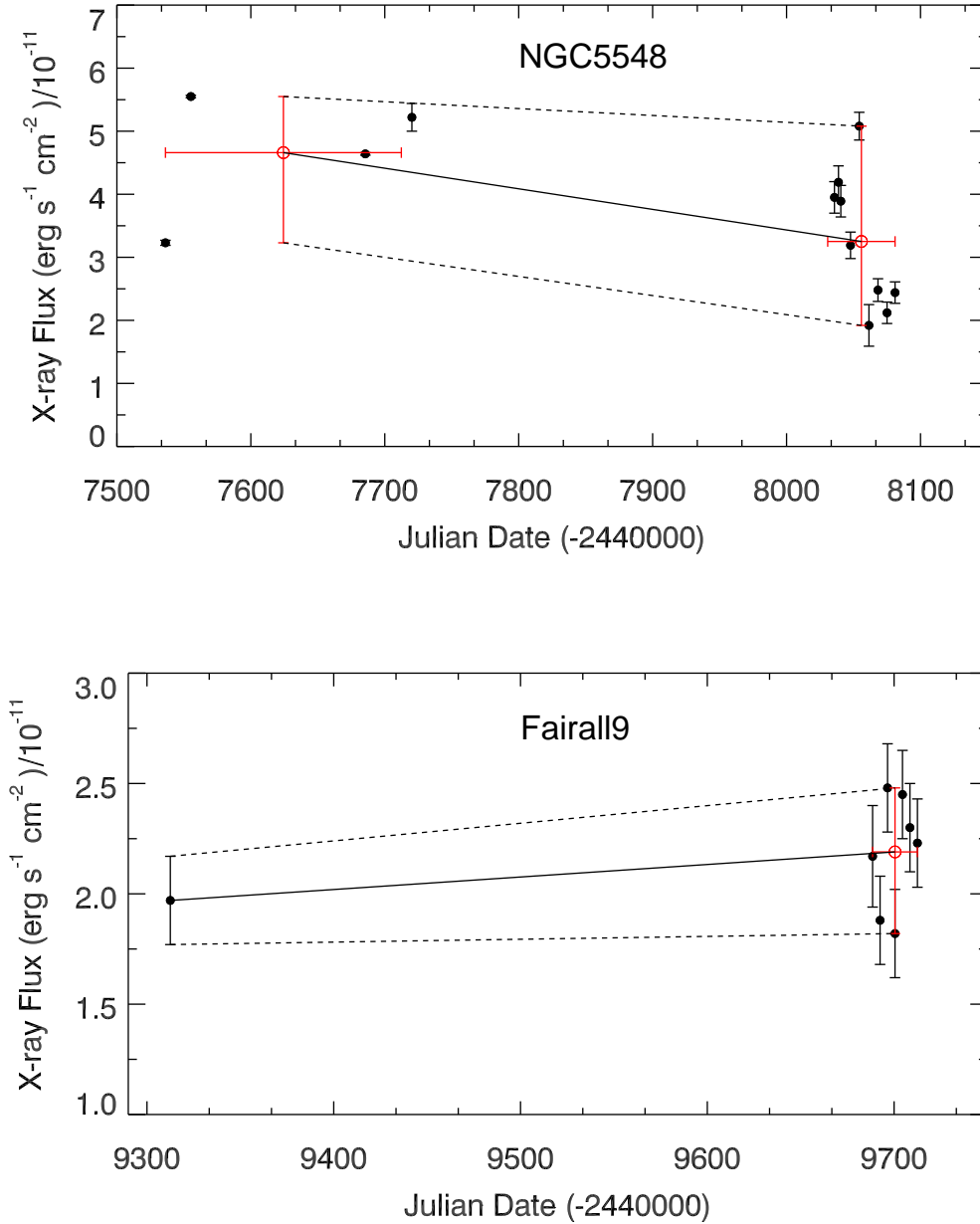


Figure 3.2 X-ray flux, $F_{2-10keV}$, interpolation for NGC 5548 and Fairall 9. The black filled circles are the observed X-ray fluxes. For NGC 5548 the open red circles represents the mean $F_{2-10keV}$ values over year 1(JDs:7500-7750) and year 2 (JDs:8000-8100). For Fairall 9 the open red circle represents the mean $F_{2-10keV}$ values between JDs 9688–9712. The solid black lines show the interpolated X-ray fluxes. The dashed gray lines indicate the $\pm 1\sigma$ uncertainties of the interpolated fluxes based on the $\pm 1\sigma$ of the mean fluxes.

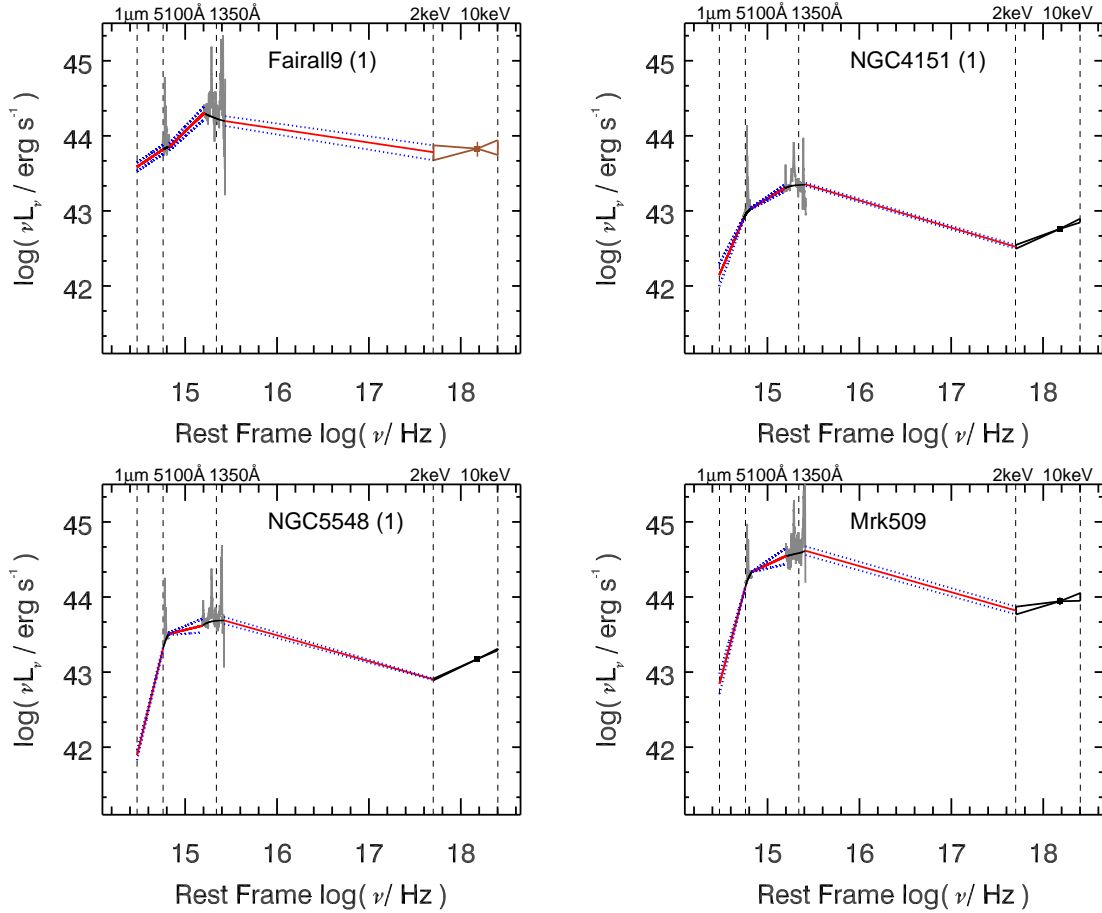


Figure 3.3 Four representative quasi-simultaneous SEDs of my sample. I present the rest of the SEDs in §A.2. The SEDs at different epochs of the same source are noted by the epoch number in the parenthesis; Table 3.6 list the relevant JDs of each epoch number. Optical and UV spectra are shown in gray and the solid black lines on the spectra show the best-fit continuum. Optical continuum is extrapolated to $1\mu\text{m}$ (§3.4) and the level of the $1\mu\text{m}$ luminosity is set by the extrapolation. The solid red line represents the linear interpolation between available datasets from $1\mu\text{m}$ to 10keV of the optical, UV and X-ray continua. The 'butterfly-shape' symbol at high energies represents the best power-law fit slope and its 1σ confidence levels of the 2-10 keV X-ray continuum. A brown 'butterfly-shape' symbol represents the X-ray continuum based on the estimated X-ray fluxes (§3.3.2) for NGC 5548 and Fairall 9. The frequency and luminosity ranges are the same in each panel to allow direct comparison.

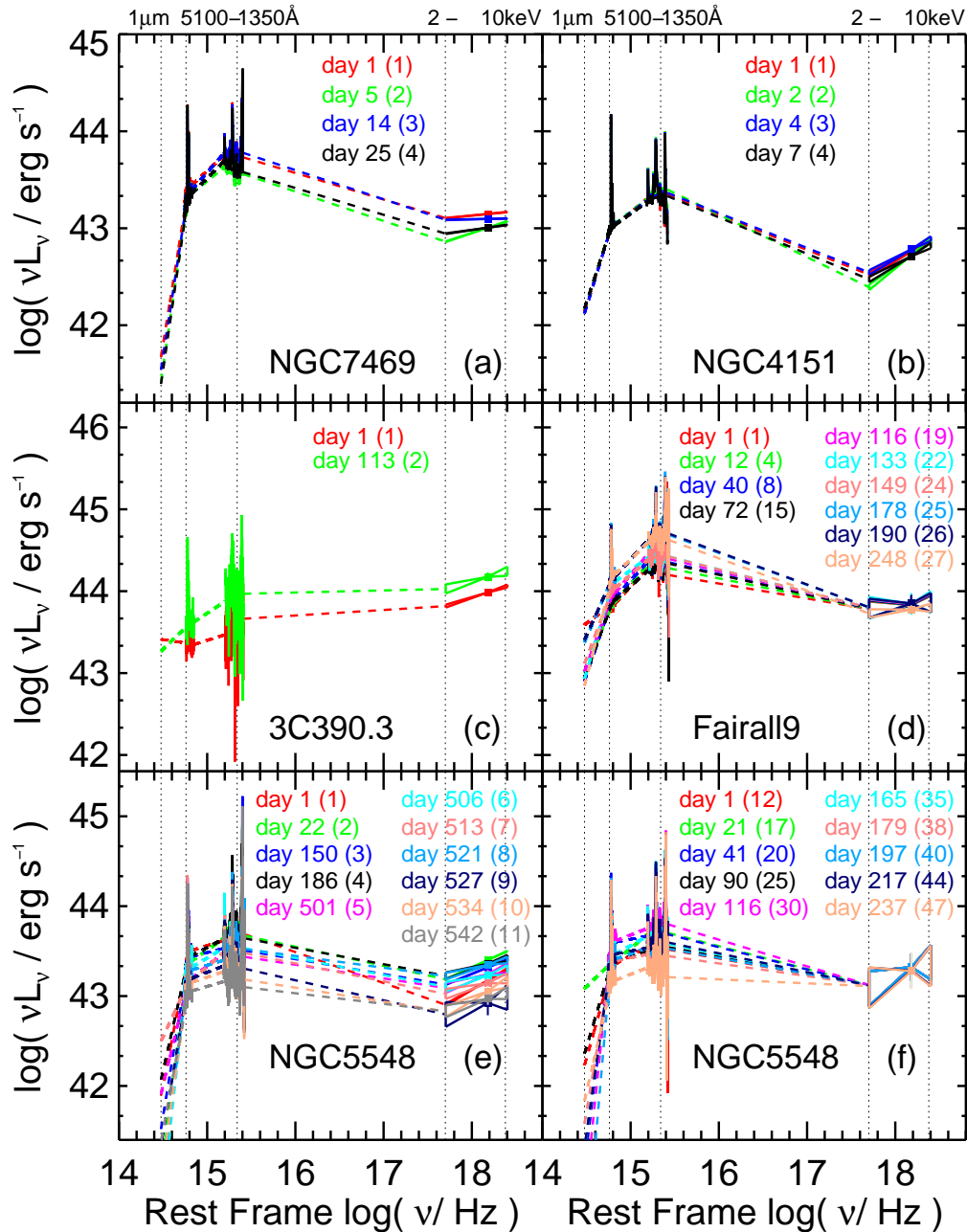


Figure 3.4 Multi-epoch SEDs of my AGN. SEDs at different epochs are shown in different colors. The day numbers and the SED epochs are shown by the same color. The day number is the JD difference to SED epoch no. (1). Dashed lines show the linearly extrapolated/interpolated regions and the butterfly shape represents the X-ray continuum (§ 3.4). For panels d (Fairall 9) and f (NGC 5548) the X-ray fluxes are *estimated* which explains the low X-ray variance there.

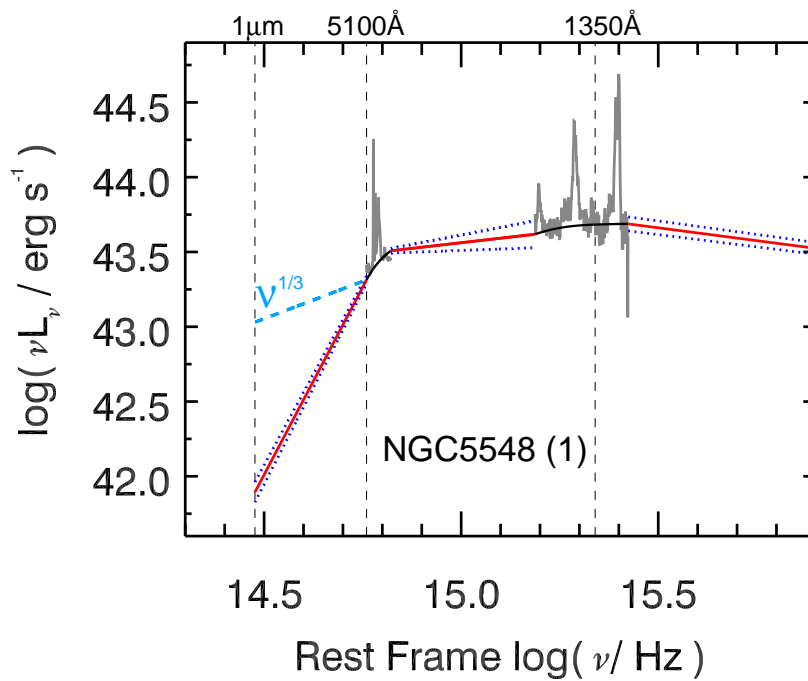


Figure 3.5 One representative SED of NGC5548 (see Figure 3.3 for symbols and color code). The $\nu^{1/3}$ disk model is shown as light blue, dashed line. The linear extrapolation from optical continuum to $1\mu\text{m}$ is shown by the red solid line. The $\nu^{1/3}$ model is not consistent with the linear extrapolation of the optical continuum and may overestimate the luminosity.

3. ON THE RELATION BETWEEN THE BROAD EMISSION LINE SHAPE AND EDDINGTON LUMINOSITY RATIO FOR LOCAL SEYFERT GALAXIES

100

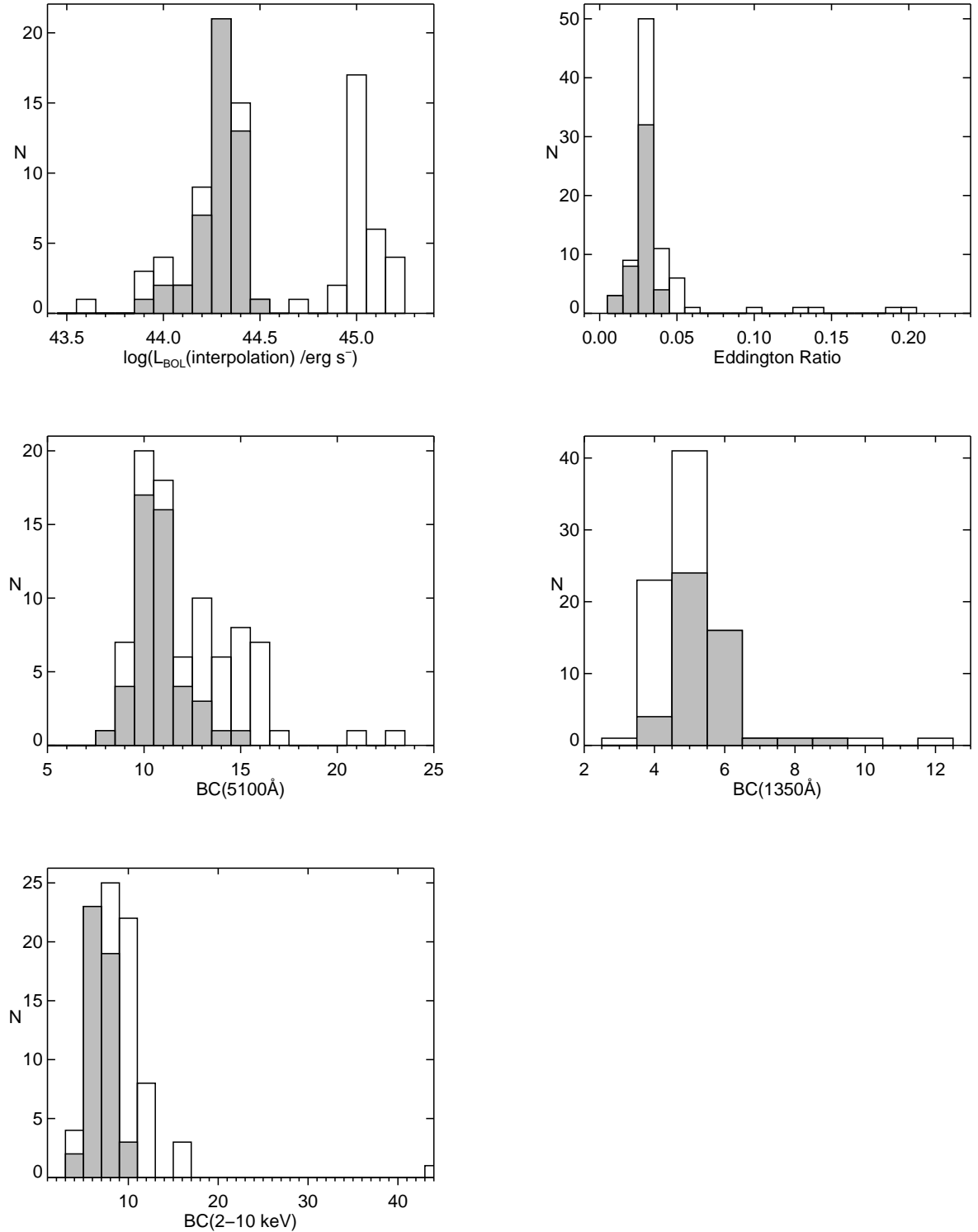


Figure 3.6 Distributions of the bolometric luminosities, Eddington ratios and BCs of my AGN sample. All of the SED epochs listed in Table 3.6 are included in the histograms. Gray shaded histograms represent NGC 5548.

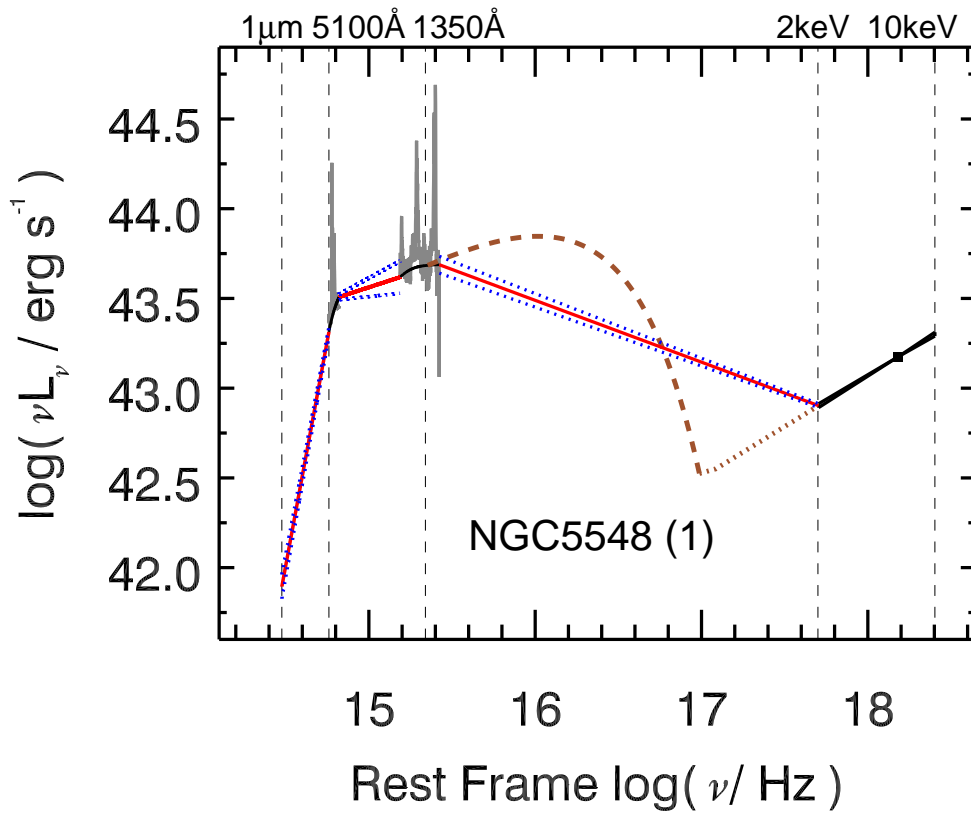


Figure 3.7 Comparison of the thermal accretion disk model of Korista et al. (1997a) to the linear interpolation adopted here for a sample SED of Seyfert galaxy NGC 5548 (see Figure 3.3 for symbols and color code). In the UV to X-ray region the SED model of Korista et al. (1997a) is shown as the brown dashed line. The dotted brown line shows the X-ray extrapolation.

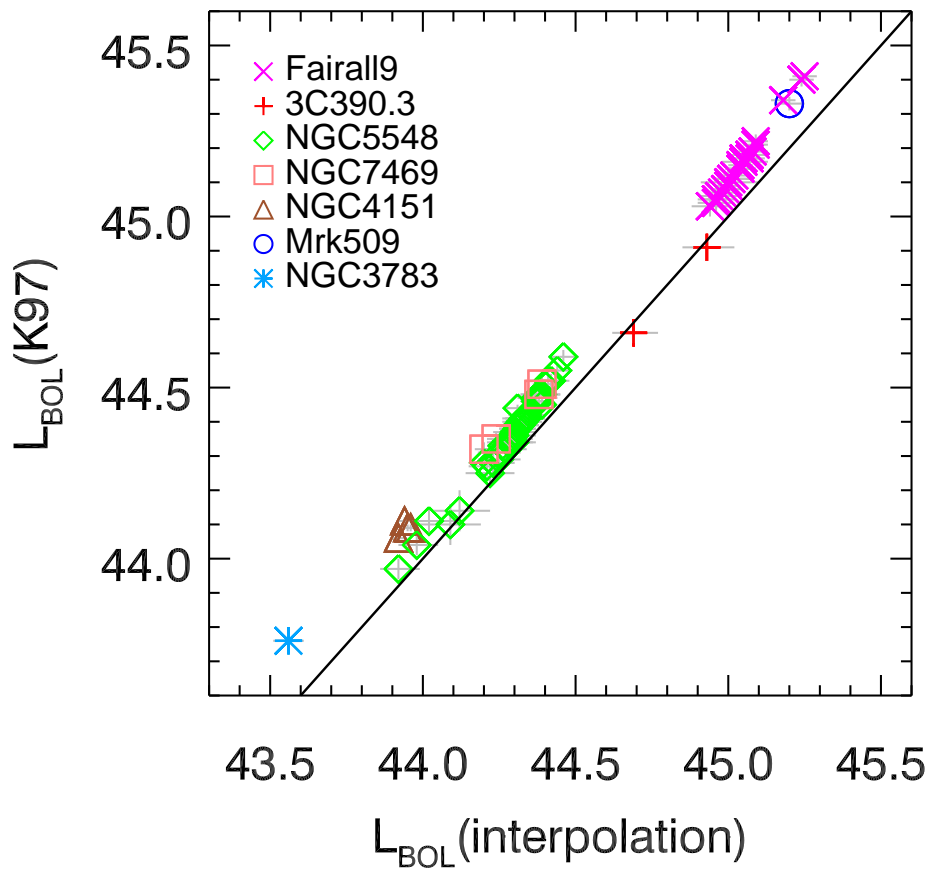


Figure 3.8 Comparison of the bolometric luminosities based on Korista et al. (1997a) model and linear interpolation. The solid line shows a one-to-one relationship.

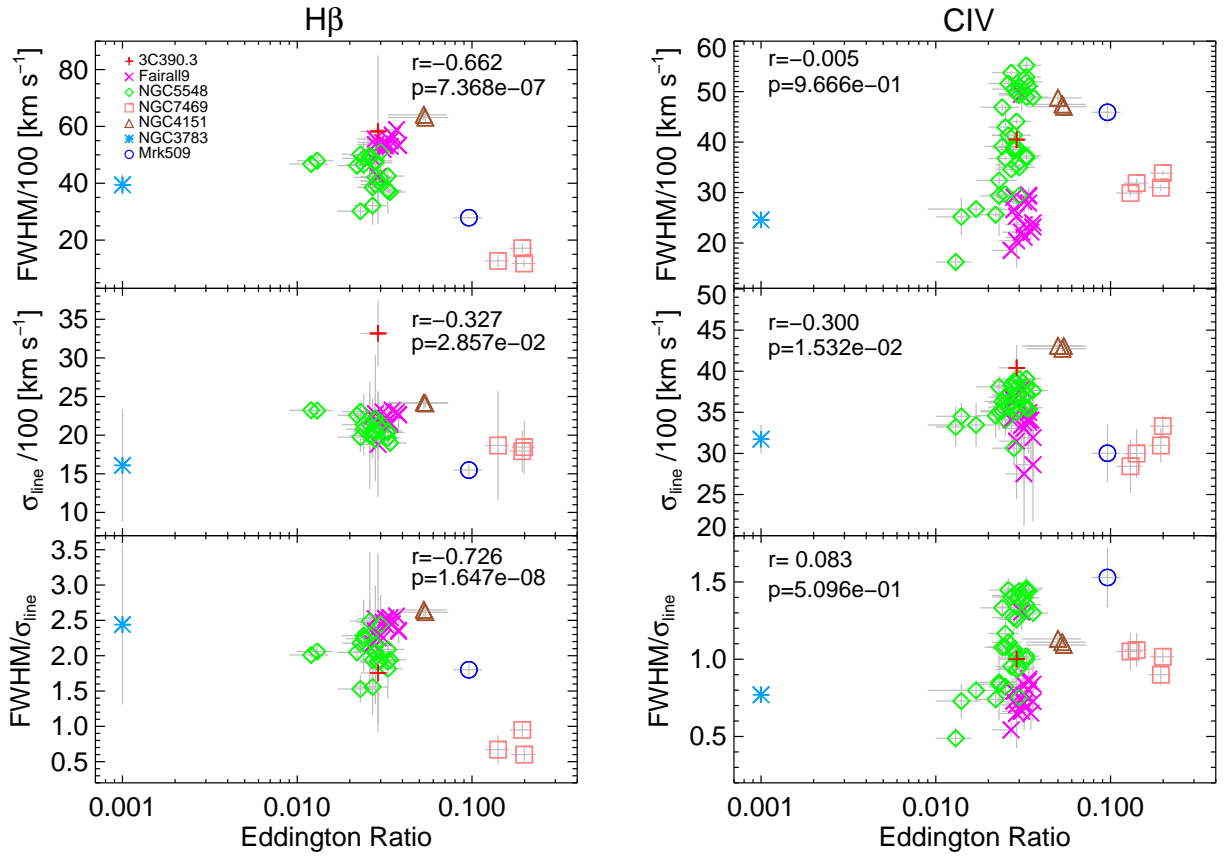


Figure 3.9 Distributions of line widths and line shape ($\text{FWHM}/\sigma_{line}$) for $\text{H}\beta$ (left column) and CIV (right column) with the Eddington luminosity ratio. Spectra are matched with the SEDs by accounting the light travel time between the disk and BLR except for Mrk 509 where I use the temporally nearest available spectra. Line widths are measured relative to the fixed limits (§3.3.1). The general trend seems mostly dominated by the FWHM and the line shape is seen to decrease with Eddington ratio for $\text{H}\beta$. A clear relationship is not observed for the CIV line.

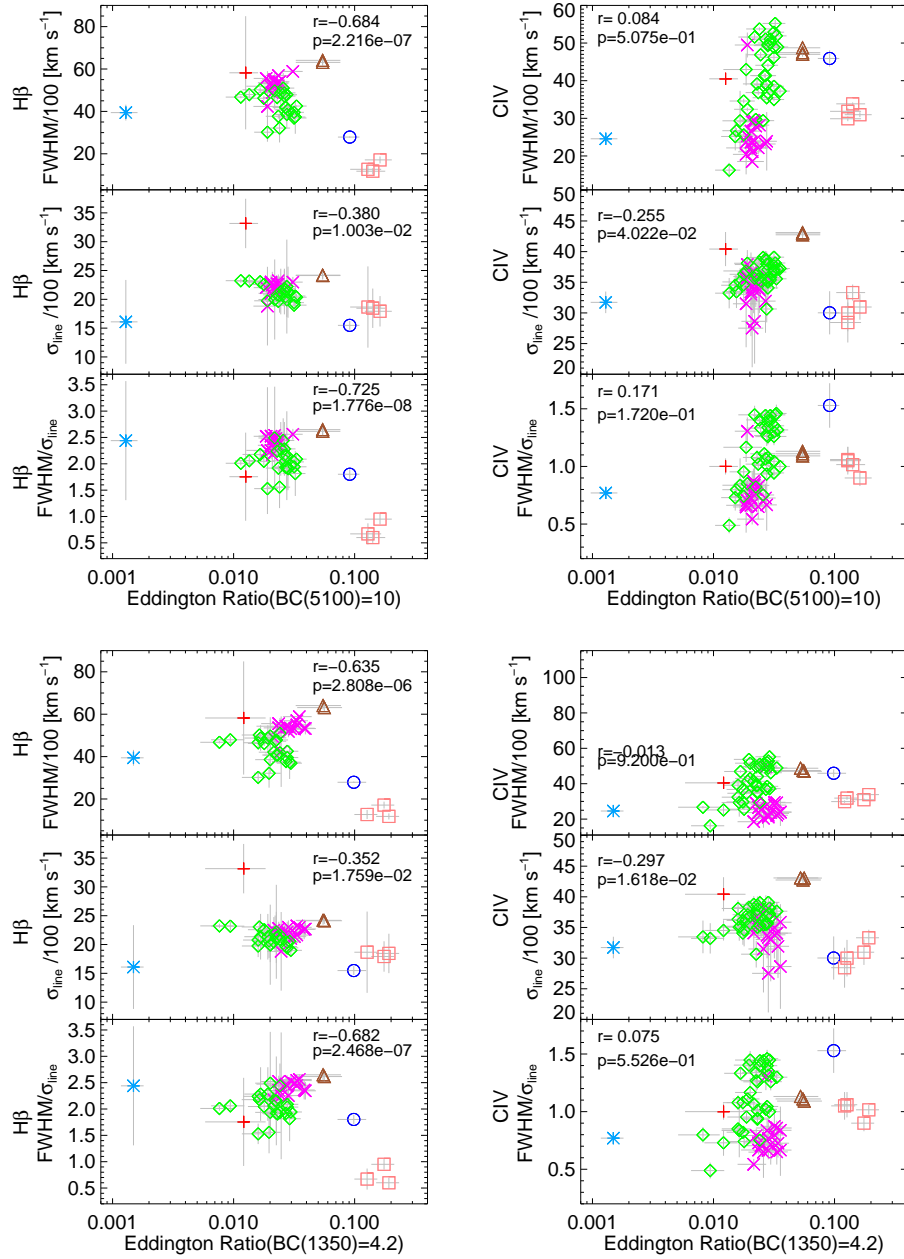


Figure 3.10 Same as Figure 3.9 but with Eddington ratios obtained by scaling $\lambda L_{\lambda}(5100)$ and $\lambda L_{\lambda}(1350)$ by $BC(5100\text{\AA})=10$ (top panels) and $BC(1350\text{\AA})=4.2$ (bottom panels), respectively. See Figure 3.9 for the symbol code. Note that although the individual data points have shifted in the diagram, the same general trend is seen here as when the Eddington ratios are based on single-epoch SEDs (see Figure 3.9)

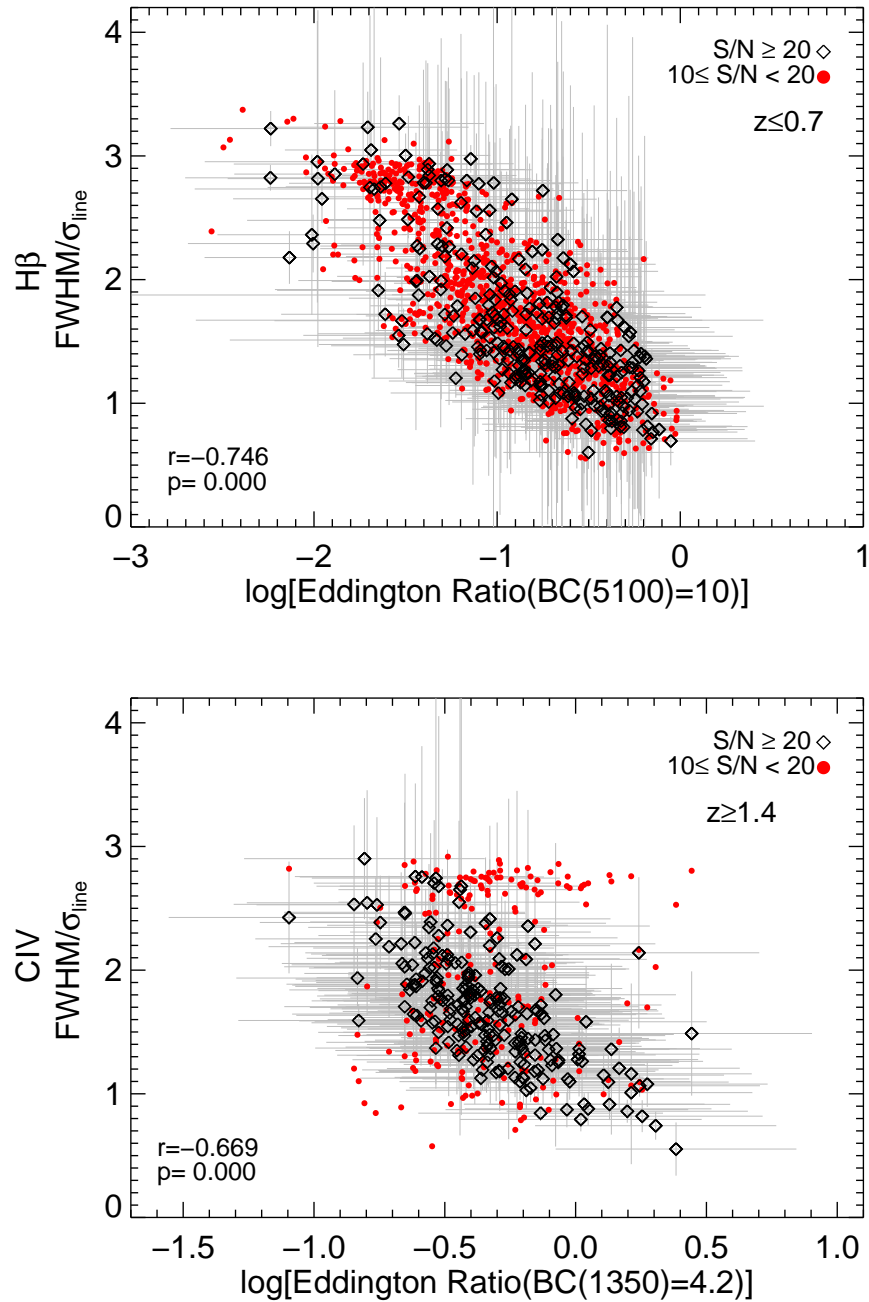


Figure 3.11 $\text{FWHM}/\sigma_{\text{line}}$ of $\text{H}\beta$ (top) and CIV (bottom) vs. Eddington ratio for the SDSS sample. The black diamonds and the red circles show measurements from median $S/N \geq 20$ and $10 \leq S/N < 20$ spectra, respectively. The top and the bottom panels show an inverse correlation independent of the median S/N in spectra.

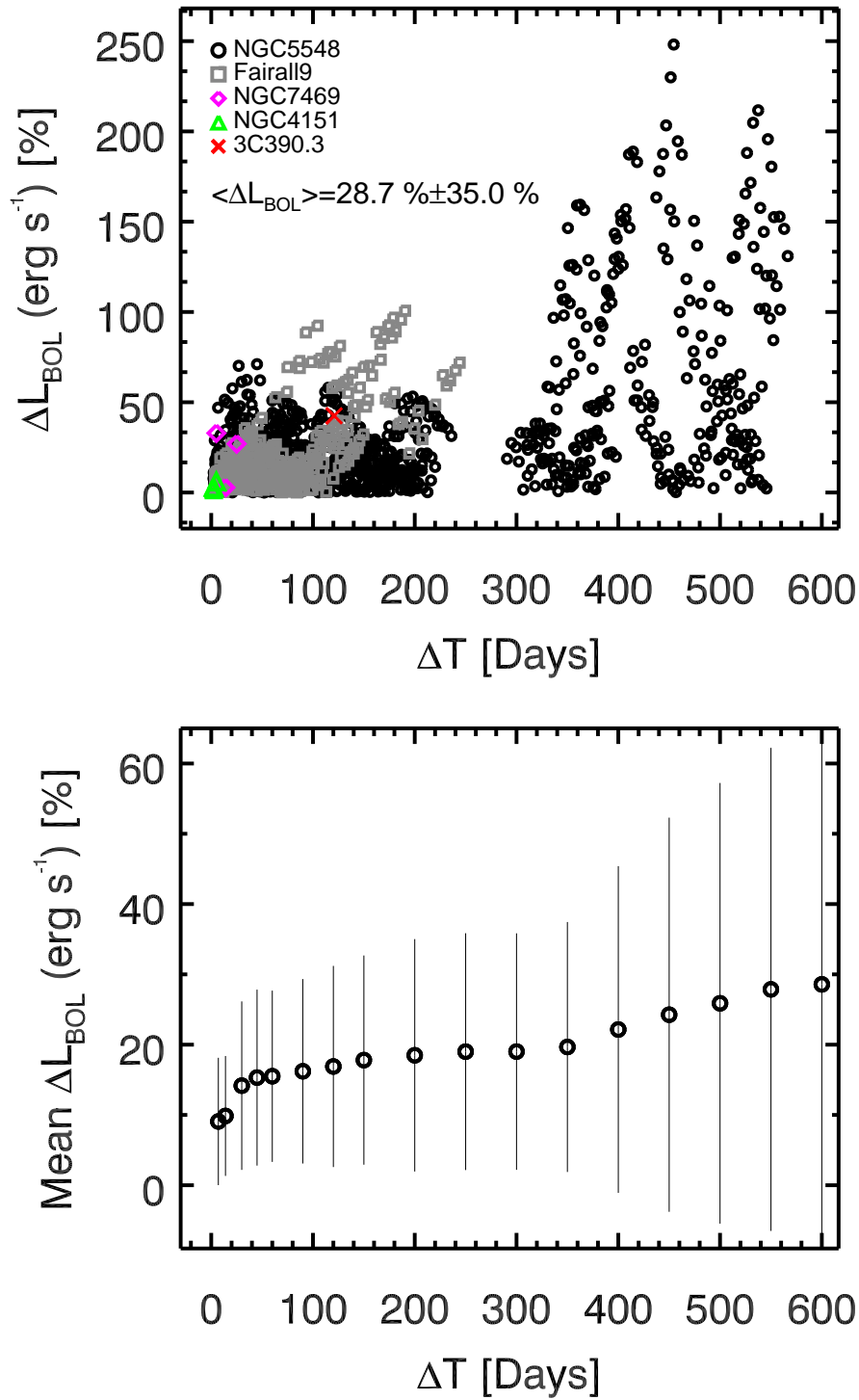


Figure 3.12 Top panel: Bolometric luminosity percent differences between all available SED epochs versus the time differences. Bottom panel: Average percent differences vs. the binned time intervals, errors are the rms deviations of the mean values.

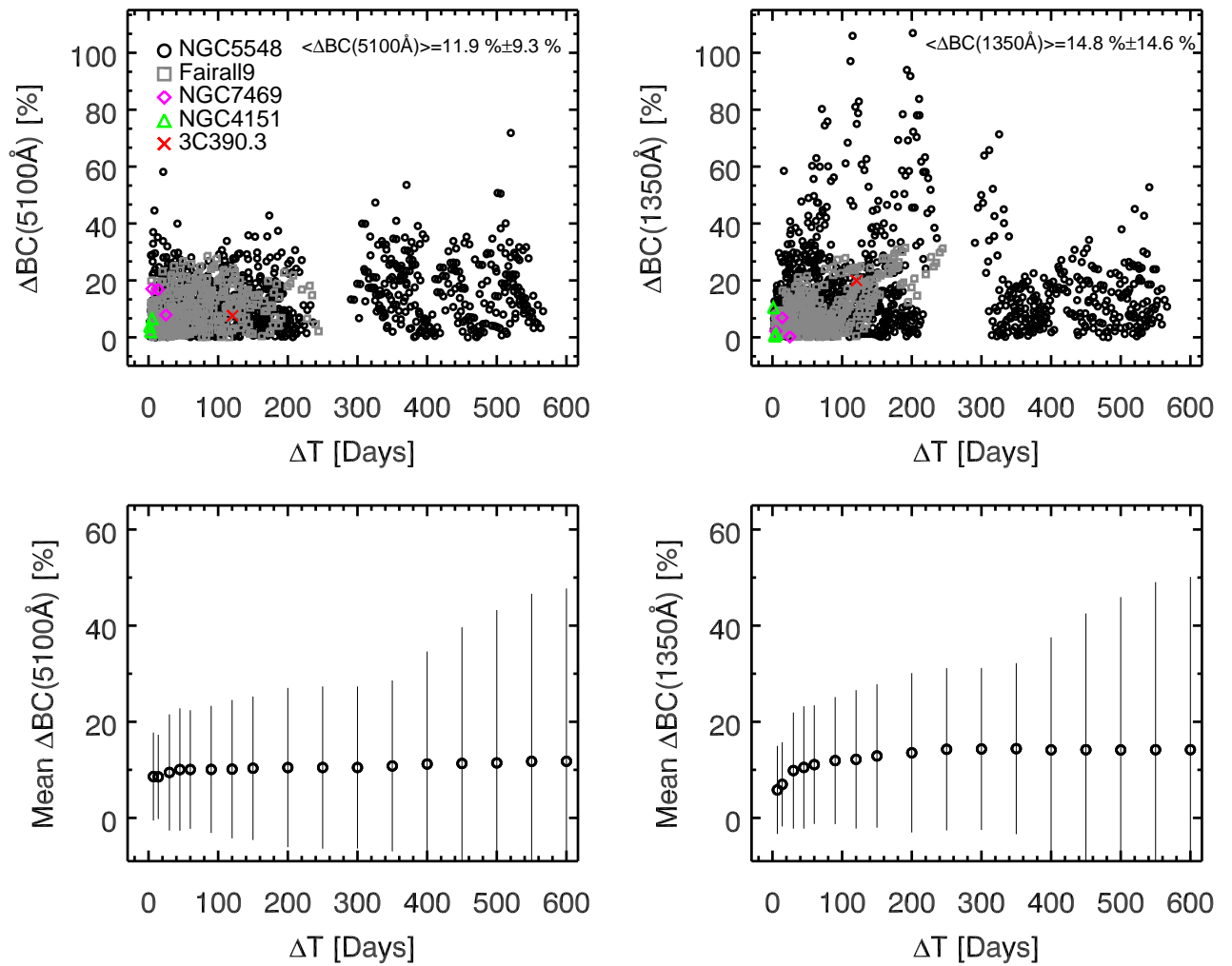


Figure 3.13 Same as Figure 3.12 but for BC(5100Å) (left) and BC(1350Å) (right).

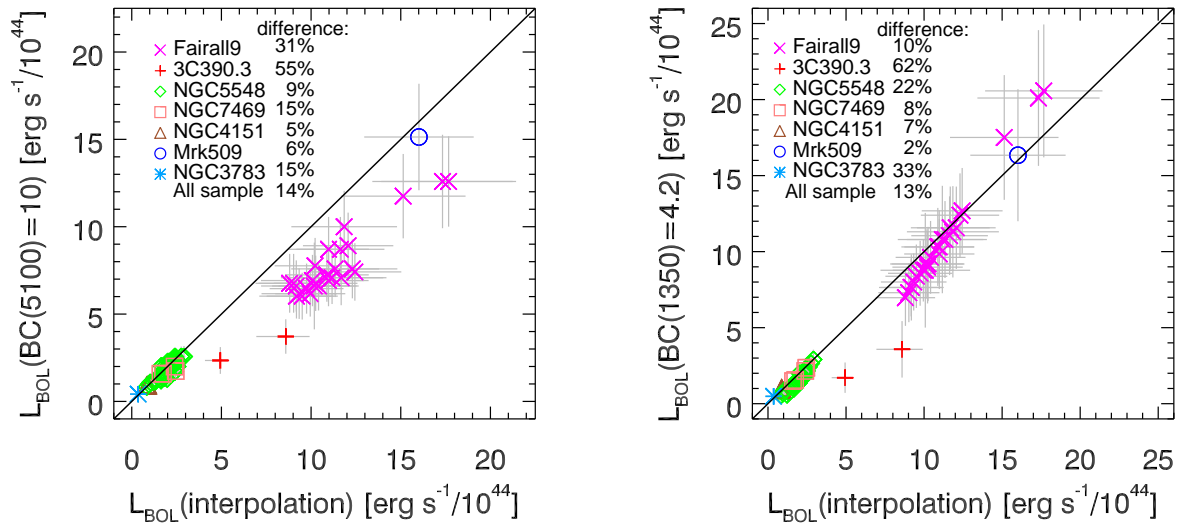


Figure 3.14 Comparison between L_{BOL} directly measured from the SEDs and estimated ones by applying a mean BC(5100Å) of 10 (left panel) and a mean BC(1350Å) of 4.2 (right panel). The solid line show where the bolometric luminosities are equal. The difference of each source is quantified as the mean of the residuals between the two bolometric luminosities, and shown in each panel.

4

ULTRALUMINOUS INFRARED GALAXIES IN THE AKARI ALL SKY SURVEY

ABSTRACT – We present a new catalog of 134 Ultraluminous Infrared Galaxies (ULIRGs) and one Hyperluminous Infrared Galaxy (HLIRG) by crossmatching AKARI all-sky survey with the Sloan Digital Sky Survey Data Release 10 (SDSS DR10) and the Final Data Release of the Two-Degree Field Galaxy Redshift Survey (2dFGRS). 48 of the ULIRGs and one HLIRG are new identifications. Based on the SDSS images we find that ULIRGs are interacting pair galaxies or ongoing/post mergers. This is consistent with the widely accepted view: ULIRGs are major mergers of disk galaxies. We confirm the previously known positive trend between the AGN fraction and IR luminosity. Our results reveal that the star formation rates (SFRs) derived from $H\alpha$ are factor of ~ 8 lower compared to the SFRs derived from infrared luminosity, indicating the insufficiency of $H\alpha$ but the necessity of IR observations to estimate SFRs of ULIRGs. We show that ULIRGs have a large off-set from the ‘main sequence’ up to $z \sim 1$; their off-set from the $z \sim 2$ ‘main sequence’ is relatively smaller. Compared to the off-main sequence galaxies at $z \sim 2$ they mostly have lower SFRs. We measure oxygen abundances of 54 ULIRGs; this is the largest ULIRG sample of which gas-metallicities are measured. Compared to local star forming SDSS galaxies of similar mass, local ULIRGs have lower oxygen abundances and they show a 0.2 dex shift with respect to the local mass–metallicity relation. We demonstrate that ULIRGs follow the fundamental metallicity relation (FMR) for the first time. The scatter of ULIRGs around FMR (0.13 dex–0.5 dex) is comparable with the scatter of $z \sim 2$ –3 galaxies. Their optical colors show that ULIRGs are not in a transition phase between the blue and red galaxies, instead they are mostly star forming blue galaxies. We provide the largest local ($0.050 < z < 0.487$) ULIRG catalog with stellar masses, SFRs, gas metallicities and optical colors. Our catalog provides us with rigorously active galaxies the -analogous to high- z galaxies- in the local Universe where they can be scrutinized.

4.1 INTRODUCTION

Luminous infrared galaxies (LIRGs), ultraluminous infrared galaxies (ULIRGs) and hyperluminous infrared galaxies (HLIRGs) are defined by their distinguished IR luminosities that are in the $10^{11} L_{\odot} \leq L_{IR} < 10^{12} L_{\odot}$, $10^{12} L_{\odot} \leq L_{IR} < 10^{13} L_{\odot}$ and $10^{13} L_{\odot} \leq L_{IR}$ ranges, respectively (see the reviews by Sanders & Mirabel, 1996b; Lonsdale et al., 2006). The observed enormous IR luminosity is driven by the optical and UV radiation generated by intense star formation and active galactic nuclei (AGN), that is absorbed by dust and re-emitted in the IR. ULIRGs have been considered as a transition phase from mergers to dusty quasars (Sanders et al., 1988c;

Veilleux et al., 2002) such that when gas-rich spiral galaxies merge, the molecular gas clouds channeling towards the merger nucleus trigger nuclear starbursts and AGN activity via the accretion of the available fuel on to the central super massive black hole (SMBH). According to this scenario, the starburst phase evolves to a dust-enshrouded AGN phase, and once the gas and dust consumed the system reaches to a bright QSO phase.

Tidal interactions and merger processes between galaxies play a major role in the formation of elliptical galaxies (Toomre & Toomre, 1972). Especially, the proposed scenario by Sanders et al. (1988c) motivated further investigation of the link between mergers and quasars in numerical simulations. Hydrodynamical simulations of mergers show that merger processes lead gas inflows towards the center that trigger starbursts and AGN activity (e.g Springel et al., 2005). In the merger-driven galaxy evolution simulations ULIRGs represent a contemporary starburst- and AGN-phase at the beginning of a rapid self-regulated SMBH growth (e.g. Di Matteo et al., 2005; Hopkins et al., 2007). ULIRGs evolve to red/elliptical-type remnants by the ‘negative feedback’ mechanisms (e.g. in the form of powerful winds and outflows) that inhibit star formation and AGN activity (e.g. Hopkins et al., 2006, 2008a,b, 2009a).

The emerged link between ULIRGs and QSOs is supported by several observational evidence. Morphological properties of ULIRGs indicate that they are interacting galaxies in pre- or ongoing- or late merger stages (Farrah et al., 2001; Kim et al., 2002; Veilleux et al., 2002, 2006). Compared to LIRGs that are disk galaxies (if $\log(L_{IR}/L_{\odot}) < 11.5$) or interacting systems (if $11.5 \leq \log(L_{IR}/L_{\odot}) < 12.0$), ULIRGs are mostly advanced mergers (Veilleux et al., 2002; Ishida, 2004). Their dynamical masses obtained from near-infrared (NIR) spectroscopy show that they are major mergers of nearly equal mass galaxies (Dasyra et al., 2006a,b). CO observations proved that ULIRGs contain the required cold molecular gas for central starbursts (Downes & Solomon, 1998). Additionally, their mid-infrared (MIR) images show that MIR emission generated in a region of diameter ~ 1 kpc (Soifer et al., 2000). At least $\sim 70\%$ of 164 local ($z \leq 0.35$) ULIRGs harbor an AGN (Nardini et al., 2010). The coexistence of a starburst and an AGN show that both energy sources contribute to the total IR luminosity. The AGN fraction and the strength of the AGN emission increases with IR luminosity; high-luminosity ULIRGs ($\log(L_{IR}/L_{\odot}) > 12.5$) and HLIRGs have a larger AGN contribution compared to lower luminosity IR galaxies (Veilleux et al., 1999b, 2002; Goto, 2005; Imanishi, 2009; Nardini et al., 2010). ULIRGs show starburst-and AGN-driven powerful outflows (e.g Heckman et al., 2000; Rupke et al., 2005; Rupke & Veilleux, 2011; Spoon et al., 2013; Veilleux et al., 2013, and references therein) that are consistent with the expected negative feedback mechanisms for their evolution.

The importance of ULIRGs in the galaxy evolution is not limited by the local ($z < 0.3$) Universe because, at high redshift ($z > 1$) they are more numerous and have a substantial contribution to the total IR luminosity density (Caputi et al., 2007) compared to local ULIRGs (Soifer & Neugebauer, 1991; Kim & Sanders, 1998b). There is a significant population of ULIRGs beyond $z \sim 1$ (e.g Goto et al., 2011). An important question is the powering mechanism of these sources: are they powered by interaction-induced nuclear starbursts/AGN or are they normal/undisturbed star forming galaxies? The key properties that would answer this question are: morphologies, spectral energy distributions (SEDs) and the extend of star forming regions. Observations have shown that ULIRGs at high redshift ($1.5 < z < 3.0$) are mostly ($\sim 47\%$) mergers or interacting galaxies, but this sample also includes non-interacting disks, spheroids and irregular galaxies (Kartaltepe et al., 2012). Beyond $z > 2$ morphological properties of sub-millimeter galaxies (SMGs) are consistent with mergers and interacting systems (e.g Tacconi et al., 2008). Morphologies of high z samples show that mergers/interactions taking place in

these systems and even, comparison of $z \sim 2$ and $z \sim 1$ sample indicates a hint for a morphological evolution such that $z \sim 1$ sample have slightly more mergers and interacting galaxies (Kartaltepe et al., 2012). The SEDs of high redshift ULIRGs are different from those of local ones: for example they exhibit prominent polycyclic aromatic hydrocarbon (PAH) features similar to those of local low IR luminosity ($10.0 \leq \log(L_{IR}/L_{\odot}) < 11.0$) star forming galaxies rather than those of local ULIRGs (e.g Farrah et al., 2008; Takagi et al., 2010). Since PAH emission indicates ongoing star formation, observations support that high z ULIRGs are starburst dominated. A similar conclusion is also achieved by the X-ray studies of high z ULIRGs (e.g Johnson et al., 2013). The size of the star forming regions of high z ULIRGs are larger than those of local ULIRGs with similar L_{IR} (Rujopakarn et al., 2011). This suggest that in these galaxies star formation do not occur in merger nuclei but, it is distributed galaxy wide. The similarities of star forming regions of high z ULIRGs and local quiescent star forming galaxies point out a diverse origin than merger-induced star formation (Rujopakarn et al., 2011). Although a complete picture of the evolution of ULIRG properties with different redshift is not pieced up yet, observations provide evidence for changing properties of ULIRGs with redshift.

Understanding the role of ULIRGs in galaxy evolution through cosmic time require extensive studies/comparison of local and high z samples. Local ULIRGs establish a ground to understand the nature of ULIRGs, the origin of their extreme luminosities and the interplay between star formation and AGN activity in the nearby mergers. Therefore, it is important to have a large local sample and to master its overall properties. The great majority of local ULIRGs are discovered with InfraRed Astronomy Satellite (*IRAS*). *IRAS* performed an all sky scan in four IR bands centered at $12\mu\text{m}$, $25\mu\text{m}$, $60\mu\text{m}$ and $100\mu\text{m}$. *IRAS* Bright Galaxy Survey (BGS) catalog (Soifer et al., 1987) includes 10 ULIRGs selected on the basis of $60\mu\text{m}$ flux, $F(60\mu\text{m})$. This catalog replaced with the *IRAS* Revised Bright Galaxy Sample (RBGS) (Sanders et al., 2003) that provided more accurate infrared luminosities and increased the number of ULIRGs to 21. The *IRAS* 2-Jy (Strauss et al., 1992) and 1.2-Jy (Fisher et al., 1995) redshift surveys identified new ULIRGs. Sanders et al. (1988a) showed that ULIRGs with ‘warm’ colors $F(25\mu\text{m})/F(60\mu\text{m}) > 0.2$ have Seyfert like spectra and thereon ULIRGs separated as ‘warm’ AGN hosting and ‘cold’ star formation dominated systems. Analysis of BGS sample showed that the $F(60\mu\text{m})/F(100\mu\text{m})$ color increases with higher L_{IR} (Soifer & Neugebauer, 1991). A widely studied large sample of local ULIRGs is the *IRAS* 1-Jy sample (Kim et al., 1998). This is a complete flux-limited sample at $60\mu\text{m}$ that is composed of 118 ULIRGs identified from *IRAS* Faint Source Catalog (FSC) (Moshir et al., 1992) and a dedicated redshift survey (Kim et al., 1998). Since previous studies (Soifer & Neugebauer, 1991; Strauss et al., 1992) showed that $F(60\mu\text{m})/F(100\mu\text{m})$ color increases with higher L_{IR} and ULIRGs colors are in the range of $-0.2 < F(60\mu\text{m})/F(100\mu\text{m}) < 0.13$, *IRAS* 1-Jy sample ULIRGs were selected based on their warm colors $F(60\mu\text{m})/F(100\mu\text{m}) > 0.3$ (Kim et al., 1998). With other redshift surveys such as the QDOT all sky *IRAS* galaxy redshift survey (Lawrence et al., 1999), the *IRAS* Point Source Catalog Redshift (PSCz) survey (Saunders et al., 2000) and the FIRST/*IRAS* radio–far-IR sample of (Stanford et al., 2000) number of *IRAS* ULIRGs increased. Large galaxy redshift surveys like the Sloan Digital Sky Survey (SDSS) (York et al., 2000) and Two-Degree Field Galaxy Redshift Survey (2dFGRS) (Colless et al., 2001) provide redshifts of millions of galaxies. Especially SDSS made it possible to study optical properties of large sample of IR galaxies. Goto (2005) cross-correlated the *IRAS* FSC with the SDSS Data Release 3 (DR3) (Abazajian et al., 2005) spectroscopic catalog and identified 178 ULIRGs. Pasquali et al. (2005) cross-correlated SDSS DR2 (Abazajian et al., 2004) with the *IRAS* FSC and investigated IR properties of local AGNs and star forming galaxies. Cao et al. (2006) cross-correlated *IRAS* FSC and the Point Source Catalog (PSC) with SDSS DR2 and identified a small

sample of ULIRGs. Hwang et al. (2007) identified 324 ULIRGs, including 190 new discoveries, by cross correlating *IRAS* FSC with SDSS DR4 (Adelman-McCarthy et al., 2006), 2dFGRS and the Second Data Release of the 6dF Galaxy Survey (6dFGS) (Jones et al., 2004). Hou et al. (2009) cross-correlated *IRAS* FSC with the SDSS DR6 (Adelman-McCarthy et al., 2008) and identified 308 ULIRGs.

23 years after *IRAS* the largest all sky IR survey completed by the Japanese IR satellite launched in 2006, *AKARI* (Murakami et al., 2007). *AKARI* scanned almost all-sky in $9\mu\text{m}$, $18\mu\text{m}$, $65\mu\text{m}$, $90\mu\text{m}$, $140\mu\text{m}$ and $160\mu\text{m}$ bands. The resolution and sensitivity of *AKARI* is better than those of *IRAS*: the Point Spread Function (PSF) of *AKARI* is $\sim 39''$ (for $90\mu\text{m}$ band) while the PSF of *IRAS* is $\sim 4'$ (for $100\mu\text{m}$ band); at $18\mu\text{m}$ *AKARI* is 10 times more sensitive. An other advantage of *AKARI* is that, it has a wider and longer wavelength coverage compared to *IRAS*. In particular the $140\mu\text{m}$ and $160\mu\text{m}$ bands are very important to measure the peak of the dust emission near $100\mu\text{m}$ and therefore obtain more accurate IR luminosity. Goto et al. (2011) matched *IRAS* IR sources with SDSS DR7 (Abazajian et al., 2009) galaxies and measured the local IR luminosity function. In this study, Goto et al. (2011) identified ULIRGs among *AKARI* sources, but did not provide a detailed catalog of these sources. In this work we search for ULIRGs and HLIRGs in the *AKARI* all-sky survey. We cross-correlate *AKARI* all-sky survey with 2dFGRS and the largest SDSS spectroscopic redshift catalogue DR 10 (Ahn et al., 2013). Beside the redshift information, SDSS has a rich view of optical properties of the sources in this database. Optical images, spectra, colors, value added catalogs with emission line properties provided by SDSS D10 give us an opportunity to investigate the morphologies, colors, stellar mass and metallicities of local ULIRGs identified in the *AKARI* all-sky survey. We provide the first catalog of ULIRGs identified in *AKARI* all-sky survey.

This paper has the following structure. We introduce the data to identify ULIRGs/HLIRGs and our final sample in §4.2. Our results are presented in §4.3. In §4.4 we discuss our results. The summarized conclusion of this work is given in §4.5. Throughout this work, we adopt a cosmology with $H_0 = 70 \text{ km s}^{-1} \text{ Mpc}^{-1}$, $\Omega_\Lambda = 0.7$ and $\Omega_m = 0.3$.

4.2 IDENTIFICATION OF ULTRALUMINOUS AND HYPERLUMINOUS INFRARED GALAXIES IN THE AKARI ALL-SKY SURVEY

4.2.1 THE SAMPLES

The AKARI All-Sky Survey Catalogs

The *AKARI* all-sky survey provides two catalogs of the IR sources across more than $\sim 97\%$ of the whole sky with fluxes centered on two mid-IR and four FIR bands. The *AKARI/IRC* all-sky survey point source catalog version 1¹ includes 870973 IR sources with fluxes at $9\mu\text{m}$ and $18\mu\text{m}$ mid-IR bands. The *AKARI/FIS* all-sky survey bright source catalog version 1² (Yamamura et al., 2010) contains 427071 sources detected at $90\mu\text{m}$ with flux measurements at $65\mu\text{m}$, $90\mu\text{m}$, $140\mu\text{m}$ and $160\mu\text{m}$ FIR bands. Especially $140\mu\text{m}$ and $160\mu\text{m}$ fluxes are very important to constrain the FIR SED peak and to measure L_{IR} .

In order to have a single *AKARI/FIS/IRC* catalog with both FIR and mid-IR fluxes, we cross-match the IR sources in the *AKARI/FIS* all-sky survey bright source catalog with the

¹http://www.ir.isas.jaxa.jp/AKARI/Observation/PSC/Public/RN/AKARI-IRC_PSC_V1_RN.pdf

²http://www.ir.isas.jaxa.jp/AKARI/Observation/PSC/Public/RN/AKARI-FIS_BSC_V1_RN.pdf

AKARI/IRC all-sky survey point source catalog within a radii of 20". The resulting *AKARI*/FIS/IRC catalog contains 24701 sources based on 90 μ m detections.

To measure the IR luminosity we obtain the spectroscopic redshifts of the IR galaxies from their optical counterparts. We cross-correlate the *AKARI*/FIS/IRC catalog with large optical redshift survey catalogs as described in the following.

The *AKARI*–SDSS DR10 Sample

The Sloan Digital Sky Survey is the largest ground-based survey providing a unique photometric and spectroscopic database of stars, galaxies and quasars. SDSS is a red magnitude limited $r < 17.7$ survey over 14555 deg² of the sky. We have downloaded the SDSS DR 10 (Ahn et al., 2013) catalogs *photoObj*³ and *specObj*³ to extract both photometric and spectroscopic information. The *photoObj* catalog includes all photometric information from previous data releases and the *specObj* catalog includes new spectra from the Baryon Oscillation Spectroscopic Survey⁴ (BOSS). We combined the two catalogs by matching 'OBJID' in *photoObj* to 'BESTOBJID' in *specObj* and obtain a full SDSS catalog of 2,745,602 sources with spectroscopic and photometric information.

AKARI/FIS/IRC catalog is cross-matched with the full SDSS catalog. The astrometric precision of SDSS ($\sim 0.1''$ at $r=19$ mag Pier et al., 2003) is much better than that of *AKARI* ($\sim 4.8''$ Yamamura et al., 2010)). We follow Goto et al. (2011) and select matching radii as 20" that is at least four times larger than the astrometric accuracy of the *AKARI*/FIS catalog. This is an ideal radius because it is large enough to contain different emission regions (e.g IR and optical) in a single galaxy; also it is small enough not to allow too many optical chance identifications that are not physically related to the IR source. We avoid any duplicated matches, i.e each IR galaxy is allowed to match only with one SDSS counterpart. We obtain 6468 matches of *AKARI*–SDSS sources. Among those we removed the sources that were classified as star in the *specObj* catalog. This resulted into a *AKARI*–SDSS sample of 6373 galaxies. For the IR sources in this sample we adopt the SDSS spectroscopic redshifts.

The *AKARI*–2dFGRS Sample

The Two-Degree Field Galaxy Redshift Survey (Colless et al., 2001) measured redshifts of 245951 galaxies within $b_j < 19.45$ limit. The median redshift of this survey is $z \sim 0.1$ (Colless, 2004). We use the Final Data Release of the 2dFGRS, the catalog of *best spectroscopic observations*⁵. We cross-match the *AKARI*/FIS/IRC catalog with the 2dFGRS catalog with a matching radii of 20". We obtain a *AKARI*–2dFGRS sample of 954 galaxies with spectroscopic redshifts from 2dFGRS.

4.2.2 INFRARED LUMINOSITY MEASUREMENTS

To estimate the total IR luminosity for the galaxies in the *AKARI*–SDSS and *AKARI*–2dFGRS samples we perform a SED-fitting using the *LePhare*⁶ (Photometric Analysis for Redshift Estimations) code (Arnouts et al., 1999; Ilbert et al., 2006). The main function of the *LePhare* is to compute photometric redshifts, but it can also find the best fitting galaxy template by a χ^2 fit for the given photometric magnitudes among the input template libraries. For the

³http://www.sdss3.org/dr10/spectro/spectro_access.php

⁴<http://www.sdss3.org/survey/boss.php>

⁵<http://www2.aao.gov.au/~TDFgg/>

⁶<http://www.cfht.hawaii.edu/~arnouts/lephare.html>

AKARI–SDSS and *AKARI*–2dFGRS samples we use the six *AKARI* bands with their associated uncertainties adopted from the *AKARI* catalogs; if the flux uncertainty is not given we adopt 25% of the measured flux as the uncertainty. We use the FIR SED templates of Dale & Helou (2002) as the input library. Dale & Helou (2002) provide 64 SED templates generated semi-empirically to represent the IR SEDs of star forming galaxies. Compared to other SED models, such as the models of Chary & Elbaz (2001), these templates include FIR improvements based on *ISO/IRAS/SCUBA* observations. However, they do not include more sophisticated dust emission modeling as provided by Siebenmorgen & Krügel (2007). Since our main focus is to measure L_{IR} we avoid more sophisticated models and prefer the templates of Dale & Helou (2002) for the SED fitting. We fix the redshift of each galaxy and fit the FIR region of the SED with the *AKARI* broadband photometry. In the fitting procedure k -corrections are applied to *AKARI* fluxes. In order to obtain the k -correction our model flux is computed integrating redshifted SED model flux through *AKARI*'s filter response function. The best-fit dust templates of Dale & Helou (2002) are shown in Figures 4.1, 4.2, 4.3 and 4.4 (left column) for representative cases. The *AKARI*/FIS name is given in the top left corner. The best-fit templates are shown as solid magenta line. The black filled circles are the optical (shown only for illustration purposes) and *AKARI* photometric fluxes; the x-axis error bars represent the wavelength range of each photometric band.

As a result of the SED fitting we obtain the total infrared luminosity integrated between $8\mu\text{m}$ – $1000\mu\text{m}$, L_{8-1000} with the maximum and minimum possible L_{8-1000} value based on the flux errors. These are used to determine the the upper and lower uncertainties of L_{8-1000} .

Based on the obtained L_{8-1000} our initial sample includes 170 ULIRG and 10 HLIRG candidates: the *AKARI*–SDSS sample has 135 ULIRG and eight HLIRG candidates; the *AKARI* – 2dFGRS has 35 ULIRG and two HLIRG candidates. In order to have a reliable sample of ULIRGs and HLIRGs, we check each case to avoid any wrong identification as described in the following.

4.2.3 ELIMINATION OF THE MISMATCHES

The (H)/ULIRG candidates in our initial sample are selected based on the optical spectroscopic redshifts; by matching the closest optical galaxy to the *AKARI* source. If there are more than one source satisfying the cross-match condition, then the one with the smallest positional difference is considered as a match. Even the positions of the optical and IR sources are close in the sky, it does not necessarily mean that the IR and optical emissions are counterparts of the same galaxy; further care is required to make this decision.

Although the optical and IR galaxies are matched within a $20''$ radius, we visually check the positional overlap of the IR and optical emission in *AKARI* images for each galaxy. For the optical counterpart we use SDSS (if available) or Digitized Sky Survey images. Examples of *AKARI* (middle panel) and optical (right panel) images are represented in Figures 4.1, 4.2, 4.3, 4.4 and 4.5. The SDSS images are *gri* combined color images downloaded from the SDSS DR10 Finding Chart Tool⁸. In the *AKARI* images (Doi et al., 2012) the green circle represents the $20''$ radius limit, whereas the optical source is marked with a $5''$ radius magenta circle. Once we make sure of the positional overlap of the matched IR and optical sources, next we check if there are any other sources overlapping with the IR source and possibly contaminate the IR emission. Such contaminating sources can be stars or other galaxies. Especially nearby bright galaxies lying over the IR source have a contribution to the observed IR emission, therefore such cases

⁸<http://skyserver.sdss3.org/dr10/en/tools/chart/chartinfo.aspx>

are eliminated from the initial sample. If there are more than one overlapping optical galaxies with similar separation values within the $20''$ radius region, the closest one does not necessarily mean the true match. Since it is difficult to select the true optical counterpart for these cases, these are eliminated.

Although SDSS provides a large redshift database, not all galaxies have the spectroscopic information. Related to this, in some cases the optical source with the smallest positional difference is not included in the cross-match procedure. Therefore, the images show that instead of the ‘true’ optical counterpart, some other optical galaxy with a large separation ($8.12'' - 18.87''$) is matched with the IR emission. If we do not find any confirmed spectroscopic redshift information in the literature we eliminate these candidates. However, if the redshift is known in the literature (e.g. Wang & Rowan-Robinson, 2009), we use the spectroscopic redshift and re-obtains L_{8-1000} and keep those in the sample with $10^{12}L_{\odot} \leq L_{8-1000}$.

After we secure the optical and IR galaxy match by visual inspection, as an additional control we check the adopted spectroscopic redshifts. For the *AKARI*–2dFGRS sample we require a redshift quality of ≥ 3 . This requirement let to eliminate two ULIRG and two HLIRG candidates from the *AKARI*–2dFGRS sample. For the *AKARI*–SDSS sample, we go through the SDSS spectra⁹. The SDSS spectra are reduced through the spectroscopic pipeline (Bolton et al., 2012). The SDSS pipeline determines the classification and the redshift of the spectra by applying a χ^2 fit with rest-frame templates of stars, galaxies and quasars. By looking at the SDSS spectra we eliminate the following cases from the sample: (1) The sources that are classified as a galaxy but show a spectrum of a star; (2) The spectra showing an unreliable template fit and therefore indicating a wrong redshift.

4.2.4 THE FINAL SAMPLE

Our final sample of (H)/ULIRGs consist of 134 galaxies, 101 are identified in the *AKARI*–SDSS sample and 33 are identified in the *AKARI*–2dFGRS sample. In order to specify the newly identified (H)/ULIRGs in this work we check our final sample against previously studied samples: Clements et al. (1996), Kim et al. (1998), Rowan-Robinson (2000), Hwang et al. (2007), Hou et al. (2009), Nardini et al. (2010). 48 ULIRGs and one HLIRG are newly identified in this work. We divide the final sample into three subsamples: (1) New ULIRGs identified in this work; (2) Known ULIRGs; (3) New HLIRG identified in this work. The properties of these subsamples are listed in Tables 4.1, 4.2 and 4.3, respectively. These tables contain the *AKARI* name (column 1), *AKARI* coordinates: RA and DEC (columns 2 and 3, respectively), other name (column 4), redshift (column 5), total IR luminosity, L_{IR} , (column 6), *AKARI* photometric fluxes of the $65\mu\text{m}$ ($F(65\mu\text{m})$), $90\mu\text{m}$ ($F(90\mu\text{m})$), $140\mu\text{m}$ ($F(140\mu\text{m})$) and $160\mu\text{m}$ ($F(160\mu\text{m})$) bands (columns 7, 8, 9 and 10, respectively), SDSS Petrosian r magnitude (column 11), Interaction Class (IC; column 12), reference for IC (column 13), note related to optical images indicating if there is a star or other galaxies in the field (column 14), spectral classification (column 15). Since we have only a few sources detected in the $9\mu\text{m}$ and $18\mu\text{m}$ bands we do not list the photometric fluxes at these bands.

In Table 4.4 we list five additional ULIRG candidates that are considered as unconfirmed cases either because their IR detection is not significant (almost at 5σ), or the separation between the matched optical and IR coordinates are large ($\sim 20''$). We do not include those five sources in the final sample.

⁹<http://dr10.sdss3.org/basicSpectra>

4.3 ANALYSIS AND RESULTS

4.3.1 BASIC PROPERTIES OF THE AKARI ULIRGS AND HLIRG SAMPLES

Redshift and L_{IR} Distributions

The redshift and IR luminosity distributions of our final sample are presented in the top and bottom panels of Figure 4.6, respectively. The redshift distribution covers $0.050 < z < 0.487$, with a median redshift of $\bar{z} = 0.177$. 120 ULIRGs are distributed over $0.050 < z \leq 0.270$ range and 14 ULIRGs are within the $0.270 < z < 0.487$ range. The IR luminosity distribution of 92 ULIRGs covers $12.0 \leq L_{IR} \leq 12.25$ range. The higher luminosity range of $12.25 < L_{IR} \leq 12.91$ includes 42 ULIRGs.

Figure 4.7 shows the IR luminosity of our sample as a function of redshift. As it is expected from the AKARI PSC detection limit (0.55 Jy at $90\mu\text{m}$), L_{IR} increases with redshift and only the bright sources can be detected towards the higher redshifts.

FIR Color Properties of Our Sample

The IR emission of the so called ‘normal’ star forming galaxies (that are not dominated by AGN activity) is mostly due to the thermal radiation from dust grains heated by star formation. The ‘normal’ star forming galaxies detected by IRAS showed a clear trend of decreasing 60- to $100\mu\text{m}$ flux ratios, $F(60\mu\text{m})/F(100\mu\text{m})$, with increasing 12- to $25\mu\text{m}$ flux ratios, $F(12\mu\text{m})/F(25\mu\text{m})$, (Helou, 1986). This trend associated with the intensity dependence of IR colors, such that ‘warm’ colors (greater $F(60\mu\text{m})/F(100\mu\text{m})$ values) are related to active star formation with high IR luminosities (Helou, 1986).

Dale et al. (2001) construct single parameter dust models of normal star forming galaxies based on the $F(60\mu\text{m})/F(100\mu\text{m})$ color and the intensity of the interstellar radiation field, U . They characterize the overall IR SED as a power law distribution of dust mass over U such that: $dM(U) \sim U^{-\alpha}dU$, where α is the exponent of the power-law distribution. Dale & Helou (2002) provide 64 SED models for a wide range of U or equivalently IRAS $F(60\mu\text{m})/F(100\mu\text{m})$ color (between -0.54 and 0.21) and α values ($0.0625 \leq \alpha \leq 4.0$). In §4.2.2 we measured L_{IR} based on these models. In the following, we investigate the AKARI color properties of our ULIRG sample and compare the observed colors with the SED models of Dale & Helou (2002).

For this investigation we use the AKARI $F(9\mu\text{m})$ and $F(18\mu\text{m})$ fluxes from the AKARI/IRC all-sky survey point source catalog. The $F(65\mu\text{m})$, $F(90\mu\text{m})$, $F(140\mu\text{m})$ and $F(160\mu\text{m})$ fluxes are listed in Tables 4.1, 4.2 and 4.3. Figure 4.8 presents the observed AKARI color-color diagrams: (a) $F(9\mu\text{m})/F(18\mu\text{m})$ vs. $F(18\mu\text{m})/F(65\mu\text{m})$; (b) $F(18\mu\text{m})/F(65\mu\text{m})$ vs. $F(65\mu\text{m})/F(90\mu\text{m})$; (c) $F(65\mu\text{m})/F(90\mu\text{m})$ vs. $F(90\mu\text{m})/F(140\mu\text{m})$; (d) $F(90\mu\text{m})/F(140\mu\text{m})$ vs. $F(140\mu\text{m})/F(160\mu\text{m})$. Panels (a) and (b) show only the two sources that are detected in all AKARI bands. Panels (c) and (d) include 81 sources that are detected in all AKARI FIS bands. Different symbols represent spectral class as listed in Tables 4.1, 4.2 and 4.3 (see §4.3.3): circle (composite), star (star forming), square (LINER), diamond (Seyfert), triangle (QSOs), plus (unclassified). In panels (c) and (d) the FIR colors of different class of galaxies distribute over the entire color range. Therefore, AGNs or star forming galaxies can not be distinguished by their FIR colors. However, this is expected because FIR is tracing star formation activity at low temperature dust and is not sensitive to AGN activity. It is known that IRAS mid-IR $F(25\mu\text{m})/F(60\mu\text{m})$ color is an indicator of ‘warm’ dust and AGN component ($F(25\mu\text{m})/F(60\mu\text{m}) \geq 0.2$) (e.g. Sanders et al., 1988a). Unfortunately, the majority of our ULIRG sample are not detected in the mid-IR colors and therefore we do not have enough data to explore the mid-IR color properties of our sample.

The color-color diagrams in panels (c) and (d) do not show a clear correlation. It is important to keep in mind that detection limits of *AKARI* bands affects the shape of the color-color diagrams. Detection limits of *AKARI* FIS bands are 3.2 Jy, 0.55 Jy, 3.8 Jy and 7.5 Jy for 65 μ m, 90 μ m, 140 μ m and 160 μ m bands (Yamamura et al., 2010), respectively. The WIDE-S filter centered at 90 μ m is the broadest and therefore it has the deepest detection limit compared to other bands. In panel (d) the distribution of the colors is shaped by the observational detection limits. This is mainly because 140 μ m is common in both axes. In the x-axis as 140 μ m flux gets brighter the $\log(F(140\mu\text{m})/F(160\mu\text{m}))$ color moves towards right, but at the same time in the y-axis the $\log(F(90\mu\text{m})/F(140\mu\text{m}))$ color moves downwards. This behavior creates a boundary on the top right corner of this diagram. Even if there was an intrinsic color-color correlation in panel (d) it would be truncated on the upper right corner due to observational limits. We expect to have a similar detection limit effect in panel (c) because 65 μ m and 140 μ m detection limits are brighter than 90 μ m, and this may cause colors to hit the boundaries of 65 μ m and 140 μ m before the limit of 90 μ m.

In Figure 4.8 the solid lines in each panel show the expected colors by the IR SED models of Dale & Helou (2002). We choose eight SEDs with different α and $F(60\mu\text{m})/F(100\mu\text{m})$ values among 64. The selected models have a sequence in terms of α and $\log(F(60\mu\text{m})/F(100\mu\text{m}))$: $0.06 \leq \alpha \leq 4.0$ and $-0.54 \leq \log(F(60\mu\text{m})/F(100\mu\text{m})) \leq 0.21$. The expected colors from the selected SEDs are shown with different colors; the α and $\log(F(60\mu\text{m})/F(100\mu\text{m}))$ parameters of each model is given in top corner of panel (b). We show colors expected from each model as a function of redshift from 0 to 0.5 in order to illustrate the redshift dependence of the colors. In panels (c) and (d) the data show a large spread around the model colors. In panel (c), the large vertical and horizontal spreads of $\log(F(65\mu\text{m})/F(90\mu\text{m}))$ and $\log(F(90\mu\text{m})/F(140\mu\text{m}))$ colors around the models are mainly due to the limited parameter coverage of the SED models. The models cover the ranges between -0.54–0.21 and -0.62–0.47 in the y- and x-axis, respectively. Therefore, the models do not overlap with the colors exceeding this range. In panel (d), especially the $\log(F(140\mu\text{m})/F(160\mu\text{m}))$ colors have a large scatter around the models, the models covers only the -0.11–0.13 range while the observed colors can exceed up to 1.27. We further discuss such outliers in color-color diagrams in § 4.4.

Since the *AKARI* $\log(F(65\mu\text{m})/F(90\mu\text{m}))$ color is equivalent to *IRAS* $\log(F(60\mu\text{m})/F(100\mu\text{m}))$ color, it is possible to make a comparison of *AKARI* and *IRAS* color distributions of ULIRGs. Hwang et al. (2007) investigate *IRAS* colors of 324 ULIRGs and report $\log(F(60\mu\text{m})/F(100\mu\text{m}))$ within -0.80–0.22 range with a mean of -0.19. The ULIRGs in our sample have a slightly larger range between -0.91–0.36, but still the *AKARI* $\log(F(65\mu\text{m})/F(90\mu\text{m}))$ colors overlap with the *IRAS* $\log(F(60\mu\text{m})/F(100\mu\text{m}))$ colors.

FIR Colors versus IR Luminosity

IR bright galaxies ($10^{9.5}L_{\odot} \leq L_{IR} < 10^{13}L_{\odot}$) studied with *IRAS* show a correlation between the IR colors and the IR luminosity: $\log(F(12\mu\text{m})/F(25\mu\text{m}))$ color decreases, and $\log(F(60\mu\text{m})/F(100\mu\text{m}))$ color increases with increasing IR luminosity (Soifer & Neugebauer, 1991). As stated in §4.3.1 $\log(F(60\mu\text{m})/F(100\mu\text{m}))$ color is related to the intensity of the radiation field. The SED models of Dale & Helou (2002) cover a wide range of *IRAS* $\log(F(60\mu\text{m})/F(100\mu\text{m}))$ colors that correlate with L_{IR} ; higher $\log(F(60\mu\text{m})/F(100\mu\text{m}))$ colors indicate higher L_{IR} (Dale & Helou, 2002). In the following we investigate the color dependence of the IR luminosities for our (H)/ULIRG sample.

Figure 4.9 presents IR luminosity versus: (a) $\log(F(65\mu\text{m})/F(90\mu\text{m}))$, (b) $\log(F(65\mu\text{m})/F(140\mu\text{m}))$,

(c) $\log(F(65\mu\text{m})/F(160\mu\text{m}))$, (d) $\log(F(90\mu\text{m})/F(140\mu\text{m}))$, (e) $\log(F(90\mu\text{m})/F(160\mu\text{m}))$, (f) $\log(F(140\mu\text{m})/F(160\mu\text{m}))$, for 81 sources that are detected in all *AKARI* FIS bands. As noted before, since we have only very few sources detected in 9- and 18- μm bands we do not include those in this investigation. Since the observed colors change as a function of redshift and luminosity depends on redshift, we apply k-correction to the *AKARI* FIS colors shown in Figure 4.9.

As noted before *AKARI* $\log(F(65\mu\text{m})/F(90\mu\text{m}))$ color is similar to *IRAS* $\log(F(60\mu\text{m})/F(100\mu\text{m}))$ color and therefore, we would expect a strong correlation in panel (a). However, none of the *AKARI* colors in Figure 4.9 show a clear dependence in L_{IR} between $12.0 \leq \log(L_{IR}/L_{\odot}) < 13.3$. Since the interested L_{IR} range in this study is very narrow compared to the L_{IR} range probed in previous studies (e.g Soifer & Neugebauer, 1991) it is natural not to see the previously discovered significant color– L_{IR} correlations. The representative SED models shown in Figure 4.8 show a luminosity dependence with color, but the observed colors show a large scatter around the models (discussed in §4.3.1 and §4.4). The large differences between the SED models and the observed colors weakens the color– L_{IR} correlation expectation.

In Figure 4.9, apart from the color dependence of IR luminosity, different galaxy types do not show a significant dependence on color.

4.3.2 THE VISUAL MORPHOLOGIES AND INTERACTION CLASSES

Morphological studies of local ULIRGs showed that they are mostly interacting galaxies showing tidal features or disturbed morphology (e.g Farrah et al., 2001; Veilleux et al., 2002, 2006). Surace (1998) introduced an interaction classification scheme based on the evolution sequence that merging galaxies follow in simulations (e.g Mihos & Hernquist, 1996). Such an interaction classification scheme is important to interpret the morphological properties of ULIRGs in the context of galaxy evolution triggered by mergers. Veilleux et al. (2002) classified 117 local ULIRGs based on this scheme and showed that ULIRGs are interacting or advanced merger systems.

Here we investigate the morphological properties of our sample with the aim of identifying interaction classes. We use the following widely preferred classification scheme that is described by Veilleux et al. (2002) :

- I: First approach. Separated galaxies with no signs of interaction or merging.
- II: First contact. Overlapped discs without interaction signs.
- III: Pre-mergers. Two nuclei separated by more than 10 kpc (a; wide binary) or less than 10 kpc (b; close binary), with interaction signs.
- Tp1: Interacting triplet system.
- IV: Merger. One nucleus with prominent tidal features.
- V: Old merger. Disturbed central morphology without clear tidal tail signs.
- NI: Non interacting. Isolated single galaxy, no signs of disturbed morphology.

Note that we added class NI to represent isolated single galaxies showing no signs of disturbed morphology. Also note that we do not subdivide class IV into two as done by Veilleux et al. (2002) because, we do not have K band luminosities.

We (two classifiers: EKE and TG) examined SDSS $g-r-i$ colors combined images and classified only the galaxies for which SDSS images are available. For the known ULIRGs, we adopt the interaction classifications from the literature. We prefer to adopt the classifications mainly from Veilleux et al. (2002) and Hwang et al. (2007). The interaction classifications of the galaxies in our sample are given in column (12) of Tables 4.1, 4.2 and 4.3. The references for the interaction classes are given in the column (13) of Tables 4.1, 4.2 and 4.3. In addition to the above interaction classification we also note if the galaxies are in a group with (G). We define groups as galaxy systems with more than two members. SDSS images showing examples of different interaction classes are represented in Figures 4.1, 4.2, 4.3, 4.4 and 4.5.

As shown in Figure 4.7 luminosity is correlated with distance and it becomes more difficult to identify the morphological details for more distant sources. To avoid uncertainties in interaction classifications due to the distances, in the following analysis we focus on a redshift limited sample of 113 ULIRGs. For comparison reasons we apply a redshift cut as $z=0.27$; this is the limit of the Veilleux et al. (2002) ULIRG sample. The distribution of interaction classes of 113 ULIRGs is shown in Figure 4.10. This Figure presents the percentage of different interaction classes. There are no ULIRGs classified as I and II, so they are not in an early interaction phase. The fraction of triplets (Tp1) in our sample is very small (4%). 44% of the ULIRGs are binary systems showing strong interaction features (IIIa and IIIb). Most of the ULIRGs (51%) are single nucleus galaxies classified as IV and V indicating a late/post merger phase. Veilleux et al. (2002) study 117 ULIRGs from *IRAS* 1 Jy sample (Kim et al., 1998) and report 56% of the sample as single nucleus systems at a late merger stage. The fraction of such systems (IV or V) in our sample is 51% and this is a consistent result with Veilleux et al. (2002). We also find 11% of the ULIRGs to be in a group environment.

In Figure 4.11 we show the fraction of ULIRGs in different interaction classes as a function of IR luminosity. We divide IR luminosities into three bins ($12.0 \leq \log(L_{IR}) < 12.25$, $12.25 \leq \log(L_{IR}) < 12.5$, $12.5 \leq \log(L_{IR})$); the number of sources in each bin is 84, 25 and 4, respectively. This Figure shows a hint for a negative trend for pre-mergers (IIIa and IIIb). The fraction of galaxies classified as IIIa and IIIb decreases from the first bin to the second, but IIIa galaxies increases in the highest L_{IR} bin. The fraction of mergers (IV) increases from the first bin to the second, but decreases in third bin. The fraction of old mergers (V) appear to be almost constant with luminosity. The fraction of triplets is constant in the first two bins, but increases in the third bin. The fractions in the highest luminosity bin is highly uncertain due to the very small number of sources. Therefore, we consider the trends including the the highest luminosity bin as unreliable. If we only take into account the first two luminosity bins then, it is clear that the fraction of pre-mergers have a negative trend while the mergers have a positive trend with increasing luminosity. This is a consistent result with Veilleux et al. (2002) who find a positive trend with the fraction of advanced mergers and IR luminosity.

The morphological properties of our sample confirms that ULIRGs are mostly either in pre-merger two galaxy systems or single galaxies in late/post merger phase. This is a consistent picture with the general idea that ULIRGs are triggered via strong interactions between galaxies.

4.3.3 THE SPECTRAL CLASSIFICATION OF OUR SAMPLE

The power sources of ULIRGs are high rates of star formation (e.g) and AGN activity (e.g Nardini et al., 2010). The traces of the dominant power source can be detected in optical spectra. Properties of the emission lines provide a practical tool to uncover the source of the ionization producing those lines. To identify the spectral classes of the ULIRGs in our sample we make

use of the available SDSS catalogs providing such a classification. SDSS spectroscopic pipeline classify objects as ‘broad-line AGNs’/‘quasars’, ‘galaxies’ or ‘stars’. We adopt this classification to identify the quasars in our sample.

Thomas et al. (2013) investigate emission line properties of SDSS sources that are already classified as ‘galaxies’ through the pipeline. They apply Baldwin-Phillips-Terlevich (BPT) diagnostics (Baldwin et al., 1981) to classify sources into: Seyfert, Low-Ionization Nuclear Emission Region (LINER), Star Forming Galaxy and Star Forming/AGN composite. We adopt the spectral classification given by Thomas et al. (2013) for the ULIRGs included in their galaxy sample. Some of the ULIRGs in our sample are not included in the sample of Thomas et al. (2013). These are mostly AGNs, but a few sources classified as ‘broad-line AGNs starbursts’ by the spectroscopic pipeline. To classify such sources we adopt the available line flux measurements in the SDSS database (see the footnotes of Table 4.1 for the SDSS references) and use a similar line diagnostic diagram as described by Thomas et al. (2013). The spectral classes listed in column (15) of Tables 4.1, 4.2 and 4.3. The spectral classes marked with a star are obtained in this work.

The distribution of the spectral classes is shown in Figure 4.12; it represents only 101 sources ULIRGs for which SDSS spectra are available. The fraction of purely star forming galaxies is 20%. The fraction of composite galaxies in our sample is 44%. The fraction of LINERs in our sample is 11%. LINERs are thought to be powered by AGNs (e.g Nagar et al., 2005), however other power sources can also produce LINER-like emission (e.g Maoz et al., 1998; Sarzi et al., 2010). Since there is a debate whether LINERs are low-luminosity AGNs or a separate class of objects, to be conservative in this work we separate LINERs from AGNs. 25% of the ULIRGs in our sample are AGNs (QSOs and Seyferts).

Most of the ULIRGs in our sample are classified as composite galaxies. In the BPT diagram, star forming and composite galaxies are separated by the empirical boundary of Kauffmann et al. (2003b). It is important to note that these are star forming galaxies possibly with a hidden AGN component. To be conservative we do not include composites to AGNs. Since both LINERs and composites may harbor an AGN, the given AGN fraction is only a lower limit.

Figure 4.13 shows the fraction of ULIRGs in different spectral classes as a function of IR luminosity. We use the same L_{IR} bins as in Figure 4.11. Each bin includes: 68 ($12.0 \leq \log(L_{IR}) < 12.25$), 23 ($12.25 \leq \log(L_{IR}) < 12.5$) and 10 ($12.5 \leq \log(L_{IR})$) sources. The fraction of AGNs grows with increasing L_{IR} . Star forming galaxies show an opposite trend, their fraction decreases with increasing L_{IR} . This is consistent with the results of previous studies showed that the fraction of AGNs in IR galaxies increases with higher IR luminosity (Kim et al., 1998; Goto, 2005). LINERs tend to be constant in each luminosity bin. Composites also tend to be almost constant in the first two bins, but they show a dramatic decrease in the highest luminosity bin. Again, since the LINERs and composites may have AGN contribution that is hidden in optical wavelengths, the AGN fractions in each luminosity bin represent the lower limit. However, the trends seen in Figure 4.13 still agree with known correlation between the AGN fraction and IR luminosity.

4.3.4 STELLAR MASSES - STAR FORMATION RATES - METALLICITIES AND OPTICAL COLORS OF ULIRGS

ULIRGs are very special galaxies that are selected according to their enormous IR luminosity, which means a rich dust content. Dust has an important role in galaxy growth and evolution because it is directly linked to the star formation and metals in the interstellar medium (ISM). The interplay between the dust and stellar content with Star Formation Rate (SFR) controls the

galaxy evolution. For normal star forming galaxies this is evident from the observed correlations between these parameters. Stellar mass (M_{star}) and SFR tightly correlates within $0 < z < 3$ range and normal star forming galaxies lie on the so called ‘main sequence’ (e.g. Noeske et al., 2007; Elbaz et al., 2007; Santini et al., 2009; Rodighiero et al., 2011; Tadaki et al., 2013). Stellar mass also strongly correlates with the metallicity (Z), massive galaxies show a higher metallicity than the less massive systems. The $M_{star} - Z$ relationship is confirmed for normal star forming galaxies in the local universe ($z \sim 0.15$) (Tremonti et al., 2004). Although there is not a strong relation between SFR and Z , metallicity is a function of SFR and M_{star} in the $M_{star} - Z - SFR$ plane (Lara-López et al., 2010; Mannucci et al., 2010). Recently, Santini et al. (2013) showed that there is a tight correlation between the dust mass and SFR and they introduce a fundamental relation between gas fraction, M_{star} and SFR. These relationships provide a basis for understanding the evolution of normal star forming galaxies. ULIRGs do not belong to this galaxy category and in order to explore their place in galaxy evolution we need to compare them with normal star forming galaxies. In the following, we investigate the position of ULIRGs in $M_{star} - SFR$, $M_{star} - Z$ relationships and in the color–magnitude diagram. Below we briefly outline the SDSS data used in this investigation.

Available SDSS photometric and spectral data allow us to obtain stellar masses, metallicities and optical colors of ULIRGs in our sample. SDSS DR10 (see Ahn et al., 2013) provides stellar masses, emission-line fluxes, stellar and gas kinematics, and velocity dispersions derived spectra of galaxies observed by Baryon Oscillation Spectroscopic Survey (BOSS). Following the spectroscopic pipeline (Bolton et al., 2012), the objects classified as a galaxy with a reliable redshifts are studied by several groups. ‘Portsmouth’ group derives photometric stellar-mass estimates (Maraston et al., 2012) and measure emission-line fluxes (Thomas et al., 2013).

Maraston et al. (2012) estimate stellar masses through SED fitting of stellar population models to u, g, r, i, z magnitudes. They use both passive (Maraston et al., 2009) and star-forming templates (Maraston, 2005) with Salpeter (1955) and Kroupa (2001) Initial Mass Functions (IMF). Maraston et al. (2012) use the fixed BOSS spectroscopic redshift values and do not include internal galaxy reddening in the SED fitting procedure. Wisconsin’ group also derives stellar masses via full spectral fitting (Chen et al., 2012). They use models based on stellar population models of Bruzual & Charlot (2003) with a Kroupa (2001) initial mass function. Chen et al. (2012) and Maraston et al. (2012) use different stellar population models based on different galaxy star formation histories, reddening, and initial mass function assumptions. Stellar masses given by Maraston et al. (2012) are ~ 0.2 dex smaller than the masses estimated by Chen et al. (2012) and for high signal to noise spectra the results from the both methods agree well (Chen et al., 2012). Since spectral data quality is an issue, in this work we prefer to adopt the stellar masses given by Maraston et al. (2012); however this preference does not change the results of this work. Maraston et al. (2012) obtain stellar masses for active and passive stellar population models. Since ULIRGs are actively star forming galaxies we adopt the stellar masses from ‘stellarMass-PortStarforming’³ catalog. These are listed in Table 4.5.

Thomas et al. (2013) fit stellar population synthesis models of Maraston & Strömbäck (2011) and Gaussian emission-line templates to the spectra by using the Gas AND Absorption Line Fitting (GANDALF) code of Sarzi et al. (2006). This code accounts for the diffuse dust on the spectral shape according to Calzetti (2001) obscuration curve. Thomas et al. (2013) correct for the diffuse dust extinction and provide de-reddened emission-line fluxes (this includes Galactic extinction). In the following analysis we adopt the emission-line fluxes from SDSS ‘emissionlinesPort’³ catalog.

³http://www.sdss3.org/dr10/spectro/galaxy_portsmouth.php

Star Formation Rate and Stellar Mass

IR luminosity measured from the SEDs (§4.2.2) between $8\mu\text{m} - 1000\mu\text{m}$ is the obscured emission from young stars that is re-emitted by dust, hence it can be converted to SFR. We use Eq. (4) given by Kennicutt (1998) to estimate the SFR based on L_{IR} , $\text{SFR}(\text{IR})$. This conversion assumes a Salpeter (1955) IMF and that L_{IR} is generated by recent star formation and re-emitted by dust. Even in the case of AGNs this assumption still valid to infer $\text{SFR}(\text{IR})$. This is because the contribution of the AGN, which is dominant at mid-IR, to the total L_{IR} is only a small fraction and the dominant energy source of L_{IR} is the FIR emission from star formation. Derived $\text{SFR}(\text{IR})$ values are tabulated in Table 4.5.

Figure 4.14 shows SFR versus M_{star} for 83 ULIRGs and one HLIRG for which M_{star} estimates are given by Maraston et al. (2012). The solid (black), dotted (blue) and dashed (red) lines represent the ‘main sequence’ of normal star-forming galaxies (SFGs) at $z \sim 0$ (Elbaz et al., 2007), $z \sim 1$ (Elbaz et al., 2007) and $z \sim 2$ (Daddi et al., 2007), respectively. For comparison we also show the 4 and 10 times above the $z \sim 2$ ‘main sequence’ (MS) relationship (top dashed lines). Local ULIRGs exhibit extremely high SFRs compared to normal SFGs with the same masses. It is evident from Figure 4.14 that local ULIRGs lie above the ‘main sequence’ up to $z \sim 2$. We note that the ‘main sequence’ relationships represent the total SFR obtained from L_{IR} and UV continuum, $\text{SFR}(\text{IR}+\text{UV})$. Since we do not include SFR from UV continuum, $\text{SFR}(\text{UV})$, our $\text{SFR}(\text{IR})$ estimates represent the minimum SFR. However, the total SFR is dominated by $\text{SFR}(\text{IR})$ and therefore the difference between $\text{SFR}(\text{IR})$ and $\text{SFR}(\text{IR}+\text{UV})$ should be small.

Previously, Elbaz et al. (2007) showed that (their Fig. 17) Arp220 (a well studied nearby ULIRG) exhibits a large off-set both from the ‘main sequence’ and $z \sim 1$ relationship. In the same Figure they also show that M82 (a starburst galaxy) lies above the local ‘main sequence’, but it is located in the 1σ confidence level of the $z \sim 1$ $\text{SFR}-M_{star}$ relationship. da Cunha et al. (2010) also compared local ULIRGs with local star forming SDSS galaxies and showed that ULIRGs have higher SFRs. In Figure 4.14 we show a large local ULIRG sample, 83 ULIRGs and one HLIRG. We find that local ULIRGs do not exhibit typical SFR for their masses even at $z \sim 2$. Compared to the ‘main sequence’ at $z \sim 0$, $z \sim 1$ and $z \sim 2$, on average ULIRGs have 86, 15 and 4 times higher SFRs, respectively. Local ULIRGs seem to be equally distributed around the dashed line representing 4 times above the $z \sim 2$ MS.

The ionizing radiation of recently formed young stars produce nebular lines such as $\text{H}\alpha$, hence it traces the unobscured radiation generated by star formation. Therefore, it can be used to derive SFR. As noted above Thomas et al. (2013) only correct for the diffuse dust extinction that affects the emission lines and stellar continuum, but they do not consider local dust component around nebular regions affecting the emission lines. This is mainly to avoid highly uncertain dust extinction values measured from Balmer decrement due to low S/N spectra. However, if we avoid this additional dust extinction we may underestimate the SFR based on $\text{H}\alpha$ luminosity, $\text{SFR}(\text{H}\alpha)$. Therefore we use the already de-reddened emission-line fluxes (only for diffuse dust component) given in ‘emissionlinesPort’³ catalog and obtain Balmer decrement. Predicted $\text{H}\alpha/\text{H}\beta$ ratio is 2.86 for 10^4 K (Osterbrock & Ferland, 2006), we adopt this value to estimate the local dust extinction around nebular regions and correct $\text{H}\alpha$ emission-line flux for the estimated extinction. Applying this additional extinction correction typically result in factor of 3.4 higher $\text{H}\alpha$ emission-line flux with large uncertainties. We apply Eq. (2) given in Kennicutt (1998) to obtain $\text{SFR}(\text{H}\alpha)$; listed in Table 4.5. Since in the presence of an AGN $\text{H}\alpha$ emission represents the photoionization from the AGN, we do not obtain $\text{SFR}(\text{H}\alpha)$ for AGNs and LINERs. Figure 4.15 shows a comparison between the $\text{SFR}(\text{IR})$ and $\text{SFR}(\text{H}\alpha)$ values (a). Note that error bars of $\text{SFR}(\text{H}\alpha)$ are dominated by the $\text{H}\alpha$ and $\text{H}\beta$ emission-line flux uncertainties. The

SFR(IR) values are systematically larger than SFR(H α) values, this difference is between factor of 2 and factor of 130 and the median difference is factor of 8. This indicates that even the highest possible dust extinction correction applied H α luminosity underestimates SFR at least by factor of 2. Therefore, it is evident that H α is not sufficient enough to trace SFR for ULIRGs and IR observations are crucial to infer SFR of these galaxies. In Figure 4.15 panels (b) and (c) show that the difference between the SFR(IR) and SFR(H α) does not depend on L_{IR} or M_{star} . In Figure 4.16 SFR(H α) versus M_{star} is shown. Although SFR(H α) underestimates SFR, Figure 4.16 shows that ULIRGs still lie above the local ‘main sequence’.

Stellar Mass and Gas Metallicity

Nuclear metallicities and stellar masses of normal star forming galaxies show a well established $M_{star} - Z$ correlation (Tremonti et al., 2004, hereafter T04). In the following, we compare the stellar masses and oxygen abundances of ULIRGs with the mass-metallicity relation of local star-forming SDSS galaxies obtained by Tremonti et al. (2004). Reliable metallicity constraints are difficult to obtain from broad-band SED fitting applied by Maraston et al. (2012). Therefore, in order to measure metallicity we adopt the relevant emission-line fluxes from Thomas et al. (2013). First, we apply the additional extinction based on Balmer decrement (see §4.3.4) to the adopted emission-line fluxes. Then we compute the line ratio $R_{23} = ([O II] \lambda\lambda 3726, 3729 + [O III] \lambda\lambda 4959, 5007) / H\beta$. We convert R_{23} values to oxygen abundances, (O/H), by following Eq. (1) of Tremonti et al. (2004). We list the derived oxygen abundances in Table 4.5. Note that this conversion and the R_{23} line ratio is only applicable to normal star forming galaxies, and they are not relevant for AGNs because the radiation from the AGN contributes to the line emission. Therefore we do not calculate metallicities for AGNs and to be conservative we also exclude LINERs from this investigation. After excluding AGNs and LINERs we are left with 54 ULIRGs and one HLIRG for which emission-line fluxes given by Thomas et al. (2013).

The $M_{star} - Z$ distribution of our ULIRG sample is shown in Figure 4.17 (top). The error bars of the oxygen abundances represent the uncertainties associated with emission-line fluxes and additional extinction obtained from Balmer decrement. The black solid line is the $M_{star} - Z$ relationship, Eq. (3) given by Tremonti et al. (2004). The vast majority of ULIRGs (51 out of 54) have lower metallicities compared to the normal star forming SDSS galaxies at similar masses. In the bottom panel of Figure 4.17, the distribution of the residuals of the measured oxygen abundances to the expected oxygen abundances from T04 relationship is displayed. The distribution of the residuals are comparable to the over plotted Gaussian distribution with standard deviation $\sigma = 0.20$ dex, therefore we consider the shift of ULIRGs from the T04 relationship as 0.20 dex. Normal star forming SDSS galaxies exhibit a scatter between 0.07 dex – 0.2 dex with a mean of 0.1 dex (Tremonti et al., 2004) around the stellar mass–metallicity relation. The scatter of normal star forming galaxies from this relationship is mostly attributed to the observational errors in the mass and metallicity measurements (Tremonti et al., 2004). The scatter of ULIRGs (0.20 dex) is equal to the upper limit of the scatter of normal star forming galaxies. The median error in metallicity measurements of ULIRGs is large ~ 0.17 dex, while the median error in mass measurements is smaller ~ 0.07 dex. If we consider the lower error bars, it is very likely that the metallicity distribution of ULIRGs may shift even lower values and this may result in a larger scatter with respect to T04 relationship. However, If we consider the upper error bars only 9 ULIRGs may move above T04 relationship and most of the ULIRGs would still lie below this relationship.

Color – Magnitude Distribution of ULIRGs

The color versus magnitude distribution, the so called ‘Color-Magnitude Diagram’ (CMD), of galaxies out to $z \sim 1$ show two separate distributions (e.g Hogg et al., 2003; Blanton et al., 2003; Baldry et al., 2004, 2006; Cooper et al., 2006; Muzzin et al., 2012): (1) ‘red sequence’ of early type galaxies, (2) ‘blue cloud’ of late type galaxies. The red sequence galaxies are bulge-dominated, more massive, non-star-forming, passive galaxies (Blanton et al., 2003, 2005; Hogg et al., 2003; Baldry et al., 2006; Driver et al., 2006, e.g.). The blue cloud galaxies are disk-dominated, less massive, actively star forming galaxies (Kauffmann et al., 2003a; Brinchmann et al., 2004; Wyder et al., 2007, e.g.). Observations show that while the number density of blue cloud galaxies has stayed almost constant, the red sequence galaxies has doubled from $z \sim 1$ to $z \sim 0$ (Bell et al., 2004; Faber et al., 2007). This suggest that star forming disk galaxies at $z \sim 1$ evolve to local passive galaxies. Such an evolution involves different physical processes that change galaxy morphology and quench star formation. As galaxies go through a transition phase from blue cloud to red sequence they reside in the region in between, the so called ‘green valley’.

The transition of a late-type galaxy to an early-type includes physical processes that are not fully understood yet. Mergers and AGN feedback are among the proposed star formation quenching mechanisms (e.g Barnes & Hernquist, 1996; Hopkins et al., 2006, 2008a). Since ULIRGs are both merging systems and mostly host an AGN they are good candidates for evolving galaxies from blue cloud to red sequence. In the following we explore the location of our ULIRG sample in the color-magnitude diagram of local SDSS galaxies.

For this investigation we have selected a local comparison sample from SDSS DR 10 database. We selected sources classified as galaxies that are brighter than $r_{Petrosian} < 17.7$ and have spectroscopic redshifts within $0.018 < z < 0.260$ interval ($z_{median} = 0.1$). We also select galaxies that have photometric measurements in u , g and r bands. Our selection criterion leads to 499953 galaxies. Throughout this analysis we use the Galactic extinction corrected ‘modelMag’ measurements from SDSS DR10 ‘PhotoObj’ catalog. K -corrections are calculated using the *kcorrect* code v4.2 of Blanton & Roweis (2007). For comparison reasons with previous studies, we derive K -corrections for a fixed bandpass shift by $z=0.1$. The absolute magnitudes and colors are denoted with $M_r^{0.1}$ and $u^{0.1} - r^{0.1}$, respectively; these are tabulated in Table 4.5. Figure 4.18 shows CMD, ($u^{0.1} - r^{0.1}$) vs $M_r^{0.1}$, of the comparison and our ULIRG samples. The contours represent the number density of the comparison sample. The distribution of local SDSS galaxies shows two separate distributions: the red sequence and the blue cloud. We determine the color-magnitude relation of the red sequence and the blue cloud by following Baldry et al. (2004). We divide the comparison sample into 16 $M_r^{0.1}$ bins from -23.5 to -15.5; bin size is 0.5 mag. For each $M_r^{0.1}$ bin we fit the color distribution with a double Gaussian and obtain mean and variance for the red and the blue distributions. We adopt the color function and the absolute magnitude functions given by Baldry et al. (2004) and obtain the color-magnitude relations as:

$$(u^{0.1} - r^{0.1})_{red-sequence} = 2.559 + (-0.045) \times (M_r^{0.1} + 20) + (-0.298) \times \tanh\left(\frac{M_r^{0.1} - (-17.757)}{2.833}\right), \quad (4.1)$$

$$(u^{0.1} - r^{0.1})_{blue-cloud} = 2.831 + 0.066 \times (M_r^{0.1} + 20) + (-2.180) \times \tanh\left(\frac{M_r^{0.1} - (-22.999)}{6.786}\right). \quad (4.2)$$

The red and blue dashed lines in Figure 4.18 represent the red and blue sequence color-magnitude relations, respectively. To derive the color-magnitude relation of the green valley we locate the

minimum in the double Gaussian functions. We then fit a linear plus a tanh function, the same function used to fit red and blue sequence relations, to the minimums. The resulting relation of the green valley is:

$$(u^{0.1} - r^{0.1})_{green-valley} = 2.232 + (-0.096) \times (M_r^{0.1} + 20) + (-0.131) \times \tanh\left(\frac{M_r^{0.1} - (-16.447)}{0.492}\right). \quad (4.3)$$

We choose the width of the green valley to be 0.1. The green dashed line in Figure 4.18 represents Equation 4.3, the solid green lines represent the 0.1 mag width.

In Figure 4.18 the color-magnitude distribution of 91 ULIRGs and one HLIRG in our sample is shown on top of the contours of the comparison sample. From our ULIRG sample 11 are in the red sequence, 6 are in the green valley and 75 are in the blue cloud. The 81% of the ULIRGs are located in ‘blue cloud’, 12% are in ‘red sequence’ and only 7% are in ‘green valley’. Two of the 6 ULIRGs in the ‘green valley’ host an AGN. 39% (35 of 91) of the ULIRGs are located out of the 90% level contour. The median absolute magnitude and the $u^{0.1}-r^{0.1}$ color of our ULIRG sample are $M_r^{0.1} = -21.37 \pm 0.71$ and $u^{0.1}-r^{0.1} = 1.94 \pm 0.63$. The median absolute magnitude of the comparison SDSS sample is $M_r^{0.1} = -20.55 \pm 1.12$. Compared to the local SDSS sample absolute magnitudes of ULIRGs are 0.82 mag brighter. The median $u^{0.1}-r^{0.1}$ of the comparison sample is $u^{0.1}-r^{0.1} = 2.56 \pm 0.55$, so ULIRGs have 0.62 mag brighter colors. As ULIRGs are selected by their star-formation powered IR luminosity we expect them to be bright optical sources. So in a sense, their bright optical colors are consistent with their identification criteria.

Chen et al. (2010) study color-magnitude properties of a sample of 54 ULIRGs from IRAS 1 Jy sample (Kim et al., 1998) and show that ULIRGs are mostly in the ‘blue cloud’. They also find that compared to SDSS galaxies local ULIRGs are 0.2 mag bluer in $g - r$. Compared to Chen et al. (2010) we study a larger ULIRG sample and find consistent results; we find very similar color–magnitude properties. The distribution of our ULIRG sample across the color–magnitude diagram is also similar to the distribution shown by Chen et al. (2010). We find a smaller fraction for the ULIRGs that lie out of the 90% level contour. While they do not find any AGN hosting ULIRGs in the ‘green valley’ we find two ULIRGs.

We note that the colors of the AGN hosting ULIRGs have a contribution from the central AGN. As shown by Chen et al. (2010) removing this AGN contribution would affect the colors. Of course the amount of AGN contribution depends on the source, but based on the comparison given by Chen et al. (2010) we predict that removing AGN contribution would not alter the main color properties of our ULIRG sample. Therefore, we do not attempt to remove the AGN contribution for the AGN hosting ULIRGs.

4.4 DISCUSSION

4.4.1 FIR COLORS

In panel (d) of Figure 4.8 four sources, J1639245+303719, J0159503+002340, J1356100+290538 and J1706529+382010, exhibit extreme $\log(F(140\mu\text{m})/F(160\mu\text{m})) > 0.9$ colors compared to the models. For these cases we check the reliability of the flux measurements from the AKARI catalogs. In all of these cases while the $90\mu\text{m}$ flux is highly reliable, the $65\mu\text{m}$, $140\mu\text{m}$ and $160\mu\text{m}$ flux measurements are low quality and the uncertainty of the $160\mu\text{m}$ flux is not given. In such cases we assumed the uncertainty as the 25% of the given flux measurement, but it seems these uncertainties could be even larger. Since the $90\mu\text{m}$ flux measurements are secure we still consider the measured IR luminosities as reliable. The SEDs of three cases, J1639245+303719,

J1356100+290538 and J1706529+382010, show that their flux densities at $140\mu\text{m}$ is ~ 0.8 dex larger than that of the models. The SED of J0159503+002340 also exhibits a large difference (> 1 dex) between the observed and model flux at $160\mu\text{m}$. We also check five more sources with $\log(F(140\mu\text{m})/F(160\mu\text{m})) > 0.5$; J1603043+094717, J0030089-002743, J1102140+380240, J1346511+074720 and J2307212-343838. The SEDs of J0030089-002743, J1102140+380240, J1346511+074720 and J2307212-343838 show that their flux densities at $140\mu\text{m}$ is 0.5-0.8 dex larger than that of the models. The SED of JJ1603043+094717 also exhibits a 0.6 dex difference between the observed and model flux at $160\mu\text{m}$. These large differences between the observed colors and that are expected from the SED models can be attributed to the low quality $140\mu\text{m}$ and $160\mu\text{m}$ flux measurements.

As mentioned in §4.3.1 the SED models covers only the $\log(F(140\mu\text{m})/F(160\mu\text{m}))$ color range between -0.5425 – -0.2135 and therefore, in panel (c) the three sources, J1202527+195458, J1559301+380843, and J1502320+142132 appear as outliers with $\log(F(140\mu\text{m})/F(160\mu\text{m})) < -0.58$. The SEDs of these sources show that their $65\mu\text{m}$ fluxes ~ 0.5 dex lower than that of the models. Although the quality of $65\mu\text{m}$ flux measurements are low for these sources, however it is more likely that the the limited parameter range of the models is the main reason for their large deviation from the models. The SED models of Dale & Helou (2002) represents especially the IR SEDs of normal star forming galaxies and they are not specifically developed for ULIRGs. Therefore, as shown in Rieke et al. (2009) they might differ from the observed SEDs of local ULIRGs. Rieke et al. (2009) compare the observed SEDs of five local purely star forming ULIRGs with the models of Dale & Helou (2002) and show that FIR peak of the models are broader compared to observations. If the intrinsic SEDs of ULIRGs are more peaked compared to the templates of Dale & Helou (2002) as shown by Rieke et al. (2009), then we might expect to have a wider distribution for the FIR colors and this might explain the large scatter seen panels (c) and (d).

The differences between the observed and model colors in Figure 4.8 indicate that the SED templates of Dale & Helou (2002) may result uncertainties in the IR luminosities. However, for all sources the $90\mu\text{m}$ flux measurements are highly reliable and even for some cases especially the $140\mu\text{m}$ and $160\mu\text{m}$ flux measurements show large deviations from the models, the SEDs show that the IR luminosity is mostly underestimated. Therefore, we consider the IR luminosity measurements based on the SED templates of Dale & Helou (2002) are reliable to identify ULIRGs. Another evidence supporting this is the high number of already known ULIRGs in our sample that are identified based on these SED templates.

4.4.2 INTERACTION CLASSES

In §4.3.2 the interaction classes of 70 sources are adopted from literature (Veilleux et al., 2002; Hwang et al., 2007) and 57 sources classified in this work based on visual inspection. Although visual classification is a subjective method, we prefer it due to its practical application. Two classifiers independently classified each source and for most of the cases there was good agreement. There was a disagreement between the classifiers only for a few cases that are single nucleus systems at higher redshifts. In such systems the identification of the disturbed morphologies or weak interaction signs is difficult. However, the number of such systems are only five and most of them are not included in our statistics due to the applied redshift limit. Even if they were included in our statistics, they would be classified as NI instead of V and this would only decrease the number of sources classified as old mergers. Such a change would not change the high percentage of IV and V systems in the overall population.

Wide binary (IIIa) systems have the largest uncertainties because, most of the companion

galaxies do not have spectroscopic redshifts. However, usually wide binary galaxies have similar colors and they show interaction signs. Therefore the chance coincidences are low and the assumed physical connection is highly likely. Even if most of the IIIa systems were instead IV, the dominance of the mergers still holds. So the overall conclusion of morphology investigation in §4.3.2, that is the vast majority of ULIRGs in the local universe are single nucleus ongoing/old mergers, is not affected by the disagreements of the classifiers or unconfirmed redshifts of the companion galaxies in wide binaries.

4.4.3 AGN FRACTION OF OUR ULIRG SAMPLE

In §4.3.3 we investigate the optical spectral types of the ULIRGs in our sample. The classification of Star Forming galaxies, composites, LINERs and Seyferts are based on empirical emission line diagnostics. ULIRGs are dust-rich systems and dust extinction at optical wavelengths is high. Therefore, the dusty nature of ULIRGs brings a large uncertainty to their optical emission line diagnostics. Nardini et al. (2010) use the rest-frame 5-8 μ m spectra to disentangle the contribution of star formation and AGN in ULIRGs. As shown by Nardini et al. (2010) optical diagnostics do not provide reliable information on the presence of AGN. They trace obscured AGN in some LINERs and even some star forming galaxies. Therefore, as stated earlier our spectral classification provides only a lower limit on the AGN fraction. This brings a large uncertainty to the AGN fraction per L_{IR} bin presented in Figure 4.13. It is very highly likely that most of the composites and LINERs may have AGN component. If all of the LINERs and composites had AGN contribution then the correlation between the AGN fraction and L_{IR} would be still valid.

Assuming all of the LINERs and composites as AGNs may be an unrealistic overestimation because we would expect at least some fraction of the low luminosity ULIRGs to be star formation dominated. To investigate the hidden AGNs among such sources in our sample we look at the result of the mid-IR diagnostic applied by Nardini et al. (2010). In total we have 31 overlapping sources with their sample. Our main interest is the AGN component of the star forming galaxies, composites and LINERs in our sample. For those sources we adopt the AGN bolometric contribution parameter given by Nardini et al. (2010) (α_{bol} parameter in their Table 1). Only one star forming galaxy (J0900252+390400) in our sample seem to have a significant AGN contribution based. If we consider this source as an AGN instead of a star forming galaxy, this would not affect the correlation of AGNs and the anti-correlation of star forming galaxies with IR luminosity. Also it would have a negligible affect on the fraction of AGNs; fraction of AGNs would increase to 26% and the fraction star forming galaxies would decrease to 19%.

4.4.4 THE OFFSET OF ULIRGS FROM THE MAIN SEQUENCE OF STAR FORMING GALAXIES

Star formation rate and M_{star} tightly correlates from $z \sim 0$ to $z \sim 2$; the slope is between ~ 0.6 and ~ 1.0 (mostly depends on the galaxy sample) but the normalization decreases with redshift. This indicates that the overall SFR increases from $z \sim 0$ to $z \sim 2$ and SFGs were forming stars more actively in the past compared to lower redshift galaxies at the same masses. Observations indicate that high redshift SFGs contain higher molecular gas reservoir (e.g Daddi et al., 2010; Tacconi et al., 2010), and therefore the star formation efficiency is higher at $z \sim 2$; in time this reservoir is used up and result in lower SFRs at $z \sim 0$. Figure 4.14 clearly demonstrates that local ULIRGs are outliers with respect to the ‘main sequence’ of the normal star-forming galaxies up to $z \sim 2$. Local ULIRGs are already known to be outliers compared to the local ‘main sequence’

(Elbaz et al., 2007). This is not surprising because, in the first place, ULIRGs are defined by their enormous IR luminosities powered by intense star-formation and in order to be defined as ULIRGs they should have $172 \leq \text{SFR}(\text{IR}) \leq 1721$. So their position on the y-axis is a pure selection effect and we expect them to have higher SFRs compared to normal star forming galaxies. We note that Figure 4.14 includes type 2 AGNs, LINERs and composites. As mentioned earlier, even the AGN has a contribution to L_{IR} , the measured IR luminosities are mainly dominated by the FIR emission. A possible AGN contribution can only cause a small increase (a few per cent at most) in SFR(IR). The offset of the local ULIRGs from the ‘main sequence’ relations from $z \sim 0-2$ is relatively large can not be attributed to any possible AGN contribution in the SFR(IR) estimates.

Normal starburst galaxies are also outliers off the ‘main sequence’ at $z \sim 0.7$ (Guo et al., 2013) and at $z \sim 2$ (Rodighiero et al., 2011). Guo et al. (2013) show their best fit ‘main sequence’ and the ‘main sequence’ relationships given by Elbaz et al. (2007) and Daddi et al. (2007) in their Fig. 7 where they report starburst galaxies as outliers. Since the local ULIRG sample lie above these ‘main sequence’ relationships and their galaxy sample, it can be concluded that compared to normal starburst galaxies at $z \sim 0.7$ local ULIRGs exhibit higher SFRs. Rodighiero et al. (2011) define off-sequence galaxies (see their Fig. 1) as the ones lying factor of 10 above the $z \sim 2$ SFR– M_{star} relation of Daddi et al. (2007). Compared to these extreme outliers at $z \sim 2$, as seen in Figure 4.14, 90% of the local ULIRGs have lower SFRs and only 10% have comparable SFRs. SMGs, often referred as high redshift analogues of local ULIRGs, are also known to be outliers compared to $z \sim 2$ SFR– M_{star} relation (Tacconi et al., 2008; Daddi et al., 2007, 2009; Takagi et al., 2008). Compared to massive SFGs at the same masses SFRs of SMGs are 10 times higher (Daddi et al., 2007). As noted by Daddi et al. (2007) SMGs at $z \sim 2$ and local ULIRGs have similar properties; both are rare sources and outliers in SFR– M_{star} relations. However compared to the location of SMGs shown by Daddi et al. (2007) (their Figure 17b) local ULIRGs occupy a wider M_{star} range and they are closer to the $z \sim 2$ SFR– M_{star} relation.

As expected galaxies with similar IR luminosities should have similar SFRs and positions in the SFR– M_{star} diagram. In particular we call attention to the role of the stellar mass as the distinguishing parameter. At this point it is important to consider the uncertainties of the stellar masses to interpret Figure 4.14. ULIRGs in our sample have moderate stellar masses within $9.42 < \log(M_{\text{star}}(M_{\odot})) < 11.61$ range where the median is 10.41. We compare the adopted stellar masses from Maraston et al. (2012) with the M_{star} estimates given by previous ULIRG studies. Rodríguez Zaurín et al. (2010) provide M_{star} estimates for 36 local ULIRGs derived by performing spectral synthesis modeling to high quality optical spectra. We have three overlapping sources with their sample: J0900252+390400, J1021426+130657, J1052232+440849 and they report 1.0 dex, 0.3 dex and 0.5 dex higher stellar masses, respectively. However, we note that J0900252+390400 is the lowest mass ULIRG in our sample, and as mentioned in §4.4.3 it has an AGN. Therefore we consider the difference of 1 dex in M_{star} for this particular object as an exceptional case. da Cunha et al. (2010) also provide M_{star} estimates for a sample of 16 purely star forming ULIRGs based on full SED modeling including UV to FIR wavelengths. We have one common source with this sample (J1213460+024844); and for this source the M_{star} estimates agree well, their estimate is just 0.06 dex higher than the adopted value from Maraston et al. (2012). As shown by Rodríguez Zaurín et al. (2010) ULIRGs contain different stellar populations (very young, young, intermediate-young and old stellar populations) at the same time and their optical light is mainly dominated by the less massive young stellar populations. Therefore, we expect the stellar mass estimates of ULIRGs to be highly dependent on the followed approach (SED or spectral fitting) together with the used data and the assumed star

formation histories (SFHs). Especially M_{star} estimates of ULIRGs like complex galaxies from SED fitting can be very sensitive to assumed SFHs. As shown by Michałowski et al. (2012) using multicomponent SFHs that fit young and old populations result in systematically higher stellar masses compared to exponentially declining SFH. Therefore, it is very likely that the adopted M_{star} values in this work are underestimated. Obtaining the most robust stellar mass estimates of ULIRGs is beyond the scope of this paper. But, with the available data we are able to assign an uncertainty limit. Considering the M_{star} differences of three (since it is an exception case we exclude J0900252+390400) ULIRGs with respect to the values reported by Rodríguez Zaurín et al. (2010) and da Cunha et al. (2010) all of the adopted M_{star} in this work values might be underestimated by 0.06 dex–0.5 dex. A natural consequent question is the affect of this underestimate in Figure 4.14. To be conservative we may assume that M_{star} are underestimated by 0.5 dex. As shown in Figure 4.19, if we shift stellar masses by 0.5 dex ULIRGs are still exhibit a large offset from the $z \sim 0$ and $z \sim 1$ ‘main sequence’, but they are consistent with the $z \sim 2$ ‘main sequence’. This shows that even the stellar masses adopted in Figure 4.14 are underestimated, this does not change the main conclusion that ULIRGs are outliers compared to the $z \sim 0$ and $z \sim 1$ ‘main sequence’. However, it indicates that their offset from the $z \sim 2$ ‘main sequence’ is very likely due to their underestimated stellar masses. Of course Figure 4.19 is a simple illustration and might not reflect the M_{star} distribution of ULIRGs at all, thus we caution against its interpretation.

4.4.5 COMPARISON OF SFRs WITH OBSERVATIONS AND SIMULATIONS OF MERGERS

ULIRGs are interacting systems and they are mostly ongoing/late mergers and their extreme SFRs are generally attributed to merger events. Observations support this link, SFRs of local ULIRGs are consistent with the observed enhanced SFR of mergers (e.g. Ellison et al., 2008, 2013). Moreover, the role of merger processes on triggering SFR is a general prediction of merger models showing that major mergers cause nuclear gas inflows (Barnes & Hernquist, 1991, 1996) and these inflows generate intense SFR that peaks around when merging galaxies coalescence (e.g Di Matteo et al., 2005, 2007; Springel et al., 2005; Montuori et al., 2010; Torrey et al., 2012). Merger models show that star formation activity increases after the first per-center passage and reaches its maximum level when two galaxies coalescence. In this picture we expect to observe lower SFRs in the pre-merger (widely or closely separated binaries) ULIRGS compared to the ULIRGs in the coalescence phase. In order to check if the observed SFRs of our ULIRG sample is consistent with this prediction, in the top panel of Figure 4.20 SFR(IR) distribution of ULIRGs is shown as a function of interaction class (defined in §4.3.2). We find that ULIRGs do not show a systematic difference in SFR(IR) for different interaction stages. We do not find coalescence stage as the peak of the SFR as suggested by general merger simulations (e.g Torrey et al., 2012). Since SFR is correlated with stellar mass, in the bottom panel of Figure 4.20 we show specific star formation rate, sSFR ($SFR(IR)/M_{star}$), as a function of interaction class. This panel shows a similar distribution as the top one, sSFR does not depend on the interaction stage. Of course this does not mean that ULIRGs are completely inconsistent with the merger models, because we are not tracing single merger events in time as simulations do. Instead we are looking at different snapshots of merger events for different sources. Therefore, Figure 4.20 is rather consistent with the observations Rodríguez Zaurín et al. (2010) showing that ULIRGs have complex multi-stellar populations. Probably, in some ULIRGs the SF activity triggered at pre-coalescence epochs are comparable with that of the others coalescence phase, thus we see a

similar distribution for different interaction phases.

Merger simulations also predict that nuclear gas inflows in the periods prior to increasing SFR epochs cause nuclear metallicity dilution, but following that high SFRs cause metallicity enhancement (e.g Torrey et al., 2012). So, the overall metallicity change has a rather complex fluctuating nature as the merger progress. In Figure 4.21 we show the oxygen abundance distribution of ULIRGs as a function of merger stage. Again the three distributions (pre-merger, mergers and post-mergers) overlap and do not show a significant difference. As discussed above, we do not probe the evolution of oxygen abundances for individual ULIRGs as simulations do, thus based on Figure 4.21 we can not conclude any inconsistency with their predictions. However, when we compare oxygen abundances of ULIRGs with that of normal SFGs we find that they systematically have lower oxygen abundances and this is consistent with the predictions of the numerical simulations (e.g Torrey et al., 2012). Similarly, interacting galaxies such as close pairs (e.g Kewley et al., 2006; Ellison et al., 2008) do not lie on the $M_{star} - Z$ relation. These interacting, merging galaxies exhibit a lower metallicity compared to the non-interacting normal SFGs.

4.4.6 ULIRGS IN THE FUNDAMENTAL METALLICITY–MASS–SFR PLANE

Figure 4.17 shows that ULIRGs have lower metallicities with respect to the $M_{star} - Z$ relation. The possible systematic uncertainties discussed in §4.4.4 are relevant to Figure 4.17, too. However, since $M_{star} - Z$ relation is rather flat with increasing stellar mass, a shift of 0.5 dex in M_{star} does not change the observed scatter of ULIRGs.

Previously, (Rupke et al., 2008) have already shown that ULIRGs have under-abundant compared to the SFGs on the $M_{star} - Z$ relation. The position of our ULIRG sample with respect to the $M_{star} - Z$ relationship of normal SFGs is consistent with the results of (Rupke et al., 2008). In Figure 4.14 indicates that local ULIRGs have comparable SFRs with $z \sim 2.0$ galaxies and it is known that $z \sim 2.2$ galaxies have lower metallicities compared to local galaxies with the same masses (Erb et al., 2006; Tadaki et al., 2013). A similar result also found for even higher redshift galaxies $z=3-4$ (Maiolino et al., 2008; Mannucci et al., 2009).

Star forming galaxies up to $z \sim 2.5$ follow the fundamental metallicity relation (FMR), a tight relation between M_{star} , gas metallicity and SFR (Mannucci et al., 2010). This relation indicates that metallicity decreases with increasing SFR for low M_{star} , but for high M_{star} it does not change with SFR. So, according to FMR at a fixed mass we expect to have lower metallicities with increasing SFR. In order to understand if the lower metallicities of ULIRGs are due to higher SFRs we need to check if they are on the FMR plane. We base this investigation on the FMR defined by Mannucci et al. (2010) for local SDSS galaxies. Following (Mannucci et al., 2010) we divide 55 (H)/ULIRGs into eleven mass bins of 0.15 dex from $\log(M_{star}(M_{\odot}))=9.70$ to 10.90. We only consider the bins containing at least 1 galaxy, this selection results in 9 mass bins. To be consistent with Mannucci et al. (2010) we use SFR($H\alpha$) estimates obtained in §4.3.4. Since ULIRGs typically have larger SFRs, we extrapolate Eq. (2) of Mannucci et al. (2010) up to $\log\text{SFR}(H\alpha)=2.4$. Left panel in Figure 4.22 shows the local FMR (Eq. 2 of Mannucci et al., 2010) for these mass bins (color coded), open circles show the distribution of ULIRGs in each mass bin (color coded with respect to mass). Right panel in Figure 4.22 shows the residuals between the measured metallicities of ULIRGs and FMR. These are the median values in each bin, but the first and the last bin represent residuals of single measurements. Without considering the uncertainties, the residuals of ULIRGs from FMR are between 0.13 dex – 0.26 dex. This is of course larger than the dispersions of the local SDSS galaxies that is ~ 0.05 dex, but it indicates

that local ULIRGs are consistent with FMR. We also note that, the residuals of local ULIRGs are comparable with that of high redshift $z \sim 2$ galaxies (Mannucci et al., 2010). If we consider the uncertainties, the largest residual is ~ 0.5 dex, this might indicate an inconsistency with FMR. We used the same recipe to infer oxygen abundances and SFRs therefore, the off-set of 0.5 dex can not be due to metallicity or SFR measurements themselves. However, the largest contribution to the metallicity uncertainties directly comes from the emission-line flux uncertainties and this point can only be addressed with higher quality data. So the large uncertainties showing ~ 0.5 dex residuals do not necessarily mean a real off-set from FMR. But, also note that ULIRGs are interacting rare local galaxies with very high SFR, and they are expected to show a large scatter around FMR (Mannucci et al., 2010).

4.4.7 ULIRGS IN COLOR – MAGNITUDE DIAGRAM

In §4.3.4 we found that local ULIRGs are optically bright and blue galaxies. As noted before this is consistent with their starburst nature. On the other hand, ULIRGs are dusty galaxies and one might expect them to have redder colors due to dust extinction. However, as suggested by (Chen et al., 2010) dust distribution in ULIRGs might not be uniform and therefore, their stellar light is not completely obscured.

The low fraction of ULIRGs in the ‘green valley’, as suggested by Chen et al. (2010), indicates that ULIRGs are rapidly star forming galaxies and they are not evolved into a transition phase yet. The evolution tracks of ULIRGs in the color–magnitude diagram is beyond the scope of this paper, therefore for a discussion on this topic we refer Chen et al. (2010).

4.5 CONCLUSIONS

We identified ULIRGs in the *AKARI* all-sky survey by crossmatching *AKARI* catalogs with SDSS DR 10 and 2dFGRS. With the advantage of *AKARI* and available SDSS data, we are able to investigate morphologies, stellar masses, SFRs, gas metallicities and optical colors of a large sample of local ULIRGs. We have examined the $\text{SFR} - M_{\text{star}}$, $M_{\text{star}} - Z$, $\text{SFR} - M_{\text{star}} - Z$ and color–magnitude relations of our local ULIRG sample. The following summarizes the main conclusions from this work:

- A sample of 134 ULIRGs and one HLIRG with $F(90\mu\text{m}) \geq 0.22\text{Jy}$ have been identified in the *AKARI* all-sky survey. 48 of the ULIRGs and one HLIRG are newly identified in the *AKARI* all-sky survey based on the spectroscopic redshifts from SDSS DR10 and 2dFGRS. The redshift range of our ULIRG sample is $0.050 < z < 0.487$ and the median redshift is 0.177.
- In the redshift ($z < 0.27$) limited sample of 113 ULIRGs 96% show interaction features either between two galaxies or in a single system. Only 4% are interacting triplets. 44% of the ULIRGs are two galaxy systems with strong tidal tails, bridges. 51% of the ULIRGs are ongoing/post mergers showing strong tidal tails or disturbed morphology. Our results support the known picture of ULIRGs as major mergers.
- Based on the adopted optical emission line diagnostics, we confirm the known trend of increasing AGN fraction with higher IR luminosity but with a greater significance.
- Compared to $\text{SFR}(\text{IR})$, $\text{SFR}(\text{H}\alpha)$ strongly underestimates SFR of local ULIRGs, by a factor of ~ 8 . This implies that IR observations provide the best estimate of SFR for highly star forming dusty galaxies.

- ULIRGs have significantly higher star formation rates compared to the ‘main sequence’ of normal SFGs up to $z \sim 2$. Local ULIRGs have 86, 15 and 4 times higher SFRs compared to ‘main sequence’ galaxies with similar mass at $z \sim 0$, $z \sim 1$ and $z \sim 2$, respectively. 90% of the local ULIRGs have lower SFRs compared to the off-main sequence galaxies at $z \sim 2$.
- We find that ULIRGs have lower gas metallicities compared to the $M_{star} - Z$ relation of normal star forming galaxies; hence we confirm previous studies. We also find that local ULIRGs follow the FMR with high dispersions between 0.13 dex–0.5 dex, that is similar to that of high redshift ($z \sim 2-3$) galaxies.
- Compared to previous studies we investigate color properties of a larger ULIRG sample and find that 81% of the ULIRGs are in ‘blue cloud’, 12% are in ‘red sequence’ and 7% are in ‘green valley’. Based on the optical colors we confirm that the vast majority of local ULIRGs are rapidly star forming blue galaxies and they are not in the evolution stage between the blue cloud and red sequence.

We provide the largest local ULIRG comparison sample to further study the M_{star} , SFRs, gas metallicities and optical colors of high redshift ULIRGs.

The authors thank Marianne Vestergaard and Jens Hjorth for their comments. The Dark Cosmology Centre is funded by the Danish National Research Foundation. AKARI is a JAXA project with the participation of universities and research institutes in Japan, the European Space Agency (ESA), the IOSG (Imperial College, UK, Open University, UK, University of Sussex, UK, and University of Groningen, Netherlands) Consortium, and Seoul National University, Korea. Funding for SDSS-III has been provided by the Alfred P. Sloan Foundation, the Participating Institutions, the National Science Foundation, and the U.S. Department of Energy Office of Science. The SDSS-III web site is <http://www.sdss3.org/>. SDSS-III is managed by the Astrophysical Research Consortium for the Participating Institutions of the SDSS-III Collaboration including the University of Arizona, the Brazilian Participation Group, Brookhaven National Laboratory, Carnegie Mellon University, University of Florida, the French Participation Group, the German Participation Group, Harvard University, the Instituto de Astrofísica de Canarias, the Michigan State/Notre Dame/JINA Participation Group, Johns Hopkins University, Lawrence Berkeley National Laboratory, Max Planck Institute for Astrophysics, Max Planck Institute for Extraterrestrial Physics, New Mexico State University, New York University, Ohio State University, Pennsylvania State University, University of Portsmouth, Princeton University, the Spanish Participation Group, University of Tokyo, University of Utah, Vanderbilt University, University of Virginia, University of Washington, and Yale University. The Digitized Sky Surveys were produced at the Space Telescope Science Institute under U.S. Government grant NAG W-2166. The images of these surveys are based on photographic data obtained using the Oschin Schmidt Telescope on Palomar Mountain and the UK Schmidt Telescope. The plates were processed into the present compressed digital form with the permission of these institutions. The National Geographic Society - Palomar Observatory Sky Atlas (POSS-I) was made by the California Institute of Technology with grants from the National Geographic Society. The Second Palomar Observatory Sky Survey (POSS-II) was made by the California Institute of Technology with funds from the National Science Foundation, the National Geographic Society, the Sloan Foundation, the Samuel Oschin Foundation, and the Eastman Kodak Corporation. The Oschin Schmidt Telescope is operated by the California Institute of Technology and Palomar Observatory. The UK Schmidt Telescope was operated by the Royal Observatory Edinburgh, with funding from the UK Science and Engineering Research Council (later

the UK Particle Physics and Astronomy Research Council), until 1988 June, and thereafter by the Anglo-Australian Observatory. The blue plates of the southern Sky Atlas and its Equatorial Extension (together known as the SERC-J), as well as the Equatorial Red (ER), and the Second Epoch [red] Survey (SES) were all taken with the UK Schmidt. This research has made use of NASA's Astrophysics Data System Bibliographic Service.

Table 4.1. New ULIRGs Sample

Name AKARI-FIS-V1	AKARI RA (J2000)	AKARI DEC (J2000)	Other Name	z^a	$\log(L_{IR}/L_{\odot})^b$	$F(5\mu m)^c$ (Jy)	$F(90\mu m)^c$ (Jy)	$F(140\mu m)^c$ (Jy)	$F(160\mu m)^c$ (Jy)	r^d (mag)	IC ^e	IC ^f Ref.	Notes ^g	Spectral ^h Class
(1)	(2)	(3)	(4)	(5)	(6)	(7)	(8)	(9)	(10)	(11)	(12)	(13)	(14)	(15)
J2216028+005813	22 16 02.82	+00 58 13.5	SDSS J221602.70+005811.0	0.21*	12.15 $^{+0.05}_{-0.05}$	0.54 \pm 0.13	0.54 \pm 0.05	0.96 \pm 0.63	1.14 \pm 0.28	14.30	IIIa	3
J0859229+473612	08 59 22.93	+47 36 11.7	SDSS J085923.61+473610.5	0.180	12.22 $^{+0.01}_{-0.01}$...	0.48 \pm 0.06	1.95 \pm 0.29	...	14.44	IIIa	3	...	Star Forming
J1443444+184950	14 43 44.44	+18 49 49.7	SDSS J144344.64+184945.7	0.177	12.08 $^{+0.15}_{-0.15}$	0.43 \pm 0.11	0.55 \pm 0.04	1.69 \pm 0.53	...	16.03	V	3	...	LINER
J0857505+512037	08 57 50.48	+51 20 37.2	SDSS J085750.79+512032.6	0.366	12.86 $^{+0.02}_{-0.02}$	1.12 \pm 0.28	0.68 \pm 0.06	1.58 \pm 0.08	...	14.40	IIIb	3	...	LINER
J1106104+023458	11 06 10.37	+02 34 57.8	SDSS J110611.44+023302.2	0.283	12.29 $^{+0.03}_{-0.03}$...	0.42 \pm 0.01	1.42 \pm 0.36	0.56 \pm 0.14	17.17	NI	3	B	Seyfert
J1157412+321316	11 57 41.21	+32 13 16.4	SDSS J115741.47+321316.4	0.160	12.10 $^{+0.07}_{-0.07}$	0.66 \pm 0.16	0.60 \pm 0.03	2.22 \pm 1.21	2.23 \pm 0.40	16.37	V	3	...	Star Forming
J0918155+295415	09 18 15.46	+29 54 14.9	SDSS J091815.56+295414.1	0.180	12.01 $^{+0.01}_{-0.01}$	0.66 \pm 0.16	0.54 \pm 0.10	0.22 \pm 0.06	...	12.33	V	3	...	Composite
J1149200+030357	11 49 20.03	-03 03 57.3	SDSS J114920.04+030402.1	0.162	12.06 $^{+0.02}_{-0.02}$	0.19 \pm 0.05	0.42 \pm 0.02	1.30 \pm 0.33	2.58 \pm 0.21	13.97	VG	3	...	Star Forming
J0126038+022456	01 26 03.80	+02 24 55.9	SDSS J012604.62+022509.9	0.242	12.27 $^{+0.05}_{-0.05}$...	0.63 \pm 0.01	0.70 \pm 0.18	...	14.73	Tp1,G	3	...	LINER
J1556089+254358	15 56 08.92	+25 43 57.8	SDSS J155609.36+254355.9	0.154	12.08 $^{+0.01}_{-0.01}$	0.56 \pm 0.14	0.51 \pm 0.01	0.26 \pm 0.57	...	16.76	IIIa,G	3	...	Composite
J0140364+260016	01 40 36.40	+26 00 15.9	SDSS J014037.36+260001.5	0.321	12.73 $^{+0.03}_{-0.03}$	0.57 \pm 0.14	0.56 \pm 0.03	0.70 \pm 0.17	2.51 \pm 0.15	16.01	IIIa,G	3	...	Seyfert
J1257392+080935	12 57 39.15	+08 09 35.1	SDSS J125739.33+080931.7	0.272	12.30 $^{+0.03}_{-0.03}$	0.46 \pm 0.12	0.51 \pm 0.01	...	0.22 \pm 0.06	17.72	NI	3	...	QSO
J0800007+152319	08 00 00.68	+15 23 18.7	SDSS J080000.05+152326.0	0.274	12.22 $^{+0.00}_{-0.00}$...	0.43 \pm 0.03	14.50	V	3	A	LINER*
J0800279+074858	08 00 27.92	+07 48 57.6	SDSS J080028.37+074915.5	0.173	12.14 $^{+0.01}_{-0.01}$	0.34 \pm 0.09	0.35 \pm 0.09	2.29 \pm 0.57	2.04 \pm 0.51	13.10	VG	3	...	LINER
J0834438+334427	08 34 43.82	+33 44 27.2	SDSS J083443.56+334432.5	0.166	12.08 $^{+0.14}_{-0.14}$	0.59 \pm 0.15	0.65 \pm 0.04	...	2.07 \pm 0.52	15.90	IIIb	3	A	Composite
J0823089+184234	08 23 08.91	+18 42 33.9	SDSS J082309.51+184233.4	0.425	12.62 $^{+0.02}_{-0.02}$	0.45 \pm 0.11	0.41 \pm 0.02	12.52	V	3
J1202527+195458	12 02 52.69	+19 54 58.4	SDSS J120252.39+195456.7	0.132	12.03 $^{+0.02}_{-0.02}$	0.11 \pm 0.03	0.54 \pm 0.05	0.69 \pm 0.10	3.43 \pm 0.04	14.50	IIIb	3	...	Star Forming
J0912533+192701	09 12 53.33	+19 27 00.8	SDSS J091253.25+192653.9	0.233	12.12 $^{+0.03}_{-0.03}$	0.17 \pm 0.04	0.44 \pm 0.04	0.68 \pm 0.17	0.93 \pm 0.23	15.49	V	3	...	Composite
J0941010+143622	09 41 01.03	+14 36 22.4	SDSS J094100.81+143614.5	0.386	12.76 $^{+0.01}_{-0.01}$	0.89 \pm 0.22	0.77 \pm 0.07	0.24 \pm 0.06	0.46 \pm 0.11	17.19	NI	3	B	QSO
J1016332+041418	10 16 33.25	+04 14 17.9	SDSS J101633.19+041422.1	0.264	12.41 $^{+0.04}_{-0.04}$	0.51 \pm 0.13	0.65 \pm 0.10	0.91 \pm 0.01	1.34 \pm 0.33	14.73	IIIb	3	...	Composite
J1401186+021131	14 01 18.61	-02 11 30.9	SDSS J140119.02+021126.7	0.172	12.09 $^{+0.08}_{-0.08}$	0.26 \pm 0.06	0.30 \pm 0.08	1.85 \pm 0.30	...	15.98	IIIa	3	...	Seyfert
J1014141+194758	10 14 14.08	+19 47 57.8	SDSS J101413.87+194754.2	0.126	12.02 $^{+0.05}_{-0.05}$...	0.52 \pm 0.05	2.02 \pm 0.01	0.16 \pm 0.04	16.11	IIIb	3	...	Star Forming
J1258241+224113	12 58 24.10	+22 41 13.0	SDSS J125824.16+224113.6	0.208	12.14 $^{+0.02}_{-0.02}$	0.97 \pm 0.24	0.60 \pm 0.05	1.44 \pm 1.09	0.86 \pm 0.21	16.62	IIIb	3	...	Composite
J1036317+022147	10 36 31.66	+02 21 47.3	SDSS J103631.88+022144.1	0.050	12.09 $^{+0.03}_{-0.03}$	13.32 \pm 1.09	14.81 \pm 0.54	10.83 \pm 1.15	8.46 \pm 0.74	14.75	IIIb	3	...	Composite
J1050567+185316	10 50 56.73	+18 53 16.1	SDSS J105056.78+185316.9	0.219	12.58 $^{+0.08}_{-0.08}$	0.67 \pm 0.17	0.93 \pm 0.10	3.08 \pm 2.13	3.32 \pm 0.45	14.91	Tp1,G	3	...	Seyfert
J1111177+192259	11 11 17.72	+19 22 58.9	SDSS J111117.46+192255.0	0.225	12.20 $^{+0.00}_{-0.00}$...	0.55 \pm 0.05	0.05 \pm 0.25	...	14.56	IIIb	3	...	Star Forming
J1219585+051745	12 19 58.50	+05 17 44.6	SDSS J121958.11+051735.1	0.487	12.86 $^{+0.03}_{-0.03}$	0.29 \pm 0.07	0.82 \pm 0.09	0.43 \pm 0.11	...	15.16	NI	3	A	...
J1414276+605726	14 14 27.55	+60 57 25.8	SDSS J141427.98+605727.0	0.151	12.04 $^{+0.03}_{-0.03}$	0.37 \pm 0.09	0.63 \pm 0.04	1.94 \pm 0.36	2.75 \pm 1.38	14.11	V	3	...	Composite
J0936293+203638	09 36 29.33	+20 36 37.6	SDSS J093629.03+203620.0	0.175	12.04 $^{+0.06}_{-0.06}$	0.42 \pm 0.11	0.57 \pm 0.09	2.05 \pm 0.23	0.83 \pm 0.21	14.12	IIIb	3	...	Composite
J1233025+452649	12 33 02.50	+45 26 48.5	SDSS J123303.03+452646.8	0.100	12.04 $^{+0.04}_{-0.04}$	2.34 \pm 0.19	2.18 \pm 0.14	1.47 \pm 1.62	2.92 \pm 0.31	14.00	V	3	A	Composite
J1509140+175716	15 09 13.98	+17 57 15.6	SDSS J150913.80+175710.0	0.171	12.04 $^{+0.17}_{-0.17}$	0.55 \pm 0.14	0.73 \pm 0.04	1.28 \pm 0.69	...	16.95	IIIb	3	...	QSO
J1533582+113413	15 33 58.15	+11 34 12.7	SDSS J153358.24+113415.8	0.337	12.34 $^{+0.03}_{-0.03}$	0.25 \pm 0.06	0.33 \pm 0.04	0.46 \pm 0.11	...	15.29	VG	3	A	...
J1425160+162313	14 25 16.02	+16 23 13.0	SDSS J142516.03+162307.9	0.185	12.01 $^{+0.05}_{-0.05}$	0.82 \pm 0.20	0.57 \pm 0.04	0.90 \pm 0.03	0.33 \pm 0.08	14.81	V	3	...	LINER
J1348483+181401	13 48 48.32	+18 14 00.9	SDSS J134848.32+181357.4	0.179	12.15 $^{+0.02}_{-0.02}$	0.42 \pm 0.11	0.66 \pm 0.04	1.66 \pm 0.03	1.17 \pm 0.29	14.89	IV	3	...	Composite
J1125319+290316	11 25 31.92	+29 03 16.2	SDSS J112531.90+290311.3	0.138	12.25 $^{+0.05}_{-0.05}$	1.98 \pm 0.14	1.84 \pm 0.09	1.53 \pm 0.56	...	13.34	IV	3	...	QSO
J1603043+094717	16 03 04.29	+09 47 17.5	SDSS J160304.57+094707.8	0.152	12.04 $^{+0.04}_{-0.04}$	0.79 \pm 0.20	0.54 \pm 0.07	1.70 \pm 0.01	0.36 \pm 0.09	13.11	V	3	...	Star Forming
J1639245+303719	16 39 24.50	+30 37 19.1	SDSS J163925.01+303709.8	0.224	12.15 $^{+0.01}_{-0.01}$	0.51 \pm 0.13	0.51 \pm 0.04	1.14 \pm 0.23	0.12 \pm 0.03	16.53	IIIb	3
J1050288+002806	10 50 28.80	+00 28 06.0	SDSS J105028.49+002807.7	0.216	12.38 $^{+0.15}_{-0.15}$	0.53 \pm 0.13	0.79 \pm 0.06	1.79 \pm 0.37	...	14.77	IIIb	3	...	Composite
J0928103+232521	09 28 10.29	+23 25 21.0	SDSS J092810.52+232515.8	0.197	12.13 $^{+0.08}_{-0.08}$	0.09 \pm 0.02	0.44 \pm 0.01	1.13 \pm 0.28	...	15.40	IIIb	3	...	Star Forming
J2344170+053520	23 44 17.04	+05 35 19.8	SDSS J234417.43+053533.5	0.267	12.50 $^{+0.14}_{-0.14}$	0.64 \pm 0.16	0.42 \pm 0.06	1.29 \pm 0.90	1.80 \pm 0.45	15.80	IIIa	3	...	Seyfert

Table 4.1 (cont'd)

Name AKARI-FIS-V1 (1)	AKARI RA (J2000) (2)	AKARI DEC (J2000) (3)	Other Name (4)	z^a (5)	$\log(L_{IR}/L_{\odot})^b$ (6)	$F(65\mu\text{m})^c$ (Jy) (7)	$F(90\mu\text{m})^c$ (Jy) (8)	$F(140\mu\text{m})^c$ (Jy) (9)	$F(160\mu\text{m})^c$ (Jy) (10)	r^d (mag) (11)	IC ^e (12)	IC ^f Ref. (13)	Note ^g Spectral ^h Class (14) (15)
J2353152-313234	23 53 15.20	-31 32 34.5	TCS430Z217	0.185	$12.08^{+0.00}_{-0.10}$	0.37 ± 0.09	0.23 ± 0.06	1.67 ± 0.44	2.78 ± 0.70	14.29
J1302051-041435	13 02 05.13	-04 14 35.3	TGN132Z081	0.158	$12.02^{+0.06}_{-0.06}$	0.15 ± 0.04	0.79 ± 0.04	1.03 ± 0.26	...	16.38
J1059519-054333	10 59 51.90	-05 43 33.1	TGN105Z150	0.214	$12.02^{+0.05}_{-0.04}$	0.28 ± 0.07	0.41 ± 0.01	1.71 ± 0.43	0.63 ± 0.16	14.38
J1222488-040307	12 22 48.78	-04 03 07.1	TGN123Z071	0.181	$12.15^{+0.02}_{-0.02}$	0.16 ± 0.04	0.59 ± 0.10	1.68 ± 0.04	1.09 ± 0.27	15.17
J1419037-034657	14 19 03.68	-03 46 56.6	TGN145Z052	0.152	$12.07^{+0.03}_{-0.03}$...	0.61 ± 0.15	1.86 ± 0.66	2.49 ± 0.62	16.95
J1048019-013017	10 48 01.87	-01 30 17.4	TGN296Z061	0.167	$12.10^{+0.05}_{-0.05}$	0.49 ± 0.12	1.10 ± 0.15	1.13 ± 0.40	...	13.53	IV	3	...
J1338353-041131	13 38 35.29	-04 11 31.4	TGN139Z200	0.175	$12.15^{+0.18}_{-0.18}$	0.40 ± 0.10	0.68 ± 0.29	1.77 ± 0.68	...	15.67
J2318556-333544	23 18 55.64	-33 35 43.6	TCS488Z224	0.165	$12.01^{+0.09}_{-0.06}$	1.10 ± 0.28	0.67 ± 0.13	0.57 ± 0.14	0.90 ± 0.23	15.06

^aBased on SDSS optical spectra. The redshifts marked with asterisk are adopted from Wang & Rowan-Robinson (2009) since there are no available SDSS spectra for these sources.

^b L_{IR} is the total IR luminosity between $8\mu\text{m}$ - $1000\mu\text{m}$ measured from the SEDs fitted to the AKARI fluxes at 65, 90, 140 and 160 μm .

^cThe AKARI flux density and the associated uncertainties are adopted from Yamamura et al. (2010). For the cases for which the flux uncertainties are not available we adopt 25% of the measured flux as the uncertainty.

^dSDSS Petrosian r magnitude.

^eInteraction Classes (IC) are described in §4.3.2. The IC listed in this Table are based on combined grz SDSS images; '...' entries in the Table indicate lack of SDSS image.

^fReferences: (1) Veilleux et al. (2002), (2) Hwang et al. (2007), (3) This work.

^gSuperposition of other sources in the field: (A) Star; (B) Galaxy.

^hClassifications based on optical spectra. For the sources that are in the SDSS DR10 *emissionlinesPort7* catalogue (Thomas et al., 2013) we adopt the given BPT classifications: 'Star Forming', 'Composite', 'LINER' and 'Seyfert'. In the case of quasars (QSO) we adopt the 'spectrotype' classification from the *galSpectInfo* catalogue (see Richards et al., 2002, for the details of SDSS spectroscopic target selection). The classifications marked with a star are based on our BPT classification based on the emission-line fluxes adopted from SDSS catalogue *galSpectLine7* (Tremonti et al., 2004; Brinchmann et al., 2004).

Table 4.2. Known ULIRGs Sample

Name AKARI-FIS-V1	AKARI RA (J2000)	AKARI DEC (J2000)	Other Name	z^a	$\log(L_{IR}/L_{\odot})^b$	$F(65\mu\text{m})^c$ (Jy)	$F(90\mu\text{m})^c$ (Jy)	$F(140\mu\text{m})^c$ (Jy)	$F(160\mu\text{m})^c$ (Jy)	r^d (mag)	IC ^e Ref.	IC ^f Ref.	Notes ^g	Spectral ^h Class
(1)	(2)	(3)	(4)	(5)	(6)	(7)	(8)	(9)	(10)	(11)	(12)	(13)	(14)	(15)
J0806507+523514	08 06 50.74	+52 35 13.9	SDSS J080650.79+523507.2	0.083	12.01 ^{+0.04} _{-0.04}	2.92±0.27	3.17±0.17	3.85±0.86	4.64±1.07	17.19	V	3	A	Star Forming
J0857064+190855	08 57 06.37	+19 08 55.4	SDSS J085706.35+190853.5	0.331	12.91 ^{+0.02} _{-0.04}	...	0.48±0.06	...	2.56±0.10	15.79	NI	3	...	QSO
J1022125+241208	10 22 12.46	+24 12 07.8	SDSS J102212.64+241202.4	0.188	12.04 ^{+0.27} _{-0.05}	...	0.59±0.03	0.90±2.81	...	15.80	IV	3	...	LINER
J1422313+260205	14 22 31.27	+26 02 05.2	SDSS J142231.37+260205.1	0.159	12.25 ^{+0.05} _{-0.04}	0.96±0.24	1.36±0.04	2.29±0.43	...	13.59	IIIa	1	...	Star Forming
J1231216+275524	12 31 21.57	+27 55 24.4	SDSS J123121.37+275524.0	0.212	12.26 ^{+0.06} _{-0.04}	0.52±0.13	0.40±0.10	1.41±0.35	1.93±0.48	17.35	IV	3	...	Composite
J1251200+021900	12 51 20.03	+02 19 00.2	SDSS J125120.04+021902.4	0.253	12.50 ^{+0.03} _{-0.03}	1.00±0.25	0.73±0.04	1.86±0.09	0.81±0.20	15.00	V	2	...	Composite
J0030089+002743	00 30 08.95	-00 27 43.5	SDSS J003009.08-002744.2	0.242*	12.22 ^{+0.03} _{-0.03}	0.37±0.09	0.62±0.06	1.34±0.30	0.40±0.10	14.56	IIIb	3
J0914140+032200	09 14 14.01	+03 22 00.4	SDSS J091413.79+032201.4	0.145	12.13 ^{+0.06} _{-0.05}	1.11±0.28	1.39±0.11	2.29±0.51	0.86±0.21	14.48	IIIa	1	...	LINER
J1105377+311432	11 05 37.71	+31 14 32.3	SDSS J110537.54+311432.2	0.199	12.27 ^{+0.05} _{-0.05}	0.71±0.18	0.98±0.06	1.31±0.33	0.59±0.15	16.03	IV	1	...	Composite
J0323227-075612	03 23 22.75	-07 56 12.1	SDSS J032322.87-075615.3	0.166	12.16 ^{+0.05} _{-0.05}	0.50±0.12	0.91±0.00	1.80±0.25	...	12.99	IV	1	...	Composite
J1632212+155145	16 32 21.24	+15 51 44.8	SDSS J163221.38+155145.5	0.242	12.71 ^{+0.05} _{-0.05}	1.50±0.13	1.46±0.03	2.42±0.48	2.75±0.06	14.27	V	1	...	Composite
J0148531+002857	01 48 53.10	+00 28 57.1	SDSS J014852.57+002859.8	0.280	12.33 ^{+0.12} _{-0.02}	0.70±0.17	0.48±0.05	0.94±0.39	...	15.49	IIIa	2	...	Composite
J0159503+002340	01 59 50.28	+00 23 39.9	SDSS J015950.25+002340.9	0.163	12.42 ^{+0.02} _{-0.02}	2.01±0.03	1.82±0.17	2.94±0.18	0.16±0.04	15.63	IV	1	...	QSO
J1553317+042809	15 53 31.72	+04 28 08.8	SDSS J155331.57+042805.3	0.136*	12.21 ^{+0.03} _{-0.03}	0.26±0.31	1.62±0.05	0.23±0.06	1.61±0.40	12.67	IV	1
J0244173+003040	02 44 17.35	-00 30 40.3	SDSS J024417.44+003041.1	0.200	12.07 ^{+0.01} _{-0.07}	0.36±0.09	0.65±0.19	0.77±0.19	0.86±0.22	15.08	IIIa,G	2	...	QSO
J1202268-012918	12 02 26.81	-01 29 18.0	SDSS J120226.76-012915.3	0.150	12.43 ^{+0.07} _{-0.08}	1.94±0.39	2.54±0.20	3.09±0.67	1.06±1.26	15.68	IV,G	3	...	Star Forming*
J1013477+465402	10 13 47.75	+46 54 02.1	SDSS J101348.09+465359.6	0.206	12.28 ^{+0.08} _{-0.05}	0.13±0.03	0.72±0.05	16.78	IV	3	...	Seyfert
J0858418+104124	08 58 41.77	+10 41 24.3	SDSS J085841.77+104122.1	0.148	12.22 ^{+0.03} _{-0.02}	1.00±0.25	1.55±0.13	2.09±0.38	2.62±0.94	16.17	IV,G	1	...	Seyfert
J1347336+121727	13 47 33.58	+12 17 27.4	SDSS J134733.36+121724.3	0.120	12.23 ^{+0.02} _{-0.03}	1.90±0.47	1.75±0.08	0.96±0.24	0.97±0.32	14.13	IIIb	1	...	Seyfert*
J0852524+252646	08 53 25.21	+25 26 45.6	SDSS J085252.07+252656.0	0.256	12.42 ^{+0.05} _{-0.06}	0.56±0.14	0.68±0.06	0.68±0.39	1.28±0.32	11.72	V	3	B	QSO
J0829512+384528	08 29 51.18	+38 45 27.8	SDSS J082951.39+384523.7	0.195	12.26 ^{+0.14} _{-0.05}	0.26±0.06	0.59±0.01	1.49±0.37	...	16.03	IIIb	2	...	Composite
J1142035+005135	11 42 03.51	+00 51 35.5	SDSS J114203.41+005135.8	0.245	12.04 ^{+0.06} _{-0.06}	0.33±0.08	0.53±0.09	0.89±0.22	...	13.34	IIIb	2	...	Composite
J0945214+173803	09 45 21.43	+17 38 02.8	SDSS J094521.33+173753.2	0.128	12.14 ^{+0.07} _{-0.07}	0.37±0.09	0.45±0.05	0.15±0.04	0.67±0.17	15.26	IV	2	...	Composite
J0810595+281354	08 10 59.51	+28 13 54.1	SDSS J081059.61+281352.2	0.336	12.01 ^{+0.04} _{-0.04}	0.86±0.22	0.89±0.04	0.78±0.07	...	16.29	V	3	...	QSO
J0900252+390400	09 00 25.21	+39 03 59.8	SDSS J090025.37+390353.7	0.058	12.10 ^{+0.03} _{-0.03}	5.93±0.70	5.13±0.19	2.62±0.91	1.43±0.36	15.97	IIIb	1	...	Star Forming
J0830197+192040	08 30 19.74	+19 20 40.0	SDSS J083019.75+192050.0	0.186	12.08 ^{+0.07} _{-0.06}	0.49±0.12	0.59±0.07	...	1.30±0.33	15.02	IIIb	3	...	Star Forming
J1121293+112233	11 21 29.25	+11 22 33.3	SDSS J112129.00+112225.7	0.185	12.33 ^{+0.03} _{-0.03}	0.83±0.21	1.07±0.03	2.16±0.11	...	13.37	IIIa	2	...	Seyfert
J1006038+411223	10 06 03.83	+41 12 23.4	SDSS J100603.85+411224.8	0.328	12.47 ^{+0.02} _{-0.04}	0.28±0.07	0.54±0.03	0.47±0.12	...	15.36	V	2	...	Star Forming
J0838034+505516	08 38 03.36	+50 55 16.5	SDSS J083803.61+505508.9	0.097	12.01 ^{+0.04} _{-0.02}	2.31±0.04	2.00±0.08	2.62±0.40	...	17.30	IV	2	...	Composite
J0902489+523623	09 02 48.87	+52 36 22.6	SDSS J090248.90+523624.7	0.157	12.10 ^{+0.02} _{-0.05}	1.20±0.30	0.87±0.04	0.25±0.06	1.56±0.39	15.72	V	1	...	Composite
J1021426+130657	10 21 42.57	+13 06 57.1	SDSS J102142.49+130653.9	0.077	12.06 ^{+0.03} _{-0.02}	3.97±0.35	4.28±0.18	2.97±2.54	5.95±0.77	14.15	IIIb	1	...	Star Forming
J12427269+005837	12 42 26.94	+00 58 37.4	SDSS J124272.28+005841.1	0.162	12.07 ^{+0.04} _{-0.04}	1.39±0.35	0.93±0.05	0.15±0.04	0.72±0.18	14.66	IIIa,G	2	...	Composite
J1246333+453425	12 46 33.32	+45 34 25.4	SDSS J124633.52+453421.8	0.196	12.00 ^{+0.04} _{-0.03}	0.23±0.06	0.60±0.04	0.77±0.18	0.52±0.13	15.50	IIIb	2	...	QSO
J0847504+232113	08 47 50.37	+23 21 12.8	SDSS J084750.26+232110.9	0.152	12.00 ^{+0.12} _{-0.03}	...	0.75±0.06	1.66±0.39	...	13.62	IIIb	3	...	Star Forming
J1559301+380843	15 59 30.13	+38 08 42.7	SDSS J155930.40+380838.8	0.218	12.17 ^{+0.03} _{-0.04}	0.07±0.02	0.58±0.06	1.36±0.14	2.17±0.38	13.85	IV	2	...	Seyfert
J1324197+053705	13 24 19.74	+05 37 05.4	SDSS J132419.89+053704.7	0.203	12.76 ^{+0.02} _{-0.04}	1.22±0.30	0.89±0.08	14.68	V	1	...	QSO
J1102140+380240	11 02 14.02	+38 02 40.0	SDSS J110214.00+380234.6	0.158	12.22 ^{+0.04} _{-0.03}	1.12±0.28	1.32±0.03	2.36±0.70	0.46±0.20	15.27	IIIb	1	...	Composite
J1204244+192509	12 04 24.41	+19 25 08.9	SDSS J120424.54+192509.8	0.168	12.22 ^{+0.03} _{-0.03}	1.62±0.41	1.24±0.03	1.19±0.04	0.79±0.20	15.38	IV	1	...	Composite
J1108513+065915	11 08 51.31	+06 59 15.1	SDSS J110851.03+065901.5	0.182	12.06 ^{+0.13} _{-0.06}	0.30±0.07	0.52±0.05	0.29±0.55	1.68±0.42	15.64	IIIa	3	B	QSO

Table 4.2 (cont'd)

Name AKARI-FIS-V1	AKARI RA (J2000)	AKARI DEC (J2000)	Other Name	z^a	$\log(L_{IR}/L_{\odot})^b$	$F(65\mu m)^c$ (Jy)	$F(90\mu m)^c$ (Jy)	$F(140\mu m)^c$ (Jy)	$F(160\mu m)^c$ (Jy)	r^d (mag)	IC ^e Ref.	IC ^f Notes ^g Ref.	Spectral ^h Class (15)
(1)	(2)	(3)	(4)	(5)	(6)	(7)	(8)	(9)	(10)	(11)	(12)	(13)	(14)
J1040290+105325	10 40 29.05	+10 53 25.3	SDSS J104029.17+105318.3	0.136	12.32 ^{+0.05} _{-0.03}	2.02 ± 0.50	2.13 ± 0.13	1.46 ± 2.03	0.75 ± 0.19	14.73	IV	1 ...	LINER
J1207210+021702	12 07 21.03	+02 17 01.7	SDSS J120721.45+021657.8	0.222	12.16 ^{+0.03} _{-0.03}	1.32 ± 0.33	0.58 ± 0.02	0.54 ± 0.13	0.81 ± 0.20	14.36	V	2 ...	Composite
J1255482-033908	12 55 48.19	-03 39 08.2	SDSS J125547.83-033909.6	0.169	12.08 ^{+0.09} _{-0.06}	...	0.73 ± 0.02	...	1.66 ± 0.41	15.53	IV	2 A	QSO
J0906339+045136	09 06 33.93	+04 51 35.5	SDSS J090634.03+045127.6	0.125	12.09 ^{+0.04} _{-0.04}	2.37 ± 0.16	1.64 ± 0.07	2.94 ± 1.55	2.43 ± 0.61	13.68	IV	1 ...	Composite
J1153144+131432	11 53 14.39	+13 14 32.1	SDSS J115314.23+131427.9	0.127	12.29 ^{+0.03} _{-0.03}	0.07 ± 0.02	2.57 ± 0.14	2.76 ± 0.55	1.03 ± 1.03	13.50	IV	1 ...	Composite
J1202054+112813	12 02 05.41	+11 28 13.2	SDSS J120205.59+112812.2	0.194	12.20 ^{+0.04} _{-0.04}	0.79 ± 0.20	1.02 ± 0.08	1.22 ± 0.30	0.42 ± 0.10	13.72	IIIb	2 ...	Composite
J1006432+091726	10 06 43.16	+09 17 26.3	SDSS J100643.50+091727.5	0.171	12.15 ^{+0.06} _{-0.03}	3.39 ± 0.27	3.53 ± 0.12	4.11 ± 0.37	2.96 ± 1.01	15.33	IV	1 ...	Composite
J1052232+440849	10 52 23.24	+44 08 48.6	SDSS J105223.52+440847.6	0.092	12.14 ^{+0.03} _{-0.02}	0.69 ± 0.17	0.79 ± 0.05	...	0.99 ± 0.25	12.99	V	3 ...	QSO
J1254008+101115	12 54 00.82	+10 11 14.6	SDSS J125400.80+101112.4	0.319	12.65 ^{+0.03} _{-0.03}	0.53 ± 0.13	1.36 ± 0.03	0.93 ± 0.23	1.26 ± 0.63	15.08	IIIb	1 ...	Composite
J1348397+581854	13 48 39.66	+58 18 54.1	SDSS J134840.08+581852.0	0.158	12.19 ^{+0.02} _{-0.04}	0.84 ± 0.21	0.64 ± 0.02	0.86 ± 0.21	0.74 ± 0.18	13.88	V	3 ...	Composite
J1015153+272717	10 15 15.33	+27 27 17.1	SDSS J101515.35+272717.1	0.210	12.16 ^{+0.04} _{-0.03}	1.70 ± 0.43	1.78 ± 0.05	2.72 ± 0.56	0.26 ± 0.07	14.21	IIIb	1 ...	Composite
J1356100+290538	13 56 09.98	+29 05 38.0	SDSS J135609.99+290535.1	0.109	12.09 ^{+0.06} _{-0.04}	0.58 ± 0.14	1.03 ± 0.06	2.58 ± 0.36	2.74 ± 1.36	16.01	IV/G	1 ...	QSO
J1502320+142132	15 02 31.95	+14 21 32.4	SDSS J150231.96+142135.3	0.162	12.12 ^{+0.02} _{-0.02}	0.46 ± 0.11	0.83 ± 0.05	1.57 ± 0.61	...	15.66	V	1 ...	Composite
J1336237+391733	13 36 23.74	+39 17 32.5	SDSS J133624.06+391731.1	0.179	12.34 ^{+0.07} _{-0.07}	0.99 ± 0.17	0.79 ± 0.05	...	0.99 ± 0.25	12.99	V	3 ...	Composite
J1141215+405951	11 41 21.52	+40 59 51.3	SDSS J114122.03+405950.3	0.149	12.09 ^{+0.06} _{-0.04}	0.58 ± 0.14	1.03 ± 0.06	2.58 ± 0.36	2.74 ± 1.36	16.01	IV/G	1 ...	QSO
J1433271+281157	14 33 27.14	+28 11 57.0	SDSS J143327.52+281159.9	0.175	12.17 ^{+0.11} _{-0.05}	0.46 ± 0.11	0.83 ± 0.05	1.54 ± 0.61	...	15.66	V	1 ...	Composite
J1450544+350835	14 50 54.40	+35 08 34.7	SDSS J145054.16+350837.9	0.206	12.35 ^{+0.08} _{-0.08}	0.34 ± 0.08	0.72 ± 0.07	1.81 ± 0.90	...	14.35	V	3 ...	Composite
J1406380+010258	14 06 37.97	+01 02 58.1	SDSS J140638.20+010254.6	0.236	12.35 ^{+0.02} _{-0.04}	0.99 ± 0.25	0.74 ± 0.09	0.18 ± 0.05	...	16.03	IV	2 ...	Composite
J1524440+234016	15 24 44.00	+23 40 16.4	SDSS J152443.88+234010.2	0.139	12.04 ^{+0.03} _{-0.03}	0.95 ± 0.24	1.11 ± 0.12	1.90 ± 0.48	1.86 ± 0.47	17.04	IV	1 ...	Composite
J1522382+333135	15 22 38.17	+33 31 35.4	SDSS J152238.10+333135.9	0.125	12.08 ^{+0.01} _{-0.01}	0.91 ± 0.23	1.26 ± 0.04	1.22 ± 0.25	...	17.23	IV	1 ...	Composite*
J1505390+574305	15 05 39.04	+57 43 04.6	SDSS J150539.55+574307.1	0.151	12.03 ^{+0.04} _{-0.05}	1.14 ± 0.28	0.87 ± 0.05	1.61 ± 0.97	0.73 ± 0.25	14.70	IIIb	1 ...	Star Forming
J1441041+532011	14 41 04.11	+53 20 10.8	SDSS J144104.38+532008.7	0.105	12.11 ^{+0.03} _{-0.03}	2.03 ± 0.45	1.78 ± 0.13	1.77 ± 0.41	0.91 ± 0.21	16.49	Tp1	1 ...	LINER*
J1706529+382010	17 06 52.87	+38 20 09.9	SDSS J170653.27+382007.1	0.168	12.19 ^{+0.01} _{-0.04}	0.79 ± 0.20	0.96 ± 0.02	1.68 ± 0.75	0.19 ± 0.05	15.16	IIIa,G	2 A	LINER
J1649140+342510	16 49 14.01	+34 25 09.8	SDSS J164914.09+342513.2	0.113	12.12 ^{+0.09} _{-0.09}	2.28 ± 0.36	2.24 ± 0.08	2.69 ± 0.95	1.96 ± 3.66	15.55	IIIb	1 ...	Star Forming
J0800310+481539	08 00 31.03	+48 15 39.3	SDSS J080031.40+481538.7	0.119	12.01 ^{+0.02} _{-0.02}	1.27 ± 0.32	1.23 ± 0.04	0.39 ± 0.08	...	13.20	IIIb	2 ...	Composite
J0823127+275140	08 23 12.66	+27 51 39.6	SDSS J082312.61+275139.8	0.168	12.15 ^{+0.02} _{-0.02}	0.53 ± 0.13	1.04 ± 0.02	0.96 ± 0.24	1.26 ± 0.32	18.30	IV	1 ...	Star Forming
J1213460+024844	12 13 45.99	+02 48 43.8	SDSS J121346.11+024841.5	0.073	12.31 ^{+0.03} _{-0.03}	7.10 ± 0.51	8.69 ± 0.31	6.17 ± 0.36	3.90 ± 1.32	15.42	IIIb	1 ...	Composite
J1346511+074720	13 46 51.09	+07 47 20.0	SDSS J134651.09+074719.0	0.135	12.15 ^{+0.06} _{-0.06}	1.71 ± 0.43	1.49 ± 0.10	2.25 ± 0.86	0.61 ± 0.15	16.68	Tp1,G	1 ...	Composite
J2257246+262120	22 57 24.65	-26 21 20.5	TCS123Z162	0.164	12.24 ^{+0.03} _{-0.03}	1.87 ± 0.32	1.17 ± 0.17	1.53 ± 1.17	1.68 ± 0.11	15.22	IIIa	2
J2223286-270006	22 23 28.57	-27 00 05.7	TCS178Z172	0.131	12.20 ^{+0.04} _{-0.04}	1.87 ± 0.08	1.90 ± 0.09	2.90 ± 0.87	1.06 ± 0.26	12.70	IIIb	1
J1132417-053940	11 32 41.68	-05 39 40.2	TGN111Z322	0.230	12.25 ^{+0.04} _{-0.04}	0.44 ± 0.11	0.64 ± 0.02	0.81 ± 0.20	...	14.46	IV	2
J0238167-322036	02 38 16.66	-32 20 36.3	TGS465Z105	0.198	12.33 ^{+0.03} _{-0.03}	1.08 ± 0.27	0.95 ± 0.11	1.66 ± 0.10	2.33 ± 0.58	13.90	V	2
J0238126-473813	02 38 12.64	-47 38 12.9	TGS875Z072	0.098	12.15 ^{+0.02} _{-0.02}	2.76 ± 0.32	3.24 ± 0.09	3.99 ± 0.42	2.34 ± 0.66	14.53	V	2
J0237297-461544	02 37 29.66	-46 15 44.4	TGS875Z471	0.206	12.41 ^{+0.04} _{-0.04}	0.90 ± 0.56	1.13 ± 0.07	1.04 ± 1.04	1.99 ± 0.50	15.94	V	2
J0048064-284820	00 48 06.37	-28 48 20.0	TGS288Z046	0.110	12.16 ^{+0.04} _{-0.04}	2.56 ± 0.64	2.45 ± 0.16	4.08 ± 0.36	...	16.85	IIIa	1
J0112165-273819	01 12 16.49	-27 38 18.8	TGS213Z002	0.222	12.26 ^{+0.12} _{-0.12}	0.43 ± 0.11	0.48 ± 0.04	0.83 ± 0.99	1.79 ± 0.45	15.05	IIIa	2
J0138061-324519	01 38 06.14	-32 45 18.6	TGS509Z038	0.198	12.19 ^{+0.07} _{-0.07}	1.23 ± 0.31	0.75 ± 0.07	0.89 ± 0.22	0.40 ± 0.10	16.99	V	2
J0302108-270725	03 02 10.82	-27 07 24.7	TGS238Z241	0.221	12.47 ^{+0.05} _{-0.05}	0.98 ± 0.24	1.22 ± 0.15	1.07 ± 0.27	0.42 ± 0.11	15.98	IV	2
J0118266-253607	01 18 26.61	-25 36 06.8	TCS147Z020	0.237	12.19 ^{+0.03} _{-0.03}	0.67 ± 0.17	0.54 ± 0.03	0.50 ± 0.13	0.59 ± 0.15	16.32	V	2
J0152042-285116	01 52 04.20	-28 51 16.5	TCS302Z057	0.184	12.12 ^{+0.03} _{-0.04}	0.46 ± 0.11	0.73 ± 0.06	2.14 ± 0.60	1.02 ± 0.26	15.63	IIIa	2

Table 4.2 (cont'd)

Name AKARI-FIS-V1 (1)	AKAIRA (J2000) (2)	AKARIDEC (J2000) (3)	Other Name (4)	z^a (5)	$\log(L_{IR}/L_{\odot})^b$ (6)	$F(65\mu\text{m})^c$ (Jy) (7)	$F(90\mu\text{m})^c$ (Jy) (8)	$F(140\mu\text{m})^c$ (Jy) (9)	$F(160\mu\text{m})^c$ (Jy) (10)	r^d (mag) (11)	IC ^e Ref. (12) (13)	Note ^f (14)	Spectral ^h Class (15)	
J0159138-292436	01 59 13.82	-29 24 36.1	TGS304Z128	0.140	$12.13^{+0.08}_{-0.01}$	2.16 ± 0.40	1.36 ± 0.05	1.61 ± 0.36	0.63 ± 0.16	16.72	IV	1
J1329391-034654	13 29 39.11	-03 46 53.7	TGN137Z043	0.222	$12.28^{+0.02}_{-0.02}$	0.58 ± 0.14	0.75 ± 0.06	...	2.49 ± 3.85	16.39	IV	2
J1143187-032549	11 43 18.72	-03 25 48.7	TGN173Z052	0.157	$12.03^{+0.06}_{-0.02}$	0.57 ± 0.14	0.94 ± 0.05	0.44 ± 0.11	2.69 ± 0.67	14.64	III2a	2
J1112034-025414	11 12 03.36	-02 54 13.8	TGN232Z018	0.106	$12.18^{+0.07}_{-0.02}$	2.55 ± 0.39	2.93 ± 0.26	1.47 ± 0.28	...	14.31	IV	1
J2307212-343838	23 07 21.24	-34 38 38.4	TGS538Z137	0.208	$12.28^{+0.02}_{-0.01}$	0.76 ± 0.19	0.89 ± 0.10	1.43 ± 0.36	0.34 ± 0.59	18.43	V	2
J2208493-344627	22 08 49.25	-34 46 27.4	TGS528Z076	0.174	$12.13^{+0.16}_{-0.10}$	0.80 ± 0.20	0.67 ± 0.02	1.88 ± 0.45	...	14.93	V	2

^eSee §4.3.2 for the details of the interaction classes. The IC listed in this Table are mostly adopted from the references given in column (13).

Note. — For a, b, c, d, f, g, h see notes in Table 4.2.

Table 4.3. New HLIRG

Name	AKARI RA (J2000)	AKARI DEC (J2000)	Other Name	z^a	$\log(L_{IR}/L_{\odot})^b$	$F(65\mu\text{m})^c$ (Jy)	$F(90\mu\text{m})^c$ (Jy)	$F(140\mu\text{m})^c$ (Jy)	$F(160\mu\text{m})^c$ (Jy)	r^d (mag)	IC ^e Ref.	Notes ^f	Spectral ^h Class	
(1)	(2)	(3)	(4)	(5)	(6)	(7)	(8)	(9)	(10)	(11)	(12)	(13)	(14)	(15)
J1425001+103045	14 25 00.06	+10 30 44.7	SDSS J142500.73+103043.6	0.480	$13.19^{+0.18}_{-0.05}$	0.95 ± 0.24	0.61 ± 0.06	1.97 ± 0.48	1.97 ± 0.49	18.51	V	3	...	Composite

Note. — For a, b, c, d, e, f, g, h see notes in Table 4.2.

Table 4.4. Unconfirmed ULIRG Candidates

Name AKARI-FIS-V1 (1)	AKARI (J2000) (2)	AKARI DEC (J2000) (3)	Other Name (4)	z^a (5)	$\log(L_{IR}/L_{\odot})^b$ (6)	$F(65\mu\text{m})^c$ (Jy) (7)	$F(90\mu\text{m})^c$ (Jy) (8)	$F(140\mu\text{m})^c$ (Jy) (9)	$F(160\mu\text{m})^c$ (Jy) (10)	r^d (mag) (11)	IC ^e (12)	IC ^f Ref. (13)	Notes ^g (14)	Spectral ^h Class (15)
J0058034-025406	00 58 03.44	-02 54 05.8	SDSS J005802.70-025401.8	0.267	$12.33^{+0.02}_{-0.42}$...	0.21 ± 0.05	5.13 ± 1.49	...	14.31	IIIb	3	B
J1444024+000415	14 44 02.37	+00 04 15.0	SDSS J144402.86+000411.9	0.330	$12.65^{+0.02}_{-0.02}$	0.09 ± 0.02	0.23 ± 0.06	0.96 ± 0.24	3.74 ± 0.32	13.44	IIIa	3
J0545295-011324	05 45 29.50	-01 13 24.5	SDSS J054529.53-011318.0	0.884	$12.81^{+0.02}_{-0.02}$	0.41 ± 0.10	0.57 ± 0.20	...	0.24 ± 0.06	12.76	NI	3
J1352265+020815	13 52 26.48	+02 08 14.9	SDSS J135227.76+020816.5	2.853	$12.95^{+0.16}_{-0.05}$...	0.39 ± 0.07	0.76 ± 0.18	3.28 ± 0.82	15.70	IIIa	3	Large Separation
J1716527+271405	17 16 52.73	+27 14 04.6	SDSS J171653.48+271406.2	0.539	$12.26^{+0.05}_{-0.10}$...	0.23 ± 0.06	1.97 ± 0.36	0.17 ± 0.04	11.74	V	3	A

Note. — For a, b, c, d, e, f, g, h see notes in Table 4.2.

Table 4.5. Stellar Masses, Star Formation Rates, Oxygen Abundances, Optical Colors and Absolute Magnitudes

AKARI-FIS-V1 Name	IRAS Name	$\log(M_{star}(M_{\odot}))$	SFR(IR) ($M_{\odot} \text{ year}^{-1}$)	SFR(H α) ($M_{\odot} \text{ year}^{-1}$)	$12+\log(\text{O}/\text{H})$	$u^{0.1-r^{0.1}}$ (mag)	$M_r^{0.1}$ (mag)
(1)	(2)	(3)	(4)	(5)	(6)	(7)	(8)
J2216028+005813	F22134+0043	...	245.13 ^{32.99}
J0859229+473612	F08559+4748	10.74 ^{0.10}	288.20 ^{5.65}	36.99 ^{10.36}	8.94 \pm 0.08	2.92 \pm 0.12	-21.41 \pm 0.01
J1443444+184950	F14414+1902	10.34 ^{0.08}	208.78 ^{89.36}	14.08 ^{18.54}	...	2.47 \pm 0.12	-21.07 \pm 0.01
J0857505+512037	F08542+5132	10.96 ^{0.04}	1259.21 ^{82.06}	77.34 ^{86.97}	...	2.23 \pm 0.43	-21.35 \pm 0.01
J1106104+023458	...	11.14 ^{0.03}	333.58 ^{28.19}	6.60 ^{85.97}	...	2.59 \pm 0.29	-21.77 \pm 0.01
J1157412+321316	F11550+3233	10.58 ^{0.03}	216.42 ^{42.48}	62.34 ^{22.43}	8.79 \pm 0.10	1.45 \pm 0.02	-21.70 \pm 0.01
J0918155+295415	F09152+3006	10.41 ^{0.01}	175.91 ^{2.95}	43.92 ^{31.77}	8.13 \pm 1.36	1.95 \pm 0.05	-21.25 \pm 0.01
J1149200-030357	F11467-0247	...	196.92 ^{30.19}	1.72 \pm 0.03	-21.29 \pm 0.01
J0126038+022456	F01234+0209	10.88 ^{0.40}	323.97 ^{37.64}	0.01 ^{0.01}	...	3.18 \pm 0.48	-21.06 \pm 0.01
J1556089+254358	F15540+2552	10.47 ^{0.06}	207.78 ^{6.13}	35.19 ^{14.13}	8.89 \pm 0.11	2.19 \pm 0.06	-21.08 \pm 0.01
J0140364+260016	F01378+2545	11.03 ^{0.32}	924.48 ^{23.69}	1.61 \pm 0.67	-21.40 \pm 0.02
J1257392+080935	F12551+0825	...	345.30 ^{32.95}	0.43 \pm 0.01	-22.52 \pm 0.01
J0800007+152319	284.45 ^{1.01}	1.34 \pm 0.06	-21.40 \pm 0.01
J0800279+074858	...	11.26 ^{0.01}	239.72 ^{5.83}	0.254 ^{4.20}	...	3.06 \pm 0.17	-21.11 \pm 0.01
J0834438+334427	F08315+3354	10.42 ^{0.07}	208.11 ^{59.75}	68.74 ^{42.31}	...	2.27 \pm 0.08	-21.30 \pm 0.01
J0823089+184234	...	10.63 ^{0.01}	711.38 ^{33.38}	1.77 \pm 0.15	-21.45 \pm 0.01
J1202527+195458	F12002+2011	10.58 ^{0.02}	184.93 ^{7.66}	50.59 ^{10.61}	8.92 \pm 0.08	1.89 \pm 0.03	-21.06 \pm 0.01
J0912533+192701	...	10.71 ^{0.17}	228.40 ^{15.51}	18.52 ^{13.78}	8.63 \pm 0.28	2.87 \pm 0.19	-22.04 \pm 0.01
J0941010+143622	F09382+1449	...	992.43 ^{13.94}	1.37 \pm 0.06	-22.29 \pm 0.01
J1016332+041418	F10139+0429	10.40 ^{0.32}	439.24 ^{45.30}	37.99 ^{20.88}	8.40 \pm 0.22	1.93 \pm 0.09	-21.37 \pm 0.01
J1401186-021131	...	10.80 ^{0.01}	210.43 ^{4.13}	6.282 ^{3.8}	...	2.01 \pm 0.06	-21.98 \pm 0.01
J1014141+194758	F10114+2002	10.49 ^{0.09}	178.40 ^{22.75}	21.26 ^{1.84}	8.96 \pm 0.06	1.56 \pm 0.02	-21.42 \pm 0.01
J1258241+224113	...	10.09 ^{0.04}	236.97 ^{10.75}	16.68 ^{13.69}	8.59 \pm 0.23	2.77 \pm 0.65	-19.93 \pm 0.02
J1036317+022147	...	9.98 ^{0.15}	212.37 ^{17.10}	7.081 ^{3.57}	8.69 \pm 0.12	1.68 \pm 0.01	-20.43 \pm 0.01
J1050567+185316	F10482+1909	10.40 ^{0.14}	652.08 ^{126.91}	153.69 ^{83.09}	...	2.49 \pm 0.11	-21.23 \pm 0.01
J1111177+192259	...	10.27 ^{0.12}	272.52 ^{3.34}	42.05 ^{7.48}	8.83 \pm 0.15	0.98 \pm 0.03	-21.62 \pm 0.01
J1219585+051745	...	10.88 ^{0.41}	1249.68 ^{74.16}	2.52 \pm 1.19	-21.66 \pm 0.01
J1414276+605726	F14129+6111	10.16 ^{0.06}	190.37 ^{22.09}	27.60 ^{9.03}	8.69 \pm 0.10	1.07 \pm 0.02	-20.69 \pm 0.01
J0936293+203638	F09336+2049	10.60 ^{0.01}	189.50 ^{15.97}	28.52 ^{10.88}	9.00 \pm 0.23	2.44 \pm 0.09	-21.34 \pm 0.01
J1233025+452649	...	10.22 ^{0.31}	186.90 ^{5.86}	22.45 ^{8.90}	8.23 \pm 1.80	1.94 \pm 0.03	-20.16 \pm 0.01
J1509140+175716	F15069+1808	...	188.06 ^{11.08}	0.46 \pm 0.01	-22.22 \pm 0.01

Table 4.5 (cont'd)

AKARI-FIS-V1 Name	IRAS Name	$\log(M_{star}(M_{\odot}))$	SFR(IR) ($M_{\odot} \text{ year}^{-1}$)	SFR(Ha) ($M_{\odot} \text{ year}^{-1}$)	$12+\log(\text{O}/\text{H})$	$u^{0.1}-r^{0.1}$ (mag)	$M_r^{0.1}$ (mag)
(1)	(2)	(3)	(4)	(5)	(6)	(7)	(8)
J1533582+113413	...	11.34 ^{0.04} _{0.32}	373.25 ^{32.38} _{10.68}	2.11±0.41	-22.18±0.01
J1425160+162313	F14228+1636	10.62 ^{0.17} _{0.01}	176.28 ^{18.14} _{9.12}	16.89 ^{8.41} _{8.41}	...	2.30±0.04	-22.12±0.01
J1348483+181401	F13464+1828	10.16 ^{0.08} _{0.07}	242.60 ^{12.04} _{18.41}	39.03 ^{18.31} _{18.31}	8.78±0.84	2.75±0.30	-19.73±0.02
J1125319+290316	308.25 ^{35.57} _{2.72}	1.96±0.03	-21.24±0.01
J1603043+094717	F16006+0955	10.51 ^{0.18} _{0.02}	189.19 ^{11.72} _{11.72}	56.94 ^{21.41} _{21.41}	...	2.37±0.06	-21.54±0.01
J1639245+303719	F16374+3043	...	240.88 ^{26.33} _{...}	1.69±0.08	-21.64±0.01
J1050288+002806	...	10.26 ^{0.01} _{0.22}	411.53 ^{131.76} _{56.28}	62.72 ^{25.60} _{25.60}	8.74±0.13	1.31±0.04	-21.58±0.01
J0928103+232521	...	10.01 ^{0.32} _{0.03}	234.15 ^{45.51} _{1.78}	10.32 ^{1.78} _{1.78}	9.06±0.09	2.18±0.17	-20.18±0.02
J2344170+053520	F23417+0518	11.61 ^{0.05} _{0.11}	546.64 ^{108.35} _{48.04}	42.52 ^{27.47} _{27.47}	...	4.00±1.64	-22.39±0.01
J2353152-313234	207.63 ^{41.70} _{...}
J1302051-041435	181.59 ^{27.30} _{14.82}
J1059519-054333	179.93 ^{40.53} _{...}
J1222488-040307	240.99 ^{16.48} _{14.56}
J1419037-034657	200.12 ^{20.22} _{...}
J1048019-013017	218.52 ^{24.88} _{25.89}
J1338353-041131	241.82 ^{32.39} _{42.14}
J2318556-333544	176.40 ^{33.81} _{4.87}
J0806507+523514	F08030+5243	10.74 ^{0.07} _{0.04}	174.82 ^{17.90} _{4.87}	62.11 ^{13.37} _{13.37}	8.64±0.08	2.71±0.07	-20.01±0.01
J0857064+190855	F08542+1920	...	1395.72 ^{57.59} _{124.77}	0.16±0.01	-23.15±0.01
J1022125+241208	F10194+2427	10.78 ^{0.03} _{0.09}	188.32 ^{16.23} _{7.20}	2.39±0.07	-21.91±0.01
J1422313+260205	F14202+2615	10.31 ^{0.36} _{0.06}	304.58 ^{36.09} _{35.56}	29.09 ^{7.93} _{7.93}	8.68±0.09	1.15±0.02	-21.47±0.01
J1231216+275524	F12288+2811	10.58 ^{0.15} _{0.04}	315.50 ^{50.80} _{23.67}	7.12 ^{5.16} _{5.16}	8.54±0.24	2.44±0.09	-21.92±0.01
J1251200+021900	F12487+0235	10.60 ^{0.24} _{0.01}	542.50 ^{39.11} _{20.36}	66.67 ^{66.75} _{40.00}	8.40±0.32	1.67±0.04	-22.24±0.01
J0030089-002743	F00275-0044	...	287.81 ^{18.76} _{...}
J0914140+032200	F09116+0334	10.56 ^{0.06} _{0.01}	234.10 ^{32.54} _{11.39}	373.92 ^{303.02} _{303.02}	...	2.21±0.03	-21.92±0.01
J1105377+311432	F11028+3130	9.97 ^{0.06} _{0.04}	319.45 ^{39.83} _{16.87}	2.45 ^{0.70} _{...}	...	1.90±0.10	-20.72±0.01
J0323227-075612	F03209-0806	10.41 ^{0.12} _{0.03}	249.98 ^{31.17} _{47.23}	36.59 ^{8.89} _{35.78}	8.75±1.21	1.37±0.03	-21.51±0.01
J1632212+155145	F16300+1558	10.65 ^{0.17} _{0.17}	874.58 ^{61.32} _{61.32}	43.43 ^{35.78} _{35.78}	8.69±0.21	1.75±0.06	-22.07±0.01
J0148531+002857	F01462+0014	10.47 ^{0.03} _{0.24}	359.17 ^{19.50} _{17.32}	73.65 ^{37.13} _{37.13}	...	1.33±0.04	-21.72±0.01
J0159503+002340	F01572+0009	...	455.93 ^{27.83} _{29.12}
J1353317+042809	F13509+0442	...	277.27 ^{22.29} _{17.47}

Table 4.5 (cont'd)

AKARI-FIS-V1 Name	IRAS Name	$\log(M_{star}(M_{\odot}))$	SFR(IR) ($M_{\odot} \text{ year}^{-1}$)	SFR(H α) ($M_{\odot} \text{ year}^{-1}$)	$12+\log(\text{O}/\text{H})$	$u^{0.1}-r^{0.1}$ (mag)	$M_r^{0.1}$ (mag)
(1)	(2)	(3)	(4)	(5)	(6)	(7)	(8)
J0244173-003040	F02417-0043	...	201.14 $^{7.13}_{-7.83}$
J1202268-012918	F11598-0112	...	459.83 $^{36.91}_{-38.88}$
J1013477+465402	F10107+4708	10.17 $^{0.30}_{-0.05}$	328.85 $^{68.92}_{-34.05}$	1.98 ± 0.13	-20.91 ± 0.01
J0858418+104124	F08559+1053	10.67 $^{0.06}_{-0.04}$	282.94 $^{22.36}_{-13.95}$	2.18 ± 0.03	-21.91 ± 0.01
J1347336+121727	F13451+1232	...	290.00 $^{31.51}_{-31.51}$
J0853252+252646	F08504+2538	...	453.63 $^{52.93}_{-54.76}$
J0825215+383306	F08220+3842	10.65 $^{0.06}_{-0.01}$	313.83 $^{124.73}_{-34.24}$	25.67 $^{17.85}_{-17.85}$	8.64 ± 0.20	2.68 ± 0.11	-21.70 ± 0.01
J0829512+384528	F08266+3855	9.66 $^{0.02}_{-0.01}$	187.33 $^{28.17}_{-18.50}$	26.37 $^{18.50}_{-18.50}$	8.40 ± 0.27	2.11 ± 0.25	-19.45 ± 0.02
J1142035+005135	F11394+0108	10.16 $^{0.21}_{-0.07}$	239.55 $^{33.05}_{-33.05}$	74.44 $^{48.13}_{-43.13}$...	1.08 ± 0.03	-21.63 ± 0.01
J0945214+173803	F09425+1751	...	178.03 $^{12.22}_{-13.96}$
J0810595+281354	F08079+2822	10.28 $^{0.36}_{-0.01}$	775.00 $^{146.79}_{-132.71}$	36.23 $^{19.21}_{-19.21}$	8.06 ± 0.26	1.23 ± 0.06	-21.43 ± 0.01
J0900252+390400	F08572+3915	9.42 $^{0.04}_{-0.04}$	219.18 $^{12.36}_{-7.36}$	5.41 $^{2.31}_{-2.31}$	8.63 ± 0.14	1.84 ± 0.03	-19.40 ± 0.01
J0830197+192040	F08274+1930	10.24 $^{0.16}_{-0.07}$	207.73 $^{37.36}_{-32.32}$	17.61 $^{5.01}_{-5.01}$	8.89 ± 0.07	1.00 ± 0.03	-21.03 ± 0.01
J1121293+112233	F11188+1138	10.46 $^{0.01}_{-0.01}$	366.69 $^{31.81}_{-20.17}$	80.63 $^{26.63}_{-26.63}$...	1.67 ± 0.03	-21.97 ± 0.01
J1006038+411223	F10030+4126	10.18 $^{0.19}_{-0.01}$	508.51 $^{29.67}_{-38.04}$	65.98 $^{40.00}_{-40.00}$	8.56 ± 0.27	1.38 ± 0.07	-21.46 ± 0.01
J0838034+505516	F08344+5105	9.96 $^{0.08}_{-0.01}$	174.98 $^{1.07}_{-1.93}$	17.49 $^{2.32}_{-2.32}$	8.63 ± 0.19	1.94 ± 0.03	-20.48 ± 0.01
J0902489+523623	F08591+5248	10.57 $^{0.11}_{-0.01}$	215.77 $^{11.28}_{-22.74}$	35.00 $^{1.98}_{-1.98}$...	2.15 ± 0.04	-21.68 ± 0.01
J1021426+130657	F10190+1322	10.34 $^{0.01}_{-0.01}$	196.20 $^{15.02}_{-6.89}$	8.27 $^{1.78}_{-1.78}$	8.99 ± 40.18	2.26 ± 0.03	-20.46 ± 0.01
J1427269-005837	F14248-0045	10.32 $^{0.06}_{-0.03}$	203.94 $^{30.88}_{-11.93}$	62.06 $^{20.01}_{-20.01}$	8.71 ± 0.12	2.29 ± 0.05	-21.17 ± 0.01
J1246333+453425	F12442+4550	...	173.58 $^{9.89}_{-9.89}$
J0847504+232113	F08449+2332	10.23 $^{0.17}_{-0.06}$	172.78 $^{24.43}_{-17.50}$	35.45 $^{8.02}_{-8.02}$	8.81 ± 0.07	1.06 ± 0.02	-20.88 ± 0.01
J1559301+380843	F15577+3816	10.70 $^{0.01}_{-0.05}$	253.16 $^{20.45}_{-20.07}$	23.24 $^{9.89}_{-9.89}$...	1.89 ± 0.08	-21.56 ± 0.01
J1324197+053705	F13218+0552	...	997.93 $^{62.13}_{-62.13}$
J1102140+380240	F10594+3818	10.47 $^{0.12}_{-0.04}$	285.10 $^{9.82}_{-9.82}$	44.64 $^{13.12}_{-13.12}$	8.89 ± 0.30	1.45 ± 0.02	-21.50 ± 0.01
J1204244+192509	F12018+1941	10.15 $^{0.02}_{-0.04}$	285.82 $^{22.02}_{-15.78}$	65.19 $^{35.08}_{-35.08}$	7.62 ± 0.37	1.90 ± 0.05	-21.30 ± 0.01
J1108513+065915	F11062+0715	...	199.16 $^{17.26}_{-25.29}$
J1040290+105325	F10378+1108	10.35 $^{0.18}_{-0.01}$	359.91 $^{34.22}_{-34.22}$	42.65 $^{13.49}_{-13.49}$...	2.21 ± 0.05	-21.35 ± 0.01
J1207210+021702	F12047+0233	10.20 $^{0.24}_{-0.11}$	246.43 $^{30.73}_{-23.23}$	48.15 $^{18.38}_{-18.38}$	8.89 ± 0.10	1.00 ± 0.03	-21.50 ± 0.01
J1255482-033908	F12532-0322	...	207.11 $^{49.42}_{-26.96}$
J0906339+045136	F09039+0503	10.45 $^{0.01}_{-0.33}$	212.67 $^{22.86}_{-11.33}$	36.24 $^{14.37}_{-14.37}$	8.22 ± 0.20	1.82 ± 0.04	-20.82 ± 0.01
J1153144+131432	F11506+1331	10.08 $^{0.05}_{-0.01}$	338.76 $^{29.22}_{-14.70}$	46.87 $^{28.16}_{-28.16}$	8.40 ± 0.28	2.17 ± 0.07	-20.51 ± 0.01

Table 4.5 (cont'd)

AKARI-FIS-V1 Name	IRAS Name	$\log(M_{star}(M_{\odot}))$	SFR(IR) ($M_{\odot} \text{ year}^{-1}$)	SFR(H α) ($M_{\odot} \text{ year}^{-1}$)	$12+\log(\text{O}/\text{H})$	$u^{0.1-r^{0.1}}$ (mag)	$M_r^{0.1}$ (mag)
(1)	(2)	(3)	(4)	(5)	(6)	(7)	(8)
J1202054+112813	F11595+1144	10.17 ^{+0.50} _{-0.01}	273.27 ^{+30.70} _{-10.65}	71.12 ^{+25.04} _{-5.04}	8.75 \pm 0.17	1.22 \pm 0.02	-21.61 \pm 0.01
J1006432+091726	F10040+0932	10.34 ^{+0.12} _{-0.03}	245.87 ^{+38.86} _{-7.40}	25.71 ^{+14.81} _{-1.81}	8.75 \pm 0.15	1.55 \pm 0.04	-21.06 \pm 0.01
J1052232+440849	F10494+4424	10.22 ^{+0.04} _{-0.03}	235.50 ^{+18.44} _{-11.51}	19.53 ^{+4.63} _{-4.63}	8.37 \pm 0.16	2.52 \pm 0.06	-20.45 \pm 0.01
J1254008+101115	F12514+1027	...	760.85 ^{+69.69} _{-69.69}
J1348397+581854	F13469+5833	10.46 ^{+0.06} _{-0.13}	267.79 ^{+31.40} _{-19.74}	12.80 ^{+6.22} _{-19.74}	8.77 \pm 0.40	2.23 \pm 0.07	-21.02 \pm 0.01
J1015153+272717	F10124+2742	10.36 ^{+0.32} _{-0.01}	246.83 ^{+22.78} _{-18.15}	48.54 ^{+19.74} _{-19.74}	8.45 \pm 0.16	1.91 \pm 0.06	-21.26 \pm 0.01
J1356100+290538	F13539+2920	11.00 ^{+0.06} _{-0.10}	210.28 ^{+14.23} _{-18.93}	38.88 ^{+4.00} _{-14.00}	...	3.09 \pm 0.11	-20.41 \pm 0.01
J1502320+142132	F15001+1433	10.44 ^{+0.07} _{-0.01}	227.56 ^{+22.66} _{-11.63}	71.16 ^{+27.79} _{-11.63}	8.38 \pm 0.21	2.07 \pm 0.04	-21.58 \pm 0.01
J1336237+391733	F13342+3932	...	373.33 ^{+33.45} _{-33.45}
J1141215+405951	F11387+4116	10.45 ^{+0.06} _{-0.02}	212.81 ^{+48.48} _{-19.96}	70.19 ^{+55.30} _{-55.30}	8.14 \pm 1.22	2.47 \pm 0.06	-21.08 \pm 0.01
J1433271+281157	F14312+2825	10.72 ^{+0.01} _{-0.06}	252.99 ^{+73.17} _{-30.03}	82.58 ^{+31.93} _{-31.93}	...	2.23 \pm 0.05	-21.79 \pm 0.01
J1450544+350835	F14488+3521	10.86 ^{+0.07} _{-0.07}	388.78 ^{+48.05} _{-17.75}	182.73 ^{+56.49} _{-17.75}	8.79 \pm 0.15	1.55 \pm 0.02	-22.33 \pm 0.01
J1406380+010258	F14041+0117	10.11 ^{+0.18} _{-0.01}	381.24 ^{+34.48} _{-17.75}	10.76 ^{+21.52} _{-8.00}	7.79 \pm 0.67	1.28 \pm 0.04	-21.40 \pm 0.01
J1524440+234016	F15225+2350	10.33 ^{+0.35} _{-0.07}	190.19 ^{+17.69} _{-10.71}	36.54 ^{+17.74} _{-17.74}	8.70 \pm 0.15	2.03 \pm 0.06	-21.30 \pm 0.01
J1522382+333135	F15206+3342	...	205.21 ^{+4.02} _{-23.81}
J1505390+574305	F15043+5754	10.45 ^{+0.06} _{-0.08}	186.34 ^{+35.97} _{-11.86}	19.34 ^{+10.76} _{-10.76}	8.85 \pm 0.13	1.29 \pm 0.03	-20.69 \pm 0.01
J1441041+532011	F14394+5332	...	219.68 ^{+15.40} _{-15.40}
J1706529+382010	F17051+3824	10.26 ^{+0.01} _{-0.01}	268.78 ^{+9.02} _{-24.59}	13.66 ^{+8.59} _{-8.59}	...	2.17 \pm 0.06	-20.94 \pm 0.01
J1649140+342510	F16474+3430	9.63 ^{+0.32} _{-0.15}	227.14 ^{+59.72} _{-3.23}	6.03 ^{+2.11} _{-3.23}	8.87 \pm 0.09	1.73 \pm 0.06	-19.69 \pm 0.01
J0800310+481539	F07568+4823	9.93 ^{+0.04} _{-0.04}	178.16 ^{+19.00} _{-19.00}	2.39 ^{+0.70} _{-0.70}	8.57 \pm 0.18	1.74 \pm 0.04	-20.82 \pm 0.01
J0823127+275140	F08201+2801	10.38 ^{+0.11} _{-0.20}	241.77 ^{+14.40} _{-17.05}	13.46 ^{+4.23} _{-4.23}	8.70 \pm 0.10	1.58 \pm 0.04	-21.19 \pm 0.01
J1213460+024844	F12112+0305	10.28 ^{+0.01} _{-0.01}	350.75 ^{+26.85} _{-24.67}	8.84 ^{+2.46} _{-2.46}	8.39 \pm 0.33	1.78 \pm 0.03	-20.14 \pm 0.01
J1346511+074720	F13443+0802	10.57 ^{+0.05} _{-0.01}	244.12 ^{+40.28} _{-33.80}	20.00 ^{+3.39} _{-3.39}	8.97 \pm 0.04	2.08 \pm 0.03	-21.49 \pm 0.01
J2257246-262120	F22546-2637	...	299.29 ^{+57.01} _{-57.01}
J223286-270006	F22206-2715	...	274.92 ^{+30.32} _{-5.62}
J1132417-053940	F11300-0522	...	303.39 ^{+28.68} _{-26.99}
J0238167-322036	F02361-3233	...	368.13 ^{+31.48} _{-32.46}
J0238126-473813	F02364-4751	...	243.89 ^{+19.13} _{-19.13}
J0237297-461544	F02356-4628	...	442.08 ^{+43.02} _{-41.83}
J0048064-284820	F00456-2904	...	251.59 ^{+26.78} _{-5.99}
J0112165-273819	F01098-2754	...	316.01 ^{+106.88} _{-172.49}

Table 4.5 (cont'd)

AKARI-FIS-V1 Name	IRAS Name	$\log(M_{star}(M_{\odot}))$	SFR(IR) ($M_{\odot} \text{ year}^{-1}$)	SFR(H α) ($M_{\odot} \text{ year}^{-1}$)	$12+\log(\text{O}/\text{H})$	$u^{0.1}-r^{0.1}$ (mag)	$M_r^{0.1}$ (mag)
(1)	(2)	(3)	(4)	(5)	(6)	(7)	(8)
J0138061-324519	F01358-3300	...	268.35 ^{49.07} _{10.16}
J0302108-270725	F03000-2719	...	503.15 ^{62.35} _{38.71}
J0118266-253607	F01160-2551	...	268.10 ^{32.32} _{16.37}
J0152042-285116	F01497-2906	...	225.73 ^{15.50} _{20.27}
J0159138-292436	F01569-2939	...	232.17 ^{6.41} _{6.41}
J1329391-034654	F13270-0331	...	331.51 ^{368.54} _{15.26}
J1143187-032549	F11407-0309	...	184.50 ^{26.28} _{9.66}
J1112034-025414	F11095-0238	...	262.78 ^{45.70} _{33.65}
J2307212-343838	F23046-3454	...	331.05 ^{36.09} _{36.09}
J2208493-344627	F22058-3501	...	232.27 ^{103.64} _{48.23}
J1425001+103045	F14225+1044	10.77 ^{0.04} _{0.05}	2673.00 ^{1354.46} _{283.37}	139.15 ^{79.91} _{79.91}	8.64 \pm 0.17	1.19 \pm 0.06	-22.62 \pm 0.00

Note. — (1) AKARI FIS-V1 Catalog Name. (2) IRAS Faint Source Catalog Name. (3) Stellar mass adopted from Maraston et al. (2012). (4) SFRs derived from IR luminosity. (5) SFRs derived from H α luminosity. (6) Oxygen abundances derived in this work. (7) $u^{0.1}-r^{0.1}$ color. (8) Absolute magnitude in r band.

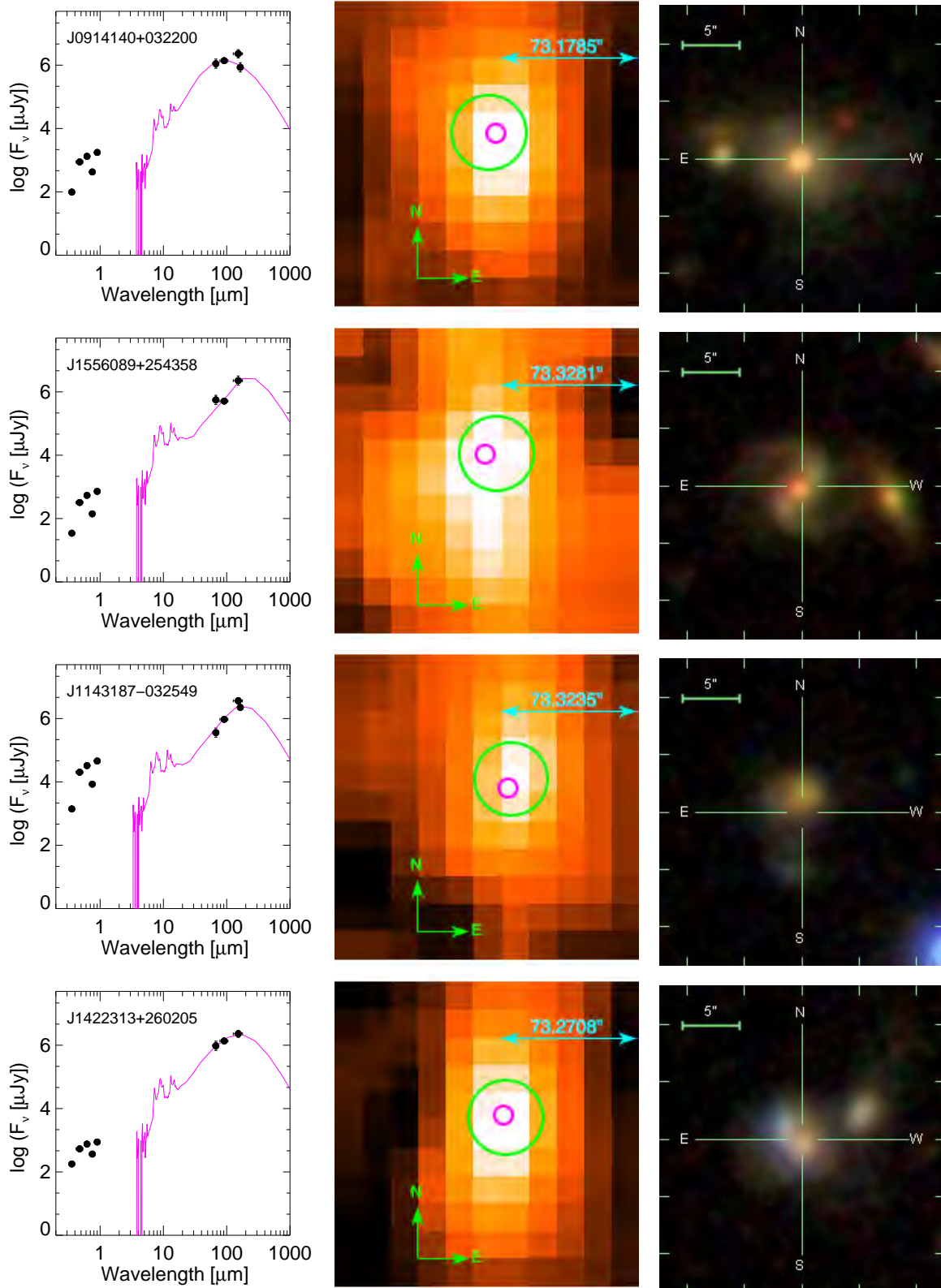


Figure 4.1 SEDs (left), AKARI (middle) and SDSS $g-r-i$ colors combined images (right) of four nearest ULIRGs classified as 'IIIa'. The scale of the AKARI 90 μm images are $165'' \times 165''$. The magenta (5'' radius) and green (20'' radius) circles, mark the optical and IR source, respectively.

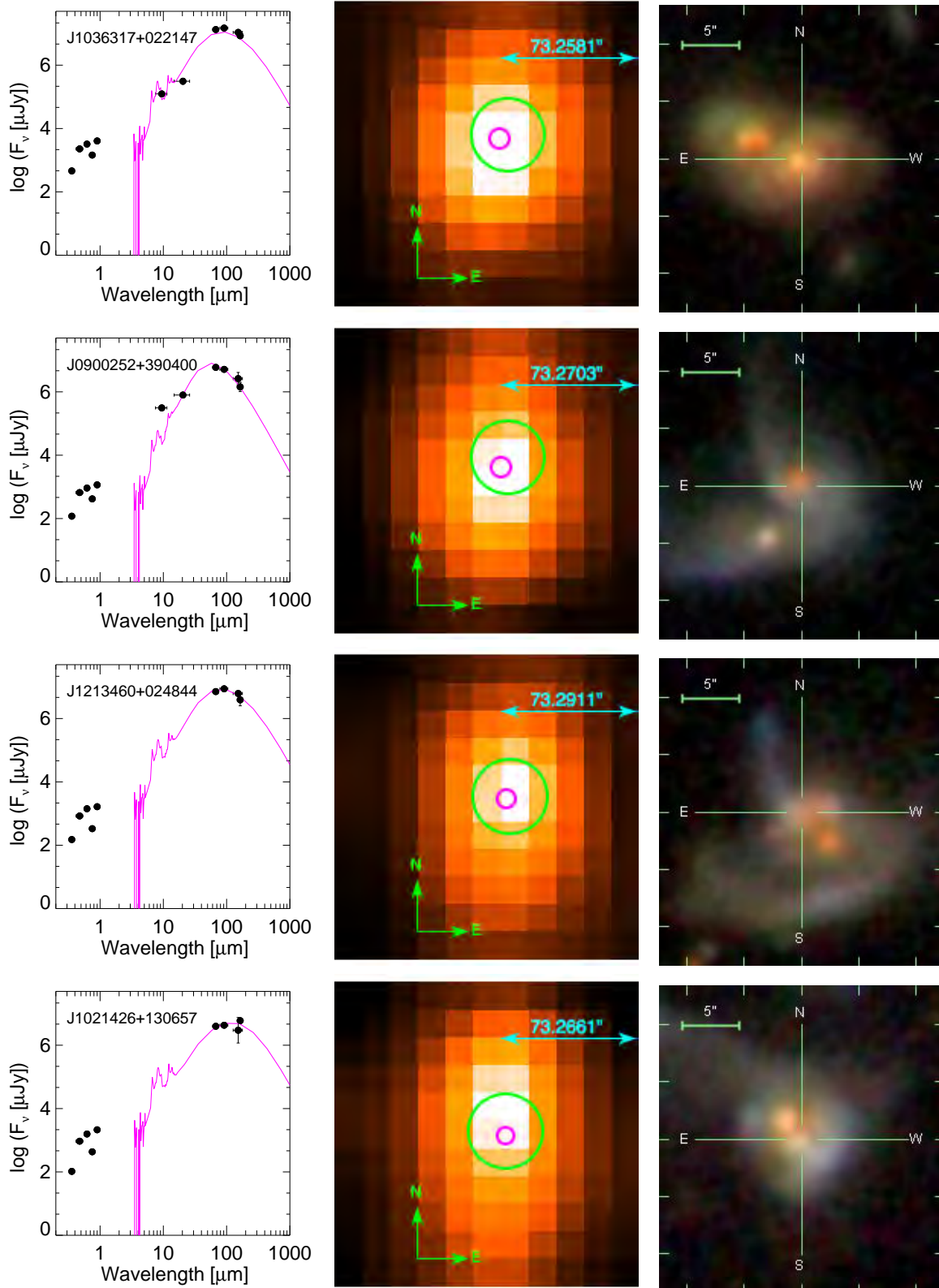


Figure 4.2 Same as Figure 4.1, but for ULIRGs classified as 'IIIb'.

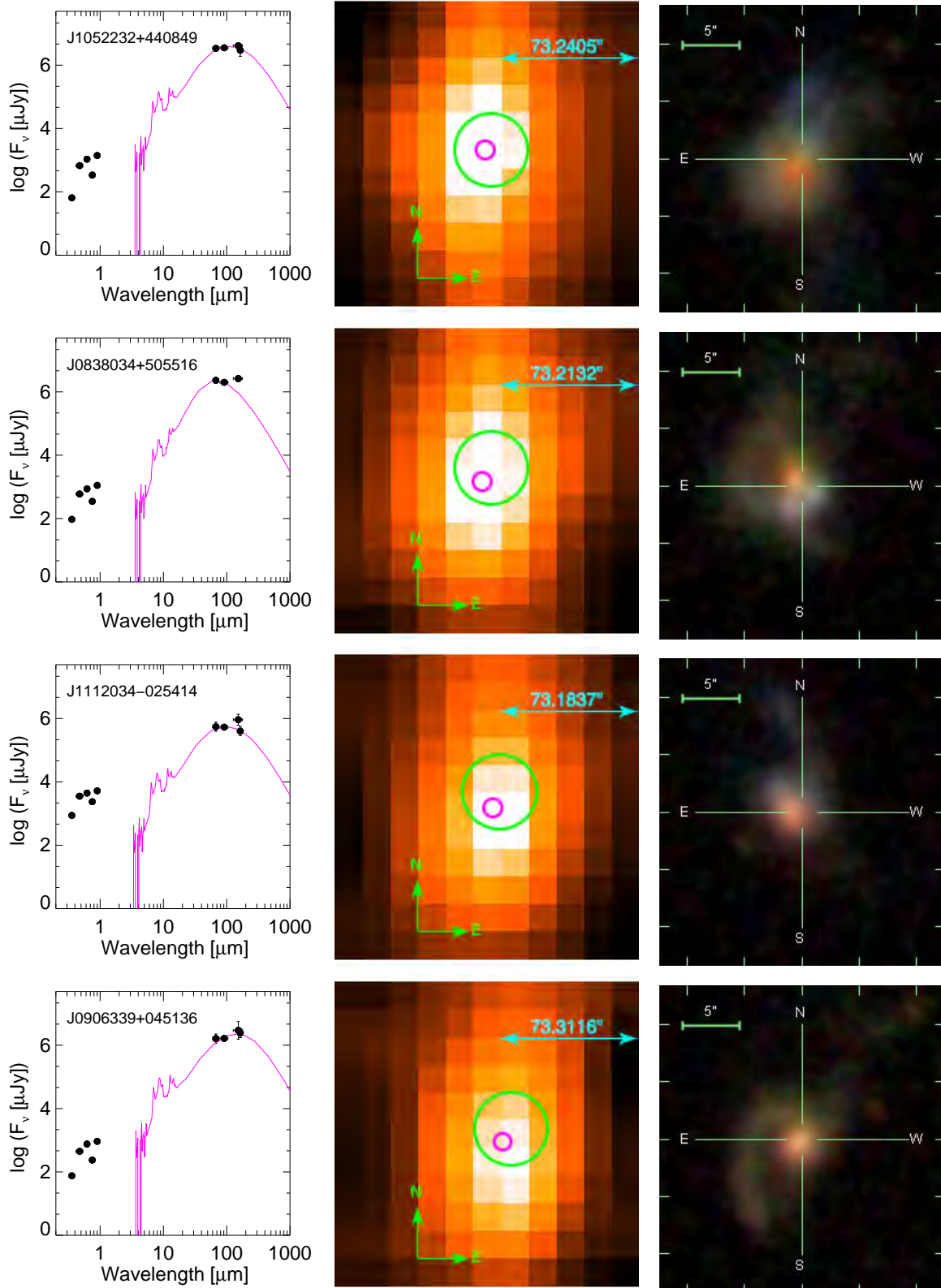


Figure 4.3 Same as Figure 4.1, but for ULIRGs classified as 'IV'.

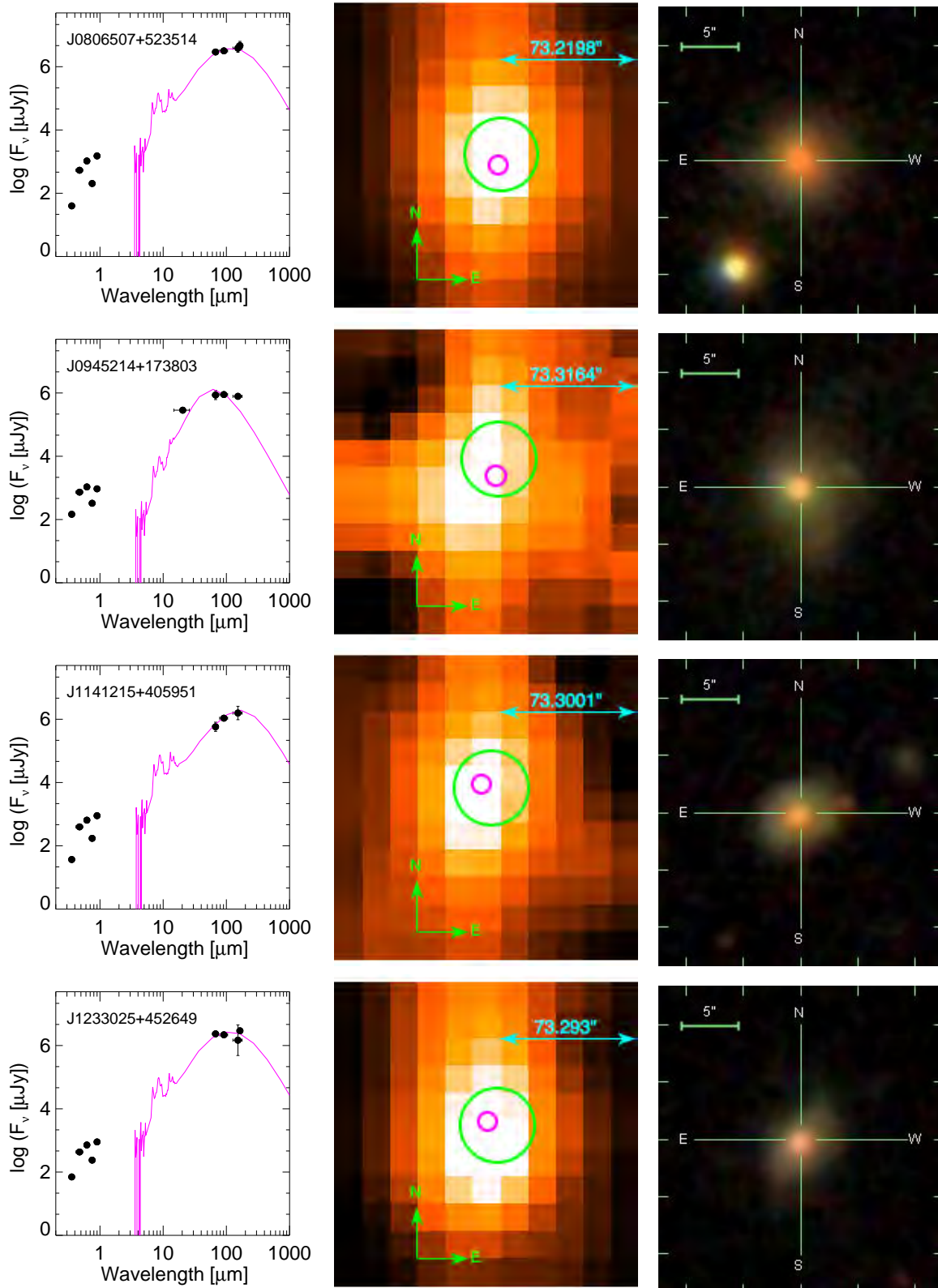


Figure 4.4 Same as Figure 4.1, but for ULIRGs classified as 'V'.

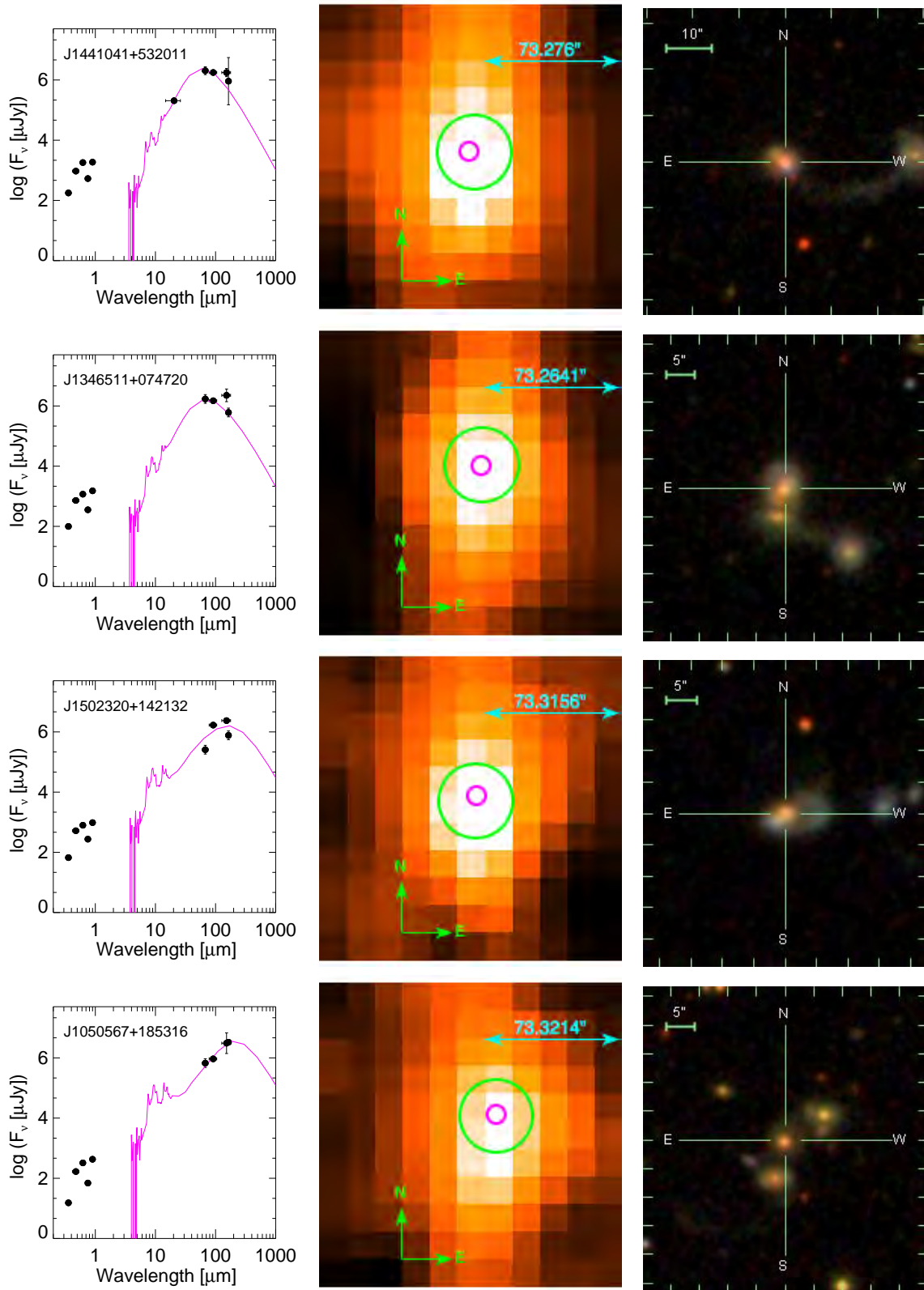


Figure 4.5 Same as Figure 4.1, but for ULIRGs classified as 'Tp1'.

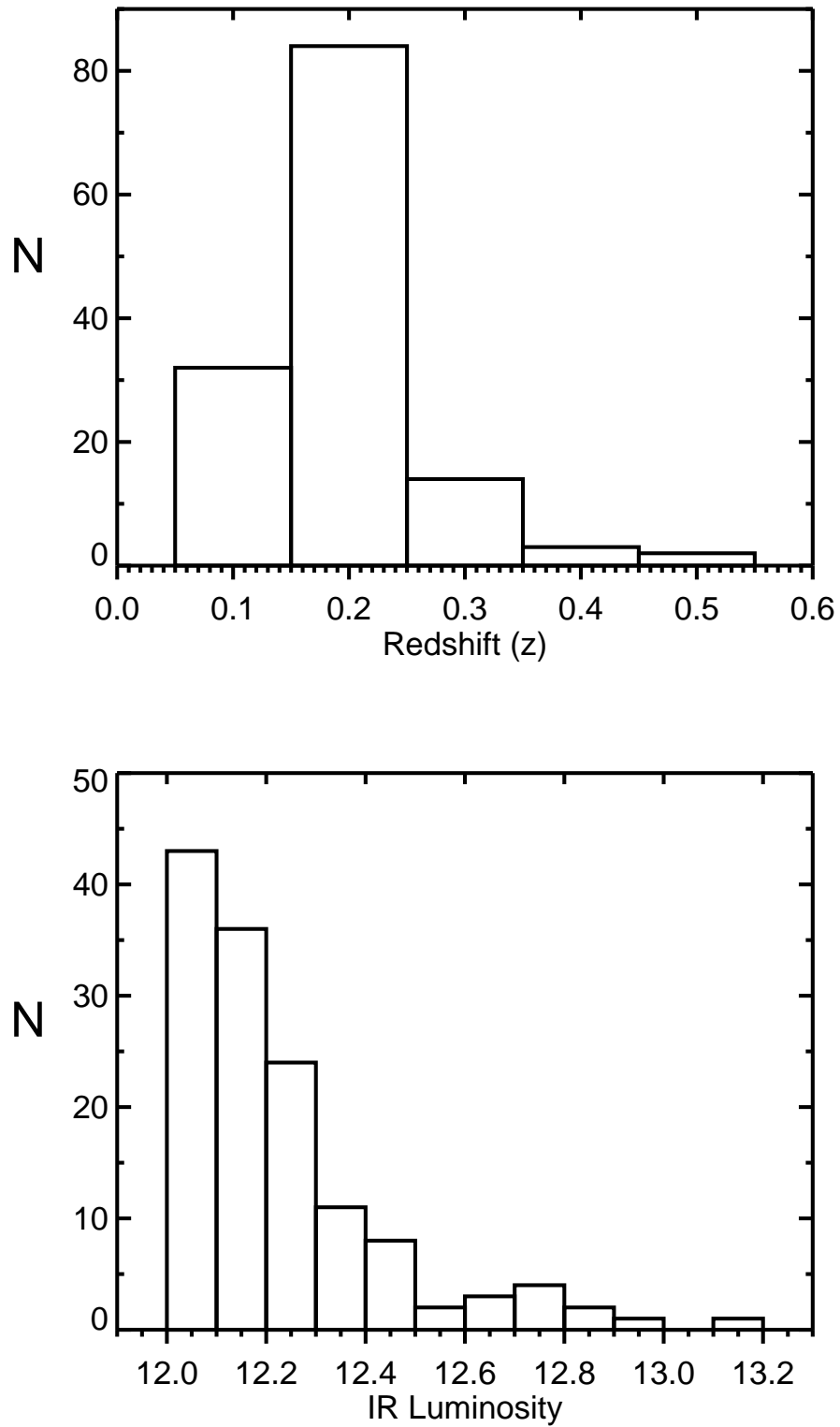


Figure 4.6 Distributions of redshift (top) and IR luminosity, $\log(L_{IR}/L_{\odot})$, (bottom) for the final (H)/ULIRG sample.

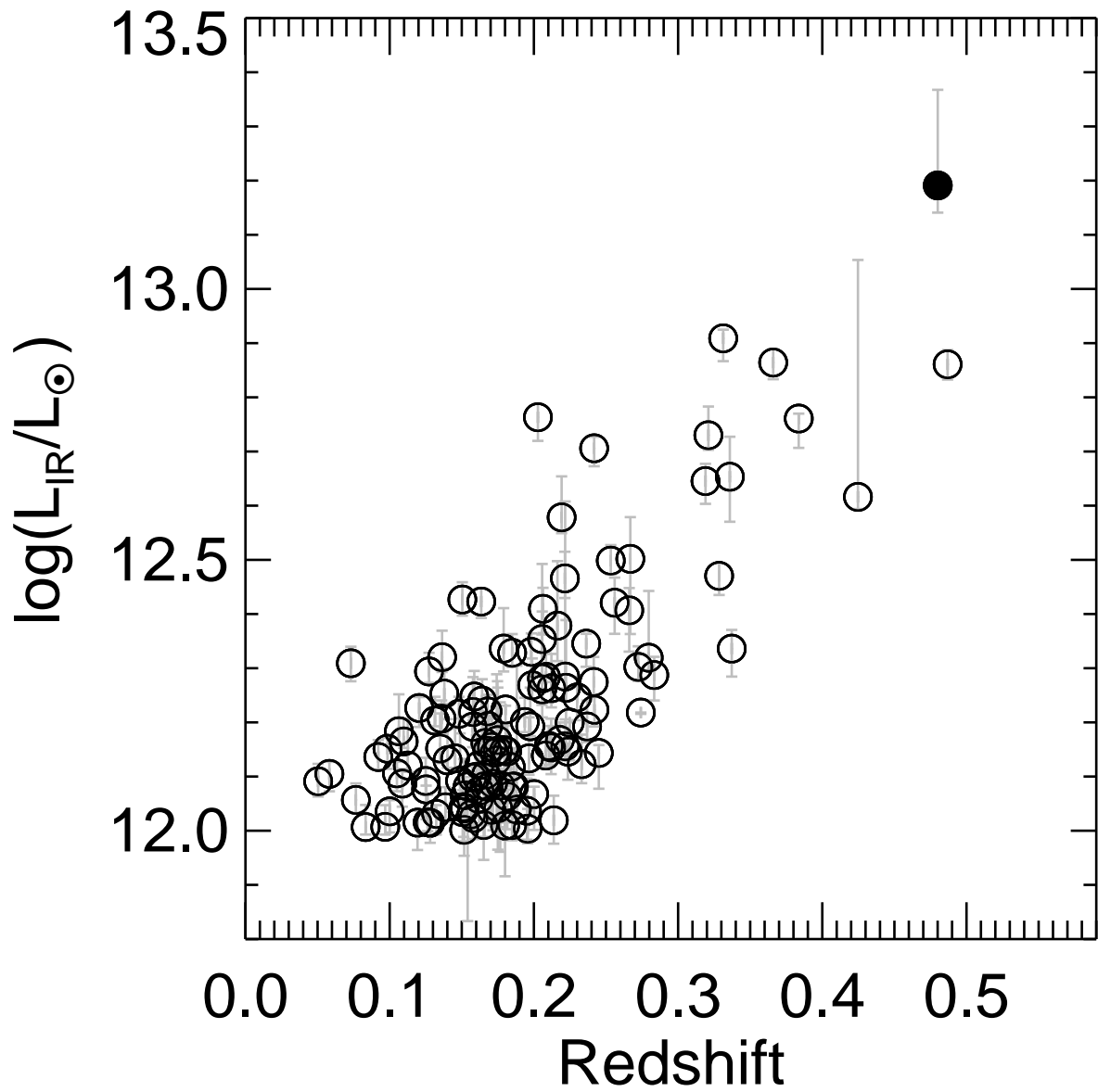


Figure 4.7 IR luminosity vs. redshift for 134 ULIRGs (open circles) and one HLIRG (filled circle) in the final sample.

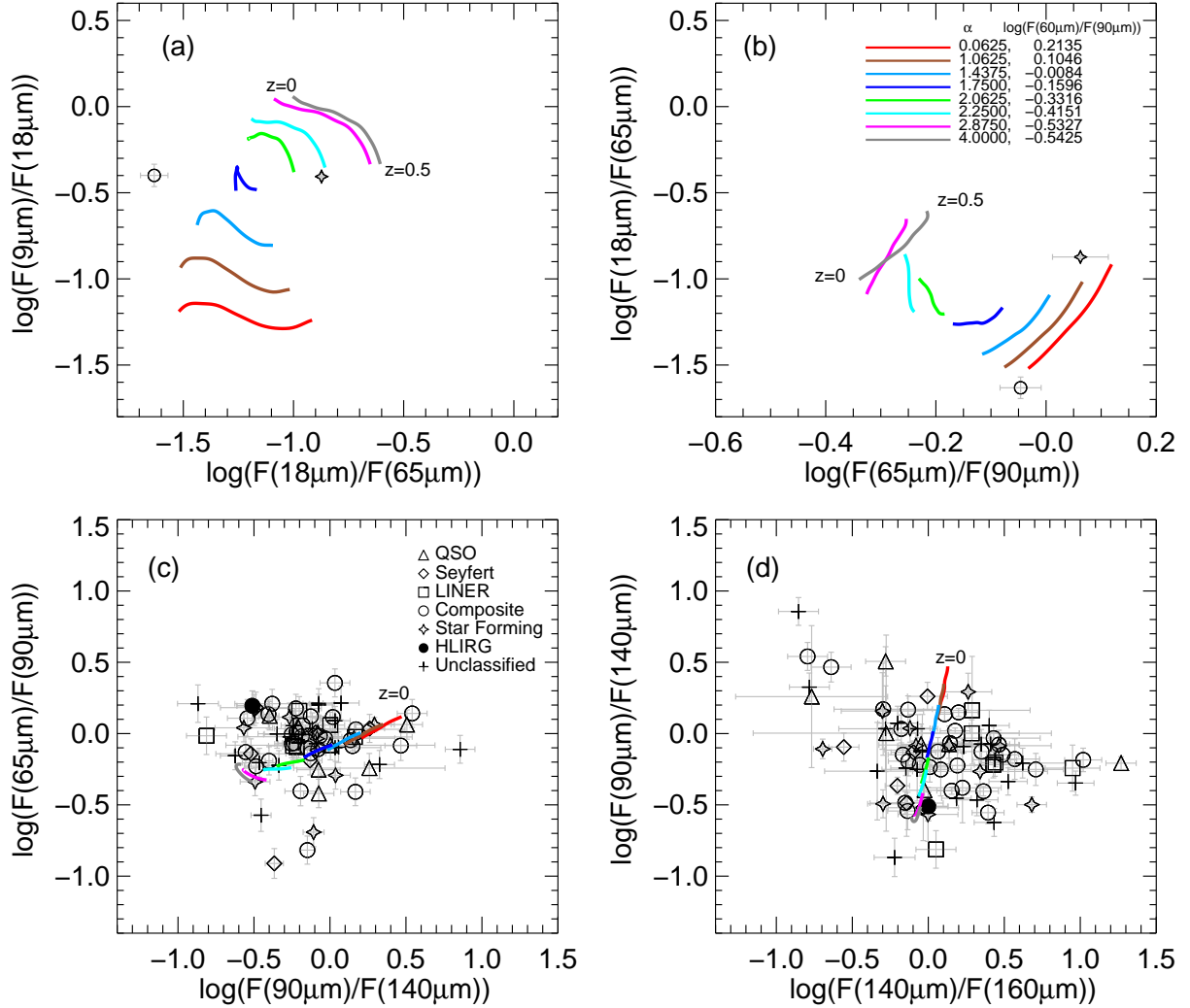


Figure 4.8 The AKARI color-color diagrams. The top left (a) and right (b) panels show $\log(F(9\mu\text{m})/F(18\mu\text{m}))$ versus $\log(F(18\mu\text{m})/F(65\mu\text{m}))$ and $\log(F(18\mu\text{m})/F(65\mu\text{m}))$ vs. $\log(F(65\mu\text{m})/F(90\mu\text{m}))$ for the two ULIRGs detected in all AKARI bands. The bottom panels show $\log(F(65\mu\text{m})/F(90\mu\text{m}))$ versus $\log(F(90\mu\text{m})/F(140\mu\text{m}))$ (c) and $\log(F(90\mu\text{m})/F(140\mu\text{m}))$ versus $\log(F(140\mu\text{m})/F(160\mu\text{m}))$ (d) colors for 81 sources that are detected in AKARI 65 μm , 90 μm , 140 μm , and 160 μm bands. Symbol code is given in the legend of panel (c). The solid lines indicate the expected colors from the SED templates of Dale & Helou (2002) as a function of redshift between $0 \leq z \leq 0.5$ (labels ‘z=0’ and ‘z=0.5’ show the z sequence for the models). We only show the expected colors for eight SED templates, different colored solid lines represent different models; parameters of the models are given in the legend of panel (b).

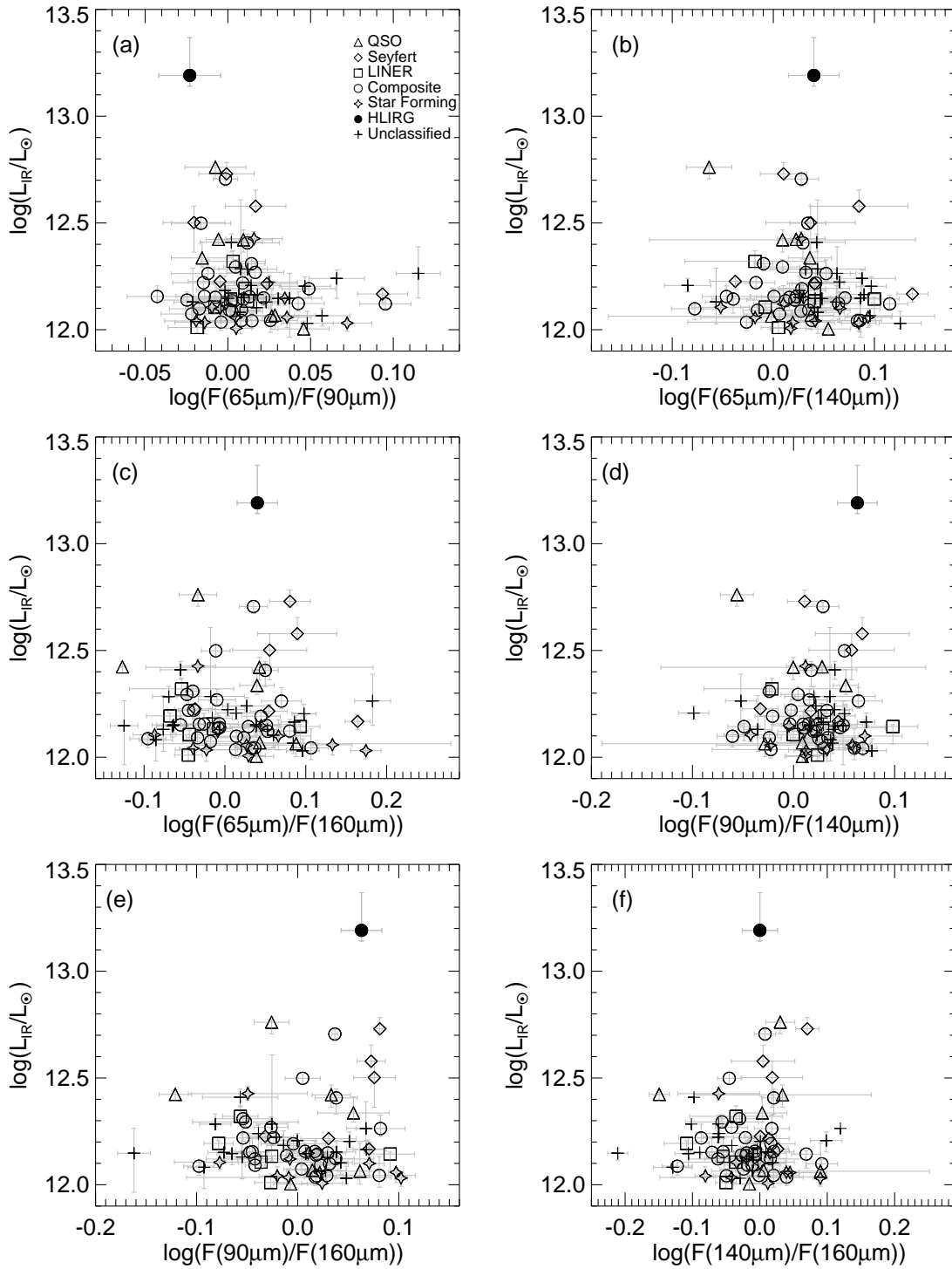


Figure 4.9 The color – luminosity diagrams of 81 (H)/ULIRGs that are detected in all *AKARI* FIS bands. Symbol code is given in panel (a).

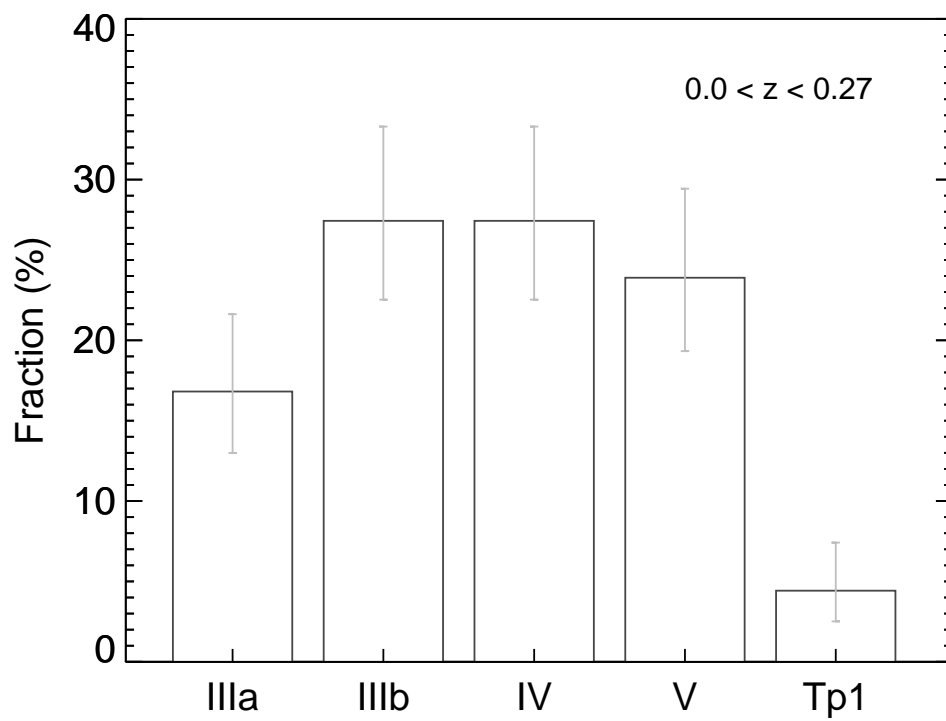


Figure 4.10 The distribution of the interaction classes for 113 ULIRGs within $0.0 < z < 0.27$ limit. Interaction classes are described in § 4.3.2. 51% of the ULIRGs are late/old mergers that are classified as IV or V. Error bars represent the 1σ Poisson errors (Gehrels, 1986).

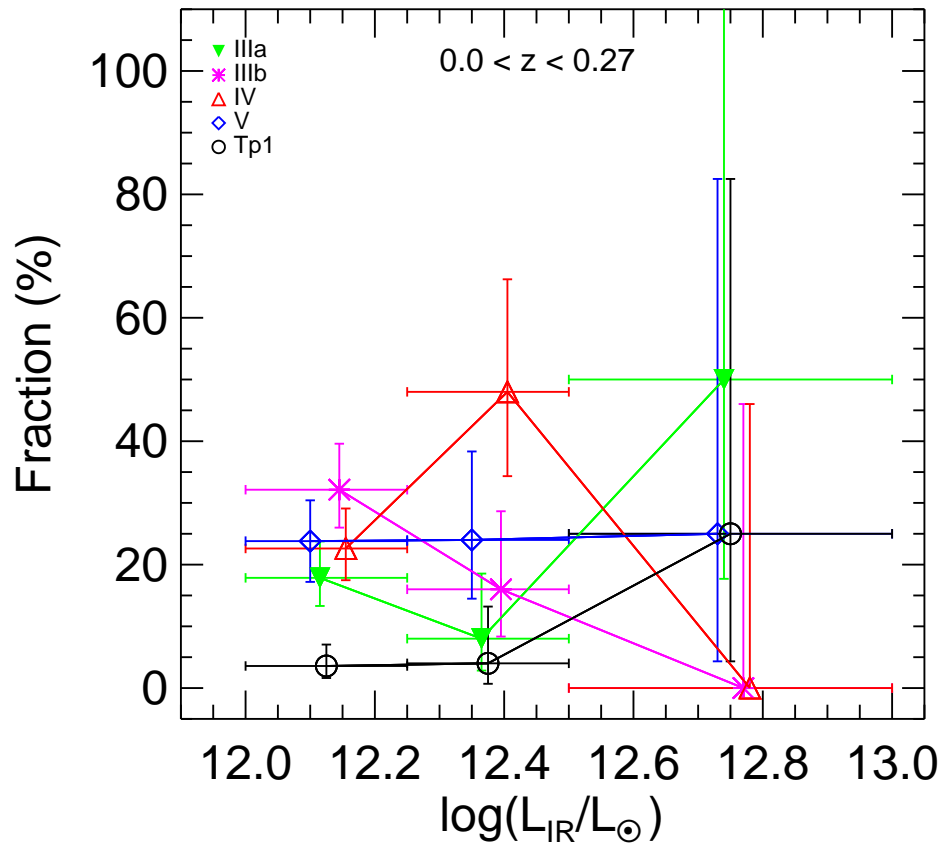


Figure 4.11 Fraction of interaction classes per IR luminosity for 113 ULIRGs within $z < 0.27$ limit. X-axis error bars represent the range of the IR luminosity bins where the highest luminosity value is not included in that bin. The y-axis error bars represent the 1σ confidence limits of the Poisson errors on the counts given by Gehrels (1986).

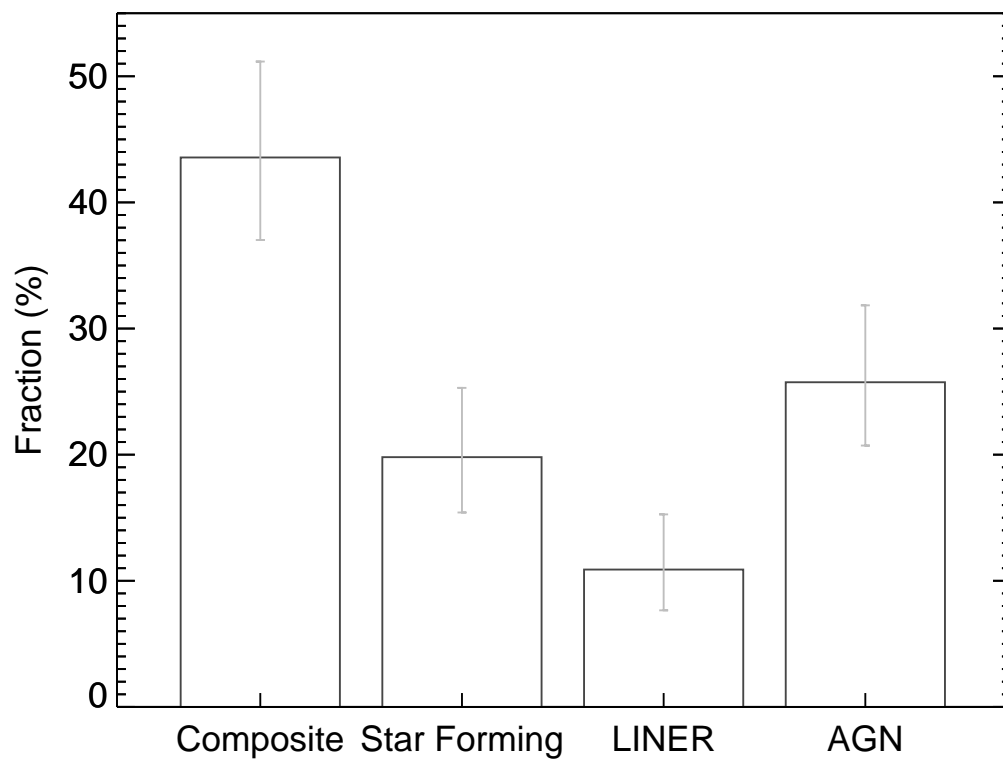


Figure 4.12 The distribution of spectral classes of 101 ULIRGs for which the SDSS spectra are available. Error bars represent the same quantity as in Figure 4.10.

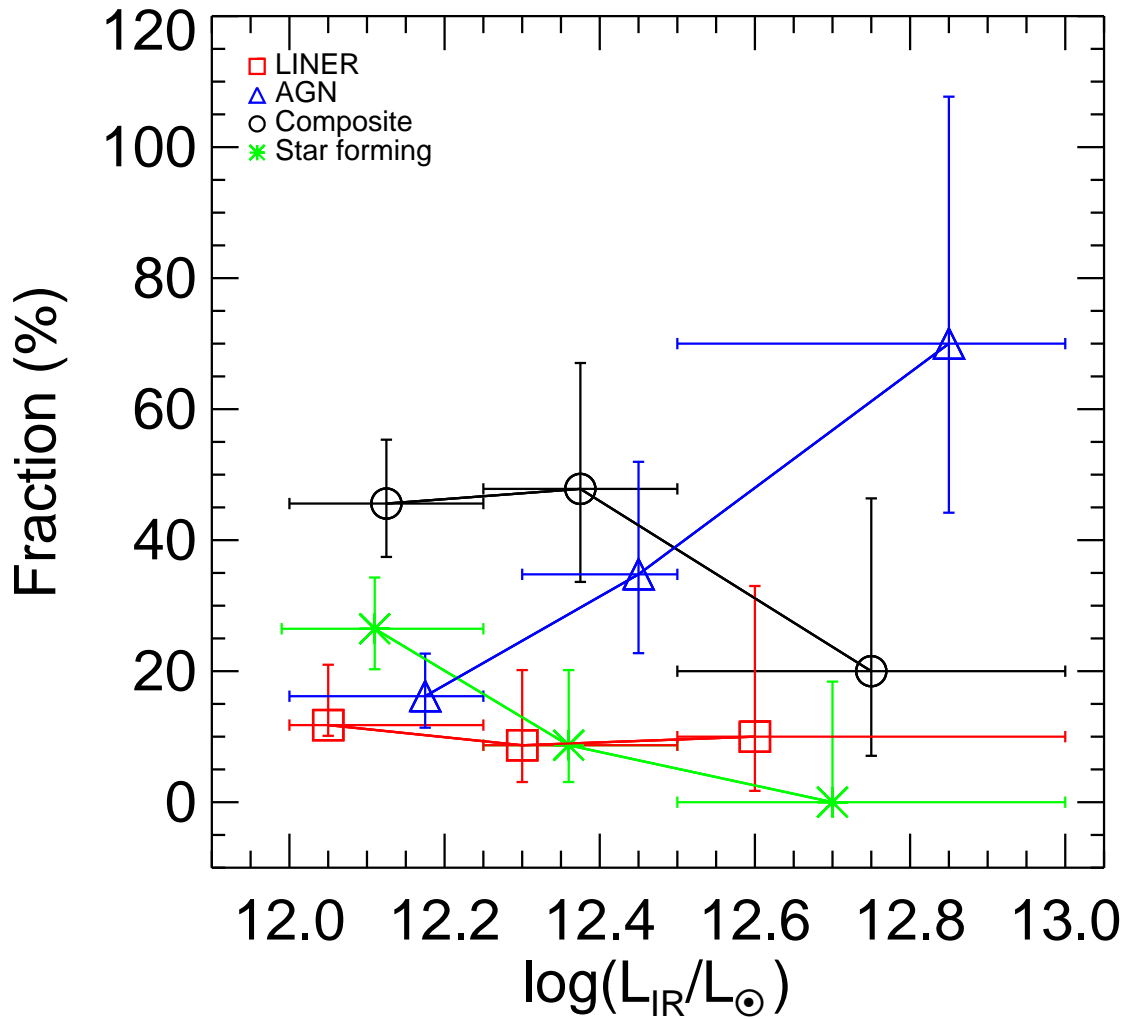


Figure 4.13 Spectral class fraction per IR luminosity bins for 101 ULIRGs. See the caption of Figure 4.11 for the error bars.

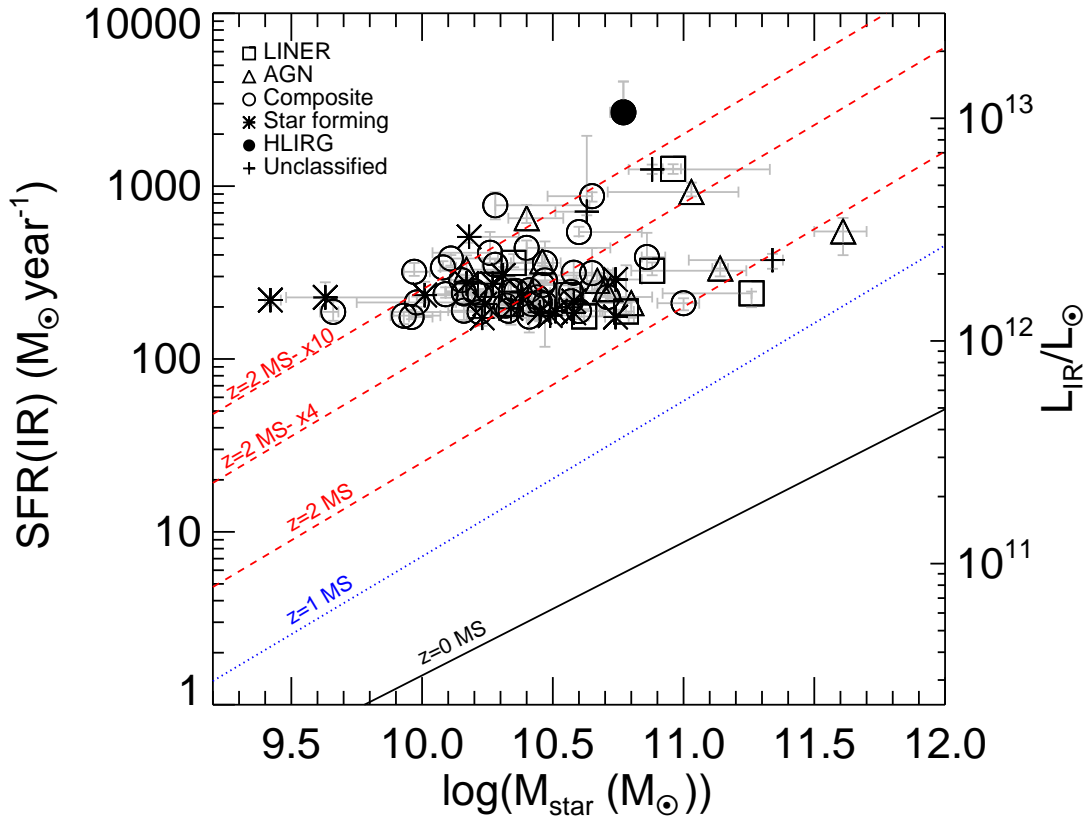


Figure 4.14 SFR(IR) versus stellar mass for 83 ULIRGs and one HLIRG. SFR(IR) values are derived from Eq. (4) of Kennicutt (1998). Error bars of SFR(IR) represent the uncertainties propagated through L_{IR} uncertainties. The black solid line is the $z=0$ ‘Main Sequence’ (MS) of normal star forming galaxies; Eq. (5) of Elbaz et al. (2007). The blue dotted line is the SFR– M_{star} relationship of $z=1$ star forming galaxies in the GOODS fields; Eq. (4) of Elbaz et al. (2007). The red dashed solid lines represent the SFR– M_{star} relationship of $z=2$ star forming galaxies in the GOODS fields (Daddi et al., 2007) and 4 and 10 times above this relationship .

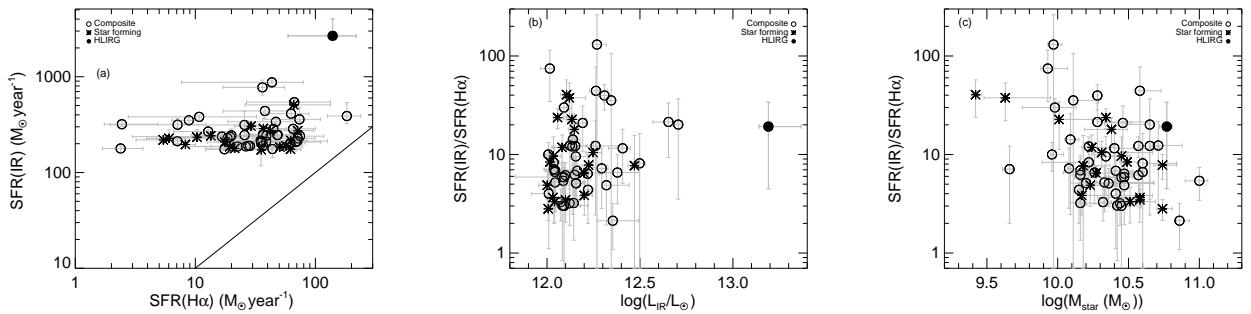


Figure 4.15 SFR(IR) versus SFR($H\alpha$) (a), SFR(IR)/SFR($H\alpha$) versus L_{IR} (b) and stellar mass (c) for 67 ULIRG and one HLIRG. In panel (a) the solid line represents the one-to-one relation.

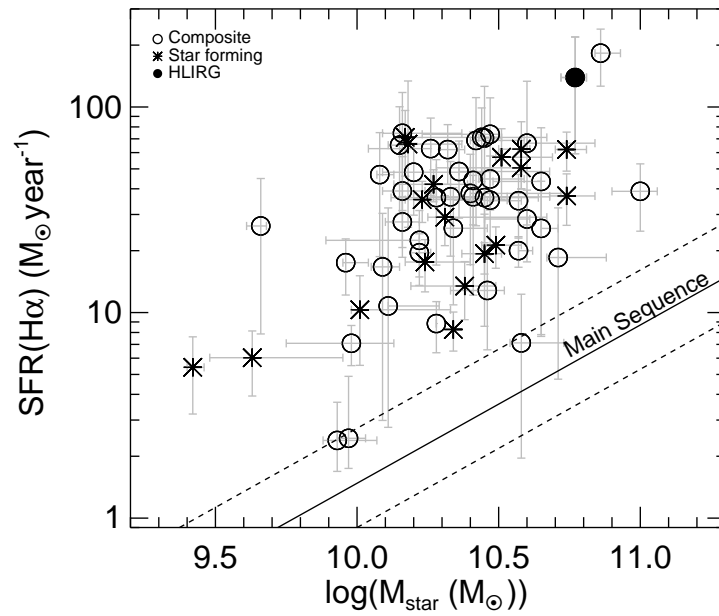


Figure 4.16 $\text{SFR}(\text{H}\alpha)$ versus stellar mass. $\text{SFR}(\text{H}\alpha)$ values are derived from Eq. (2) of Kennicutt (1998). Error bars of $\text{SFR}(\text{H}\alpha)$ are dominated by the emission-line fluxes. Black solid line is the 'Main Sequence' from Elbaz et al. (2007), dashed lines represent the 1σ width of the 'Main Sequence'.

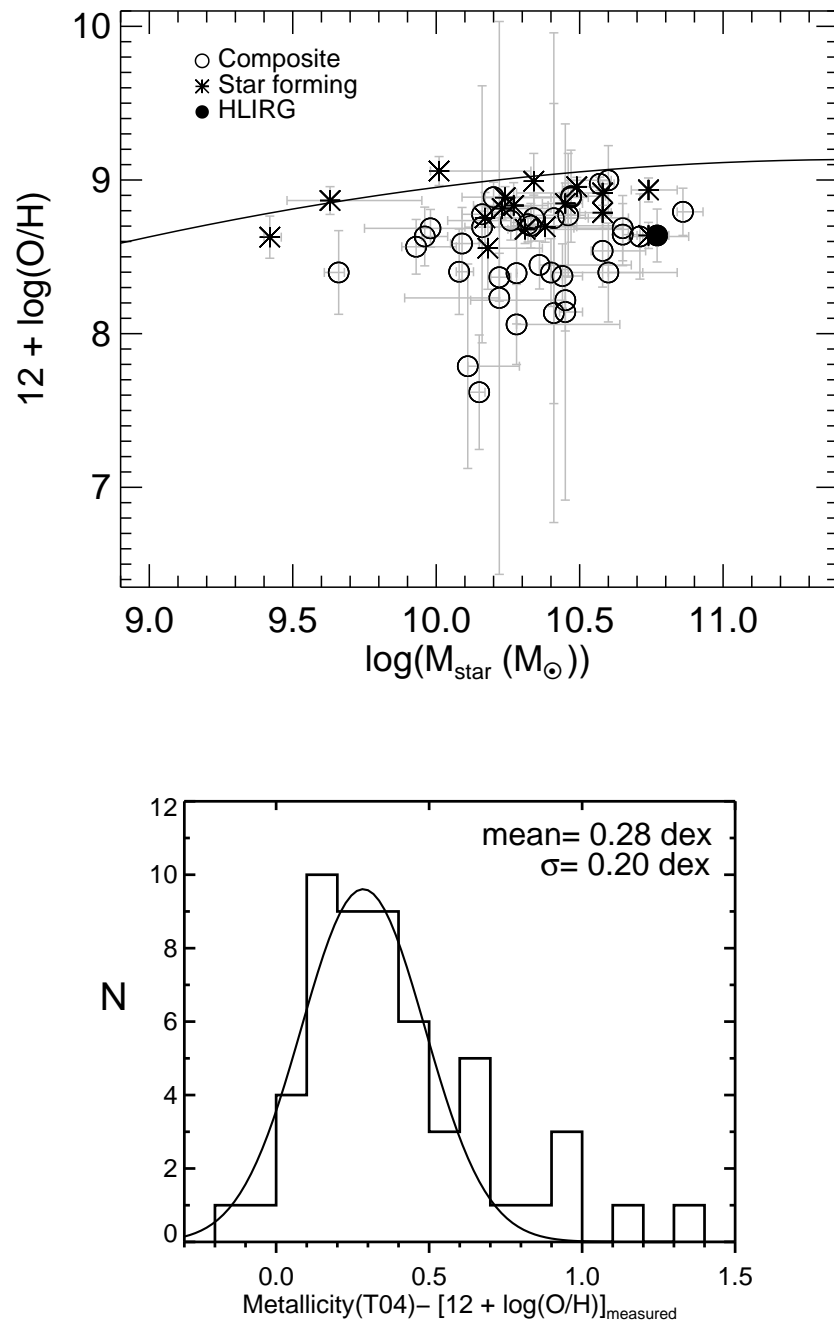


Figure 4.17 Top: Oxygen abundances versus stellar mass for 54 ULIRGs and one HLIRG. The black solid line represents the mass–metallicity relation of the local SDSS galaxies given by Tremonti et al. (2004). Error bars of the oxygen abundances represent the uncertainties of emission-line fluxes (including the uncertainties associated additional extinction based on Balmer decrement) propagated through Eq. (1) and (2) of Tremonti et al. (2004). Bottom: The distribution of the residuals between the measured oxygen abundances and the ones expected from T04 relation. The over plotted Gaussian function demonstrates that the residuals have a normal distribution with a few outliers.

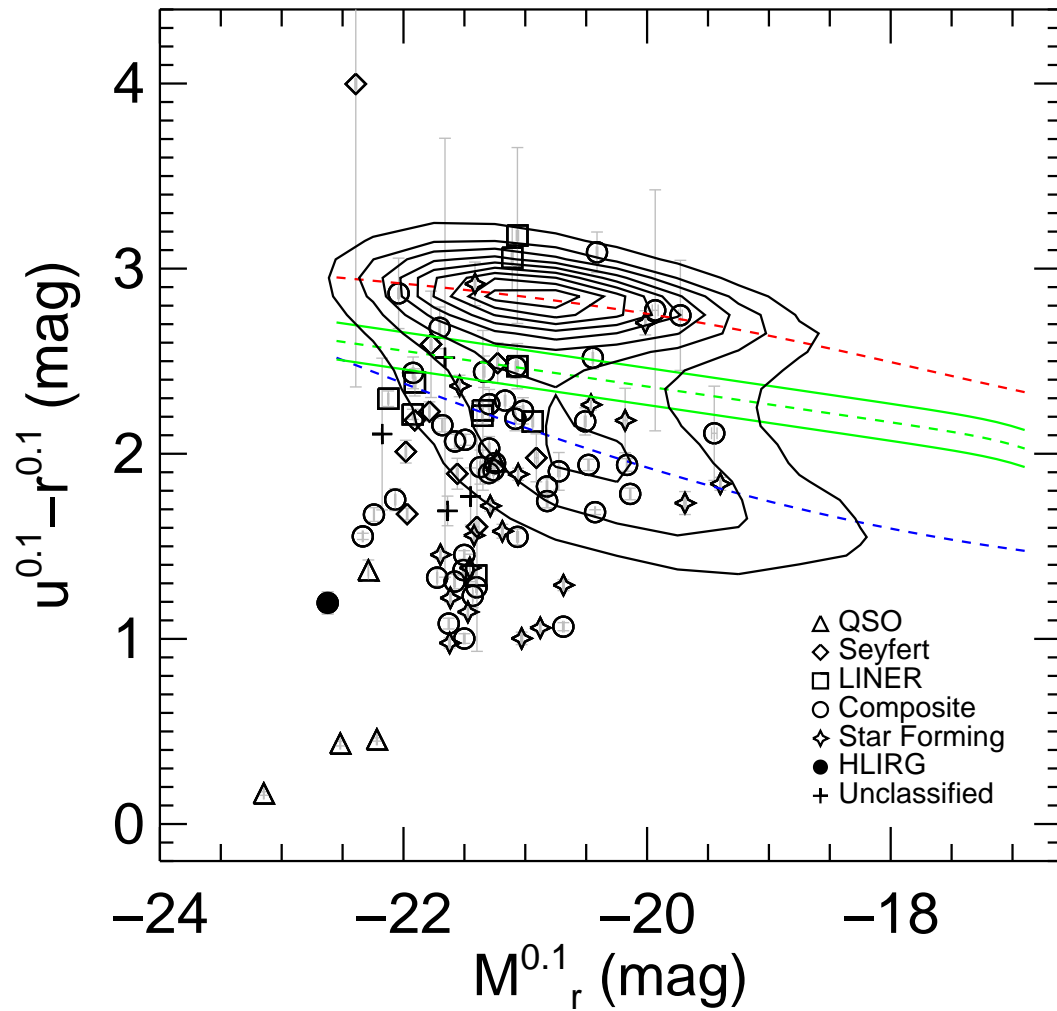


Figure 4.18 Color-magnitude diagram for local SDSS comparison sample, 91 ULIRGs and one HLIRG. Contours represent the number densities for 10 levels. (H)/ULIRGs are shown on top of the contours. The color-magnitude relations for red, blue sequences and green valley are shown with the red, blue and green dashes lines. The solid green lines show the ± 0.1 mag width of the green valley. See the text for the detailed descriptions of these relations. The vertical and horizontal error bars represent the uncertainties in the model magnitude measurements.

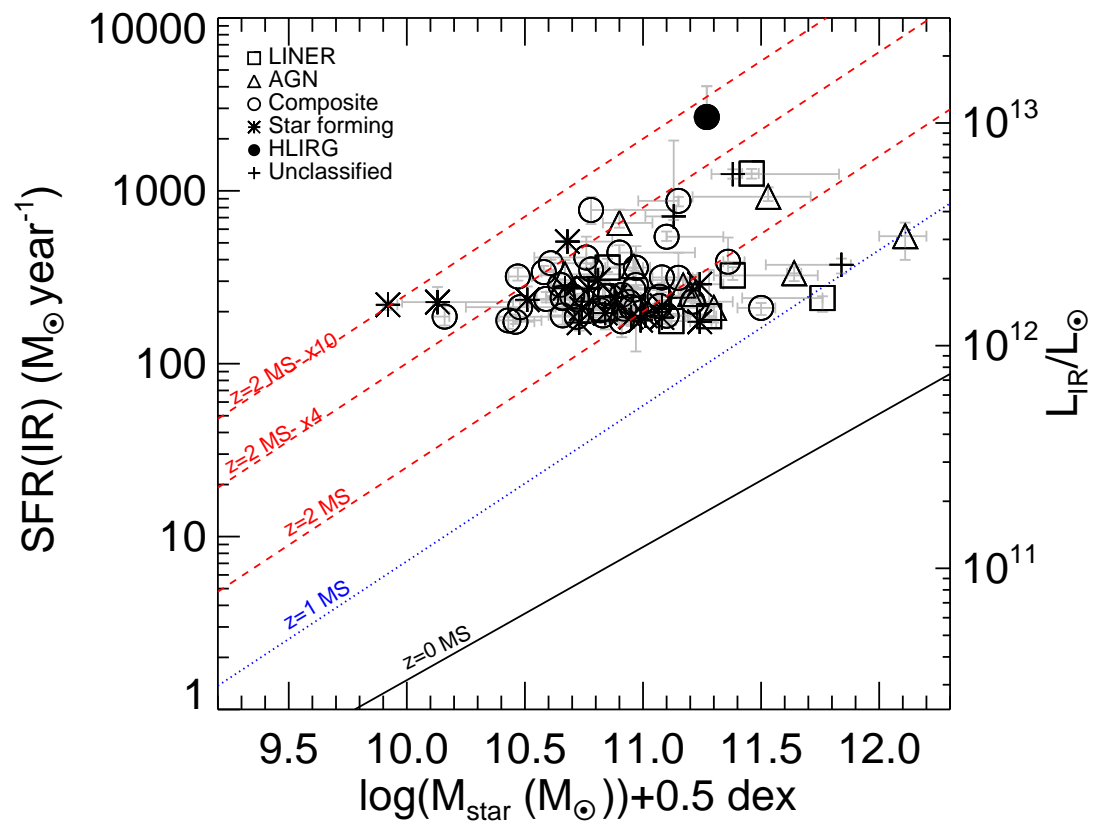


Figure 4.19 Same as Figure 4.14 but stellar mass are shifted by 0.5 dex.

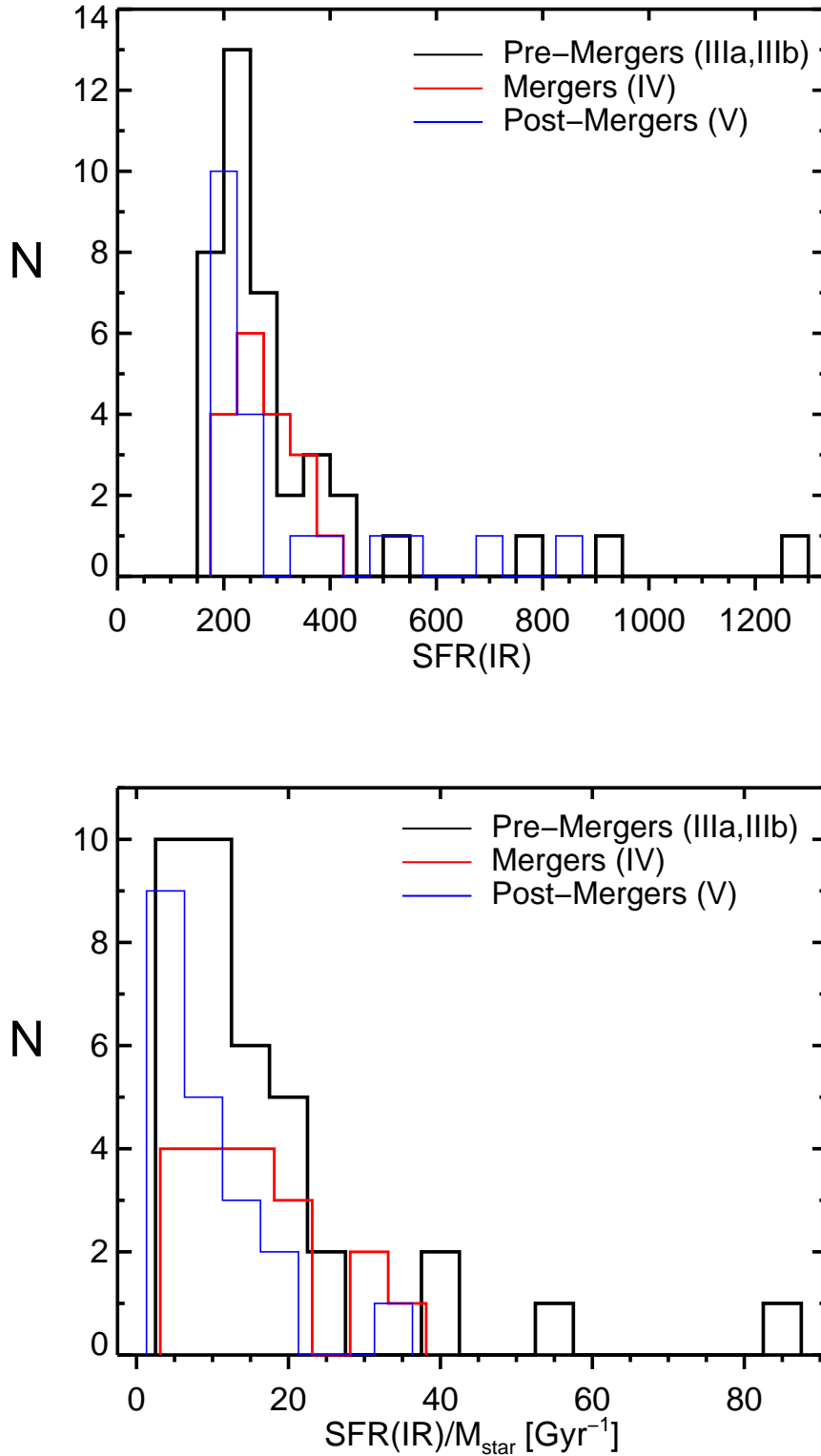


Figure 4.20 SFR(IR) (top) and specific star formation rate (SFR/M_{star}) (bottom) distribution of 77 ULIRGs as a function of interaction stage.

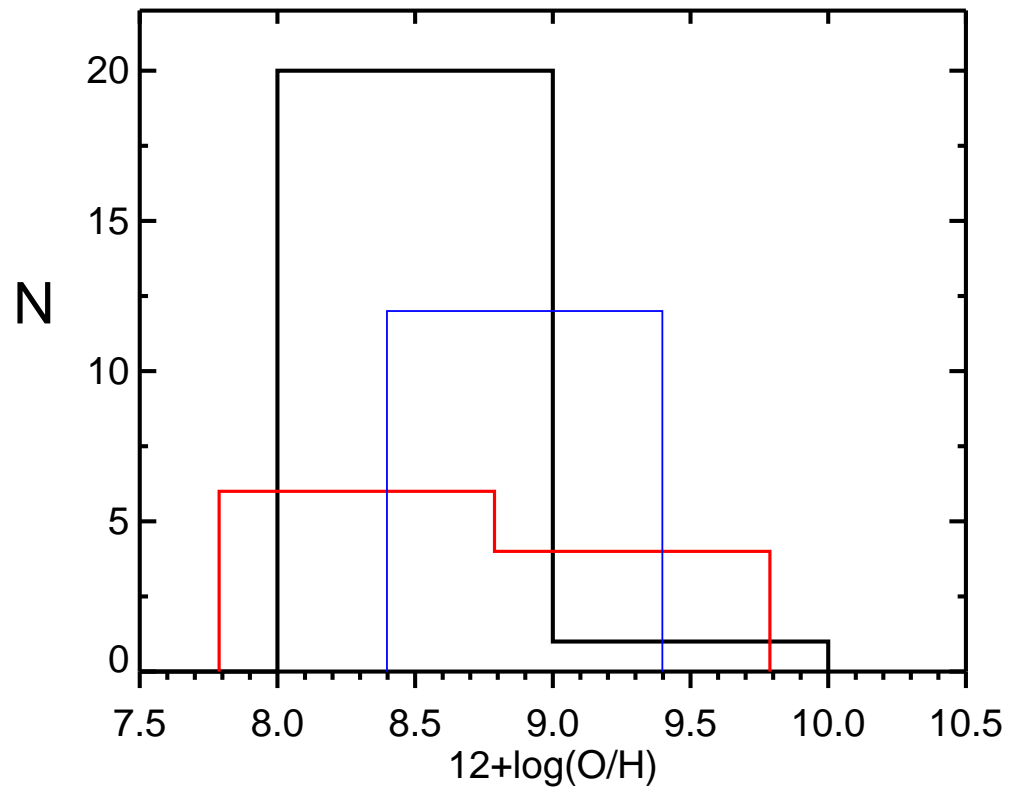


Figure 4.21 Oxygen abundances distribution of 43 ULIRGs as a function of interaction stage. Color code is the same as in Figure 4.20.

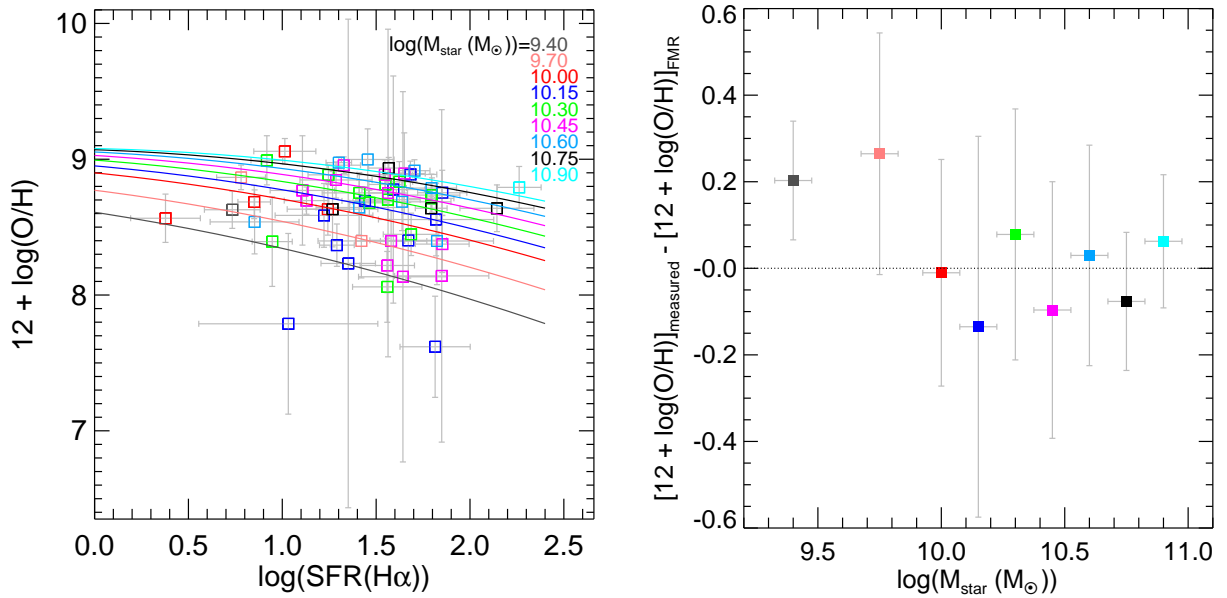


Figure 4.22 Left panel: FMR (Eq. 2 of Mannucci et al., 2010) for different mass bins as a function of SFR. The colored lines show the mass bin. The colored open circles show the ULIRGs in each mass bin. Right panel: Metallicity residuals of ULIRGs from the FMR, colors represent the same mass bins labeled in the left panel. The residuals represent the median values in each bin, except the first and the last bins that have single measurements.

5

CONCLUSION

5.1 SUMMARY

In this thesis, I have explored the scatter in the most recently established $R - L$ relationship of local RM AGN and the relation between the Eddington ratio and broad emission line profiles. I also performed studies of local ULIRGs.

The AGN $R - L$ relationship has a great potential as a cosmological probe beyond the local Universe. The slope of the $R - L$ relationship is ~ 0.5 which is consistent with the expected photo-ionization of the BLR. Based on the R and L measurements of NGC 5548 obtained over 20 years, I show that R changes with L with a steeper slope (0.79) compared to 0.5 and this steeper slope alone introduces a scatter of ~ 0.08 dex in the $R - L$ relationship. I perform Monte Carlo simulations and show that when this behavior is generalized to other sources in the RM sample, the resultant scatter in the $R - L$ relationship is ~ 0.11 dex. This scatter includes the 0.08 dex scatter in the relationship traced by NGC 5548 as it varies intrinsically. This shows that a significant fraction of the observed scatter of 0.13 dex (Bentz et al., 2013) can be due to the steeper slopes of the individual $R - L(\text{optical})$ relationships traced by intrinsic variability of each source in the RM sample. We also show that while the slope of the $R - L(\text{UV})$ relations is closer to the slope of 0.5 and the scatter of the $R - L(\text{UV})$ relationship is expected to be smaller, the 0.08 dex scatter of the relationship pertaining to the source variability of the individual objects will remain. Therefore, we conclude that using $R - L(\text{UV})$ relationship instead of $R - L(\text{optical})$ can potentially reduce the scatter in the AGN Hubble diagram to ~ 0.26 mag and increase the reliability of AGN as competitive distance indicators.

The mass scaling relationships of Type 1 AGN are used to estimate BH mass estimates at any redshift and their accuracy is important to understand the role of BHs in galaxy evolution across cosmic time. In this thesis, the Eddington ratio– $H\beta$ line shape correlation presented by Collin et al. (2006) was revisited and confirmed with a detailed analysis. In order to measure the bolometric luminosities and Eddington ratios, I used quasi-simultaneous SEDs of optical, UV and X-ray data from public archives. However, I show that using such SEDs instead of applying mean bolometric corrections do not significantly change the observed Eddington ratio–line shape dependence for my nearby AGN sample because, the SED variations of my sample are small. I also investigated the Eddington ratio–C IV line shape correlation for the first time, and I do not find a similar inverse correlation for C IV profiles for my small sample of nearby AGN. I show that the inverse correlation between the $H\beta$ and C IV line shapes and Eddington ratio also present for higher redshift quasars selected from SDSS DR3.

I present a new catalog of local ULIRGs identified in the *AKARI* all-sky survey. These

galaxies are locally rare and extremely bright IR galaxies and they are important for our understanding of the AGN-starburst connection in mergers and the nature high-redshift star-forming galaxies. In order to compute the IR luminosities of the galaxies observed by *AKARI*, I cross-correlate *AKARI* catalogs with the catalogs of optical spectroscopic surveys such as the SDSS and the 2dF Galaxy Redshift Survey. I discovered new ULIRGs in the *AKARI* all-sky survey and increased the number of local ULIRGs. I extract the available photometric and spectroscopic measurements from the SDSS catalogs in order to investigate colors, stellar masses and metallicities of my local ULIRG sample. I compare ULIRGs with normal star forming galaxies and show that ULIRGs are the most rapidly star forming galaxies in the local universe: their SFRs are comparable with that of $z \sim 2$ star forming galaxies. As expected, the properties of my ULIRG sample is consistent with the known *IRAS* and *ISO* ULIRGs.

5.2 FUTURE WORK

- **The $R - L$ relationship:** In order to use $R - L$ relationship as a distance indicator for high redshift AGN we need to establish a $R - L(\text{UV})$ relationship. Contemporaneous optical and UV monitoring of a larger AGN sample is necessary to have a $R - L(\text{UV})$ relationship for the RM sample. Such observations would also help to understand the true relation between the optical and the UV luminosities that is important to understand the origin of the scatter in the $R - L$ relationship.
- **Eddington ratio – line shape relation:** I investigated the Eddington ratio – emission-line shape relation for a very small sample of nearby AGN and a larger sample of higher redshift quasars. Individual sources in my sample do not show an inverse correlation between the line shape and the Eddington luminosity ratio. This is mainly because, I did not have multiple epoch SEDs across several monitoring campaigns, but most of the available data (and SEDs) pertain to individual campaigns - during which the objects often did not vary sufficiently to exhibit a dramatic change in line shapes or Eddington luminosity, in particular. Actually, I do see changes in line shape, but measurement uncertainties are currently too large to identify whether other factors play a role for the line shape changes. Instead, comparison of the mean profiles of different sources as Collin et al. (2006) did seem to be a more reasonable way to investigate Eddington ratio – emission-line shape relation. But here the caveat is to eliminate other possible source-to-source differences (such as inclination, and different BLR geometries) that could affect the line shapes. Investigating the Eddington ratio – emission-line shape relation for individual sources is the best option to eliminate other possibilities that could affect the line shapes. The best way to examine profile changes with respect to accretion state is to perform a similar analysis (account for BLR radius but apply a mean BC) as I did here for long term monitoring campaign dataset. In this thesis I just used the RM monitoring data of NGC 5548 covering 2 years because, the data for the SEDs were only available for these epochs. But, this source has spectroscopic monitoring ranging more than 20 year, therefore it would be the most ideal source for this investigation.
- **Local ULIRGs:** By constructing spectral energy distributions based on *AKARI* All-Sky survey catalogs, I have identified new ultra/hyper-luminous infrared galaxies in the local Universe. The number of ULIRGs identified in this work depends strongly on the specific optical redshift catalogs. With the future SDSS data releases including more spectroscopic redshift it may be possible to increase the number of *AKARI* galaxies with redshift

and this sample might be have new *AKARI* ULIRGs. I have investigated morphological and physical properties of these galaxies, and generated a catalog with stellar masses, metallicities and colors based on available SDSS images and spectroscopy. In my future research, I want to investigate multi-wavelength properties of ultra/hyper luminous infrared galaxies with a larger database, and study these galaxies in detail. So far I just used BPT diagrams to identify AGN in my ULIRG sample, but I would like to search for signs of possible AGN at other wavelengths.

Appendices

A

APPENDIX

A.1 ERROR-BAR SENSITIVITY TEST

Neither the Bayesian regression method (Kelly, 2007) nor the FITEXY method of (Press et al., 1992) can account for the asymmetric uncertainties in our R_{BLR} measurements (§ 2.3.2). Therefore, we performed a so-called ‘error-bar sensitivity test’ to test how sensitive the regression analysis is to the adopted (symmetric) error bar. In this test, for the symmetric measurement errors in the R_{BLR} values we assume either:

- a) the ‘positive’ 1σ uncertainties (i.e., upper error bar),
- b) the ‘negative’ 1σ uncertainties (i.e., lower error bar),
- c) the error computed as: $([\sigma(\text{positive})^2 + \sigma(\text{negative})^2]/2)^{1/2}$, since this behaves correctly in the limit $\sigma(\text{positive}) = \sigma(\text{negative})$,
- d) the ‘largest’ of the two 1σ uncertainties,
- e) the ‘smallest’ of the two 1σ uncertainties, or
- f) the error bar that points toward the fitted relation.

Option ‘f’ involves an iterative process after an initial selection of error bars until the relative change in slope and zero point between two iterations is less than 10^{-11} ; typically, only about four iterations are needed. To test the sensitivity of option ‘f’ to the choice of error-bar in the first iteration, we run this test three times: first with the ‘positive’ uncertainty (option a), second with the ‘negative’ uncertainty (option b), and third with the ‘largest’ uncertainty (option c).

Applying this ‘error-bar sensitivity test’ to the $R(\text{H}\beta) - L(5100\text{\AA})$ relationship of NGC 5548 we find slopes in the range from 0.79 to 0.85 with similar uncertainties of ± 0.20 for the CCF dataset. For the JAVELIN dataset we find slopes between 0.88 to 0.90 with uncertainties of ± 0.17 . The results are insensitive to the choice of the initial error-bar in option ‘f’. For example, the difference in slope (and uncertainty) is at most 0.01 when the extreme ‘largest’ and ‘smallest’ error bars are adopted. The change of the slope given the adopted error bar is in any case within the 1σ uncertainty.

Our estimates of the scatter in the $R(\text{H}\beta) - L(5100\text{\AA})$ relationship of NGC 5548 for the CCF data are 0.075 ± 0.040 dex and 0.077 ± 0.043 dex when we adopt the ‘largest’ and ‘smallest’ uncertainties, respectively. For the JAVELIN dataset the equivalent values are 0.070 ± 0.039 dex and 0.073 ± 0.037 dex, respectively. Thus, in both datasets, the inferred scatter is essentially the same

for these two extreme error-bar settings. Similarly, we find the scatter to be insensitive to the initial choice of error-bar (option ‘f’) – it agrees to within the 1σ uncertainty of ~ 0.040 dex.

When we apply this sensitivity test to the local $R(\text{H}\beta) - L(1350\text{\AA})$ relationship of NGC 5548 we see no or insignificant changes in the slopes. We find best fit slopes of $0.47 \lesssim \beta(\text{CCF}) \lesssim 0.50$ and $0.51 \lesssim \beta(\text{JAVELIN}) \lesssim 0.53$ with uncertainties of ~ 0.15 (CCF) and ~ 0.12 (JAVELIN). The slopes based on the ‘largest’ and ‘smallest’ uncertainties are 0.47 ± 0.15 and 0.49 ± 0.15 , respectively, for the CCF dataset. The equivalent values for the JAVELIN dataset are 0.52 ± 0.12 and 0.52 ± 0.15 , respectively. For the different sub-options of option ‘f’ there is no difference in the slopes. We determine the scatter in the UV relationship to be in the range of 0.078 dex– 0.083 dex and 0.067 dex– 0.072 dex for each of the CCF and JAVELIN datasets, respectively.

In summary, we have demonstrated very little sensitivity of the slopes and the estimated scatter to the specific adopted symmetric error-bar for either of the datasets and for either of the radius – luminosity relations addressed here. While the differences are insignificant, we are conservative and adopt the ‘largest’ 1σ uncertainty for our regressions throughout (Table 2.8).

A.2 SEDS OF MY SAMPLE

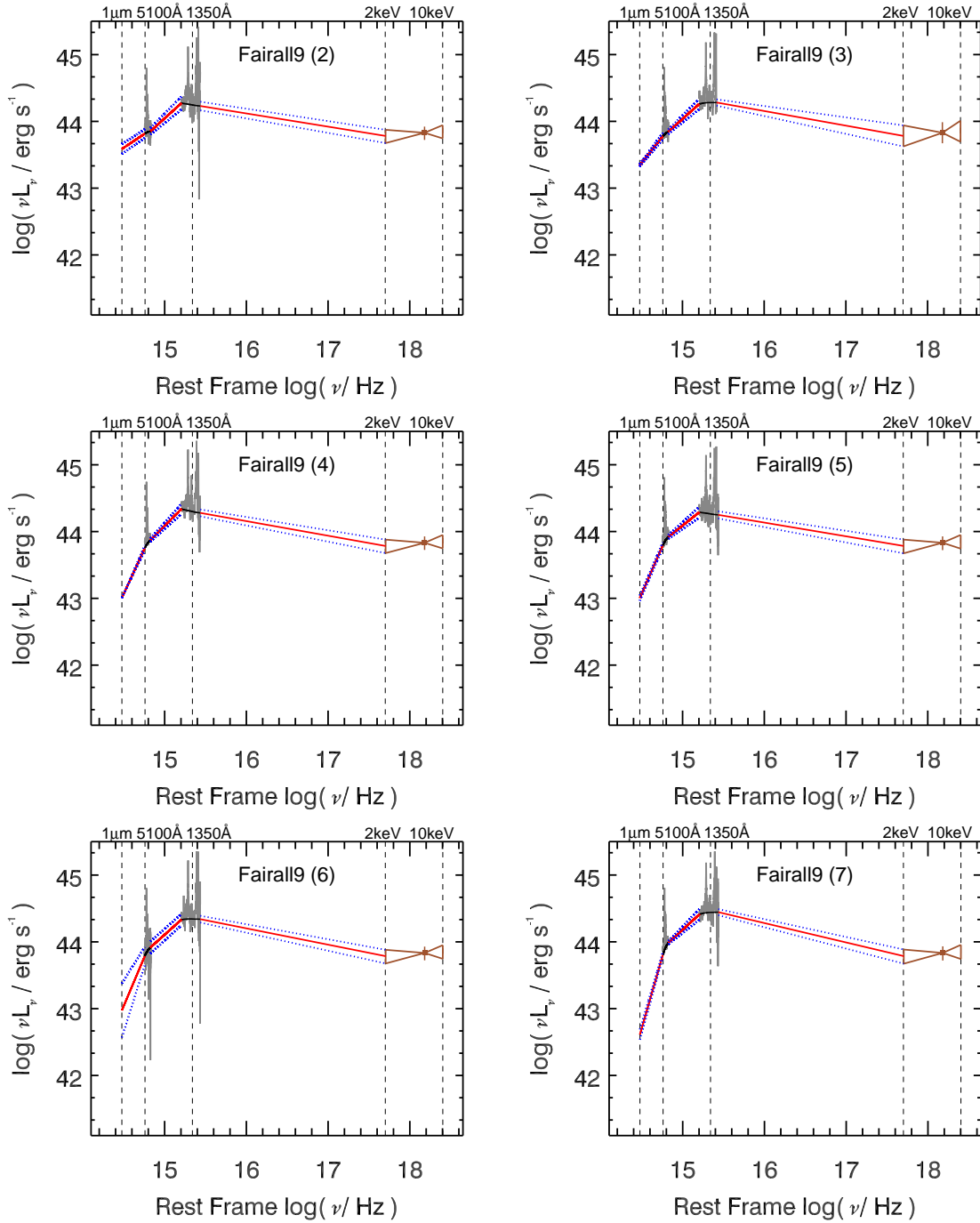


Figure A.1

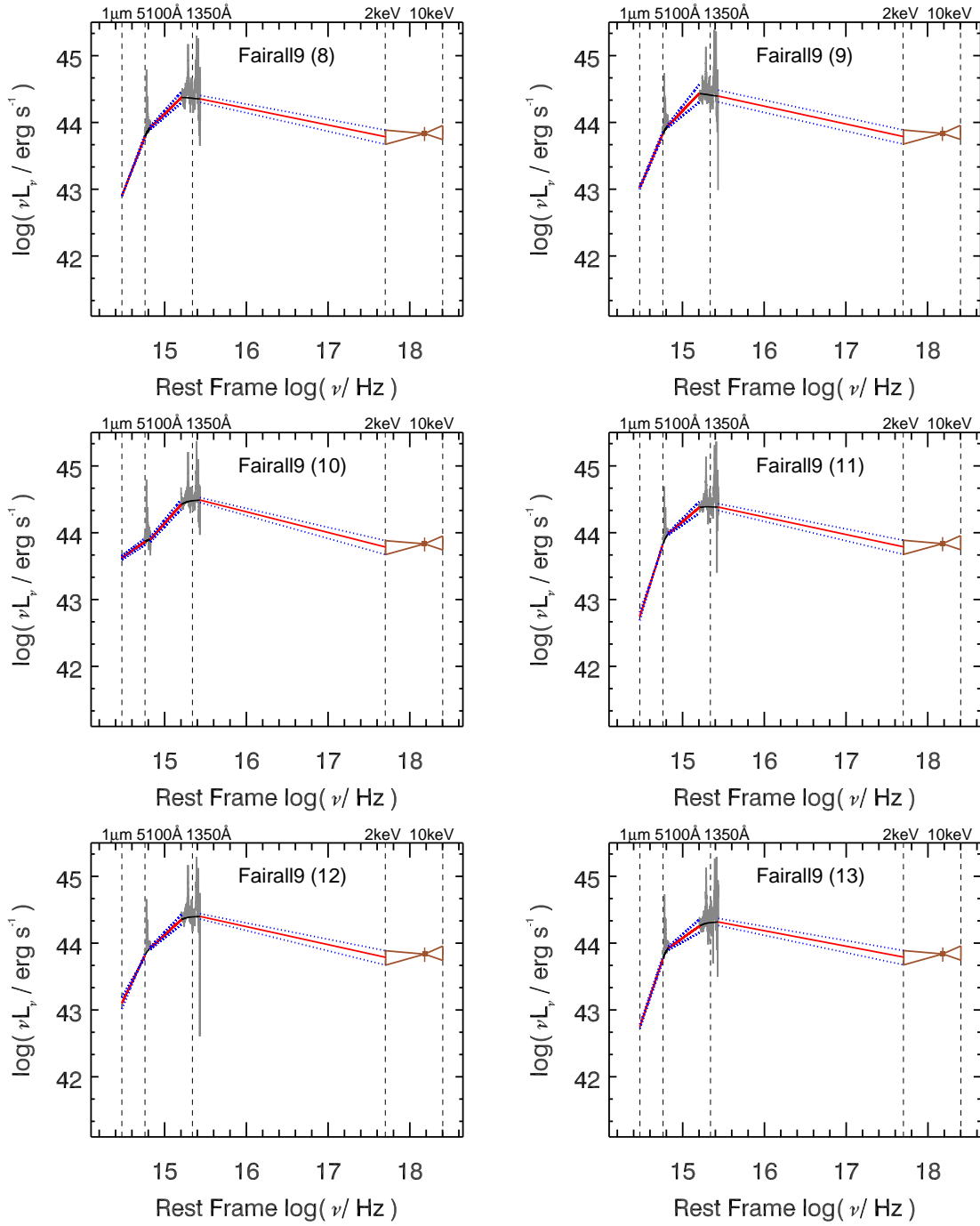


Figure A.1 continued.

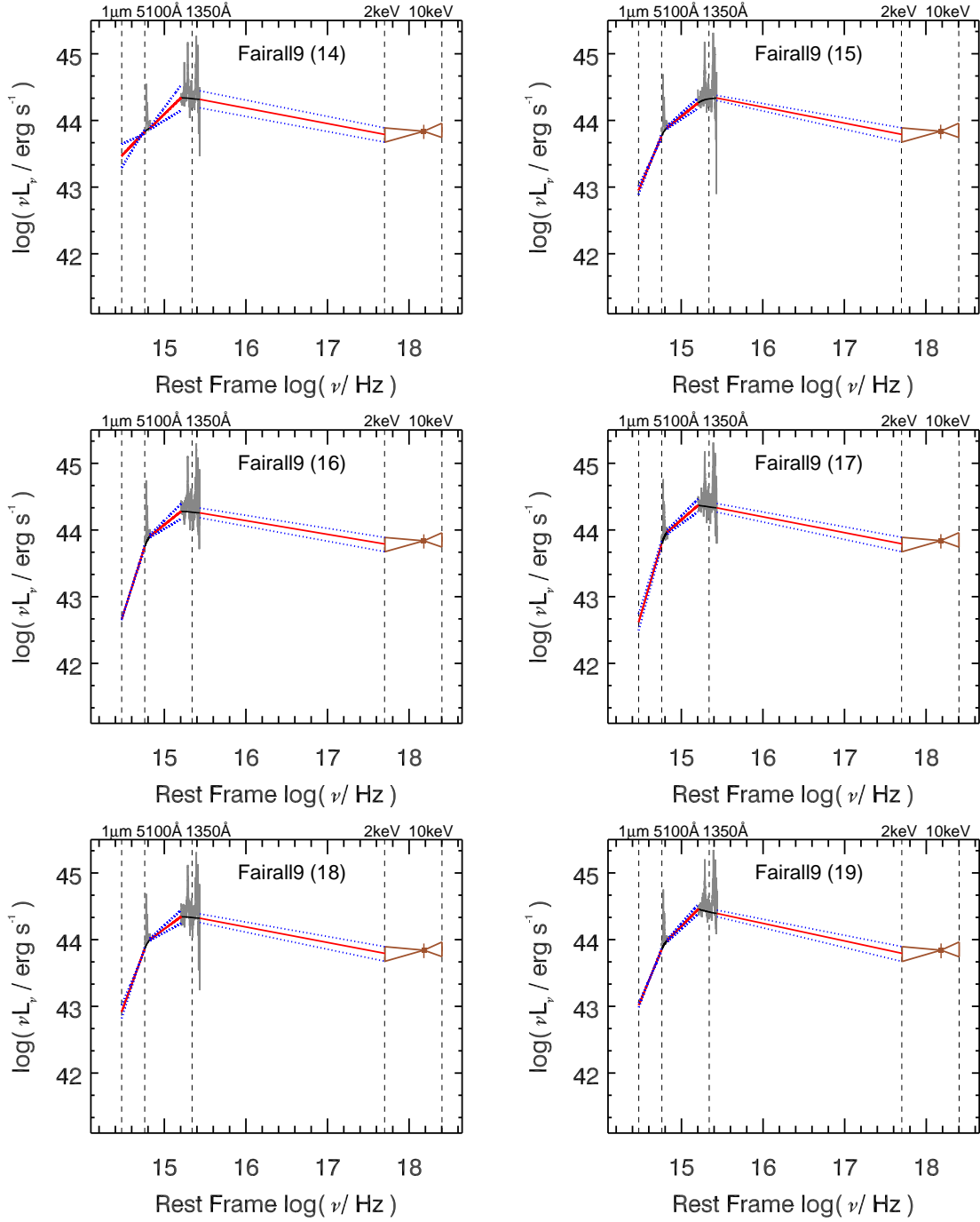


Figure A.1 continued.

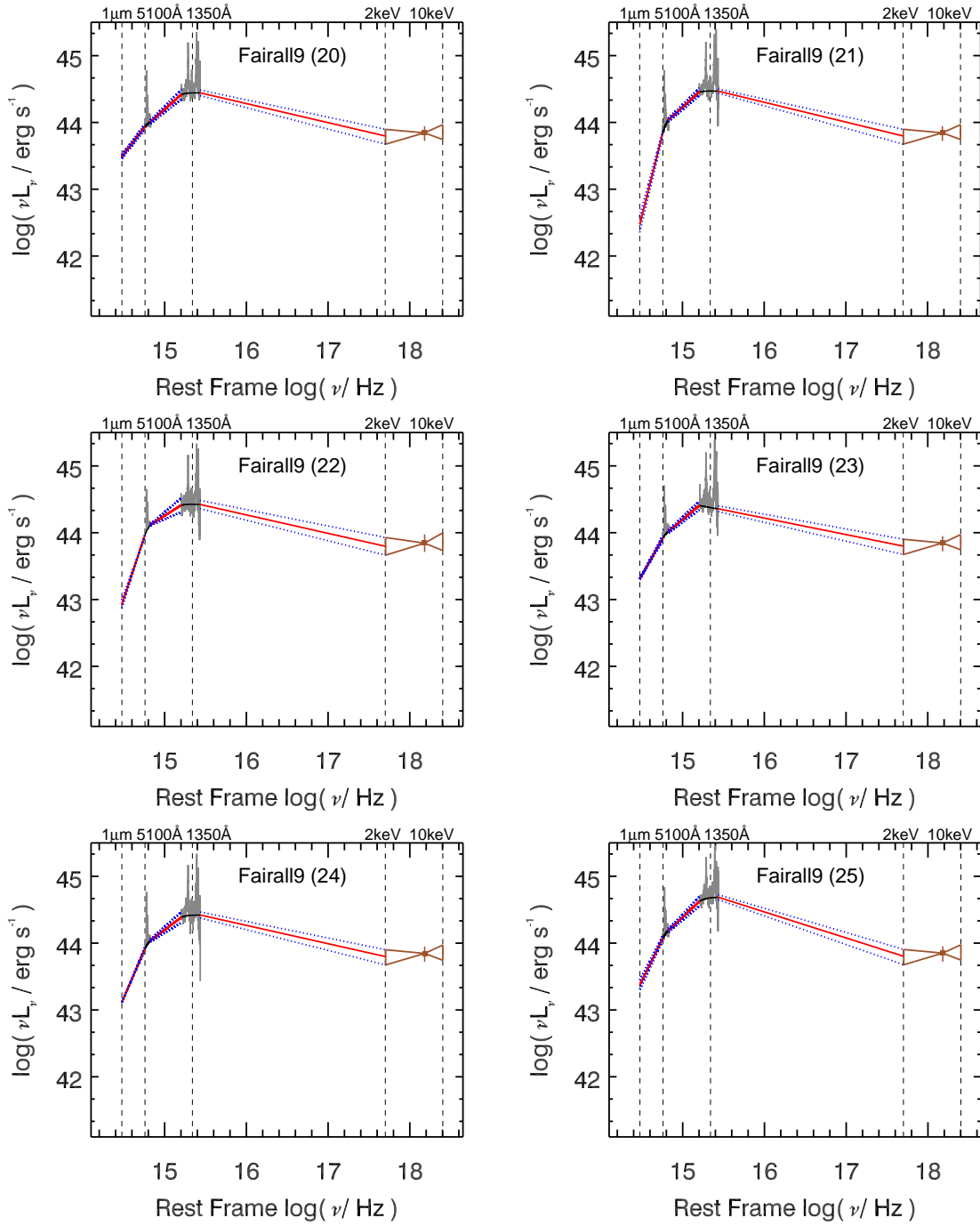


Figure A.1 continued.

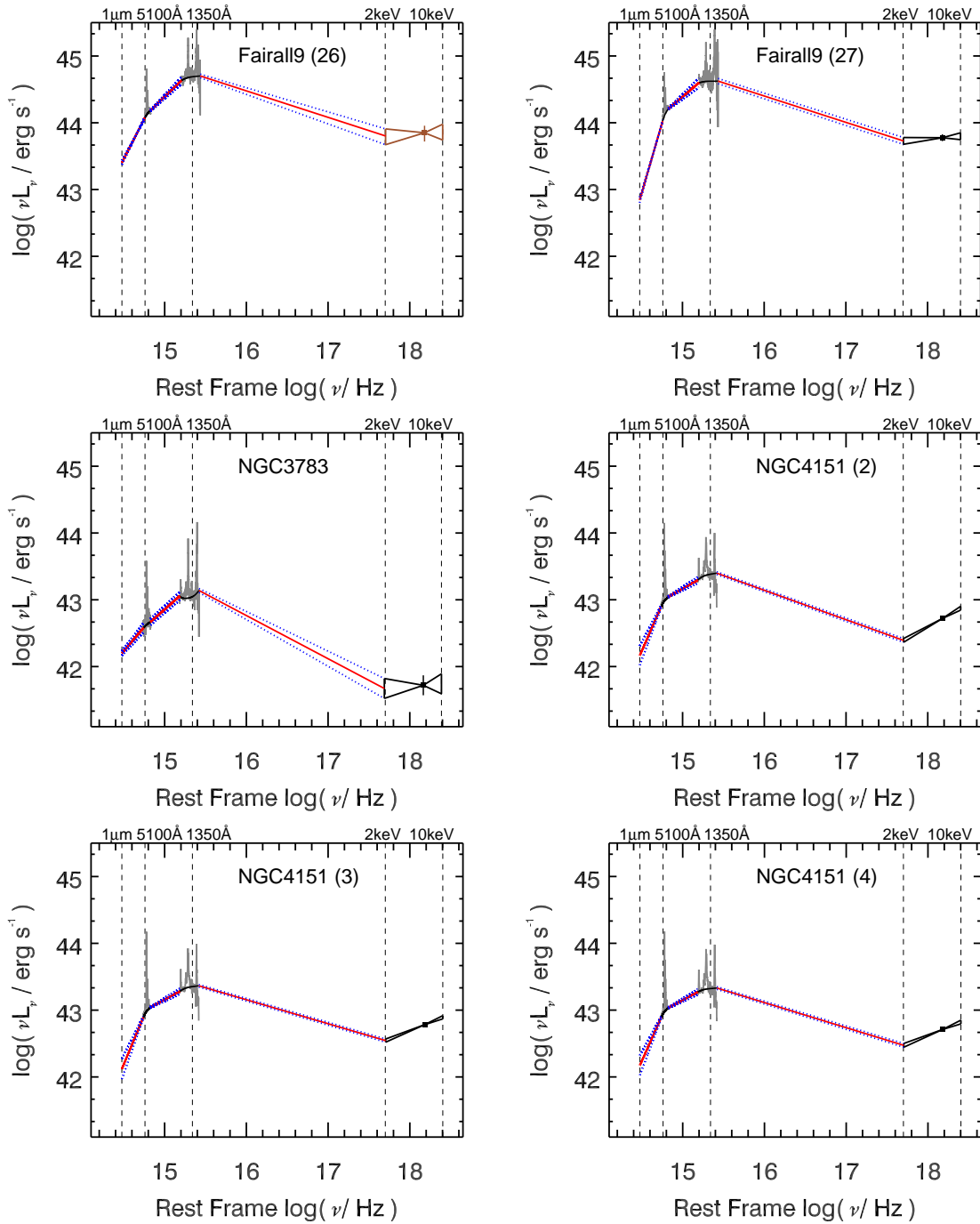


Figure A.1 continued. For Fairall 9 (27) only the X-ray and UV data are simultaneous, the optical data are obtained 12 days later. The X-ray data of NGC 3783 is extrapolated from 0.1-2 keV observations.

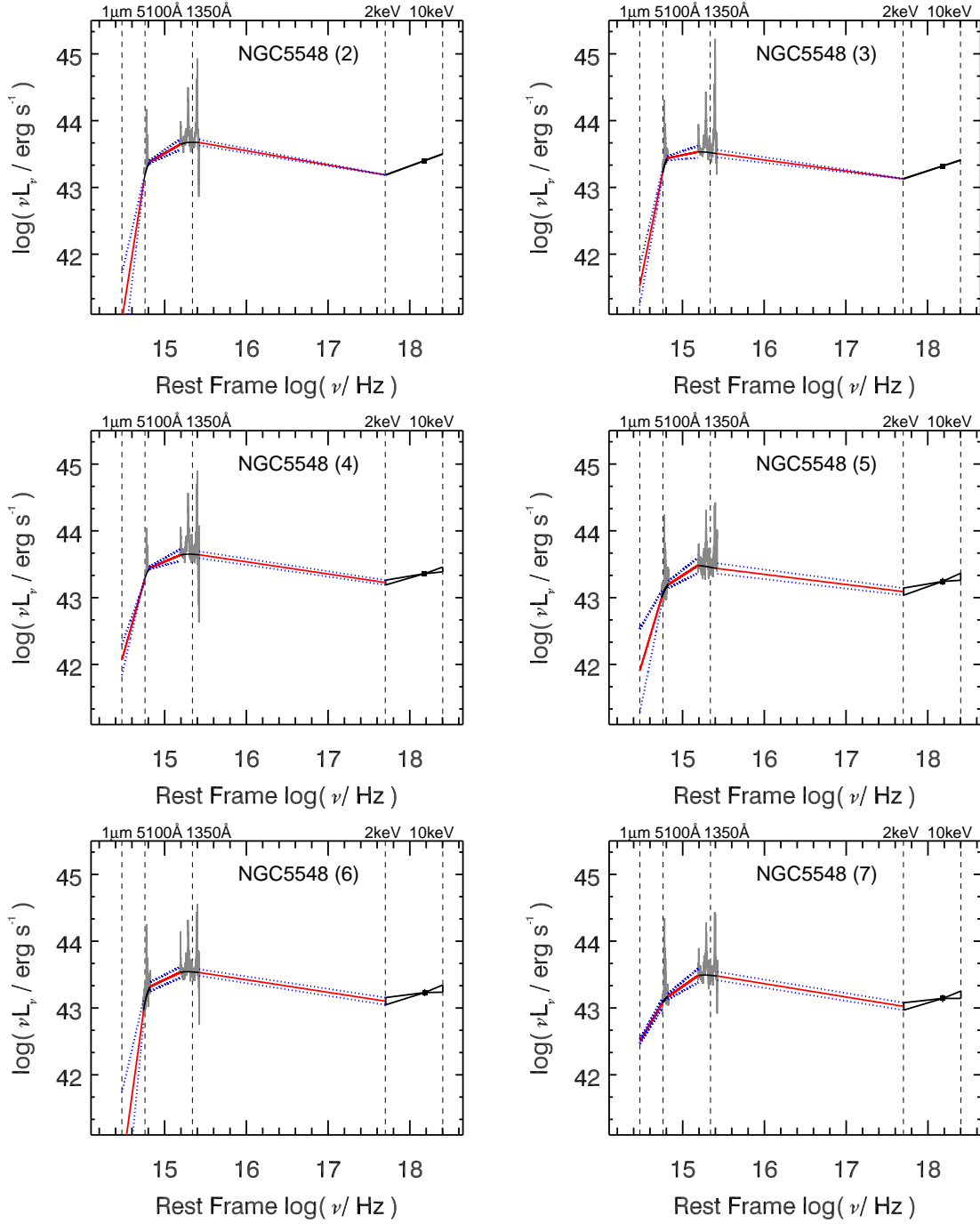


Figure A.1 continued.

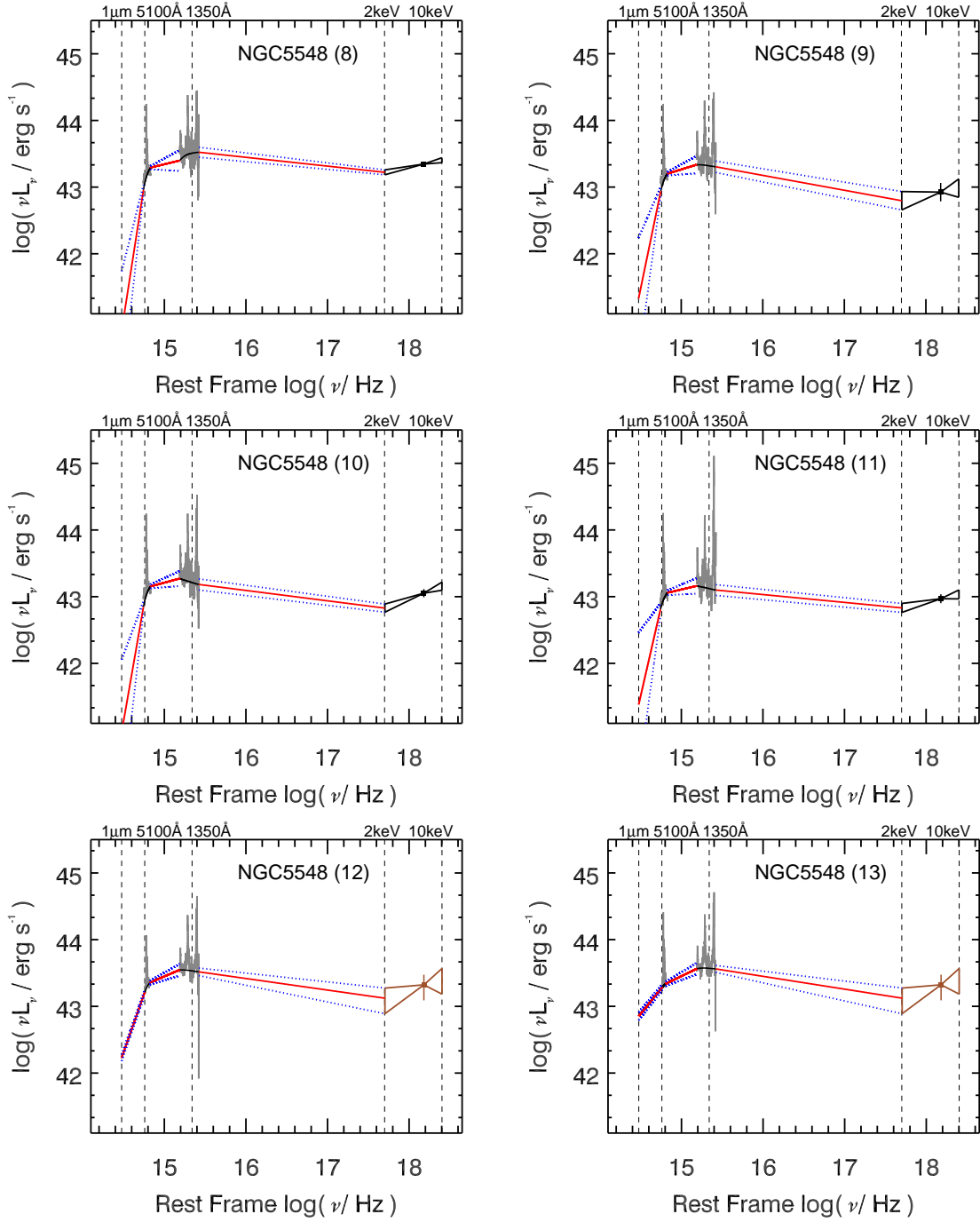


Figure A.1 continued.

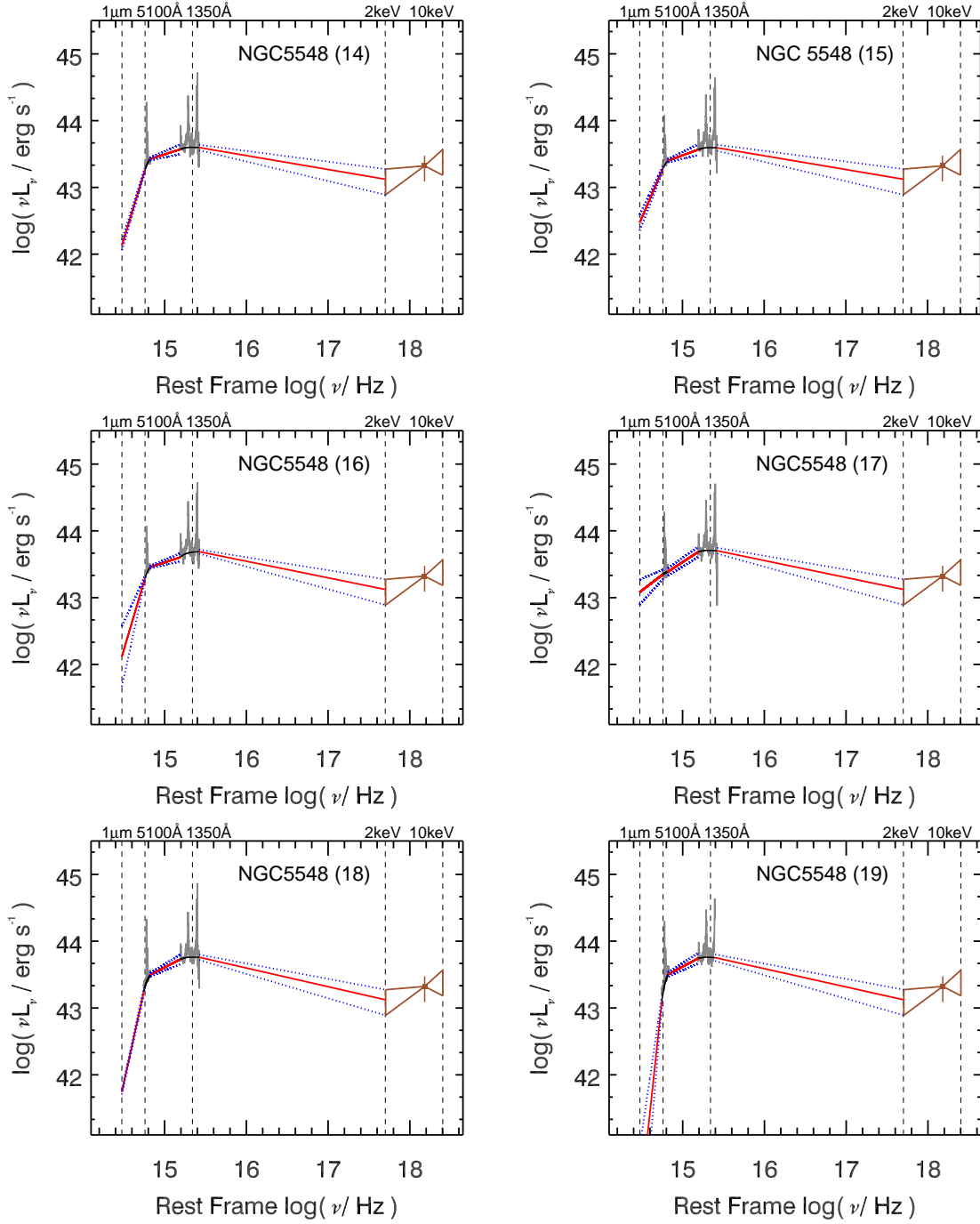


Figure A.1 continued.

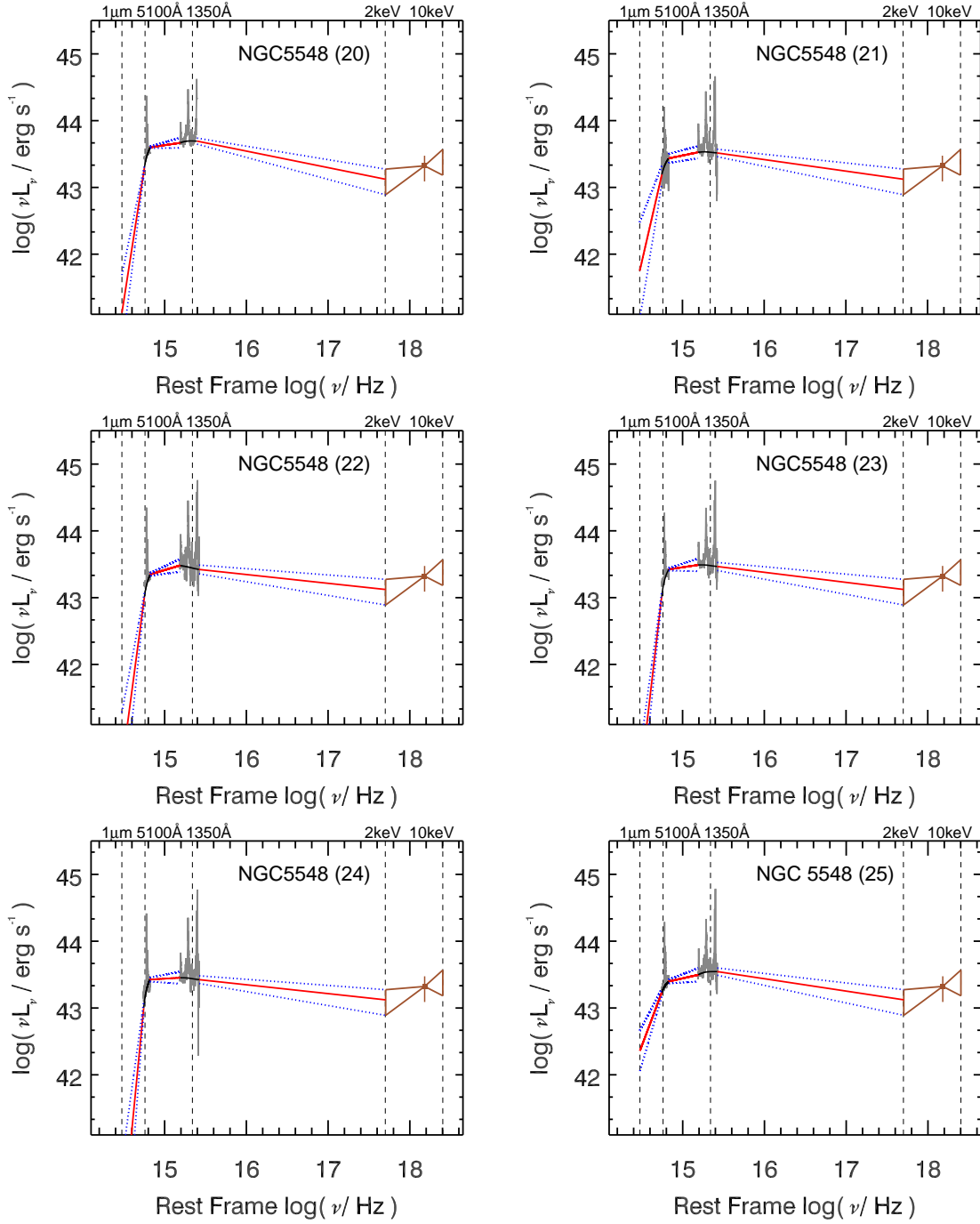


Figure A.1 continued.

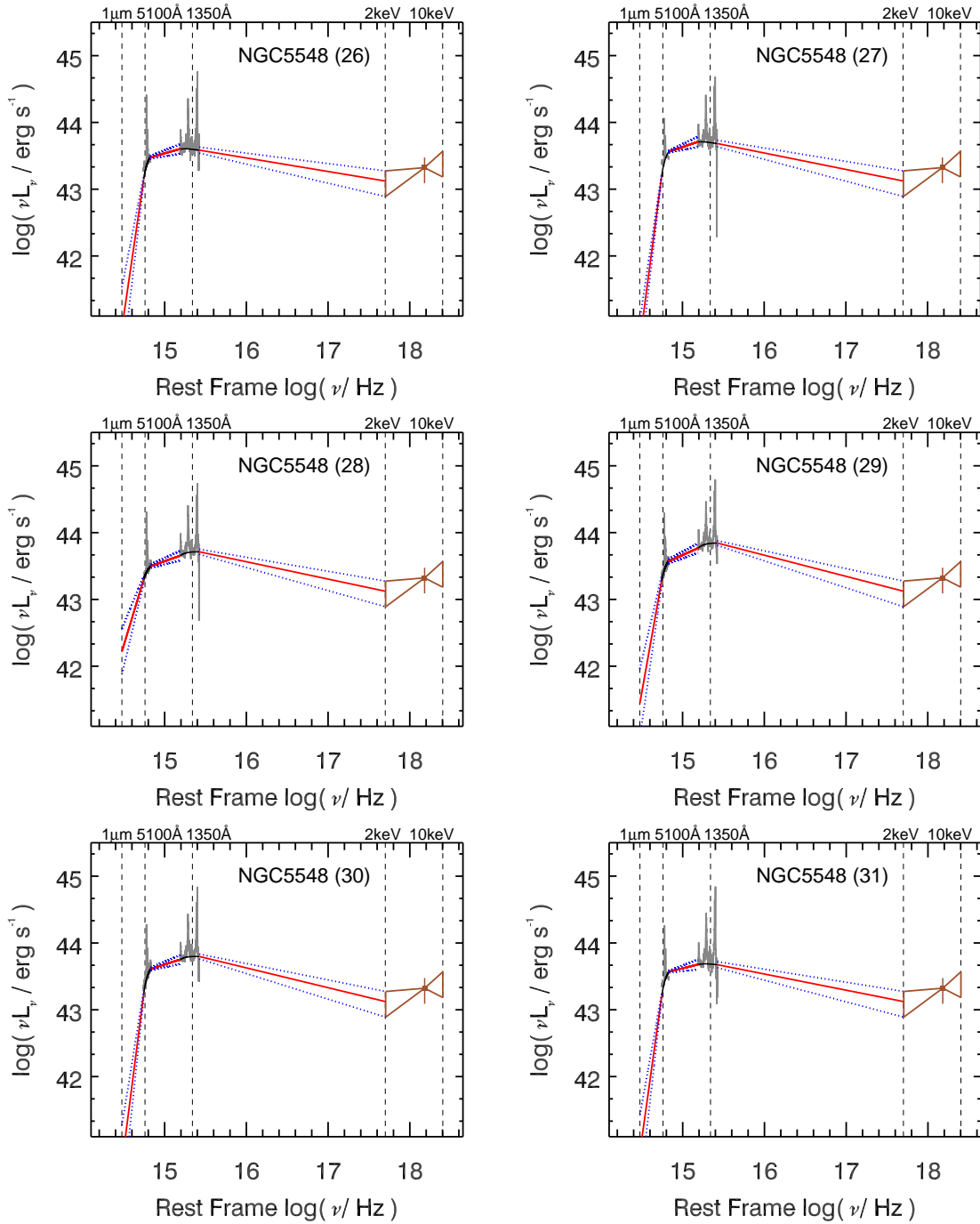


Figure A.1 continued.

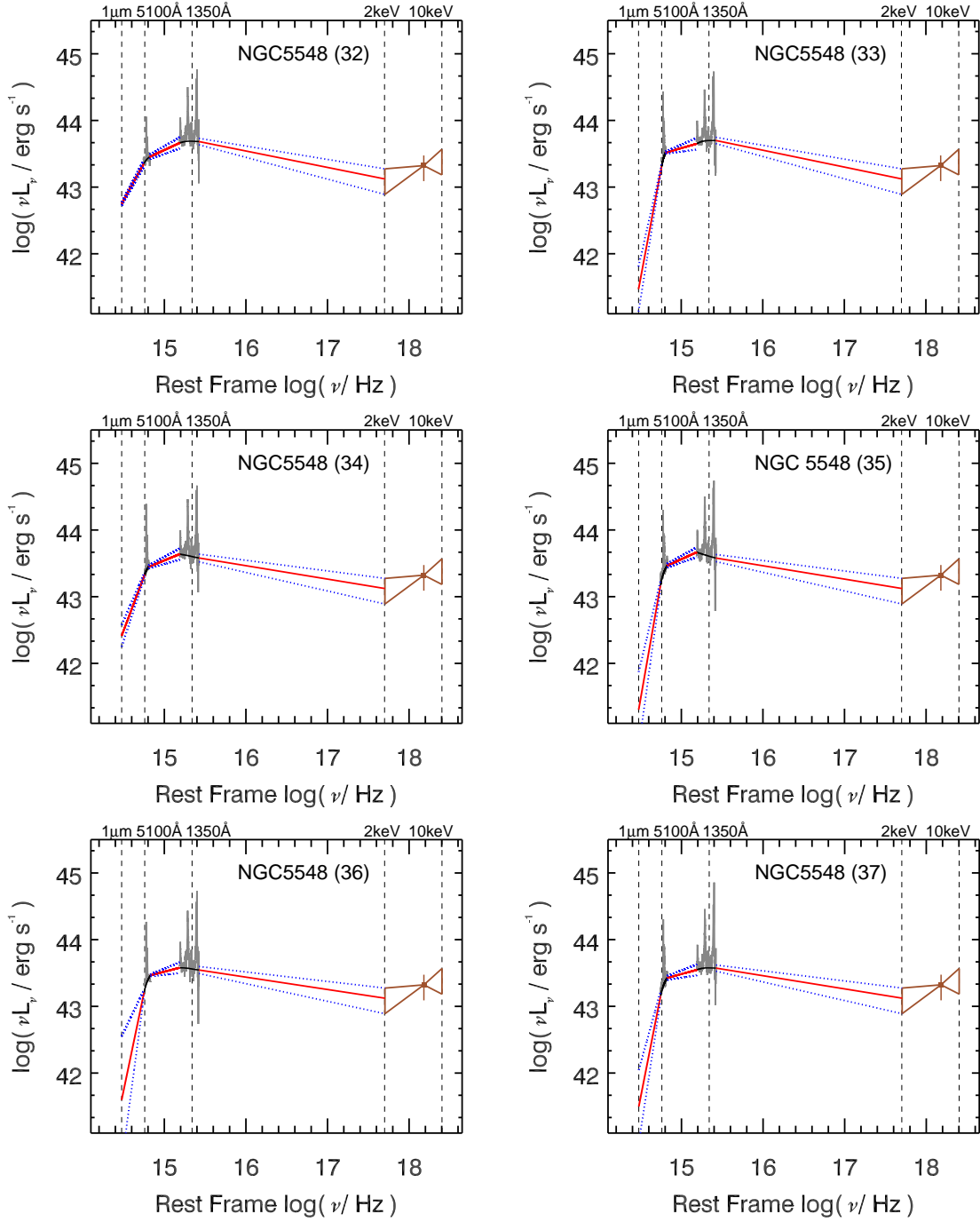


Figure A.1 continued.

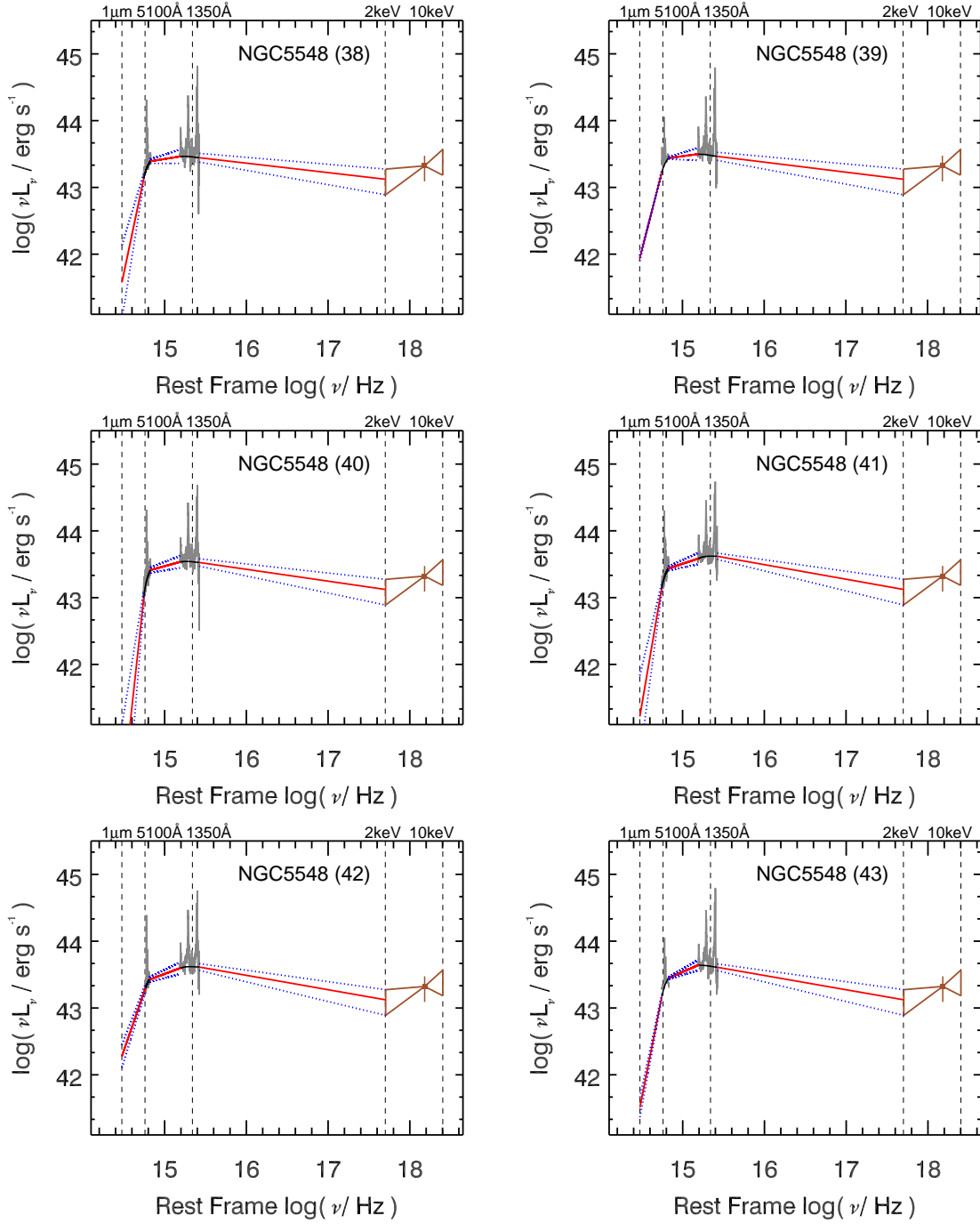


Figure A.1 continued.

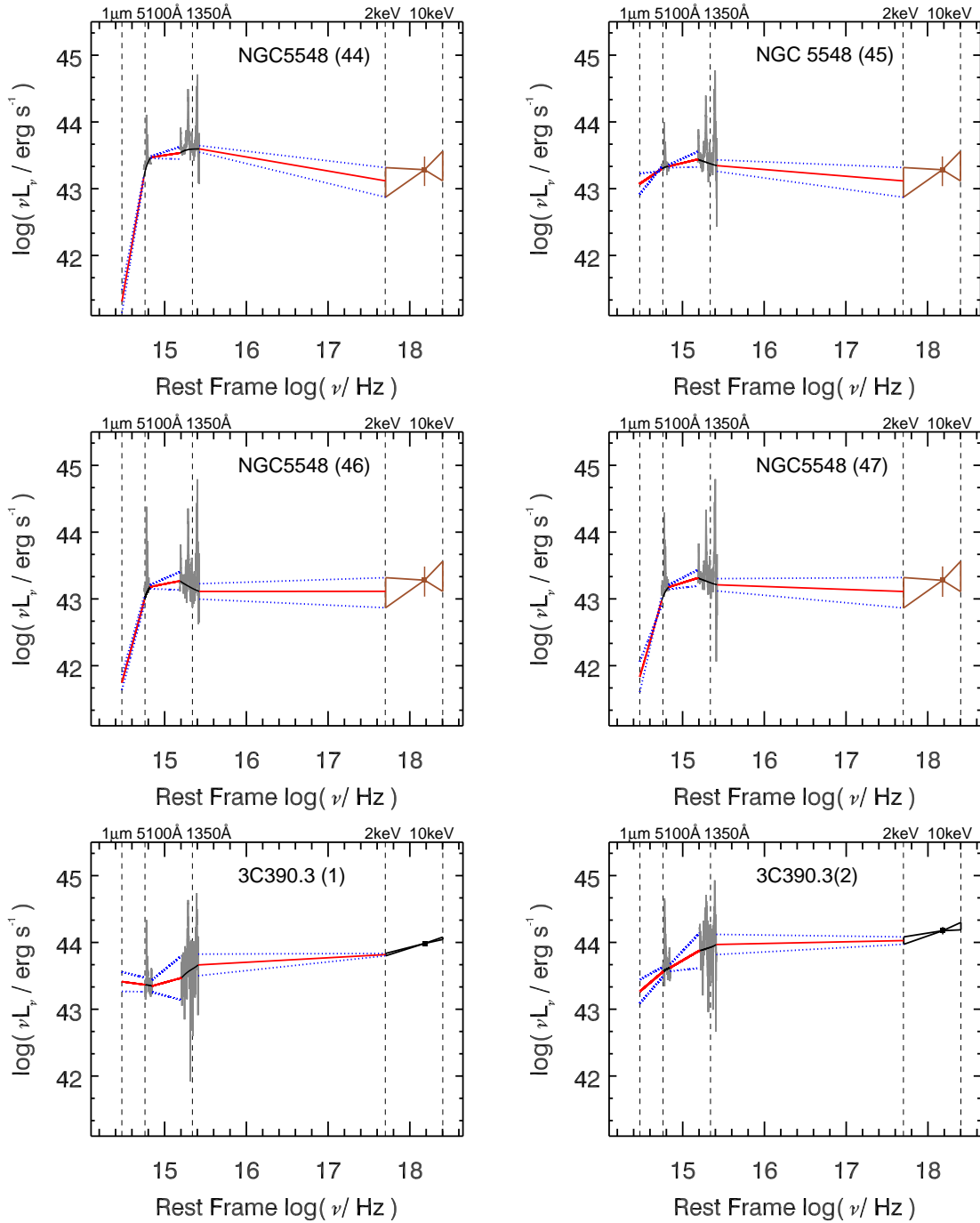


Figure A.1 continued. For 3C390.3 (2) the optical and UV data are simultaneous, but the X-ray data are obtained 20 days earlier.

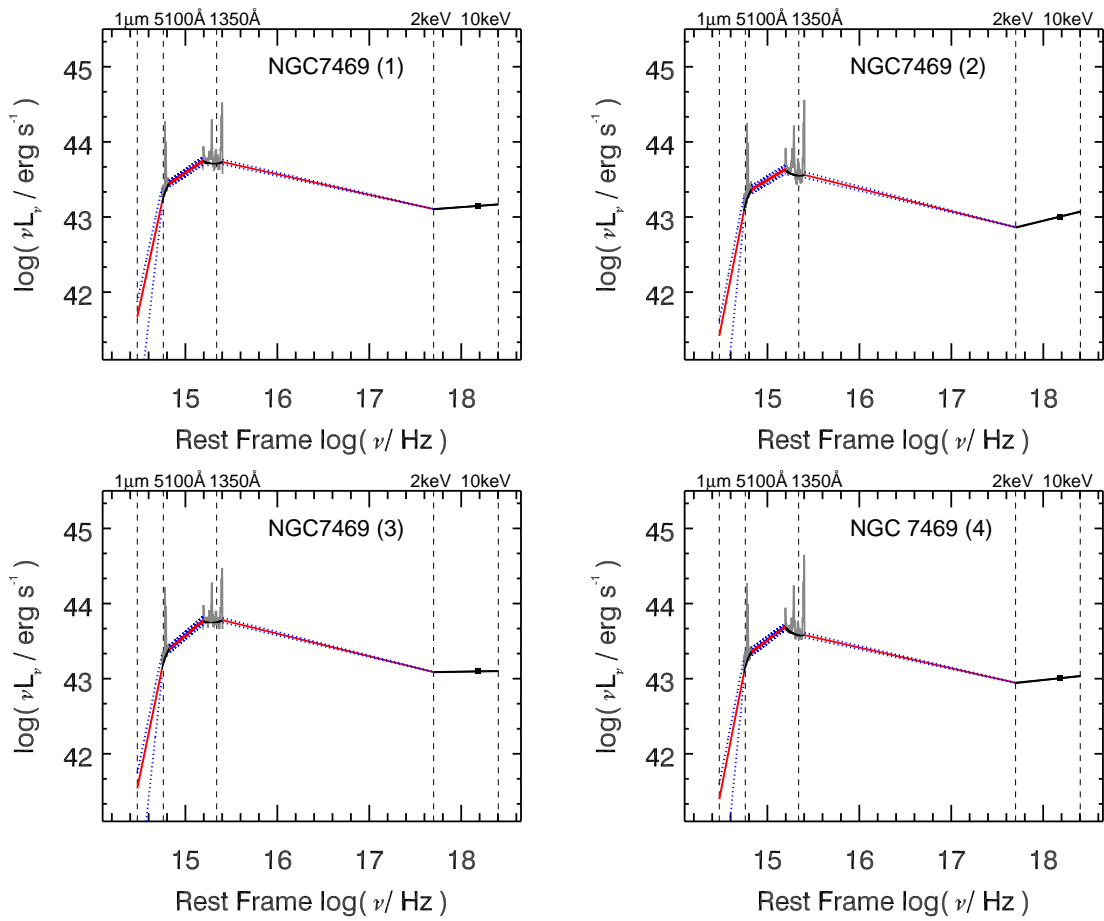


Figure A.1 continued.

A.3 MEASUREMENTS BASED ON KORISTA ET AL. (1997A) MODEL

Table A.1. Bolometric Luminosities, Eddington Ratios, and Bolometric Corrections Based on Korista et al. (1997a) Model

Object	Epoch	$\log(L_{\text{BOL}}(K97))$	$\lambda_{\text{Edd}}(K97)$	BC(5100)(K97)	BC(1350)(K97)	BC(2-10keV)(K97)
(1)	(2)	(3)	(4)	(5)	(6)	(7)
Fairall 9	1	45.03 ^{+0.03} _{-0.03}	0.033 ^{+0.002} _{-0.002}	15.89 ^{+2.46} _{-2.41}	6.35 ^{+1.19} _{-1.17}	10.08 ^{+1.31} _{-1.17}
	2	45.04 ^{+0.03} _{-0.03}	0.034 ^{+0.002} _{-0.002}	16.28 ^{+2.72} _{-2.67}	6.22 ^{+1.19} _{-1.17}	10.31 ^{+1.35} _{-1.20}
	3	45.06 ^{+0.03} _{-0.03}	0.035 ^{+0.002} _{-0.002}	18.46 ^{+2.38} _{-2.29}	5.98 ^{+0.87} _{-0.84}	10.80 ^{+2.27} _{-1.90}
	4	45.07 ^{+0.02} _{-0.02}	0.036 ^{+0.002} _{-0.002}	19.54 ^{+2.03} _{-1.97}	5.98 ^{+0.89} _{-0.88}	11.13 ^{+1.41} _{-1.26}
	5	45.05 ^{+0.02} _{-0.03}	0.035 ^{+0.002} _{-0.002}	16.77 ^{+1.85} _{-1.79}	6.13 ^{+0.96} _{-0.95}	10.54 ^{+1.34} _{-1.20}
	6	45.11 ^{+0.02} _{-0.02}	0.039 ^{+0.002} _{-0.002}	19.36 ^{+6.54} _{-6.50}	5.81 ^{+0.95} _{-0.91}	11.95 ^{+1.59} _{-1.40}
	7	45.18 ^{+0.02} _{-0.02}	0.047 ^{+0.002} _{-0.002}	21.52 ^{+2.19} _{-2.14}	5.54 ^{+0.76} _{-0.75}	14.33 ^{+1.85} _{-1.65}
	8	45.12 ^{+0.02} _{-0.02}	0.041 ^{+0.002} _{-0.002}	20.18 ^{+1.90} _{-1.84}	5.78 ^{+0.88} _{-0.87}	12.41 ^{+1.62} _{-1.44}
	9	45.16 ^{+0.03} _{-0.03}	0.045 ^{+0.003} _{-0.003}	20.35 ^{+2.19} _{-2.04}	5.69 ^{+1.50} _{-1.48}	13.54 ^{+1.87} _{-1.64}
	10	45.22 ^{+0.02} _{-0.02}	0.051 ^{+0.002} _{-0.002}	22.01 ^{+2.55} _{-2.49}	5.44 ^{+0.61} _{-0.60}	15.41 ^{+1.90} _{-1.70}
	11	45.14 ^{+0.02} _{-0.02}	0.043 ^{+0.002} _{-0.002}	19.18 ^{+1.48} _{-1.42}	5.73 ^{+0.86} _{-0.85}	12.99 ^{+1.67} _{-1.49}
	12	45.15 ^{+0.02} _{-0.02}	0.043 ^{+0.002} _{-0.002}	20.19 ^{+1.53} _{-1.48}	5.64 ^{+0.69} _{-0.68}	13.04 ^{+1.66} _{-1.48}
	13	45.08 ^{+0.02} _{-0.02}	0.037 ^{+0.002} _{-0.002}	18.71 ^{+1.98} _{-1.91}	5.88 ^{+0.96} _{-0.95}	11.09 ^{+1.46} _{-1.30}
	14	45.10 ^{+0.04} _{-0.03}	0.039 ^{+0.003} _{-0.003}	18.01 ^{+1.94} _{-1.62}	5.93 ^{+2.36} _{-2.33}	11.63 ^{+1.73} _{-1.46}
	15	45.09 ^{+0.02} _{-0.03}	0.038 ^{+0.002} _{-0.002}	19.75 ^{+1.65} _{-1.60}	5.80 ^{+0.69} _{-0.68}	11.38 ^{+1.45} _{-1.29}
	16	45.05 ^{+0.03} _{-0.02}	0.035 ^{+0.002} _{-0.002}	18.41 ^{+1.89} _{-1.78}	6.08 ^{+0.83} _{-0.81}	10.39 ^{+1.41} _{-1.25}
	17	45.11 ^{+0.03} _{-0.02}	0.040 ^{+0.002} _{-0.002}	19.03 ^{+2.38} _{-2.32}	5.87 ^{+1.11} _{-1.10}	11.96 ^{+1.59} _{-1.41}
	18	45.11 ^{+0.02} _{-0.02}	0.039 ^{+0.002} _{-0.002}	16.37 ^{+1.30} _{-1.21}	5.97 ^{+1.14} _{-1.12}	11.73 ^{+1.58} _{-1.40}
	19	45.17 ^{+0.02} _{-0.02}	0.046 ^{+0.002} _{-0.002}	19.27 ^{+1.48} _{-1.42}	5.74 ^{+0.82} _{-0.81}	13.58 ^{+1.78} _{-1.59}
	20	45.19 ^{+0.02} _{-0.02}	0.048 ^{+0.002} _{-0.002}	17.47 ^{+1.62} _{-1.53}	5.65 ^{+0.70} _{-0.69}	14.32 ^{+1.86} _{-1.66}
	21	45.21 ^{+0.02} _{-0.02}	0.050 ^{+0.002} _{-0.002}	21.38 ^{+2.16} _{-2.13}	5.53 ^{+0.92} _{-0.91}	14.90 ^{+1.91} _{-1.70}
	22	45.18 ^{+0.03} _{-0.02}	0.047 ^{+0.003} _{-0.002}	15.38 ^{+1.12} _{-1.01}	5.75 ^{+1.07} _{-1.06}	14.01 ^{+2.45} _{-2.11}
	23	45.14 ^{+0.02} _{-0.02}	0.043 ^{+0.002} _{-0.002}	15.94 ^{+1.33} _{-1.29}	5.91 ^{+0.74} _{-0.73}	12.70 ^{+1.70} _{-1.51}
	24	45.17 ^{+0.02} _{-0.02}	0.046 ^{+0.002} _{-0.002}	17.05 ^{+1.32} _{-1.27}	5.70 ^{+0.78} _{-0.77}	13.59 ^{+1.83} _{-1.63}
	25	45.40 ^{+0.02} _{-0.01}	0.077 ^{+0.003} _{-0.003}	19.68 ^{+1.62} _{-1.62}	5.22 ^{+0.58} _{-0.58}	22.48 ^{+2.93} _{-2.65}
	26	45.41 ^{+0.01} _{-0.01}	0.079 ^{+0.002} _{-0.002}	20.25 ^{+0.94} _{-0.90}	5.19 ^{+0.42} _{-0.42}	23.02 ^{+3.06} _{-2.71}
	27	45.34 ^{+0.01} _{-0.01}	0.068 ^{+0.002} _{-0.002}	18.70 ^{+1.00} _{-0.97}	5.26 ^{+0.60} _{-0.59}	23.59 ^{+1.60} _{-1.50}
NGC 3783	1	43.76 ^{+0.02} _{-0.01}	0.002 ^{+0.000} _{-0.000}	14.02 ^{+2.16} _{-2.15}	5.10 ^{+0.46} _{-0.45}	70.69 ^{+13.51} _{-11.40}
	1	44.09 ^{+0.01} _{-0.01}	0.073 ^{+0.025} _{-0.025}	13.36 ^{+0.50} _{-0.49}	5.52 ^{+0.35} _{-0.35}	14.88 ^{+0.53} _{-0.51}
NGC 4151	2	44.11 ^{+0.01} _{-0.01}	0.077 ^{+0.027} _{-0.027}	13.79 ^{+0.52} _{-0.51}	5.30 ^{+0.31} _{-0.31}	17.70 ^{+0.68} _{-0.65}
	3	44.09 ^{+0.01} _{-0.01}	0.074 ^{+0.026} _{-0.026}	13.53 ^{+0.45} _{-0.48}	5.50 ^{+0.31} _{-0.31}	14.36 ^{+0.48} _{-0.46}
	4	44.06 ^{+0.01} _{-0.01}	0.069 ^{+0.024} _{-0.024}	12.61 ^{+0.46} _{-0.46}	5.50 ^{+0.32} _{-0.31}	15.78 ^{+0.60} _{-0.58}
NGC 5548	1	44.44 ^{+0.01} _{-0.01}	0.038 ^{+0.001} _{-0.001}	12.00 ^{+0.80} _{-0.77}	5.64 ^{+0.76} _{-0.76}	12.94 ^{+0.47} _{-0.42}
	2	44.46 ^{+0.01} _{-0.01}	0.040 ^{+0.001} _{-0.001}	16.78 ^{+1.33} _{-1.31}	6.10 ^{+0.77} _{-0.77}	7.94 ^{+0.22} _{-0.20}
	3	44.34 ^{+0.02} _{-0.02}	0.030 ^{+0.001} _{-0.001}	11.41 ^{+1.42} _{-1.40}	6.66 ^{+1.06} _{-1.05}	7.22 ^{+0.29} _{-0.25}
	4	44.45 ^{+0.02} _{-0.02}	0.039 ^{+0.002} _{-0.002}	13.38 ^{+0.98} _{-0.95}	6.39 ^{+0.93} _{-0.92}	8.31 ^{+0.48} _{-0.44}
	5	44.27 ^{+0.03} _{-0.02}	0.026 ^{+0.002} _{-0.001}	15.29 ^{+3.12} _{-3.06}	6.58 ^{+1.48} _{-1.46}	7.19 ^{+0.67} _{-0.58}
	6	44.33 ^{+0.02} _{-0.02}	0.030 ^{+0.002} _{-0.002}	15.84 ^{+4.75} _{-4.73}	6.25 ^{+0.92} _{-0.90}	8.47 ^{+0.73} _{-0.66}
	7	44.28 ^{+0.02} _{-0.02}	0.026 ^{+0.001} _{-0.001}	14.85 ^{+2.15} _{-2.11}	6.22 ^{+1.15} _{-1.13}	9.11 ^{+0.77} _{-0.70}
	8	44.34 ^{+0.02} _{-0.02}	0.030 ^{+0.002} _{-0.002}	16.83 ^{+2.15} _{-2.05}	6.68 ^{+1.52} _{-1.51}	6.52 ^{+0.47} _{-0.41}
	9	44.11 ^{+0.04} _{-0.03}	0.018 ^{+0.002} _{-0.001}	11.84 ^{+1.75} _{-1.64}	6.20 ^{+0.59} _{-0.55}	10.22 ^{+1.97} _{-1.66}
	10	44.04 ^{+0.03} _{-0.03}	0.015 ^{+0.001} _{-0.001}	11.34 ^{+1.68} _{-1.62}	6.83 ^{+1.63} _{-1.60}	6.77 ^{+0.68} _{-0.60}
	11	43.97 ^{+0.03} _{-0.03}	0.013 ^{+0.001} _{-0.001}	11.27 ^{+1.97} _{-1.89}	7.12 ^{+1.69} _{-1.65}	6.70 ^{+0.76} _{-0.65}
	12	44.35 ^{+0.03} _{-0.03}	0.031 ^{+0.002} _{-0.002}	12.70 ^{+1.60} _{-1.51}	6.55 ^{+1.13} _{-1.09}	7.28 ^{+1.50} _{-1.26}
	13	44.38 ^{+0.03} _{-0.03}	0.033 ^{+0.002} _{-0.002}	12.12 ^{+1.45} _{-1.42}	6.45 ^{+1.02} _{-0.99}	7.83 ^{+1.60} _{-1.34}
	14	44.40 ^{+0.03} _{-0.02}	0.034 ^{+0.002} _{-0.002}	12.52 ^{+1.21} _{-1.14}	6.27 ^{+0.80} _{-0.77}	8.19 ^{+1.65} _{-1.39}
	15	44.39 ^{+0.03} _{-0.03}	0.034 ^{+0.002} _{-0.002}	12.28 ^{+1.20} _{-1.13}	6.30 ^{+0.89} _{-0.87}	8.14 ^{+1.65} _{-1.39}
16	44.46 ^{+0.02} _{-0.02}	0.040 ^{+0.002} _{-0.002}	13.50 ^{+1.12} _{-1.04}	5.95 ^{+0.58} _{-0.56}	9.41 ^{+1.87} _{-1.57}	

Table A.1 (cont'd)

Object	Epoch	$\log(L_{\text{BOL}}(K97))$	$\lambda_{\text{Edd}}(K97)$	BC(5100)(K97)	BC(1350)(K97)	BC(2 – 10keV)(K97)
(1)	(2)	(3)	(4)	(5)	(6)	(7)
	17	44.48 ^{+0.03} _{-0.03}	0.042 ^{+0.003} _{-0.003}	13.37 ^{+2.47} _{-2.41}	5.99 ^{+0.84} _{-0.81}	9.98 ^{+2.04} _{-1.71}
	18	44.52 ^{+0.02} _{-0.02}	0.046 ^{+0.003} _{-0.002}	14.66 ^{+1.67} _{-1.62}	5.77 ^{+0.70} _{-0.69}	10.93 ^{+2.17} _{-1.83}
	19	44.52 ^{+0.03} _{-0.02}	0.045 ^{+0.003} _{-0.003}	16.60 ^{+2.36} _{-2.30}	5.76 ^{+0.81} _{-0.79}	10.79 ^{+2.16} _{-1.82}
	20	44.48 ^{+0.02} _{-0.02}	0.041 ^{+0.003} _{-0.002}	11.79 ^{+0.94} _{-0.87}	6.07 ^{+0.80} _{-0.78}	9.87 ^{+1.97} _{-1.66}
	21	44.34 ^{+0.04} _{-0.03}	0.031 ^{+0.003} _{-0.002}	11.47 ^{+3.38} _{-3.32}	6.61 ^{+1.20} _{-1.14}	7.26 ^{+1.55} _{-1.29}
	22	44.28 ^{+0.04} _{-0.03}	0.026 ^{+0.002} _{-0.002}	13.90 ^{+1.81} _{-1.69}	6.90 ^{+1.36} _{-1.33}	6.23 ^{+1.30} _{-1.10}
	23	44.31 ^{+0.03} _{-0.03}	0.028 ^{+0.002} _{-0.002}	12.59 ^{+1.52} _{-1.43}	6.78 ^{+1.24} _{-1.21}	6.67 ^{+1.38} _{-1.16}
	24	44.28 ^{+0.04} _{-0.03}	0.026 ^{+0.002} _{-0.002}	11.42 ^{+1.76} _{-1.68}	6.95 ^{+1.26} _{-1.21}	6.23 ^{+1.31} _{-1.10}
	25	44.36 ^{+0.03} _{-0.03}	0.031 ^{+0.003} _{-0.002}	11.31 ^{+1.47} _{-1.39}	6.48 ^{+1.11} _{-1.08}	7.43 ^{+1.54} _{-1.29}
	26	44.40 ^{+0.03} _{-0.03}	0.034 ^{+0.002} _{-0.002}	12.13 ^{+1.24} _{-1.17}	6.32 ^{+0.87} _{-0.84}	8.15 ^{+1.65} _{-1.39}
	27	44.48 ^{+0.03} _{-0.02}	0.041 ^{+0.003} _{-0.002}	13.16 ^{+1.12} _{-1.05}	6.06 ^{+0.88} _{-0.86}	9.86 ^{+1.98} _{-1.66}
	28	44.48 ^{+0.03} _{-0.02}	0.042 ^{+0.003} _{-0.002}	12.54 ^{+1.41} _{-1.36}	5.93 ^{+0.71} _{-0.68}	10.01 ^{+2.00} _{-1.68}
	29	44.59 ^{+0.02} _{-0.02}	0.053 ^{+0.003} _{-0.003}	14.94 ^{+2.10} _{-2.06}	5.57 ^{+0.61} _{-0.59}	12.64 ^{+2.51} _{-2.11}
	30	44.55 ^{+0.02} _{-0.02}	0.049 ^{+0.003} _{-0.002}	13.88 ^{+1.45} _{-1.40}	5.72 ^{+0.63} _{-0.61}	11.78 ^{+2.33} _{-1.96}
	31	44.47 ^{+0.03} _{-0.02}	0.040 ^{+0.003} _{-0.002}	12.35 ^{+1.06} _{-1.00}	6.09 ^{+0.84} _{-0.81}	9.61 ^{+1.92} _{-1.62}
	32	44.47 ^{+0.03} _{-0.03}	0.041 ^{+0.003} _{-0.002}	11.93 ^{+1.50} _{-1.45}	6.07 ^{+0.90} _{-0.88}	9.69 ^{+1.96} _{-1.65}
	33	44.47 ^{+0.03} _{-0.02}	0.041 ^{+0.003} _{-0.002}	12.68 ^{+1.09} _{-1.01}	5.93 ^{+0.86} _{-0.84}	9.72 ^{+1.95} _{-1.64}
	34	44.41 ^{+0.03} _{-0.03}	0.035 ^{+0.003} _{-0.002}	11.05 ^{+1.13} _{-1.05}	6.43 ^{+1.09} _{-1.07}	8.37 ^{+1.71} _{-1.44}
	35	44.41 ^{+0.03} _{-0.03}	0.035 ^{+0.003} _{-0.002}	12.61 ^{+1.69} _{-1.63}	6.37 ^{+1.00} _{-0.97}	8.35 ^{+1.70} _{-1.43}
	36	44.37 ^{+0.03} _{-0.03}	0.032 ^{+0.002} _{-0.002}	11.88 ^{+1.17} _{-1.06}	6.50 ^{+1.04} _{-1.00}	7.71 ^{+1.58} _{-1.32}
	37	44.38 ^{+0.03} _{-0.03}	0.033 ^{+0.002} _{-0.002}	12.56 ^{+1.73} _{-1.67}	6.33 ^{+0.93} _{-0.89}	7.81 ^{+1.60} _{-1.34}
	38	44.29 ^{+0.04} _{-0.03}	0.027 ^{+0.003} _{-0.002}	11.09 ^{+1.72} _{-1.63}	6.91 ^{+1.40} _{-1.36}	6.47 ^{+1.37} _{-1.15}
	39	44.32 ^{+0.03} _{-0.03}	0.029 ^{+0.002} _{-0.002}	10.19 ^{+1.04} _{-0.95}	6.91 ^{+1.26} _{-1.23}	6.81 ^{+1.41} _{-1.18}
	40	44.34 ^{+0.03} _{-0.03}	0.030 ^{+0.003} _{-0.002}	13.95 ^{+2.80} _{-2.73}	6.45 ^{+1.12} _{-1.08}	7.26 ^{+1.51} _{-1.27}
	41	44.41 ^{+0.03} _{-0.03}	0.035 ^{+0.003} _{-0.002}	13.63 ^{+1.93} _{-1.86}	6.14 ^{+0.90} _{-0.88}	8.41 ^{+1.71} _{-1.44}
	42	44.41 ^{+0.03} _{-0.03}	0.035 ^{+0.003} _{-0.002}	12.55 ^{+1.85} _{-1.79}	6.21 ^{+0.99} _{-0.96}	8.44 ^{+1.73} _{-1.45}
	43	44.42 ^{+0.03} _{-0.03}	0.036 ^{+0.002} _{-0.002}	13.33 ^{+1.24} _{-1.15}	6.24 ^{+0.94} _{-0.91}	8.56 ^{+1.73} _{-1.46}
	44	44.39 ^{+0.03} _{-0.03}	0.034 ^{+0.003} _{-0.002}	12.29 ^{+1.28} _{-1.15}	6.24 ^{+0.99} _{-0.95}	8.65 ^{+2.33} _{-1.86}
	45	44.25 ^{+0.04} _{-0.04}	0.025 ^{+0.003} _{-0.002}	8.71 ^{+1.08} _{-0.91}	7.67 ^{+1.98} _{-1.91}	6.34 ^{+1.78} _{-1.40}
	46	44.10 ^{+0.06} _{-0.06}	0.017 ^{+0.003} _{-0.002}	11.18 ^{+2.14} _{-1.87}	8.89 ^{+3.13} _{-3.02}	4.46 ^{+1.36} _{-1.08}
	47	44.14 ^{+0.06} _{-0.05}	0.019 ^{+0.003} _{-0.002}	12.19 ^{+2.27} _{-2.02}	8.06 ^{+2.33} _{-2.23}	4.98 ^{+1.52} _{-1.20}
3C 390.3	1	44.66 ^{+0.03} _{-0.02}	0.015 ^{+0.001} _{-0.001}	19.53 ^{+5.53} _{-5.40}	11.02 ^{+5.95} _{-5.91}	3.19 ^{+0.27} _{-0.19}
	2	44.91 ^{+0.04} _{-0.03}	0.028 ^{+0.003} _{-0.002}	21.84 ^{+4.40} _{-4.17}	9.50 ^{+4.62} _{-4.58}	3.66 ^{+0.43} _{-0.35}
Mrk 509	1	45.33 ^{+0.02} _{-0.02}	0.129 ^{+0.005} _{-0.005}	14.25 ^{+0.64} _{-0.56}	5.52 ^{+0.93} _{-0.93}	16.25 ^{+1.21} _{-1.11}
NGC 7469	1	44.48 ^{+0.02} _{-0.01}	0.245 ^{+0.012} _{-0.010}	15.22 ^{+2.45} _{-2.42}	5.85 ^{+0.52} _{-0.49}	13.68 ^{+0.51} _{-0.35}
	2	44.32 ^{+0.02} _{-0.01}	0.168 ^{+0.010} _{-0.008}	12.93 ^{+2.67} _{-2.62}	5.86 ^{+0.64} _{-0.60}	13.76 ^{+0.71} _{-0.44}
	3	44.51 ^{+0.02} _{-0.01}	0.260 ^{+0.013} _{-0.011}	18.39 ^{+3.40} _{-3.37}	5.63 ^{+0.49} _{-0.47}	16.03 ^{+0.60} _{-0.40}
	4	44.35 ^{+0.02} _{-0.01}	0.181 ^{+0.010} _{-0.008}	14.24 ^{+2.92} _{-2.87}	5.95 ^{+0.54} _{-0.49}	14.19 ^{+0.66} _{-0.40}

A.4 BOLOMETRIC LUMINOSITY BASED ON THE OPTXAGNF MODEL

In the following I attempt to fit one SED of NGC 5548 (epoch (1)) in order to test the effectiveness of *optxagnf* model to represent my multi-wavelength quasi-simultaneous SEDs. The *optxagnf* model of Done et al. (2012) includes three different emission components to model the optical to X-ray broadband SED. The optical-UV emission is the blackbody radiation produced in the outer disk ($\sim 1000R_g$). In this model, the X-ray emission is produced in a two-phase medium that is between the last stable orbit and the corona radius (R_{cor}) that is the transition radius between the blackbody and X-ray radiation. The low temperature (~ 0.1 - 0.3 keV) plasma generates the soft excess X-ray emission (below ~ 2 keV) by inverse-Compton scattered optical/UV photons. The hot (~ 100 keV) plasma produces the hard X-ray power-law between $2 - 10$ KeV. The advantage of this model is the energy conservation between the different emission components such that accretion disk generates the total energy output and, the soft and hard X-ray emission is restricted to reprocess the emission produced by the disk. Therefore, this model provides a physical description of the optical to X-ray AGN SEDs.

I perform the SED fitting with the XSPEC v12.8.1 (Arnaud, 1996) software. In order to have a nearly equal number of data points in the optical/UV and X-ray regimes, I bin each optical and UV continuum into ~ 10 number of bins. The optical, UV and X-ray continuum fluxes are converted to the required format for XSPEC using the FLX2XSP tool of HEASOFT. Since the continuum fluxes are already corrected for Galactic gas absorption and dust extinction, they do not require any further correction.

The *optxagnf* model has 12 parameters: Black hole mass, M_{BH} ; Distance of the source, D_L ; Eddington ratio, λ_{Edd} ; Spin of the BH, a_* ; Radius of the corona, R_{cor} , in units of gravitational radii; Outer radius of the disk, R_{out} ; Electron temperature of the soft Comptonization component, kT_e ; Optical depth of the soft Comptonization region, τ ; Slope of the hard X-ray power-law, Γ ; The fraction of the power below R_{cor} which is emitted in the hard Comptonisation component, f_{pl} ; Redshift of the source, z ; Normalization.

Four of these parameters hold fixed in the modeling by default: D_L and z as given in Table 3.1, Γ to the value adopted from literature (references given in Table 3.2), normalization to 1. My X-ray data do not cover the soft X-ray emission (§3.3.2), and therefore my database can not constrain the soft excess emission sufficiently. First, I set M_{BH} to the value obtained by RM analysis (Peterson et al., 2004), assume a non-rotating Schwarzschild black hole and set the spin to zero. With no soft X-ray data at hand I set f_{pl} to 1, such that the soft excess Comptonisation is not considered. I refer to this case as model ‘A’, the resultant model parameters are tabulated in Table A.2 and the model is shown in Figure A.2 (the light blue dashed lines). Model ‘A’ significantly underestimates the UV emission and overestimates the optical continuum and therefore it is not satisfactory.

Next, I tested different parameter settings in order to obtain a good fit. In order to account for soft excess emission with no data to constrain it I set Comptonisation components to the typical values given by Jin et al. (2012a), namely $kT_e=0.2$ and $\tau=16$ and let f_{pl} be a freely varying parameter. I also set M_{BH} to be in the range between 2.4×10^7 and 10.2×10^7 that is consistent with the black hole mass estimates given by different studies (Peterson et al., 2004; Bentz et al., 2009b; Pancoast et al., 2013). I call this case model ‘B’. It is shown in Figure A.2 as the orange dashed-dotted curve. For a lower M_{BH} of 2.97×10^7 , I obtain a somewhat better fit compared to model ‘A’.

I then test the effect of a non-zero spin model ‘B’. First I set the M_{BH} to the best-fit result

of model ‘B’ and allow the spin to be a free parameter. In this case, I obtain a spin parameter that is consistent with zero. When I set the spin $a=0.5$ for $M_{\text{BH}} = 2.97 \times 10^7$, and the resultant model overestimates the UV continuum (model ‘B(i)’ in Figure A.2; brown dash-dots). Model ‘Bi’ over predicts the UV emission. Then I set M_{BH} and spin as a free parameters (f_{pl} is also a free parameter). I obtain $a_* = 0.73$ and $M_{\text{BH}} = 5.49 \times 10^7$ (model ‘B(ii)’ in Figure A.2). The latter comparison shows that M_{BH} and spin are degenerate parameters, and it is not possible to measure these parameters robustly.

Although I have RM based mass estimates and simultaneous optical/UV and X-ray continuum data that eliminate variability effects, the results of the obtained fits are not robust. Therefore I consider the bolometric luminosity obtained from model ‘B’ a lower limit. It is 23% lower compared to L_{BOL} (interpolation). The Eddington ratio constrained from model ‘B’ is factor of ~ 3 higher than the one computed from the interpolated SED, because model ‘B’ has a lower black hole mass. If I also manipulate parameters as in model ‘Bi’ I may obtain a higher L_{BOL} that is only 5% lower than L_{BOL} (interpolation), but of course these parameters are highly uncertain and the process is adhoc. Since the results of the *optxagnf* model are not sufficiently robust I do not attempt to model any other SED with this model. Therefore, I conclude that it is reasonable to adopt the model independent approach of §3.5.2.

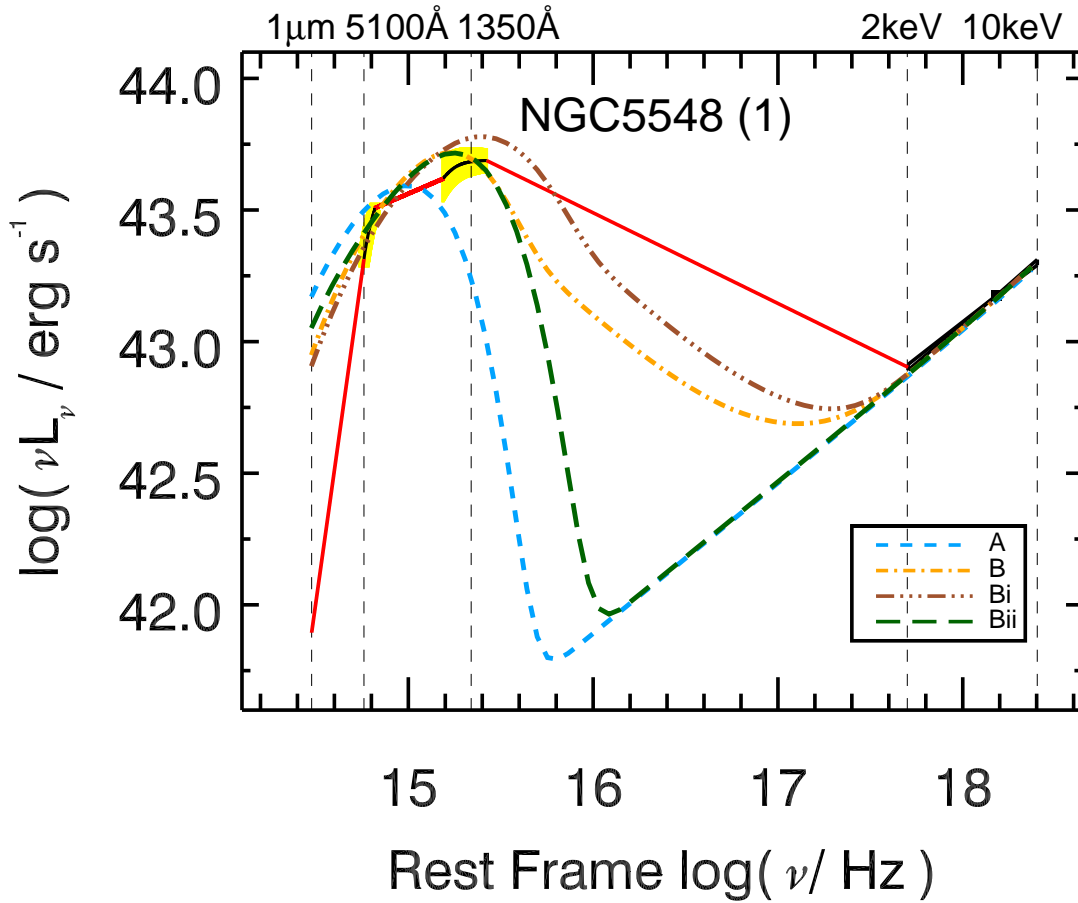


Figure A.2 OPTXAGNF model fits for NGC 5548 SED epoch 1. The dashed blue line (A), the dot-dashed orange curve (B), the three dot-dashed brown curve (Bi) and the long dashed green curve (Bii) show the best-fit models for different parameter settings (§A.4). Model A has $M_{\text{BH}} = 6.71 \times 10^6 M_{\odot}$, $a_{\star}=0.0$, $\lambda_{\text{Edd}}=0.043$; Model B has $M_{\text{BH}} = 2.97 \times 10^7 M_{\odot}$, $a_{\star}=0.0$, $\lambda_{\text{Edd}}=0.094$; Model Bi has $M_{\text{BH}} = 5.49 \times 10^7 M_{\odot}$, $a_{\star}=0.73$, $\lambda_{\text{Edd}}=0.048$; Model Bii has $M_{\text{BH}} = 2.97 \times 10^7 M_{\odot}$, $a_{\star}=0.5$, $\lambda_{\text{Edd}}=0.10$. The red solid line shows the linearly interpolated SED, the solid black lines represent the observed optical and UV continua and the yellow shades show the continuum uncertainties (§3.4).

Table A.2. OPTXAGNF fit results

Object	Epoch	M_{BH} ($10^7 M_{\odot}$)	a_*	λ_{Edd}	R_{cor} (R_g)	$\log R_{\text{out}}$ (R_g)	kT_e (keV)	τ	f_{pl}	$\log(L_{\text{BOL}}(\text{optxagnf}))$
A										
NGC 5548	1	6.71	0.0	0.043	89.02	3.0	0.20	16.00	1.00	43.99
B										
NGC 5548	1	2.97	0.0	0.094	99.56	3.0	0.20	16.00	0.83	44.19
Bi										
NGC 5548	1	2.97	0.5	0.10	50.70	3.0	0.20	16.00	0.83	44.12
Bii										
NGC 5548	1	5.49	0.73	0.048	32.90	3.0	0.20	16.00	1.00	44.28

A.5 LINE SHAPE VS. OPTICAL AND UV CONTINUUM LUMINOSITY PLOTS

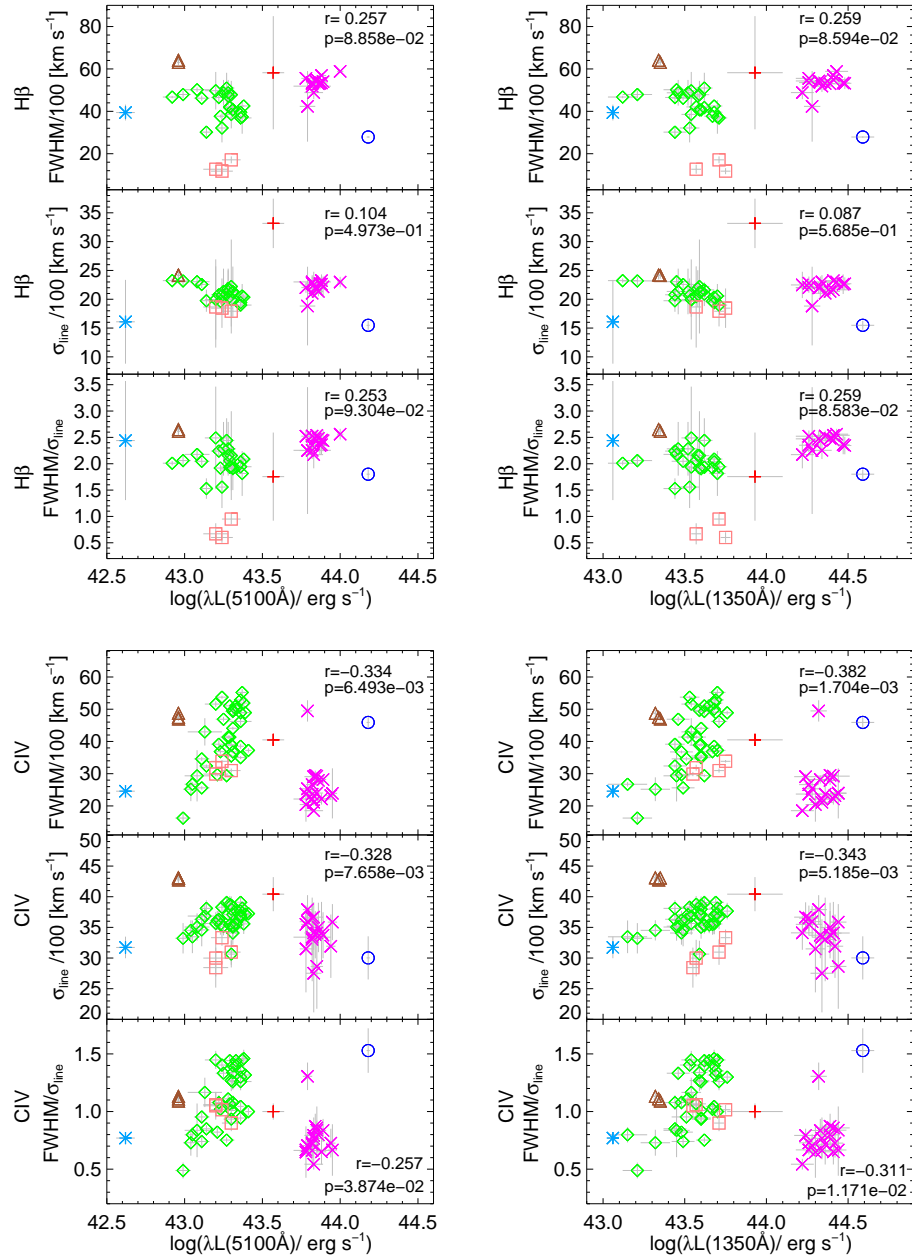


Figure A.3 H β (top panels) and C IV (bottom panels) line shape vs. $\lambda L_{\lambda}(5100)$ and $\lambda L_{\lambda}(1350)$. The symbol code same as in Figure 3.9.

BIBLIOGRAPHY

- Abazajian, K., et al. 2004, *AJ*, 128, 502
- . 2005, *AJ*, 129, 1755
- Abazajian, K. N., et al. 2009, *ApJS*, 182, 543
- Adelman-McCarthy, J. K., et al. 2006, *ApJS*, 162, 38
- . 2008, *ApJS*, 175, 297
- Ahn, C. P., et al. 2013, *ArXiv e-prints*
- Akritas, M. G., & Siebert, J. 1996, *MNRAS*, 278, 919
- Alloin, D., et al. 1995, *A&A*, 293, 293
- Amblard, A., et al. 2010, *A&A*, 518, L9
- Antonucci, R. 1993, *ARA&A*, 31, 473
- Antonucci, R. R. J., & Miller, J. S. 1985, *ApJ*, 297, 621
- Arav, N., Barlow, T. A., Laor, A., Sargent, W. L. W., & Blandford, R. D. 1998, *MNRAS*, 297, 990
- Arnaud, K. A. 1996, in *Astronomical Society of the Pacific Conference Series, Vol. 101, Astronomical Data Analysis Software and Systems V*, ed. G. H. Jacoby & J. Barnes, 17
- Arnouts, S., Cristiani, S., Moscardini, L., Matarrese, S., Lucchin, F., Fontana, A., & Giallongo, E. 1999, *MNRAS*, 310, 540
- Baldry, I. K., et al. 2004, *ApJ*, 600, 681
- . 2006, *MNRAS*, 373, 469
- Baldwin, J., Ferland, G., Korista, K., & Verner, D. 1995, *ApJ*, 455, L119
- Baldwin, J. A. 1977, *ApJ*, 214, 679
- Baldwin, J. A., Phillips, M. M., & Terlevich, R. 1981, *PASP*, 93, 5
- Barnes, J. E., & Hernquist, L. 1996, *ApJ*, 471, 115
- Barnes, J. E., & Hernquist, L. E. 1991, *ApJ*, 370, L65
- Bauer, A., et al. 2009, *ApJ*, 696, 1241

- Bell, E. F., et al. 2004, *ApJ*, 608, 752
- Bentz, M. C., Peterson, B. M., Netzer, H., Pogge, R. W., & Vestergaard, M. 2009a, *ApJ*, 697, 160
- Bentz, M. C., Peterson, B. M., Pogge, R. W., Vestergaard, M., & Onken, C. A. 2006a, *ApJ*, 644, 133
- Bentz, M. C., et al. 2006b, *ApJ*, 651, 775
- . 2007, *ApJ*, 662, 205
- . 2009b, *ApJ*, 705, 199
- . 2010, *ApJ*, 716, 993
- . 2013, *ApJ*, 767, 149
- Blandford, R. D., & McKee, C. F. 1982, *ApJ*, 255, 419
- Blanton, M. R., Eisenstein, D., Hogg, D. W., Schlegel, D. J., & Brinkmann, J. 2005, *ApJ*, 629, 143
- Blanton, M. R., & Roweis, S. 2007, *AJ*, 133, 734
- Blanton, M. R., et al. 2003, *ApJ*, 594, 186
- Bolton, A. S., et al. 2012, *AJ*, 144, 144
- Bowyer, S., Byram, E. T., Chubb, T. A., & Friedman, H. 1965, *Science*, 147, 394
- Brewer, B. J., et al. 2011, *ApJ*, 733, L33
- Brinchmann, J., et al. 2004, *MNRAS*, 351, 1151
- Bruzual, G., & Charlot, S. 2003, *MNRAS*, 344, 1000
- Cackett, E. M., Horne, K., & Winkler, H. 2007, *MNRAS*, 380, 669
- Calzetti, D. 2001, *PASP*, 113, 1449
- Camenzind, M. 2007, *Compact objects in astrophysics : white dwarfs, neutron stars, and black holes*
- Cao, C., et al. 2006, *CJAA*, 6, 197
- Caputi, K. I., Dole, H., Lagache, G., McLure, R. J., Dunlop, J. S., Puget, J.-L., Le Floc'h, E., & Pérez-González, P. G. 2006, *A&A*, 454, 143
- Caputi, K. I., et al. 2007, *ApJ*, 660, 97
- Cardelli, J. A., Clayton, G. C., & Mathis, J. S. 1989, *ApJ*, 345, 245
- Carone, T. E., et al. 1996, *ApJ*, 471, 737
- Chapman, S. C., Blain, A. W., Smail, I., & Ivison, R. J. 2005, *ApJ*, 622, 772
- Chary, R., & Elbaz, D. 2001, *ApJ*, 556, 562
- Chen, Y., Lowenthal, J. D., & Yun, M. S. 2010, *ApJ*, 712, 1385
- Chen, Y.-M., et al. 2012, *MNRAS*, 421, 314

- Clavel, J., et al. 1991, *ApJ*, 366, 64
- . 1992, *ApJ*, 393, 113
- Clements, D. L., et al. 1996, *MNRAS*, 279, 459
- Colless, M. 2004, *PASA*, 21, 352
- Colless, M., et al. 2001, *MNRAS*, 328, 1039
- Collier, S., Horne, K., Wanders, I., & Peterson, B. M. 1999, *MNRAS*, 302, L24
- Collier, S. J., et al. 1998, *ApJ*, 500, 162
- Collin, S., Kawaguchi, T., Peterson, B. M., & Vestergaard, M. 2006, *A&A*, 456, 75
- Cooper, M. C., et al. 2006, *MNRAS*, 370, 198
- Corbett, E. A., et al. 2003, *MNRAS*, 343, 705
- Crenshaw, D. M., Kraemer, S. B., Bruhweiler, F. C., & Ruiz, J. R. 2001, *ApJ*, 555, 633
- Crenshaw, D. M., et al. 1996, *ApJ*, 470, 322
- Croton, D. J., et al. 2006, *MNRAS*, 365, 11
- Crummy, J., Fabian, A. C., Gallo, L., & Ross, R. R. 2006, *MNRAS*, 365, 1067
- da Cunha, E., Charmandaris, V., Díaz-Santos, T., Armus, L., Marshall, J. A., & Elbaz, D. 2010, *A&A*, 523, A78
- Daddi, E., et al. 2005, *ApJ*, 631, L13
- . 2007, *ApJ*, 670, 156
- . 2009, *ApJ*, 694, 1517
- . 2010, *ApJ*, 713, 686
- Dale, D. A., & Helou, G. 2002, *ApJ*, 576, 159
- Dale, D. A., Helou, G., Contursi, A., Silbermann, N. A., & Kolhatkar, S. 2001, *ApJ*, 549, 215
- Dasyra, K. M., et al. 2006a, *ApJ*, 638, 745
- . 2006b, *ApJ*, 651, 835
- Davidson, K. 1972, *ApJ*, 171, 213
- De Rosa, G., et al. 2013, *ArXiv e-prints:arXiv:1311.3260*
- Denney, K. D. 2012, *ApJ*, 759, 44
- Denney, K. D., Peterson, B. M., Dietrich, M., Vestergaard, M., & Bentz, M. C. 2009a, *ApJ*, 692, 246
- . 2009b, *ApJ*, 692, 246

- Denney, K. D., Pogge, R. W., Assef, R. J., Kochanek, C. S., Peterson, B. M., & Vestergaard, M. 2013, *ApJ*, 775, 60
- Denney, K. D., et al. 2006, *ApJ*, 653, 152
- . 2010, *ApJ*, 721, 715
- Di Matteo, P., Combes, F., Melchior, A.-L., & Semelin, B. 2007, *A&A*, 468, 61
- Di Matteo, T., Springel, V., & Hernquist, L. 2005, *Nature*, 433, 604
- Díaz-Santos, T., Alonso-Herrero, A., Colina, L., Ryder, S. D., & Knapen, J. H. 2007, *ApJ*, 661, 149
- Dietrich, M., et al. 1998, *ApJS*, 115, 185
- . 2002, *ApJ*, 581, 912
- Doi, Y., et al. 2012, *Publication of Korean Astronomical Society*, 27, 111
- Done, C., Davis, S. W., Jin, C., Blaes, O., & Ward, M. 2012, *MNRAS*, 420, 1848
- Downes, D., & Solomon, P. M. 1998, *ApJ*, 507, 615
- Driver, S. P., et al. 2006, *MNRAS*, 368, 414
- Du, P., Hu, C., Lu, K.-X., Wang, F., Qiu, J., Li, Y.-R., Bai, J.-M., Kaspi, S., Netzer, H., Wang, J.-M., & SEAMBH Collaboration. 2014, *ApJ*, 782, 45
- Elbaz, D., Le Floc'h, E., Dole, H., & Marcillac, D. 2005, *A&A*, 434, L1
- Elbaz, D., et al. 2007, *A&A*, 468, 33
- Ellison, S. L., Mendel, J. T., Scudder, J. M., Patton, D. R., & Palmer, M. J. D. 2013, *MNRAS*, 430, 3128
- Ellison, S. L., Patton, D. R., Simard, L., & McConnachie, A. W. 2008, *AJ*, 135, 1877
- Elvis, M. 2000, *ApJ*, 545, 63
- Elvis, M., & Karovska, M. 2002, *ApJ*, 581, L67
- Elvis, M., et al. 1994, *ApJS*, 95, 1
- Erb, D. K., Shapley, A. E., Pettini, M., Steidel, C. C., Reddy, N. A., & Adelberger, K. L. 2006, *ApJ*, 644, 813
- Faber, S. M., et al. 2007, *ApJ*, 665, 265
- Fabian, A. C. 1999, *MNRAS*, 308, L39
- . 2012, *ARA&A*, 50, 455
- Fabian, A. C., Iwasawa, K., Reynolds, C. S., & Young, A. J. 2000, *PASP*, 112, 1145
- Farrah, D., et al. 2001, *MNRAS*, 326, 1333
- . 2008, *ApJ*, 677, 957

- Ferland, G. J., Peterson, B. M., Horne, K., Welsh, W. F., & Nahar, S. N. 1992, *ApJ*, 387, 95
- Ferrarese, L., & Ford, H. 2005a, *Space Sci. Rev.*, 116, 523
- . 2005b, *Space Sci. Rev.*, 116, 523
- Ferrarese, L., & Merritt, D. 2000, *ApJ*, 539, L9
- Fine, S., et al. 2010, *MNRAS*, 409, 591
- Fisher, K. B., Huchra, J. P., Strauss, M. A., Davis, M., Yahil, A., & Schlegel, D. 1995, *ApJS*, 100, 69
- Fynbo, J. P. U., et al. 2013, *MNRAS*, 436, 361
- Gaskell, C. M., & Peterson, B. M. 1987, *ApJS*, 65, 1
- Gebhardt, K., et al. 2000, *ApJ*, 539, L13
- Gehrels, N. 1986, *ApJ*, 303, 336
- George, I. M., & Fabian, A. C. 1991, *MNRAS*, 249, 352
- Ghez, A. M., et al. 2008, *ApJ*, 689, 1044
- Gierliński, M., & Done, C. 2004, *MNRAS*, 349, L7
- Gies, D. R., & Bolton, C. T. 1986, *ApJ*, 304, 371
- Gilbert, K. M., & Peterson, B. M. 2003, *ApJ*, 587, 123
- Gillessen, S., Eisenhauer, F., Trippe, S., Alexander, T., Genzel, R., Martins, F., & Ott, T. 2009, *ApJ*, 692, 1075
- Gillispie, C. C. 1997, *Pierre-Simon Laplace (1749-1827) : a life in exact science*
- Goto, T. 2005, *MNRAS*, 360, 322
- Goto, T., et al. 2011, *MNRAS*, 414, 1903
- Graham, A. W. 2007, *MNRAS*, 379, 711
- Graham, A. W., Onken, C. A., Athanassoula, E., & Combes, F. 2011, *MNRAS*, 412, 2211
- Greene, J. E., & Ho, L. C. 2005, *ApJ*, 630, 122
- . 2007, *ApJ*, 667, 131
- Greene, J. E., et al. 2010, *ApJ*, 723, 409
- Grier, C. J., et al. 2012a, *ApJ*, 744, L4
- . 2012b, *ApJ*, 755, 60
- . 2013a, *ApJ*, 773, 90
- . 2013b, *ApJ*, 764, 47
- Grupe, D., Komossa, S., Leighly, K. M., & Page, K. L. 2010, *ApJS*, 187, 64

- Gültekin, K., et al. 2009, *ApJ*, 698, 198
- Guo, K., Zheng, X. Z., & Fu, H. 2013, *ApJ*, 778, 23
- Haardt, F., & Maraschi, L. 1991, *ApJ*, 380, L51
- Haas, M., Chini, R., Ramolla, M., Pozo Nuñez, F., Westhues, C., Watermann, R., Hoffmeister, V., & Murphy, M. 2011, *A&A*, 535, A73
- Häring, N., & Rix, H.-W. 2004, *ApJ*, 604, L89
- Harms, R. J., et al. 1994, *ApJ*, 435, L35
- Heckman, T. M., Lehnert, M. D., Strickland, D. K., & Armus, L. 2000, *ApJS*, 129, 493
- Helou, G. 1986, *ApJ*, 311, L33
- Hogg, D. W., Blanton, M. R., Eisenstein, D. J., Gunn, J. E., Schlegel, D. J., Zehavi, I., Bahcall, N. A., Brinkmann, J., Csabai, I., Schneider, D. P., Weinberg, D. H., & York, D. G. 2003, *ApJ*, 585, L5
- Hönig, S. F. 2014, ArXiv e-prints: arXiv:1401.2999
- Hönig, S. F., Beckert, T., Ohnaka, K., & Weigelt, G. 2006, *A&A*, 452, 459
- Hopkins, P. F., Cox, T. J., Dutta, S. N., Hernquist, L., Kormendy, J., & Lauer, T. R. 2009a, *ApJS*, 181, 135
- Hopkins, P. F., Cox, T. J., Kereš, D., & Hernquist, L. 2008a, *ApJS*, 175, 390
- Hopkins, P. F., Hernquist, L., Cox, T. J., Di Matteo, T., Robertson, B., & Springel, V. 2006, *ApJS*, 163, 1
- Hopkins, P. F., Hernquist, L., Cox, T. J., & Kereš, D. 2008b, *ApJS*, 175, 356
- Hopkins, P. F., Hernquist, L., Cox, T. J., Robertson, B., & Krause, E. 2007, *ApJ*, 669, 45
- Hopkins, P. F., Murray, N., & Thompson, T. A. 2009b, *MNRAS*, 398, 303
- Hou, L. G., Wu, X.-B., & Han, J. L. 2009, *ApJ*, 704, 789
- Hubeny, I., Blaes, O., Krolik, J. H., & Agol, E. 2001, *ApJ*, 559, 680
- Hwang, H. S., Serjeant, S., Lee, M. G., Lee, K. H., & White, G. J. 2007, *MNRAS*, 375, 115
- Ilbert, O., et al. 2006, *A&A*, 457, 841
- Imanishi, M. 2009, *ApJ*, 694, 751
- Ishida, C. M. 2004, PhD thesis, UNIVERSITY OF HAWAII
- Jahnke, K., & Macciò, A. V. 2011, *ApJ*, 734, 92
- Jiang, L., Fan, X., Brandt, W. N., Carilli, C. L., Egami, E., Hines, D. C., Kurk, J. D., Richards, G. T., Shen, Y., Strauss, M. A., Vestergaard, M., & Walter, F. 2010, *Nature*, 464, 380
- Jiang, L., et al. 2007, *AJ*, 134, 1150

- Jin, C., Ward, M., Done, C., & Gelbord, J. 2012a, MNRAS, 420, 1825
— . 2012b, MNRAS, 420, 1825
- Johnson, S. P., et al. 2013, MNRAS, 431, 662
- Jones, D. H., et al. 2004, MNRAS, 355, 747
- Kartaltepe, J. S., et al. 2012, ApJ, 757, 23
- Kaspi, S., Brandt, W. N., Maoz, D., Netzer, H., Schneider, D. P., & Shemmer, O. 2007a, ApJ, 659, 997
— . 2007b, ApJ, 659, 997
- Kaspi, S., Maoz, D., Netzer, H., Peterson, B. M., Vestergaard, M., & Jannuzi, B. T. 2005, ApJ, 629, 61
- Kaspi, S., Smith, P. S., Netzer, H., Maoz, D., Jannuzi, B. T., & Giveon, U. 2000, ApJ, 533, 631
- Kaspi, S., et al. 1996, ApJ, 470, 336
- Kauffmann, G., et al. 2003a, MNRAS, 341, 54
— . 2003b, MNRAS, 346, 1055
- Kellermann, K. I., Sramek, R., Schmidt, M., Shaffer, D. B., & Green, R. 1989, AJ, 98, 1195
- Kelly, B. C. 2007, ApJ, 665, 1489
- Kelly, B. C., Bechtold, J., & Siemiginowska, A. 2009, ApJ, 698, 895
- Kelly, B. C., & Merloni, A. 2012, *Advances in Astronomy*, 2012
- Kelly, B. C., & Shen, Y. 2013a, ApJ, 764, 45
— . 2013b, ApJ, 764, 45
- Kelly, B. C., Vestergaard, M., Fan, X., Hopkins, P., Hernquist, L., & Siemiginowska, A. 2010, ApJ, 719, 1315
- Kennicutt, Jr., R. C. 1998, ARA&A, 36, 189
- Kerr, R. P. 1963, Phys. Rev. Lett., 11, 237
- Kewley, L. J., Geller, M. J., & Barton, E. J. 2006, AJ, 131, 2004
- Khachikian, E. Y., & Weedman, D. W. 1974, ApJ, 192, 581
- Kilerci Eser, E., Vestergaard, M., Peterson, B. M., Denney, K., & Bentz, M. C. 2014, Submitted to ApJ
- Kim, D.-C., & Sanders, D. B. 1998a, ApJS, 119, 41
— . 1998b, ApJS, 119, 41
- Kim, D.-C., Veilleux, S., & Sanders, D. B. 1998, ApJ, 508, 627

- . 2002, *ApJS*, 143, 277
- King, A. 2003, *ApJ*, 596, L27
- King, A. L., Davis, T. M., Denney, K., Vestergaard, M., & Watson, D. 2013a, ArXiv e-prints
- . 2013b, ArXiv e-prints: arXiv:1311.2356
- Kinney, A. L., Calzetti, D., Bohlin, R. C., McQuade, K., Storchi-Bergmann, T., & Schmitt, H. R. 1996, *ApJ*, 467, 38
- Kollatschny, W. 2003, *A&A*, 407, 461
- Kollatschny, W., & Zetzl, M. 2011, *Nature*, 470, 366
- Komatsu, E., et al. 2011, *ApJS*, 192, 18
- Koratkar, A., & Blaes, O. 1999, *PASP*, 111, 1
- Koratkar, A. P., & Gaskell, C. M. 1991, *ApJ*, 370, L61
- Korista, K., Baldwin, J., Ferland, G., & Verner, D. 1997a, *ApJS*, 108, 401
- Korista, K., Ferland, G., & Baldwin, J. 1997b, *ApJ*, 487, 555
- Korista, K. T., et al. 1995, *ApJS*, 97, 285
- Kormendy, J., & Ho, L. C. 2013, *ARA&A*, 51, 511
- Kormendy, J., & Richstone, D. 1995, *ARA&A*, 33, 581
- Kozłowski, S., et al. 2010, *ApJ*, 708, 927
- Krogager, J.-K., et al. 2013, *MNRAS*, 433, 3091
- Kroupa, P. 2001, *MNRAS*, 322, 231
- Laor, A. 1998, *ApJ*, 505, L83
- Laor, A., Fiore, F., Elvis, M., Wilkes, B. J., & McDowell, J. C. 1997, *ApJ*, 477, 93
- Lara-López, M. A., et al. 2010, *A&A*, 521, L53
- Lawrence, A., Rowan-Robinson, M., Ellis, R. S., Frenk, C. S., Efstathiou, G., Kaiser, N., Saunders, W., Parry, I. R., Xiaoyang, X., & Crawford, J. 1999, *MNRAS*, 308, 897
- Le Floch, E., et al. 2005, *ApJ*, 632, 169
- Lo, K. Y. 2005, *ARA&A*, 43, 625
- Lonsdale, C. J., Farrah, D., & Smith, H. E. 2006, *Ultraluminous Infrared Galaxies*, ed. J. W. Mason, 285
- Lynden-Bell, D. 1969, *Nature*, 223, 690
- MacLeod, C. L., et al. 2010, *ApJ*, 721, 1014
- Madau, P., & Rees, M. J. 2001, *ApJ*, 551, L27

- Magdziarz, P., Blaes, O. M., Zdziarski, A. A., Johnson, W. N., & Smith, D. A. 1998a, *MNRAS*, 301, 179
- . 1998b, *MNRAS*, 301, 179
- Magorrian, J., et al. 1998, *AJ*, 115, 2285
- Maiolino, R., et al. 2008, *A&A*, 488, 463
- Malkan, M. A. 1983, *ApJ*, 268, 582
- Mannucci, F., Cresci, G., Maiolino, R., Marconi, A., & Gnerucci, A. 2010, *MNRAS*, 408, 2115
- Mannucci, F., et al. 2009, *MNRAS*, 398, 1915
- Maoz, D., et al. 1998, *AJ*, 116, 55
- Maraston, C. 2005, *MNRAS*, 362, 799
- Maraston, C., & Strömbäck, G. 2011, *MNRAS*, 418, 2785
- Maraston, C., Strömbäck, G., Thomas, D., Wake, D. A., & Nichol, R. C. 2009, *MNRAS*, 394, L107
- Maraston, C., et al. 2012, *ArXiv e-prints*
- Marconi, A., Axon, D. J., Maiolino, R., Nagao, T., Pietrini, P., Risaliti, G., Robinson, A., & Torricelli, G. 2009, *ApJ*, 698, L103
- Marconi, A., & Hunt, L. K. 2003, *ApJ*, 589, L21
- Marconi, A., et al. 2008, *ApJ*, 678, 693
- Markwardt, C. B. 2009, in *Astronomical Society of the Pacific Conference Series*, Vol. 411, *Astronomical Data Analysis Software and Systems XVIII*, ed. D. A. Bohlender, D. Durand, & P. Dowler, 251
- Marziani, P., Sulentic, J. W., Zamanov, R., Calvani, M., Dultzin-Hacyan, D., Bachev, R., & Zwitter, T. 2003, *ApJS*, 145, 199
- Mason, R. E., et al. 2006, *ApJ*, 640, 612
- Mathews, W. G., & Capriotti, E. R. 1985, in *Astrophysics of Active Galaxies and Quasi-Stellar Objects*, ed. J. S. Miller, 185–233
- McGill, K. L., Woo, J.-H., Treu, T., & Malkan, M. A. 2008, *ApJ*, 673, 703
- McLure, R. J., & Dunlop, J. S. 2004, *MNRAS*, 352, 1390
- McLure, R. J., & Jarvis, M. J. 2002a, *MNRAS*, 337, 109
- . 2002b, *MNRAS*, 337, 109
- McNamara, B. R., & Nulsen, P. E. J. 2007, *ARA&A*, 45, 117
- Melia, F. 2013, *ArXiv e-prints*: arXiv:1312.5798
- Merloni, A., & Heinz, S. 2007, *MNRAS*, 381, 589

- Michałowski, M. J., Dunlop, J. S., Cirasuolo, M., Hjorth, J., Hayward, C. C., & Watson, D. 2012, *A&A*, 541, A85
- Michell, J. 1784, *Royal Society of London Philosophical Transactions Series I*, 74, 35
- Mihos, J. C., & Hernquist, L. 1996, *ApJ*, 464, 641
- Miller, M. C., & Hamilton, D. P. 2002, *MNRAS*, 330, 232
- Miyoshi, M., Moran, J., Herrnstein, J., Greenhill, L., Nakai, N., Diamond, P., & Inoue, M. 1995, *Nature*, 373, 127
- Molina, M., et al. 2013, *MNRAS*, 433, 1687
- Montuori, M., Di Matteo, P., Lehnert, M. D., Combes, F., & Semelin, B. 2010, *A&A*, 518, A56
- Mortlock, D. J., Warren, S. J., Venemans, B. P., Patel, M., Hewett, P. C., McMahon, R. G., Simpson, C., Theuns, T., González-Solares, E. A., Adamson, A., Dye, S., Hambly, N. C., Hirst, P., Irwin, M. J., Kuiper, E., Lawrence, A., & Röttgering, H. J. A. 2011, *Nature*, 474, 616
- Moshir, M., & et al. 1990, in *IRAS Faint Source Catalogue, version 2.0 (1990)*, 0
- Moshir, M., Kopman, G., & Conrow, T. A. O. 1992, *IRAS Faint Source Survey, Explanatory supplement version 2*
- Murakami, H., et al. 2007, *PASJ*, 59, 369
- Murdin, P., & Webster, B. L. 1971, *Nature*, 233, 110
- Murray, N., Quataert, E., & Thompson, T. A. 2005, *ApJ*, 618, 569
- Mushotzky, R. F., Done, C., & Pounds, K. A. 1993, *ARA&A*, 31, 717
- Muzzin, A., et al. 2012, *ApJ*, 746, 188
- Nagar, N. M., Falcke, H., & Wilson, A. S. 2005, *A&A*, 435, 521
- Nandra, K., George, I. M., Mushotzky, R. F., Turner, T. J., & Yaqoob, T. 1997, *ApJ*, 488, L91
- Nandra, K., Le, T., George, I. M., Edelson, R. A., Mushotzky, R. F., Peterson, B. M., & Turner, T. J. 2000, *ApJ*, 544, 734
- Nandra, K., & Pounds, K. A. 1994, *MNRAS*, 268, 405
- Nandra, K., Pounds, K. A., Stewart, G. C., George, I. M., Hayashida, K., Makino, F., & Ohashi, T. 1991, *MNRAS*, 248, 760
- Nardini, E., Risaliti, G., Watabe, Y., Salvati, M., & Sani, E. 2010, *MNRAS*, 405, 2505
- Natarajan, P., & Volonteri, M. 2012, *MNRAS*, 422, 2051
- Netzer, H. 2009, *ApJ*, 695, 793
- Netzer, H., & Marziani, P. 2010, *ApJ*, 724, 318
- Neugebauer, G., et al. 1984, *ApJ*, 278, L1
- Newman, E. T., Couch, E., Chinnapared, K., Exton, A., Prakash, A., & Torrence, R. 1965, 6, 918

- Noeske, K. G., et al. 2007, *ApJ*, 660, L43
- O'Brien, P. T., et al. 1998, *ApJ*, 509, 163
- Onken, C. A., & Peterson, B. M. 2002, *ApJ*, 572, 746
- Onken, C. A., et al. 2004, *ApJ*, 615, 645
- Oppenheimer, J. R., & Snyder, H. 1939, *Physical Review*, 56, 455
- Orosz, J. A., McClintock, J. E., Aufdenberg, J. P., Remillard, R. A., Reid, M. J., Narayan, R., & Gou, L. 2011, *ApJ*, 742, 84
- Osterbrock, D. E., & Ferland, G. J. 2006, *Astrophysics of gaseous nebulae and active galactic nuclei* (CA: University Science Books)
- Pancoast, A., Brewer, B. J., Treu, T., Park, D., Barth, A. J., Bentz, M. C., & Woo, J.-H. 2013, *ArXiv e-prints*
- Pancoast, A., et al. 2012, *ApJ*, 754, 49
- Park, D., Kelly, B. C., Woo, J.-H., & Treu, T. 2012a, *ApJS*, 203, 6
- Park, D., Woo, J.-H., Denney, K. D., & Shin, J. 2013, *ApJ*, 770, 87
- Park, D., et al. 2012b, *ApJ*, 747, 30
- Pasquali, A., Kauffmann, G., & Heckman, T. M. 2005, *MNRAS*, 361, 1121
- Pearson, K. 1895, *Proc. Royal Soc. London*
- Peng, C. Y. 2007, *ApJ*, 671, 1098
- Penrose, R. 1965, *Phys. Rev. Lett.*, 14, 57
- Perlmutter, S., et al. 1999, *ApJ*, 517, 565
- Peterson, B. M. 1988, *PASP*, 100, 18
- . 1993, *PASP*, 105, 247
- . 1997, *An Introduction to Active Galactic Nuclei* (Cambridge, New York Cambridge University Press)
- Peterson, B. M. 2010, in *IAU Symposium, Vol. 267, IAU Symposium*, 151–160
- Peterson, B. M., & Wandel, A. 1999, *ApJ*, 521, L95
- Peterson, B. M., et al. 1991, *ApJ*, 368, 119
- . 1992, *ApJ*, 392, 470
- . 1998, *PASP*, 110, 660
- . 2002, *ApJ*, 581, 197
- . 2004, *ApJ*, 613, 682

- . 2013a, *ApJ*, 779, 109
- . 2013b, *ApJ*, 779, 109
- Pier, J. R., et al. 2003, *AJ*, 125, 1559
- Planck Collaboration, Ade, P. A. R., Aghanim, N., Armitage-Caplan, C., Arnaud, M., Ashdown, M., Atrio-Barandela, F., Aumont, J., Baccigalupi, C., Banday, A. J., & et al. 2013, ArXiv e-prints
- Pounds, K. A., Nandra, K., Fink, H. H., & Makino, F. 1994, *MNRAS*, 267, 193
- Pounds, K. A., Stanger, V. J., Turner, T. J., King, A. R., & Czerny, B. 1987, *MNRAS*, 224, 443
- Press, W. H., Teukolsky, S. A., Vetterling, W. T., & Flannery, B. P. 1992, *Numerical recipes in FORTRAN. The art of scientific computing* (Cambridge: University Press)
- Rafiee, A., & Hall, P. B. 2011, *ApJS*, 194, 42
- Rees, M. J. 1984, *ARA&A*, 22, 471
- Reichert, G. A., et al. 1994, *ApJ*, 425, 582
- Reynolds, C. S. 1997, *MNRAS*, 286, 513
- Reynolds, C. S., & Nowak, M. A. 2003, *Phys. Rep.*, 377, 389
- Richards, G. T., et al. 2002, *AJ*, 123, 2945
- . 2003, *AJ*, 126, 1131
- . 2006a, *ApJS*, 166, 470
- . 2006b, *AJ*, 131, 2766
- Rieke, G. H. 1978, *ApJ*, 226, 550
- Rieke, G. H., & Low, F. J. 1972, *ApJ*, 176, L95
- Rieke, G. H., et al. 2009, *ApJ*, 692, 556
- Riess, A. G., et al. 1998, *AJ*, 116, 1009
- Rodighiero, G., et al. 2011, *ApJ*, 739, L40
- Rodríguez-Pascual, P. M., et al. 1997, *ApJS*, 110, 9
- Rodríguez Zaurín, J., Tadhunter, C. N., & González Delgado, R. M. 2010, *MNRAS*, 403, 1317
- Ross, R. R., & Fabian, A. C. 1993, *MNRAS*, 261, 74
- . 2005, *MNRAS*, 358, 211
- Rowan-Robinson, M. 2000, *MNRAS*, 316, 885
- Rujopakarn, W., Rieke, G. H., Eisenstein, D. J., & Juneau, S. 2011, *ApJ*, 726, 93
- Runnoe, J. C., Brotherton, M. S., & Shang, Z. 2012, ArXiv e-prints
- Rupke, D. S., Veilleux, S., & Sanders, D. B. 2005, *ApJS*, 160, 115

- Rupke, D. S. N., & Veilleux, S. 2011, *ApJ*, 729, L27
- Rupke, D. S. N., Veilleux, S., & Baker, A. J. 2008, *ApJ*, 674, 172
- Salpeter, E. E. 1955, *ApJ*, 121, 161
- Sanders, D. B., Mazzarella, J. M., Kim, D.-C., Surace, J. A., & Soifer, B. T. 2003, *AJ*, 126, 1607
- Sanders, D. B., & Mirabel, I. F. 1996a, *ARA&A*, 34, 749
- . 1996b, *ARA&A*, 34, 749
- Sanders, D. B., Phinney, E. S., Neugebauer, G., Soifer, B. T., & Matthews, K. 1989, *ApJ*, 347, 29
- Sanders, D. B., Soifer, B. T., Elias, J. H., Neugebauer, G., & Matthews, K. 1988a, *ApJ*, 328, L35
- . 1988b, *ApJ*, 328, L35
- Sanders, D. B., et al. 1988c, *ApJ*, 325, 74
- Santini, P., et al. 2009, *A&A*, 504, 751
- . 2013, ArXiv e-prints
- Santos-Lleo, M., et al. 1997, *ApJS*, 112, 271
- Sarzi, M., et al. 2006, *MNRAS*, 366, 1151
- . 2010, *MNRAS*, 402, 2187
- Saunders, W., et al. 2000, *MNRAS*, 317, 55
- Schartmann, M., Meisenheimer, K., Camenzind, M., Wolf, S., Tristram, K. R. W., & Henning, T. 2008, *A&A*, 482, 67
- Schlafly, E. F., & Finkbeiner, D. P. 2011, *ApJ*, 737, 103
- Schlegel, D. J., Finkbeiner, D. P., & Davis, M. 1998, *ApJ*, 500, 525
- Schmidt, K. B., Marshall, P. J., Rix, H.-W., Jester, S., Hennawi, J. F., & Dobler, G. 2010, *ApJ*, 714, 1194
- Schmidt, M. 1963, *Nature*, 197, 1040
- Schulze, A., & Wisotzki, L. 2010, *A&A*, 516, A87
- Schwarzschild, K. 1916, *Abh. Konigl. Preuss. Akad. Wissenschaften Jahre 1906,92*, Berlin, 1907, 1916, 189
- Sergeev, S. G., Doroshenko, V. T., Dzyuba, S. A., Peterson, B. M., Pogge, R. W., & Pronik, V. I. 2007a, *ApJ*, 668, 708
- . 2007b, *ApJ*, 668, 708
- Seyfert, C. K. 1943, *ApJ*, 97, 28
- Shakura, N. I., & Sunyaev, R. A. 1973, *A&A*, 24, 337

- Shen, Y., & Kelly, B. C. 2012, *ApJ*, 746, 169
- Shen, Y., et al. 2011, *ApJS*, 194, 45
- Shields, G. A. 1978, *Nature*, 272, 706
- Siebenmorgen, R., & Krügel, E. 2007, *A&A*, 461, 445
- Silk, J., & Rees, M. J. 1998, *A&A*, 331, L1
- Sobolewska, M. A., Siemiginowska, A., & Życki, P. T. 2004, *ApJ*, 617, 102
- Soifer, B. T., & Neugebauer, G. 1991, *AJ*, 101, 354
- Soifer, B. T., et al. 1987, *ApJ*, 320, 238
- . 2000, *AJ*, 119, 509
- Spoon, H. W. W., et al. 2013, *ApJ*, 775, 127
- Springel, V., Di Matteo, T., & Hernquist, L. 2005, *MNRAS*, 361, 776
- Stanford, S. A., Stern, D., van Breugel, W., & De Breuck, C. 2000, *ApJS*, 131, 185
- Stirpe, G. M., et al. 1994, *ApJ*, 425, 609
- Strauss, M. A., Huchra, J. P., Davis, M., Yahil, A., Fisher, K. B., & Tonry, J. 1992, *ApJS*, 83, 29
- Sunyaev, R. A., & Titarchuk, L. G. 1980, *A&A*, 86, 121
- Surace, J. A. 1998, PhD thesis, Institute for Astronomy University of Hawaii 2680 Woodlawn Dr. Honolulu, HI 96822
- Tacconi, L. J., et al. 2008, *ApJ*, 680, 246
- . 2010, *Nature*, 463, 781
- Tadaki, K.-i., Kodama, T., Tanaka, I., Hayashi, M., Koyama, Y., & Shimakawa, R. 2013, *ApJ*, 778, 114
- Takagi, T., Ono, Y., Shimasaku, K., & Hanami, H. 2008, *MNRAS*, 389, 775
- Takagi, T., et al. 2010, *A&A*, 514, A5
- Tanaka, Y., et al. 1995, *Nature*, 375, 659
- Taylor, J. 1997, *Introduction to Error Analysis, the Study of Uncertainties in Physical Measurements*, 2nd Edition (University Science Books)
- Thomas, D., et al. 2013, *MNRAS*, 431, 1383
- Toomre, A., & Toomre, J. 1972, *ApJ*, 178, 623
- Torrey, P., Cox, T. J., Kewley, L., & Hernquist, L. 2012, *ApJ*, 746, 108
- Trakhtenbrot, B., & Netzer, H. 2012, *MNRAS*, 427, 3081
- Tremaine, S., et al. 2002, *ApJ*, 574, 740

- Tremonti, C. A., et al. 2004, *ApJ*, 613, 898
- Tully, R. B., Rizzi, L., Shaya, E. J., Courtois, H. M., Makarov, D. I., & Jacobs, B. A. 2009, *AJ*, 138, 323
- Turner, T. J., & Pounds, K. A. 1989, *MNRAS*, 240, 833
- Urry, C. M., & Padovani, P. 1995, *PASP*, 107, 803
- Vanden Berk, D. E., et al. 2004, *ApJ*, 601, 692
- Vasudevan, R. V., & Fabian, A. C. 2007, *MNRAS*, 381, 1235
- . 2009, *MNRAS*, 392, 1124
- Vasudevan, R. V., Mushotzky, R. F., Winter, L. M., & Fabian, A. C. 2009, *MNRAS*, 399, 1553
- Veilleux, S., Kim, D.-C., & Sanders, D. B. 1999a, *ApJ*, 522, 113
- . 2002, *ApJS*, 143, 315
- Veilleux, S., Sanders, D. B., & Kim, D.-C. 1999b, *ApJ*, 522, 139
- Veilleux, S., et al. 2006, *ApJ*, 643, 707
- . 2009, *ApJS*, 182, 628
- . 2013, *ApJ*, 776, 27
- Vestergaard, M. 2002, *ApJ*, 571, 733
- . 2004, *ApJ*, 601, 676
- Vestergaard, M., Fan, X., Tremonti, C. A., Osmer, P. S., & Richards, G. T. 2008, *ApJ*, 674, L1
- Vestergaard, M., & Osmer, P. S. 2009, *ApJ*, 699, 800
- Vestergaard, M., & Peterson, B. M. 2006, *ApJ*, 641, 689
- Vestergaard, M., et al. 2011, in *Narrow-Line Seyfert 1 Galaxies and their Place in the Universe*
- Volonteri, M., & Bellovary, J. 2012, *Reports on Progress in Physics*, 75, 124901
- Walter, R., & Fink, H. H. 1993, *A&A*, 274, 105
- Wandel, A., Peterson, B. M., & Malkan, M. A. 1999, *ApJ*, 526, 579
- Wanders, I., et al. 1997, *ApJS*, 113, 69
- Wang, J.-G., et al. 2009, *ApJ*, 707, 1334
- Wang, L., & Rowan-Robinson, M. 2009, *MNRAS*, 398, 109
- Warner, C., Hamann, F., & Dietrich, M. 2003, *ApJ*, 596, 72
- Warwick, R. S., et al. 1996, *ApJ*, 470, 349
- Watson, D., Denney, K. D., Vestergaard, M., & Davis, T. M. 2011, *ApJ*, 740, L49

- Werner, N., Oonk, J. B. R., Sun, M., Nulsen, P. E. J., Allen, S. W., Canning, R. E. A., Simionescu, A., Hoffer, A., Connor, T., Donahue, M., Edge, A. C., Fabian, A. C., von der Linden, A., Reynolds, C. S., & Ruszkowski, M. 2014, *MNRAS*, 439, 2291
- Wheeler, J. A. 1968, *American Scientist*, 56, 1
- White, R. J., & Peterson, B. M. 1994, *PASP*, 106, 879
- Wilhite, B. C., et al. 2005, *ApJ*, 633, 638
- Wolfe, A. M., Gawiser, E., & Prochaska, J. X. 2005, *ARA&A*, 43, 861
- Woo, J.-H., Schulze, A., Park, D., Kang, W.-R., Kim, S. C., & Riechers, D. A. 2013, *ApJ*, 772, 49
- Woo, J.-H., et al. 2010, *ApJ*, 716, 269
- Wright, E. L. 2006, *PASP*, 118, 1711
- Wu, X.-B., Wang, R., Kong, M. Z., Liu, F. K., & Han, J. L. 2004, *A&A*, 424, 793
- Wyder, T. K., Martin, D. C., Schiminovich, D., Seibert, M., Budavári, T., Treyer, M. A., Barlow, T. A., Forster, K., Friedman, P. G., Morrissey, P., Neff, S. G., Small, T., Bianchi, L., Donas, J., Heckman, T. M., Lee, Y.-W., Madore, B. F., Milliard, B., Rich, R. M., Szalay, A. S., Welsh, B. Y., & Yi, S. K. 2007, *ApJS*, 173, 293
- Yamamura, I., et al. 2010, *VizieR Online Data Catalog*, 2298, 0
- York, D. G., et al. 2000, *AJ*, 120, 1579
- Yuan, T.-T., Kewley, L. J., & Sanders, D. B. 2010, *ApJ*, 709, 884
- Zu, Y., Kochanek, C. S., & Peterson, B. M. 2011, *ApJ*, 735, 80
- Zuo, W., Wu, X.-B., Liu, Y.-Q., & Jiao, C.-L. 2012, *ApJ*, 758, 104
- Zwicky, F. 1933, *Helvetica Physica Acta*, 6, 110